Investigation of Heat-driven Polygeneration and Adsorption Cooling Systems

by

Sami M. Alelyani

A Dissertation Presented in Partial Fulfillment
of the Requirements for the Degree
Doctor of Philosophy

Approved July 2018 by the
Graduate Supervisory Committee:

Patrick E Phelan, Chair
Liping Wang
Ellen B Stechel
Ronald J Calhoun
Ali R Alalili

ARIZONA STATE UNIVERSITY

August 2018

ABSTRACT

Just for a moment! Imagine you live in Arizona without air-conditioning systems!

Air-conditioning and refrigeration systems are one of the most crucial systems in anyone's house and car these days. Energy resources are becoming more scarce and expensive. Most of the currently used refrigerants have brought an international concern about global warming. The search for more efficient cooling/refrigeration systems with environmental friendly refrigerants has become more and more important so as to reduce greenhouse gas emissions and ensure sustainable and affordable energy systems. The most widely used air-conditioning and refrigeration system, based on the vapor compression cycle, is driven by converting electricity into mechanical work which is a high quality type of energy. However, these systems can instead be possibly driven by heat, be made solid-state (i.e., thermoelectric cooling), consist entirely of a gaseous working fluid (i.e., reverse Brayton cycle), etc. This research explores several thermally driven cooling systems in order to understand and further overcome some of the major drawbacks associated with their performance as well as their high capital costs. In the second chapter, we investigate the opportunities for integrating single- and double-stage ammonia-water (NH_3–H_2O) absorption refrigeration systems with multi-effect distillation (MED) via cascade of rejected heat for large-scale plants. Similarly, in the third chapter, we explore a new polygeneration cooling-power cycle's performance based on Rankine, reverse Brayton, ejector, and liquid desiccant cycles to produce power, cooling, and possibly fresh water for various configurations. Different configurations are considered from an energy perspective and are compared to stand-alone systems. In the last chapter, a new simple, inexpensive, scalable, environmentally friendly cooling system based on an adsorption heat pump system and evacuated tube solar collector is experimentally and theoretically studied. The system is destined as a small-scale system to harness solar radiation to provide a cooling effect directly in one system.

This dissertation is dedicated to

My Mother & Father

for making me who I am

ACKNOWLEDGMENTS

TABLE OF CONTENTS

LIST OF TABLES

LIST OF FIGURES

NOMENCLATURE

A	Area [m^2]
ACC	Annual capital cost [$ yr^{-1}]
AOC	Annual operational cost [$ yr^{-1}]
AOH	Annual operation hours [hr yr^{-1}]
COP	Coefficient of performance
dP	Pressure difference between the effects of MED [kPa]
dT	Temperature rise of seawater in preheater [$^{\circ}C$]
dx	Mass concentration swing between strong-and-weak solution [%]
η	Efficiency [%]
ε	Effectiveness [%]
GOR	Gained output ratio [kg_{water} kg^{-1}_{steam}]
h	Enthalpy [kJ kg^{-1}]
HHV	Higher heating value [kJ kg^{-1}]
LMTD	Logarithmic mean temperature difference [$^{\circ}C$]
$\dot{m}$	Mass flow rate [kg]
$\dot{Q}$	Heat flow rate [kW]
ρ	Density [kg m^{-3}]
s	Specific entropy [kJ kg^{-1} K^{-1})
S	Entropy generation [kW K^{-1}]
T	Absolute temperature [K^{-1}]
TAC	Total annual cost [$ yr^{-1}]
U	Overall heat transfer coefficient [kW m^{-2} K^{-1}]
UPC	Unit product cost [$ m^{-3} *or* $ ton^{-1}]
v	Specific volume [m^{-3} kg^{-1}]
W	Power [kW]
x	Ammonia mass fraction in the solution [%]
$\dot{X}$	Exergy rate [kW]
x	Water salinity [ppm]
Z	Capital cost [$]
ZF	Amortization factor

Abbreviations

ARS	Absorption refrigeration systems
LC	Plant life cycle [years]
LiBr-H_2O	Water-lithium bromide
MED	Multi effect distillation
TVC	Thermal vapor compression
MSF	Multi stage flash
NH_3-H_2O	Ammonia-water
Nom	Nominal
Opt	Optimal
RO	Reverse osmosis
SW	Seawater feed
TBT	Top brine temperature
mgd	Millon gallons per day

Subscripts

0	Conditions of the environment (dead state)
abs	Absorber
B	Brine stream
C	Cell (effect)
con	Condenser
D	Demister
dest	Destruction
E	Internal surface of the bundle evaporation tubes
EV	Expansion valve
eva	Evaporator
ex	External surface of the bundle evaporation tubes
F	Flash
gen	Generator
H	Hot stream
i	Effect number
II	Second law
L	Water saturated liquid

M	Mixer
p	Pump
P	Preheater
R	Reference component
rec	Rectifier
rej	Rejected seawater
v	Water saturated vapor

1. INTRODUCTION

Since the beginning of the 20th century, different schemes have been emerging in an effort to increase the performance of thermally driven refrigeration systems, but those available to date suffer various drawbacks and challenges compared to the high performing, inexpensive, and uncomplicated vapor compression refrigeration (VCR) system. However, VCR systems typically utilize chlorofluorocarbons (CFCs), hydrochlorofluorocarbons (HCFCs), or hydrofluorocarbons (HFCs) as refrigerants which play a vital role in global warming and ozone depletion. CFCs and HCFCs have been banned and phased out under the Montreal and Kyoto Protocols in 1987 and 1997, respectively, as they were responsible for the depletion of the ozone layer. Accordingly, HFCs are being used as a new refrigerant for VCR systems which have essentially zero ozone depletion potential since they do not contain chlorine. Nevertheless, HFCs and other greenhouse gases have been limited recently due to their high contribution to global warming which brings about international concern. Researchers have been focusing their efforts on developing new, environmental friendly refrigeration systems or refrigerants as HFCs are expected to be prohibited and phased out in the near future [1].

Global energy consumption has been increasing significantly and is estimated to increase by 71% between 2012 and 2040 [2]. For this reason, power utilities have been urgently looking for alternative ways, such as renewable energies, to meet this energy demand growth. VCR systems are high energy-consuming devices which require a high quality of energy since they are electrically driven. From an economic perspective, VCRs may also negatively impact consumers since utilities are able to charge their customers for peak time electricity demand for the sake of preventing power blackouts.

1.1. Motivation

According to the 2016 Future of Air Conditioning for Buildings Report prepared for the USA Department of Energy (DOE), the world annually consumes 1,250 TWh (4.26 Quadrillion Btu) by air conditioning systems which represents 4% of global building site-energy consumption. Air conditioning energy consumption is projected to increase globally 4.5 times by 2050 over 2010 for developing countries versus 1.3 times for developed countries [3].

In a recent report [4] prepared for Oak Ridge National Laboratory (ORNL), an assessment of the potential market for exhaust heat in the industrial sector in the United States was provided. A

breakdown of the exhaust heat energy based on temperature has estimated that 12% is available below 150°C, 25% from 150 to 235°C, 53% from 235 to 650°C, and 12% is above 650°C. Exhaust heat with a temperature over 235°C clearly seems more appealing for power generation than any other applications. On the other hand, thermal energy with a temperature below 235°C still has a broad spectrum of applications [5].

Darwish et al. [6] pointed out that co-generation power desalination plants based on multi-stage flash (MSF) which is widely used, is no longer a viable choice as much more energy-efficient seawater reverse osmosis (SWRO) systems emerge. New configurations for existing and future co-generation power desalination plants are crucial and must be considered.

1.2.   Research Objective

A polygeneration system is an improved version of a cogeneration system in which more than two products are attained such as electricity, refrigeration, or fresh water. Combinations of different types of conventional and renewable energy sources such as fossil fuels or solar thermal energy can be leveraged together into one cycle that provides various services such as electricity, refrigeration, desalinized water, etc. Such systems are capable of ensuring high overall energy conversion efficiency with less environmental impact compared to conventional systems. Furthermore, polygeneration systems are more effective than standalone systems in facing energy price demand fluctuations, which is mutually beneficial to both owners and end-users. Polygeneration has occupied the attention of many researchers and governments focusing on possible configurations of different technologies into one combined system. In fact, the European Union (EU) considers polygeneration as a strategic technology plan with the intention of reducing greenhouse gas emissions and the total cost of energy [7]. For this strategic plan as well as the mentioned motivations above, we present this work with the focus on improving thermally driven polygeneration and adsorption cooling systems from both energy and economic standpoints in which low- and mid-grade heat sources at 200°C and below are utilized.

Three different heat-driven air conditioning and refrigeration systems are examined in three different sections of the dissertation with the goal of eliminating some of the thermal refrigeration systems drawbacks. We propose in the first part (Chapter 2) a new polygeneration configuration that demonstrates the advantages of integrating cooling and desalination based on an ammonia-water absorption refrigeration system and a multi-effect distillation unit, respectively. In the second part (Chapter 3), we explore a new cooling cycle's performance based on the 'Sherbeck' cycle, invented by our colleague Jonathan Sherbeck, which is capable of producing power, cooling, and

possibly fresh water for various configurations. In the third part (Chapter 4), we develop a new simple, inexpensive, scalable, environmentally friendly cooling system based on an adsorption heat pump system.

2. COMBINED COOLING AND DESALINATION

Fresh water demand has gradually increased due to the rapid growth of population and domestic, industrial, and agricultural use. Seawater desalination has been the main, if not only, source of potable water in regions where physical water scarcity is the main challenge. Currently over 30% of the world's population lives in areas suffering from physical water scarcity, and this figure is estimated to surpass 50% by 2025 [8].

Furthermore, drought and desertification have been increasing remarkably in regions worldwide for the past few years, resulting from deficiencies in surface and ground water [9]. In addition, global warming will escalate the risk of drought thus placing more stress on water supplies, even in countries that may not face water shortages today [10]. Refrigeration and air-conditioning demands are also expected to increase from the rise of global temperatures. This makes the environmental impact worse since, as mentioned above, many common refrigerants in use today pose a threat to the environment because of their global warming potential (GWP) and ozone depletion potential (ODP) [11]. In hot and dry climates, such as the Middle East, desalination and refrigeration systems provide two essential products that can be generated in a combined system instead of by separate systems.

In this chapter, we investigate mathematically how integrating the absorption refrigeration system based on ammonia (environmentally friendly refrigerant) with thermally driven desalination unit could decrease the overall energy usage and the operating cost compared with stand-alone systems.

2.1. Review of Literature

With the intention of minimizing the exergy destruction (irreversibility) associated with thermal desalination technologies, and improving the absorption refrigeration system (ARS) performance by operating at lower condenser and absorber temperatures, the possibility of integrating both systems has been previously investigated. Alarcón-Padilla and García-Rodríguez [12] showed that one of the best techniques for thermal desalination processes, to compete with RO, is by integrating an absorption heat pump with an MED system.

Li et al. [9] studied the feasibility of coupling an ammonia-water absorption heat pump with an MED system, where superheated ammonia vapor generated by low-grade heat gets compressed, releasing heat to the MED system as the ammonia vapor is absorbed into the ammonia-water weak solution. The results compared favorably to RO in terms of specific power consumption with a

possible return of investment in three years. It is worth mentioning that their system provides only freshwater—no cooling.

Recently, Esfahani et al. [13] investigated, based on energy and cost measurements, a new system composed of a multi effect evaporation–absorption heat pump (MEE-ABHP) desalination system and a vapor compression refrigeration (VCR) system. The results show that the coupled system can save 57.1% in electrical energy, 5.6% in thermal energy, and 25.6% in total annual cost compared with individual MEE-ABHP and VCR systems.

Aly [14] proposed a system that combines LiBr-H2O ARS with a multi-effect evaporation (MEE) desalination system. He suggested replacing the single-stage ARS condenser and evaporator with the MEE. The system was estimated to produce 1.53 mgd (5.8 ML/d) of fresh water at a performance ratio (PR) of 14.2, and a by-product cooling capacity equivalent to a 220-kWth air conditioning unit at 6.5°C.

Wang and Lior [15, 16] considered replacing a single-effect LiBr–H2O ARS condenser with a low-temperature MEE desalination system. The proposed system achieved an energy consumption reduction of 42%, compared to the stand-alone MEE and ARS systems, with a COP of 1.6 and an exergetic efficiency above 60%.

Gomri [17] proposed to utilize the heat rejection from the absorbers of single- and double-stage absorption heat transformer systems using a separation vessel for seawater desalination purposes. He studied the impact of absorber temperature on COP, second-law efficiency, and fresh water production, and found that fresh water production for the single-stage absorption heat transformer is slightly higher than that for the double stage combined with the desalination unit.

Gude and Nirmalakhandan [18] investigated the possibility of harnessing heat rejected by the condenser of a modified single stage LiBr–H_2O ARS to drive a desalination process. Their results showed that rejected heat by ARS with cooling capacity of about one ton of refrigeration (~3.5 kWth) along with an auxiliary heat input of 208 kJ/kg can produce fresh water at an average rate of 4.5 kg/h.

Recently, Abdulrahim and Darwish [19] considered a new configuration of an absorption cycle, based on LiBr–H_2O, to provide cooling and supply saturated steam to the thermal desalination unit, based on multi-effect distillation, using solar energy as the main energy source. It was found that although the cooling load changes the amount of water production, the gain output ratio is kept constant at 5.7 kg of freshwater per one kg of steam.

5

Jana [20] presented a review about developments in the field of heat pump-assisted distillation technology in general and vapor recompression column in particular for chemical and refinery industries. He suggested that further efforts in improving such an integrated system are needed in order to explore its widespread usage specifically for industrial applications and batch processing.

Li et al. [21] proposed a new distillation system based on absorption heat pump (AHP) where exhaust heat by the AHP's absorber and condenser were used to preheat the feed materials, while cooling capacity was used to cool down the column condenser. Their numerical simulation showed that the steam consumption decreased by 23.3% compared to the base case.

According to this literature review, only LiBr–H2O absorption cycles have been widely studied in connection to integrating with a desalination process, since water acts as a refrigerant in LiBr–H2O ARS. However, ammonia-water ARS has apparently not yet been considered in a system that would generate both fresh water and cooling.

2.2. Absorption Refrigeration System

Absorption refrigeration systems (ARS) are becoming more attractive than before because they provide promising replacements for vapor compression systems by using working fluids with zero ODP, zero GWP, and can be thermally driven. Table 1 provides briefly the advantages and disadvantages of absorption refrigeration over vapor compression refrigeration (VCR) [22].

As presented in Table 1, substantial amounts of heat must be rejected by the condenser and absorber of the ARS into the environment. In fact, the heat rejection factor (ratio of heat rejection to the cooling capacity) is about 2.5 for ARS compared to 1.2 for VCR systems [22]. Consequently, the cooling tower and associated pumping system capacities of ARS are twice the size of those of VCR systems, which leads to higher initial and operating costs.

Table 1. Advantages and Disadvantages of Absorption Over Vapor Compression Refrigeration

Advantages		Disadvantages	
1. Method of Compression of the Refrigerant		1. Corrosion	
VCR	Done by a Compressor	*VCR*	None
ARS	Done by a Pump (after the refrigerant's vapor gets converted to liquid state by the absorbent)	*ARS*	Lithium bromide (LiBr) is highly corrosive in nature. Ammonia (NH3) is highly corrosive to copper

2. Type of Energy Required		2. Initial Capital Cost	
VCR	Electrical	*VCR*	High
ARS	Thermal + Electrical	*ARS*	Very High
3. Amount of Required Electrical Power		3. Working Pressure	
VCR	High	*VCR*	High
ARS	Very Low	*ARS*	Lithium bromide (LiBr): Very Low, Ammonia (NH3): High
4. Running Cost:		4. Coefficient of Performance (COP)	
VCR	High	*VCR*	High
ARS	Low	*ARS*	Low
5. Maintenance		5. Heat Rejection Factor[+]	
VCR	High	*VCR*	Low ≈ 1.2
ARS	Low	*ARS*	High ≈ 2.5

[+] Ratio of heat rejection to the cooling capacity.

2.2.1. Ammonia-water (NH3-H2O) Absorption Refrigeration System

Unlike water-lithium bromide (LiBr–H2O) ARS, ammonia-water (NH3–H2O) ARS can provide very low refrigeration temperatures (down to -60°C), compact unit size due to the low specific volume of NH3 operating at high pressures, and trouble-free operation with no risk of crystallization [23]. Table 2 shows a comparison between two of the most common refrigerants, namely R22 and R134a, and ammonia.

Table 2. Comparison Between Two Common Refrigerants and Ammonia

	NH$_3$ (R717)	**R22**	**R134a**	**Water**
Relative Cost to NH3 per kg	1	2.5 times	7 times	<< 1
Latent heat of vaporization (kJ/kg)	1371	234	216	2257
Boiling point (°C)	-33.34	-40.7	-26.3	100
ODP	0	0.034	0	0
GWP	0	1700	1300	0

In general, the absorption refrigeration system is similar to the vapor compression refrigeration system, except that the compressor in the VCR is replaced by an absorber, pump, and generator. In order to replace the compressor with a pump, the vapor coming out of the evaporator needs to be converted from the vapor state to the liquid state. This is achieved by the absorber where the absorbent (water in NH3-H2O ARS) absorbs the refrigerant vapor (ammonia). Thermal energy is

then added to the compressed weak solution in order to separate the refrigerant from the absorbent by desorption. Single- and double-absorption refrigeration systems are shown in Figure 1 and Figure 2, respectively.

2.2.2. System Description

Following the stream numbering in Figure 1, ammonia vapor (stream 14), coming out of heat exchanger (HX2) where it subcools the condenser outlet stream, is absorbed by the strongly absorbing (i.e., high water content) solution (stream 6), mixing to result in a weaker solution. Heat of absorption released in the absorber is then removed by cooling water (streams C1, C2). The weak solution (stream 1) is brought to a higher pressure (stream 2) using a pump. Heat coming from the generator solution outlet (stream 4) is then recovered to preheat the weak solution (stream 2) through the solution heat exchanger (HX1). In the generator, the heat source, e.g. steam (stream A1, A2), heats up the ammonia-water mixture causing the ammonia (refrigerant) to vaporize along with some water. The rectifier then purifies the ammonia vapor by condensing the water vapor back to the generator (stream 8), an exothermic process. Purified ammonia vapor then continues (stream 9) to be completely condensed at the condenser (stream 10). The liquid refrigerant (stream 12) continues through an expansion valve (EV2), after exchanging heat with the colder evaporator outlet vapor (stream 13, 14). It then flows through the evaporator, providing cooling to the load (stream B1, B2) as it vaporizes (Stream 13).
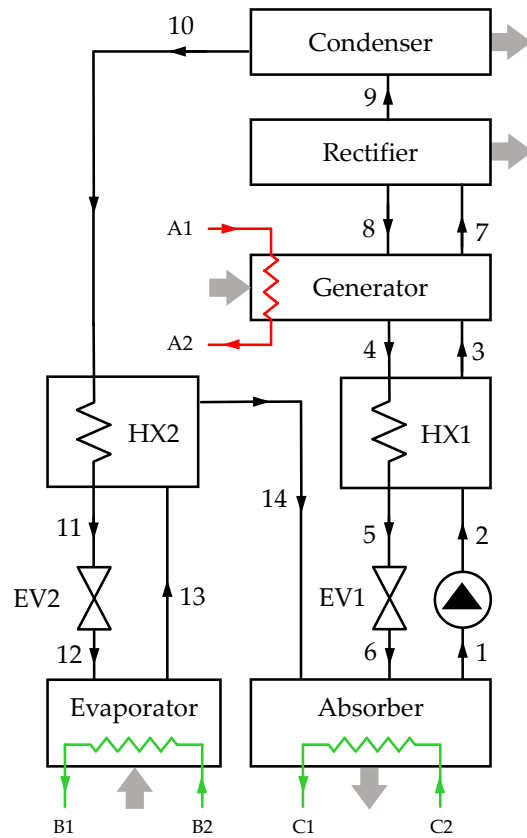
Figure 1. Schematic Diagram of the Single-stage Absorption Refrigeration System

2.2.2.1.   Thermodynamic Model

Although only a system description of the single-stage–NH_3H_2O will be explained in detail, analogous steps can be applied on the double-stage–NH_3H_2O system.

The following assumptions are applied for the thermodynamic model:

  i.   Steady-state operation with negligible kinetic and potential energy.

 ii.   Heat losses and pressure drops in the components and piping are not considered.

iii.   The refrigerant (NH_3), weak solution, and strong solution leaving the condenser, absorber, and generator, respectively, are saturated liquids.

Under the above-mentioned assumptions, the mass (continuity), energy (the first law of thermodynamics), and exergy (the second law of thermodynamics) balance equations are derived for each component of the system [24].
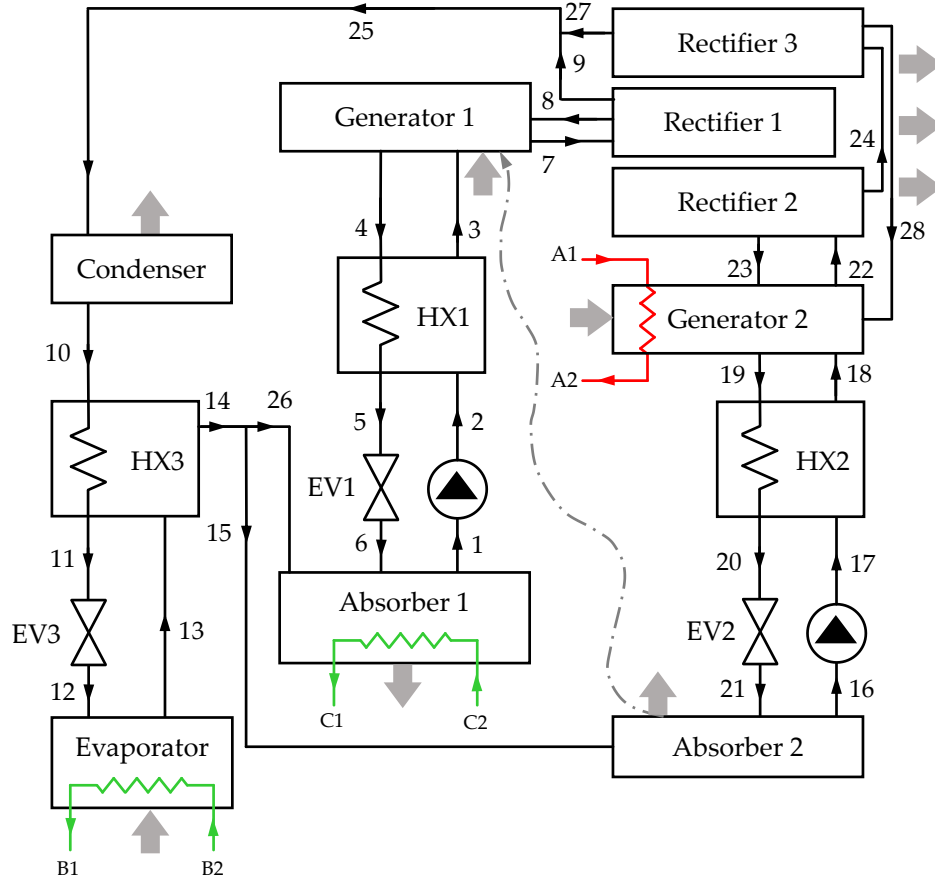
Figure 2. Schematic Diagram of the Double-stage Absorption Refrigeration System

A. The absorber

$$\dot{m}_1 = \dot{m}_6 + \dot{m}_{14} \tag{2.1}$$

$$\dot{m}_1 x_1 = \dot{m}_6 x_6 + \dot{m}_{14} x_{14} \tag{2.2}$$

$$\dot{Q}_{abs} = \dot{m}_6 h_6 + \dot{m}_{14} h_{14} - \dot{m}_1 h_1 \tag{2.3}$$

$$\dot{X}_{dest,abs} = \dot{X}_6 + \dot{X}_{14} + \dot{X}_{C2} - \dot{X}_1 - \dot{X}_{C1} \tag{2.4}$$

where $\dot{m}$ is the mass flow rate, x the ammonia mass fraction, $\dot{Q}_{abs}$ the released heat in the absorber, h the specific enthalpy, and $\dot{X}_{dest,abs}$ the exergy destruction rate in the absorber.

Note that $\dot{X}$ is the flow exergy and is expressed for a given stream as

$$\dot{X} = \dot{m} \cdot \left((h - h_0) - T_0(s - s_0) \right) \tag{2.5}$$

10

where s is the specific entropy, T the absolute temperature (K), and the subscript 0 indicates a reference or dead state, taken to be that of the environment: 25°C and 101.3 kPa.

B. The pump

$$\dot{W}_p = \frac{\dot{m}_1 v_1 (P_2 - P_1)}{\eta_p} \tag{2.6}$$

$$\dot{m}_1 = \dot{m}_2 \tag{2.7}$$

$$x_1 = x_2 \tag{2.8}$$

$$\dot{W}_p = \dot{m}_2 h_2 - \dot{m}_1 h_1 \tag{2.9}$$

$$\dot{X}_{dest,p} = \dot{W}_p + \dot{X}_1 - \dot{X}_2 \tag{2.10}$$

where $\dot{W}_p$ is the pump power, v the weak solution specific volume, P the pressure, η_p the pump isentropic efficiency, and $\dot{X}_{des,p}$ the exergy destruction rate in the pump.

C. The solution heat exchanger (HX1)

$$\dot{m}_4 h_4 - \dot{m}_5 h_5 = \dot{m}_3 h_3 - \dot{m}_2 h_2 \tag{2.11}$$

$$\dot{X}_{dest,HX1} = \dot{X}_4 + \dot{X}_2 - \dot{X}_3 - \dot{X}_5 \tag{2.12}$$

where $\dot{X}_{des,HX1}$ is the exergy destruction rate in the solution heat exchanger.

D. The generator

$$\dot{m}_3 + \dot{m}_8 = \dot{m}_4 + \dot{m}_7 \tag{2.13}$$

$$\dot{m}_3 x_3 + \dot{m}_8 x_8 = \dot{m}_4 x_4 + \dot{m}_7 x_7 \tag{2.14}$$

$$\dot{Q}_{gen} = \dot{m}_4 h_4 + \dot{m}_7 h_7 - \dot{m}_3 h_3 - \dot{m}_8 h_8 \tag{2.15}$$

$$\dot{X}_{dest,gen} = \dot{X}_{A2} + \dot{X}_3 + \dot{X}_8 - \dot{X}_{A1} - \dot{X}_4 - \dot{X}_7 \tag{2.16}$$

where $\dot{Q}_{gen}$ is the required heat input rate of the generator, and $\dot{X}_{des,gen}$ the exergy destruction rate in the generator.

E. The expansion valve 1 (EV1)

$$\dot{m}_5 = \dot{m}_6 \tag{2.17}$$

$$\dot{m}_5 h_5 = \dot{m}_6 h_6 \tag{2.18}$$

$$\dot{X}_{dest,EV1} = \dot{X}_5 - \dot{X}_6 \tag{2.19}$$

where $\dot{X}_{des,EV1}$ is the exergy destruction rate in the expansion valve (EV1).

F. The rectifier

$$\dot{m}_8 + \dot{m}_9 = \dot{m}_7 \tag{2.20}$$

$$\dot{m}_8 x_8 + \dot{m}_9 x_9 = \dot{m}_7 x_7 \tag{2.21}$$

$$\dot{Q}_{rec} = \dot{m}_7 h_7 - \dot{m}_8 h_8 - \dot{m}_9 h_9 \tag{2.22}$$

where $\dot{Q}_{rec}$ is the released heat in the rectifier.

G. The ARS condenser

$$\dot{m}_9 = \dot{m}_{10} \tag{2.23}$$

$$\dot{Q}_{con} = \dot{m}_9 h_9 - \dot{m}_{10} h_{10} \tag{2.24}$$

$$\dot{X}_{dest,rec-con} = \dot{X}_7 + \dot{X}_{swP_1} - \dot{X}_8 - \dot{X}_{10} - \dot{X}_{vex_1} - \dot{X}_{BC_1} \tag{2.25}$$

where $\dot{Q}_{con}$ is the released heat in the condenser, and $\dot{X}_{des,rec-con}$ the exergy destruction rate in the rectifier and condenser. Subscripts swP_1, vex_1, and BC_1 represent seawater feed after preheating 1, generated water vapor, and brine in the first effect, respectively.

H. The condenser-evaporator heat exchanger (HX2)

$$\dot{m}_{10} h_{10} - \dot{m}_{11} h_{11} = \dot{m}_{14} h_{14} - \dot{m}_{13} h_{13} \tag{2.26}$$

$$\dot{X}_{dest,HX2} = \dot{X}_{10} + \dot{X}_{13} - \dot{X}_{11} - \dot{X}_{14} \tag{2.27}$$

where $\dot{X}_{des,HX2}$ is the exergy destruction rate in the condenser-evaporator heat exchanger.

I. The expansion valve 2 (EV2)

$$\dot{m}_{11} = \dot{m}_{12} \tag{2.28}$$

$$\dot{m}_{11} h_{11} = \dot{m}_{12} h_{12} \tag{2.29}$$

$$\dot{X}_{dest,EV2} = \dot{X}_{11} - \dot{X}_{12} \tag{2.30}$$

where $\dot{X}_{des,EV2}$ is the exergy destruction rate in the expansion valve (EV2).

J. The ARS evaporator

$$\dot{m}_{12} = \dot{m}_{13} \tag{2.31}$$

$$\dot{Q}_{eva} = \dot{m}_{13} h_{13} - \dot{m}_{12} h_{12} \tag{2.32}$$

$$\dot{X}_{dest,eva} = \dot{X}_{12} + \dot{X}_{19} - \dot{X}_{20} - \dot{X}_{13} \tag{2.33}$$

where $\dot{Q}_{eva}$ is the absorbed heat in the evaporator, and $\dot{X}_{des,eva}$ the exergy destruction rate in the evaporator.

K. ARS System performance criteria

$$\text{COP} = \frac{\dot{Q}_{eva}}{\dot{Q}_{gen} + \dot{W}_p} \tag{2.34}$$

$$\dot{X}_{dest,ARS} = \dot{X}_{dest,abs} + \dot{X}_{dest,p} + \dot{X}_{dest,HX1} + \dot{X}_{dest,gen} + \dot{X}_{dest,EV1} + \dot{X}_{dest,rec-con}$$
$$+ \dot{X}_{dest,HX2} + \dot{X}_{dest,EV2} + \dot{X}_{dest,eva} \tag{2.35}$$

where COP is the coefficient of performance, and $\dot{X}_{des,ARS}$ the total exergy destruction rate in the ARS subsystem, which for a standalone ARS with no exergy output in the heat rejection streams can be also calculated as:

$$\dot{X}_{dest,ARS} = \dot{X}_{15} - \dot{X}_{16} + \dot{W}_p + \dot{X}_{19} - \dot{X}_{20} \tag{2.36}$$

$$\dot{S}_{gen,ARS} = \frac{\dot{X}_{dest,ARS\ sys}}{T_0} \tag{2.37}$$

$$\eta_{II,ARS} = 1 - \frac{\dot{X}_{dest,ARS\ sys}}{\dot{X}_{15} + \dot{W}_p} \tag{2.38}$$

where $\dot{S}_{gen,ARS}$ is the total entropy generation in the ARS subsystem, and $\eta_{II,ARS}$ the exergetic efficiency (second law efficiency) of the ARS subsystem.

2.2.2.2. Model Validation

The ARS' model was developed using the Engineering Equation Solver (EES) software [25]. The correlations of ammonia-water (NH_3-H_2O) solution, water, and steam properties, provided by EES, were taken in this study. The thermodynamic model was validated by comparing the ARS model with the related work in literature [24, 26] and the obtained results were within ±1%, under the same conditions as shown in Table 3.

Table 3. Validation of Single- and Double-NH_3-H_2O ARS Models

	Model	Ref. [26]	Diff.
Single stage NH_3-H_2O			
COP	0.6	0.598	0.3%
Total entropy generation (kW/K)	0.74	0.736	0.5%
Double stage NH_3-H_2O			
COP	0.1985	0.1973	0.6%
Total entropy generation (kW/K)	0.4568	0.4627	1.3%

The main assumptions for the reference case of both the single- and double-stage NH_3-H_2O systems are summarized in Table 4.

Table 4. Operating Condition Assumptions for Single- and Double- NH_3-H_2O ARS

Parameter	Value	Unit
Absorber outlet temperature (T_1)	40	ºC
Condenser outlet temperature (T_{10})	40	ºC
Evaporator outlet temperature (T_{13})	-10	ºC
Mass flow rate of external heat source ($\dot{m}_A$)	1	kg/s
Specific heat input ($\dot{q}_{source}$)[+]	1940	kJ/kg
Inlet cooling water temperature ($T_{inlet,cooling}$)	27	ºC
Outlet cooling water temperature ($T_{outlet,cooling}$)	32	ºC
Inlet chilled water temperature ($T_{inlet,chilled}$)	2	ºC
Outlet chilled water temperature ($T_{outlet,chilled}$)	-10	ºC
Pump efficiency (η_{pump})	75	%
Heat exchanger 1 effectiveness (ε_{HX1})	100	%
Heat exchanger 2 effectiveness (ε_{HX2})	95	%
Mass concentration between strong-and-weak solution (dx)	0.1	
Ammonia-water mass fraction (q_{13})	99.5	%

[+] Enthalpy of vaporization of water at 200 ºC

2.2.3. Sensitivity Analysis on ARS Performance

2.2.3.1. Effect of Absorber Temperatures on ARS Performance

It can be seen from Figure 3 that the COP of the ARS decreases as the absorber temperature increases. On the other hand, Figure 4 shows that heat rejection through the rectifier(s) increases as the absorber temperature increases for both single- and double-stage NH_3-H_2O ARS.
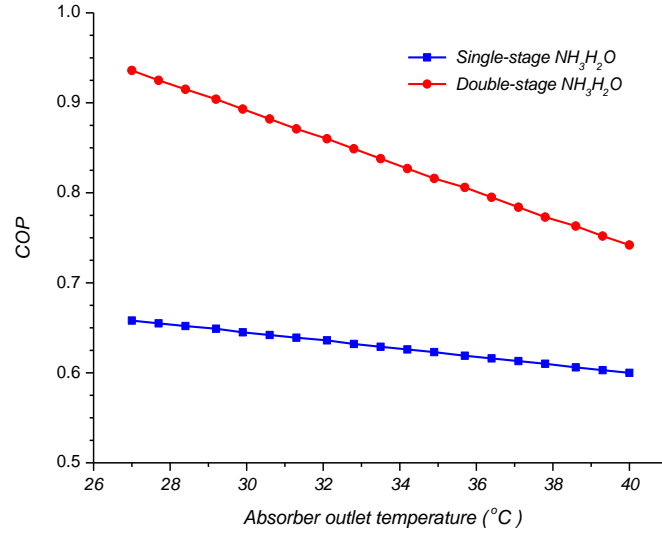
Figure 3. Effect of Absorber Outlet Temperature on COP
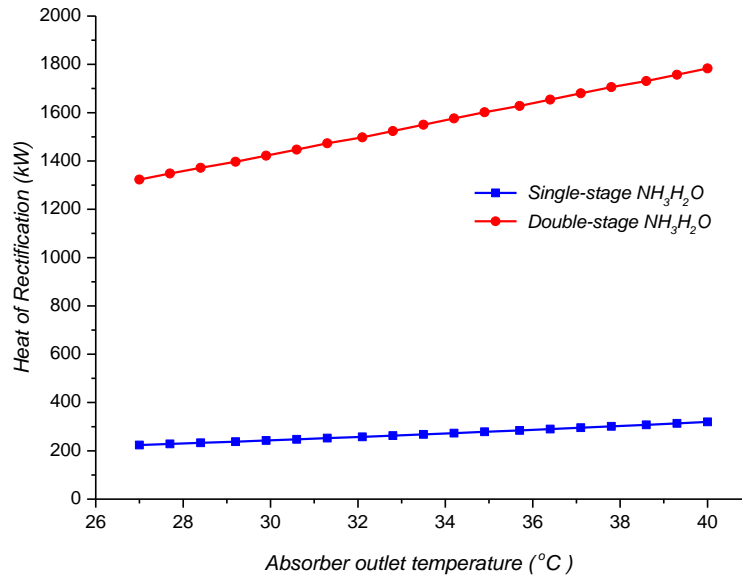
Figure 4. Effect of Absorber Outlet Temperature on Heat of Rectification System

15

2.2.3.2. Effect of Condenser Temperatures on ARS Performance

In the same way, Figure 5 shows that COP of the ARS decreases as the condenser temperature increases. In contrast, Figure 6 shows that heat rejection through the rectification system increases as the absorber temperature increases for both single- and double-stage NH_3-H_2O ARS.
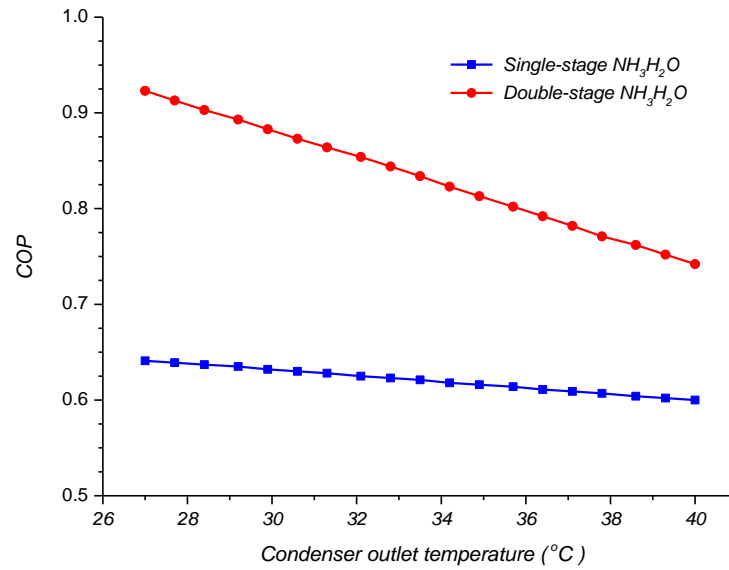
Figure 5. Effect of Condenser Outlet Temperature on COP
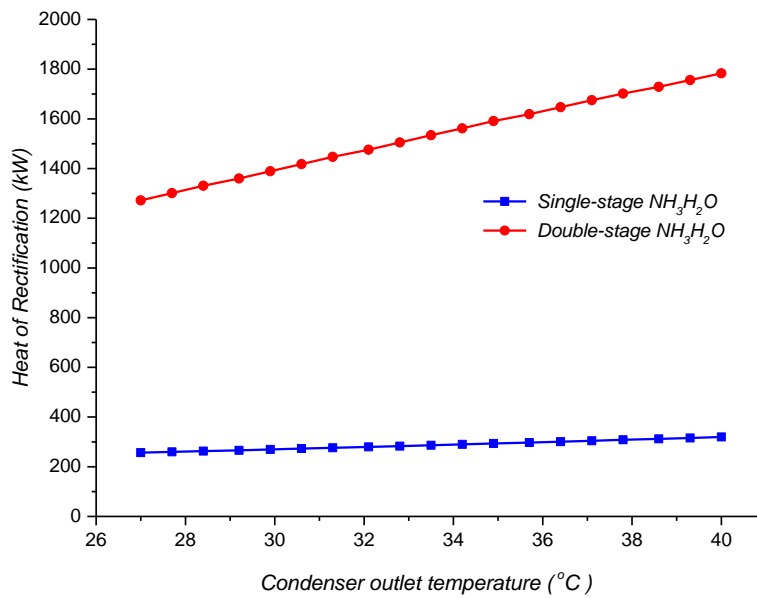
Figure 6. Effect of Condenser Outlet Temperature on Heat of Rectification System

2.2.3.3. Effect of Evaporator Temperatures on ARS Performance

Similarly, Figure 7 shows that COP of the ARS decreases as the evaporator temperature decreases. Conversely, Figure 8 shows that heat rejection through the rectification system increases as the evaporator temperature decreases for both single- and double-stage NH_3-H_2O ARS.
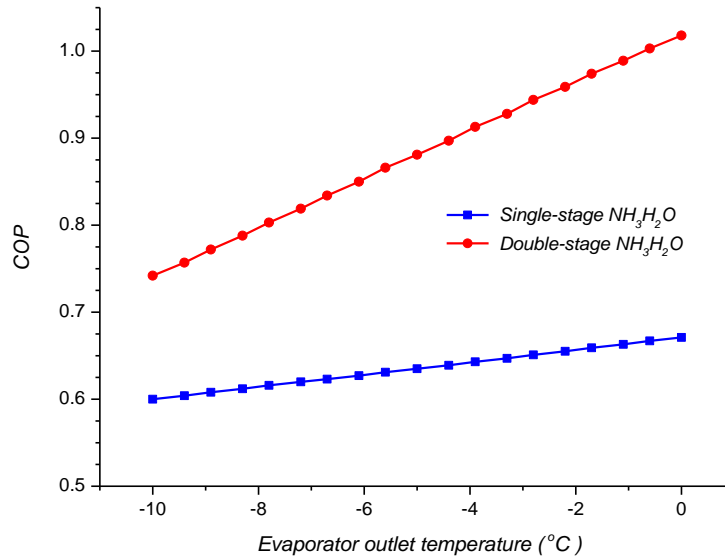
Figure 7. Effect of Evaporator Outlet Temperature on COP
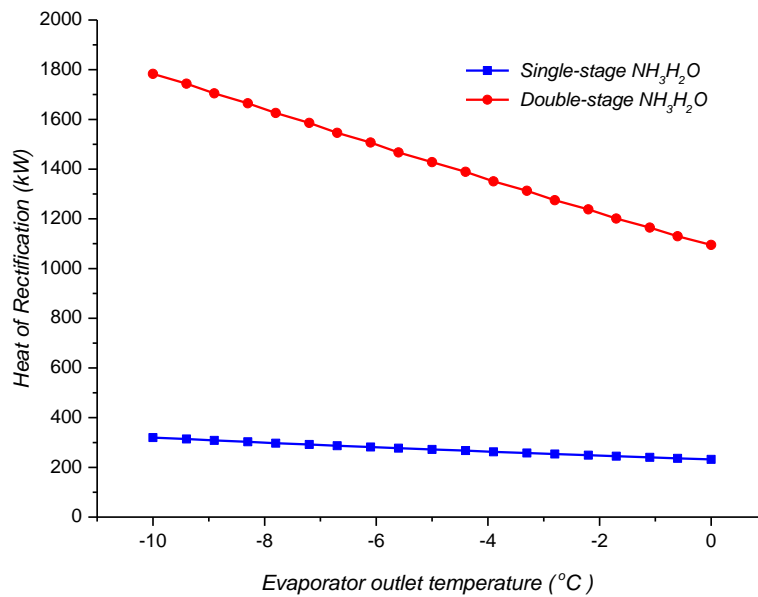
Figure 8. Effect of Evaporator Outlet Temperature on Heat of Rectification System

2.2.4. ARS' Heat Rejection Assessment

With the aim of harnessing the heat rejection by the ARS system, rejected heat through the absorber, rectifier(s), and condenser are to be measured regarding its quality as well as the quantity. It can be clearly seen from Figure 9 that there is an abundant amount of heat rejection by a single-stage NH_3-H_2O ARS through its absorber and condenser compared to heat rejection through its rectifier. Nevertheless, the quality of heat rejection by the absorber and condenser is very low relative to the quality of heat rejection by the rectifier.
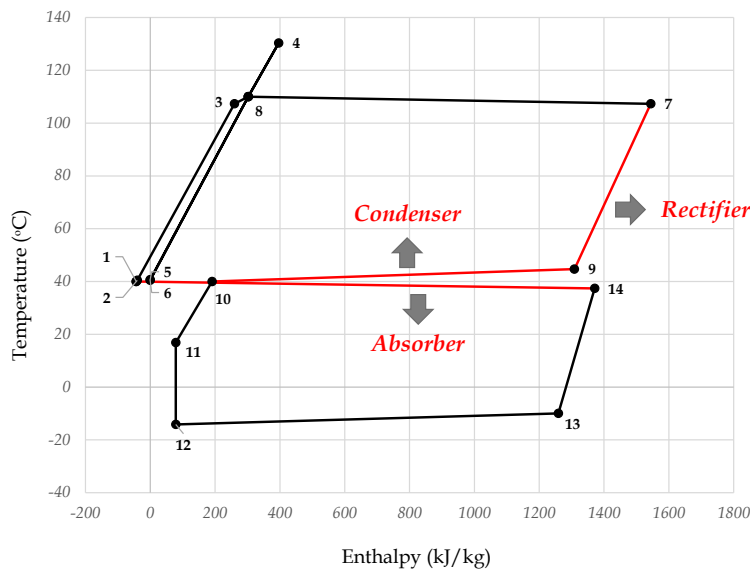
Figure 9. T-h Diagram of Typical Single-stage NH_3-H_2O ARS

Consequently, operating the single-stage NH_3-H_2O ARS at a higher condenser pressure will allow us to harness heat rejection by both the rectifier and condenser at a higher temperature as shown in Figure 10. Recall from Figure 5 that the ARS coefficient of performance considerably decreases as the condenser temperature (pressure) increases. It also can be seen from both T-h diagrams that the required heat source temperature goes up in order to achieved the operating pressure. Technically speaking, the amount of heat rejection through the rectifier and condenser, and the absorbed heat by the evaporator can be controlled by adjusting the heat source temperature and pump power. Such a system would be very attractive where refrigeration and another low process heating (from 60 – 90 ºC) are needed interchangeably.
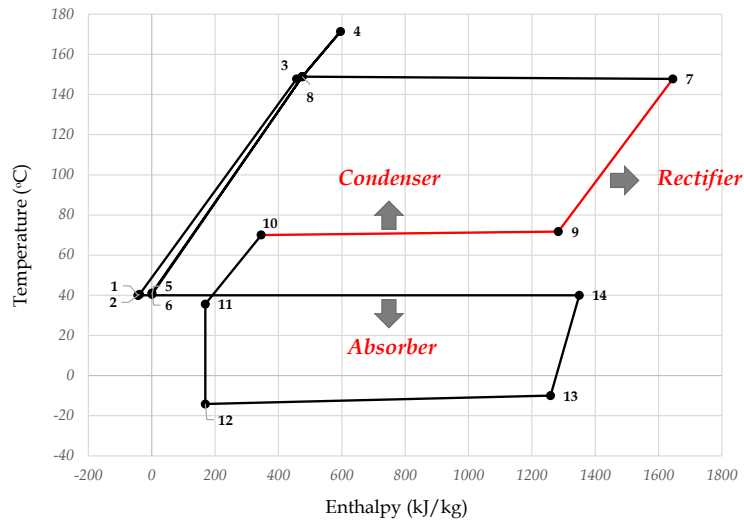
Figure 10. T-h Diagram of Modified Single-stage NH_3-H_2O ARS

Unlike single-stage NH_3-H_2O ARS, double-stage NH_3-H_2O ARS provides an enormous amount of heat rejection through its rectification system as shown in Figure 11. Heat rejection by the three rectifiers are at medium quality where the temperature varies roughly from 70 – 180 ℃. Such a heat rejection can be utilized to drive power cycles or process heating such as an Organic Rankine Cycle and thermally driven desalination plant. Additionally, heat rejection by the condenser and absorber can be harnessed, though their heat rejection is at lower temperature relative to the rectifiers.
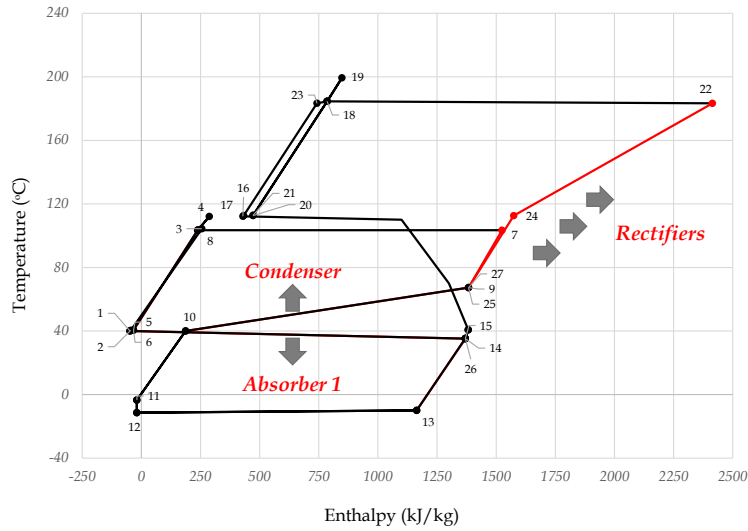
Figure 11. T-h Diagram of Typical NH_3-H_2O ARS

Recall from Figure 3 – Figure 6 that as the absorber and condenser temperatures increase, the ARS' coefficient of performance decreases significantly. On the other hand, heat rejection by the rectifiers increases. If this heat rejection is to be utilized to run any process heating, the optimal operational point is to be considered based on the desired amount of cooling and the other process heating.

Among all thermally driven applications, seawater desalination is the most attractive application to be integrated to the ARS for different reasons. Recall from Table 1 that the high heat rejection factor by ARS is one of the major disadvantages of the system. Being located by the shore, seawater can be used to cool down the absorber and condenser which also indirectly controls the ARS coefficient of performance. In fact, these low-temperature heat rejections can possibly be utilized to preheat seawater feed to the thermal desalination unit. Furthermore, the second product (freshwater) could be cooled down by the ARS and delivered to the end-user as a chilled freshwater to provide both cooling and freshwater.

2.3. Thermal Desalination

Widely used desalination technologies can be categorized, based on the method of water-salt separation, into membrane and thermal desalination. The potential advantage of thermal desalination over membrane separation is the capability to utilize low-grade exhaust heat at a low top brine temperature (TBT): lower than 70°C for Multi Effect Distillation (MED) and Multi Effect

Distillation–Thermal Vapor Compression (MED–TVC), and 90–110°C for Multi Stage Flash (MSF) [27]. Table 5 shows a comparison between the main desalination processes [27-31].

Reverse osmosis (RO) is the most efficient existing desalination technology with an exergetic efficiency of about 32% [32]. It is worth pointing out that the RO exergetic efficiency is only in the form of shaft work (electrical energy). The exergetic efficiency of an RO system would be substantially lower if exergetic efficiencies are reported relative to fuel input exergy; note that the exergetic efficiency of a modern power plant is just over 50% [33]. Following RO in order are MED–TVC, MED, then MSF, with internal exergetic efficiencies of 9%, 6%, and 3%, respectively [32]. Despite the low exergetic efficiencies of thermal desalination systems, these technologies are still widely used in many areas, like the Middle East, due mainly to the low cost of fossil fuel. Table 6 shows briefly the advantages and disadvantages of the most common desalination processes [28-30].

Table 5. Performance Comparison of Most Common Desalination Processes

Properties	Multi-Stage Flash Distillation (MSF)	Multi-Effect Distillation (MED)	Thermal Vapor Compression (TVC)	MED-TVC [6]	Seawater Reverse Osmosis (SWRO)
Typical unit size* (m³/day)	50,000 – 90,000	600 – 38,000	10,000 – 30,000	600 – 68,000	Up to 98,000
Electrical energy consumption* (kWh/m³)	2.5 – 5	2 – 2.5	1.6 – 1.8	< 1	4 – 6
Thermal energy consumption* (MJ/m³)	190 – 282	145 – 230	227	120 – 150	None
Performance Ratio (PR) (kg distillate /2326 kJ)	9 – 11	10 – 12	11	16 – 18	–
Avg. Water production cost (US$/m³)**	0.56 – 1.75	0.52 – 1.5	0.87 – 0.95	< MED	0.45 – 1.6
Capital Expenditure (CAPEX) ** (US$/m³/day)	1700 – 2900	1700 – 2700	> MSF	1,700 – 2,700	1300 – 2500
Operational Expenditure (OPEX)** (US$/m³)	0.65	0.54	< MED	0.54	0.46
Produced water quality (ppm)	≈10	≈10	≈10	≈10	400 – 500
Top brine temperature (°C)***	< 120	< 70	< 70	< 70	Ambient
Possible recovery ratio (%)	25 – 50	40 – 65	50	40 – 65	30 – 60 [+]

*   Per distillate water
**   Water production cost varies with location, water quality, contract type, and plant capacity
***   Maximum temperature of seawater inside the unit
\+   For single pass (higher recovery ratio can be possibly achieved for multiple passes)

Table 6. Advantages and Disadvantages of Most Common Desalination processes

	Advantages	Disadvantages
MSF	• Can handle salty water (70 ppt) • Less scaling formation than MED, MED-TVC, and VC since it works with flashing rather than boiling.	▪ Cannot be operated below 60% capacity. ▪ Not suitable to be integrated with renewable energies. ▪ Not easy to operate (qualified personnel recommended).
MED	▪ Can be operated between 0 – 100 % capacity. ▪ Suitable to be integrated to renewable energies. ▪ Easy to operate (personnel needs minimal training)	▪ To avoid corrosion, material need to be made of high quality materials. ▪ Steam at final stage requires cooling system to be condensed.
VC	▪ Requires less energy than MED and MSF	▪ Additional heating is required for the start-up to generate vapor. ▪ Dealing with the compressor which requires higher level of maintenance.
MED – TVC	▪ Minimize number of effects of MED with same water production.	▪ Cannot be operated below 60% capacity. ▪ Not suitable to be integrated with renewable energies since steam jet requires the external steam of minimum 2.5 bar.
RO	▪ Easy to operate ▪ Fast start-up ▪ Easily scalable	▪ Requires qualified personnel. ▪ Requires higher level of pre-treatment which makes it sensitive to the quality of feed water ▪ Membrane need to be replaced frequently.

Among all thermally driven desalination technologies, MED–TVC and MED have received more attention than other thermal desalination processes due to low TBT (<70°C), low corrosion rate, and low specific energy consumption which ultimately leads to mitigating greenhouse gas emissions especially when exhaust heat is employed. Although MED–TVC is more efficient than MED as a result of reducing the required steam by recovering steam at the final effect through a steam jet ejector [34], MED can be operated below 60% capacity, which makes it suitable to be integrated with intermittent energy supplies such as exhaust heat and renewable energies [30].

2.3.1. Multi Effect Distillation (MED) unit

Multi effect distillation (MED) is simply an evaporator that contains several evaporating compartments (stages) which are maintained at decreasing pressures corresponding to the boiling temperature of water at that specific stage's temperature. Seawater enters the first cell (stage) after being preheated through all previous stages. The main external heat source, such as power-plant waste heat or fossil fuel boiler, transfers heat to the feed seawater which causes an increase in its temperature up to 70°C maximum in order to avoid scale formation and corrosion [28]. As seawater gets introduced to the first stage which has a relatively lower pressure, seawater tends to vaporize (flash) due to the corresponding boiling temperature. The produced vapor inside each cell transfers its latent heat to the next vessel by moving vapor through pipes to the next cell as shown in Figure 12.
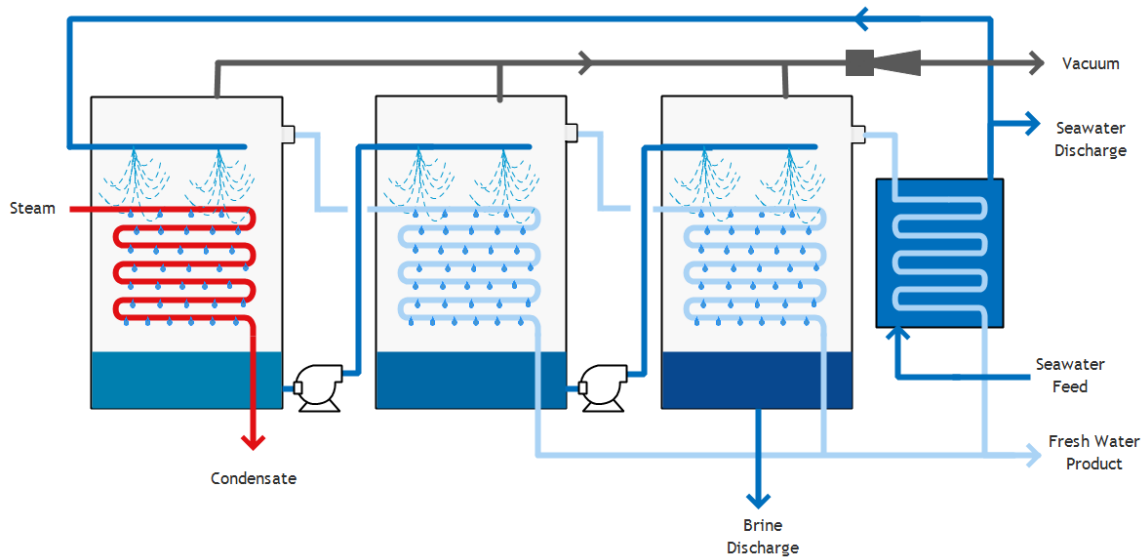
Figure 12. Schematic Diagram of Multi-effect Distillation (MED) Unit

Seawater is introduced to each cell in MED by spraying seawater on top of the tubes (heat exchanger) that carry the steam from the previous vessel. Hence, the generated vapor in the final cell gets completely condensed by preheating feed seawater. Over 60% of incoming seawater gets discharged back to the sea after exchanging heat with the MED's condenser, while the rest is pumped to the first effect [35].

2.3.2. System Description

The MED consists primarily of the following components, namely multiple effects, and condenser. Mass, energy, and exergy balances are performed below for a typical cell, which can be divided into six control volumes, as illustrated in Figure 13 in order to simplify the analysis as recommended by [36].
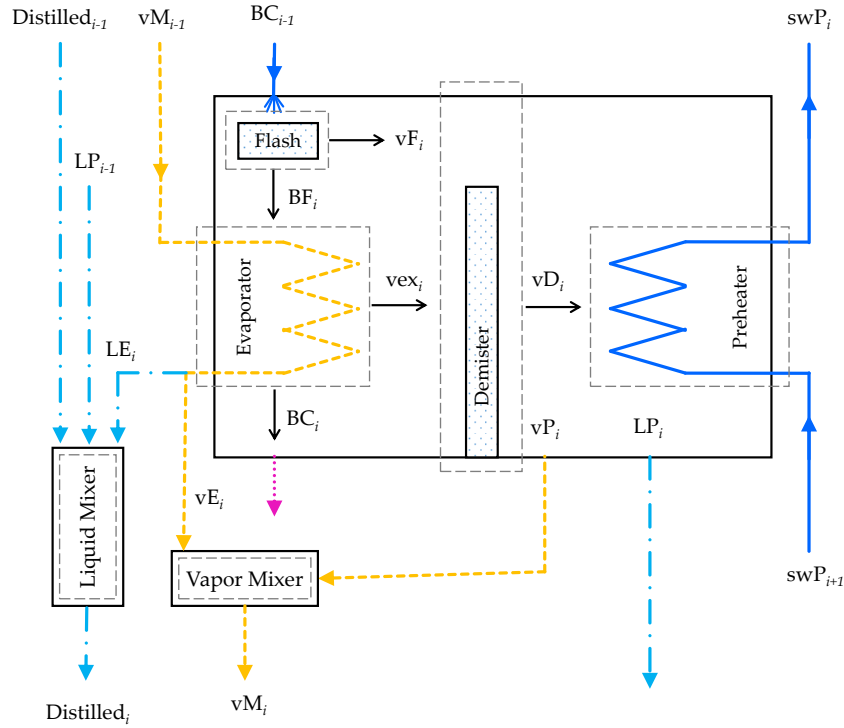
Figure 13. Schematic Diagram of a Typical MED Effect

Following the stream labels in Figure 13, the brine stream (BC_{i-1}) from the preceding effect flashes as it is introduced to the effect (i) since it is superheated at the effect's operating pressure. The remaining brine (BF_i) is then sprayed over a bundle of evaporation tubes, where steam is generated and the rest of the brine stream (BC_i) goes to the succeeding effect. The circulating steam inside the tubes (VM_{i-1}), from the preceding steam mixer, provides the needed heat for the evaporation. Generated steam gets partially condensed (LP_i) by preheating incoming seawater (swP_{i+1}), while the rest of the steam (vP_i) is transported to provide needed heat for the following effect.

2.3.2.1. Thermodynamic Model

The following assumptions are applied for the thermodynamic model:

iv. Steady-state operation with negligible kinetic and potential energy.

v. Heat losses and pressure drops in the components and piping are not considered.

vi. The distilled fresh water is salt free.

vii. During phase change processes, the bulk liquid and vapor flows are at equilibrium in each cross section.

Under the above-mentioned assumptions, the mass (continuity), energy (the first law of thermodynamics), and exergy (the second law of thermodynamics) balance equations are derived for each component of the system.

A. The flash

$$\dot{m}_{BC_{i-1}} = \dot{m}_{BF_i} + \dot{m}_{vF_i} \tag{2.39}$$

$$\dot{m}_{BC_{i-1}} x_{BC_{i-1}} = \dot{m}_{BF_i} x_{BF_i} + \dot{m}_{vF_i} x_{vF_i} \tag{2.40}$$

$$\dot{m}_{BC_{i-1}} h_{BC_{i-1}} = \dot{m}_{BF_i} h_{BF_i} + \dot{m}_{vF_i} h_{vF_i} \tag{2.41}$$

$$\dot{X}_{dest,flash_i} = T_0 \cdot \left(\dot{m}_{BF_i} s_{BF_i} + \dot{m}_{vF_i} s_{vF_i} - \dot{m}_{BC_{i-1}} s_{BC_{i-1}} \right) \tag{2.42}$$

where $\dot{m}$ is the mass flow rate, x the water salinity, and $\dot{X}_{dest,flash_i}$ the exergy destruction rate in the flash. Subscript i represents the effect number, B the brine stream, C the cell (effect), F the flash, and v the fresh water saturated vapor.

B. The MED evaporator

$$\dot{m}_{BF_i} = \dot{m}_{BC_i} + \dot{m}_{vex_i} \tag{2.43}$$

$$\dot{m}_{vM_{i-1}} = \dot{m}_{LE_i} + \dot{m}_{vE_i} \tag{2.44}$$

$$\dot{m}_{BF_i} x_{BF_i} = \dot{m}_{BC_i} x_{BC_i} \tag{2.45}$$

$$\dot{m}_{vM_{i-1}} h_{vM_{i-1}} - \dot{m}_{LE_i} h_{LE_i} - \dot{m}_{vE_i} h_{vE_i} = \dot{m}_{vex_i} h_{vex_i} + \dot{m}_{BF_i} h_{BF_i} - \dot{m}_{BF_i} h_{BF_i} \tag{2.46}$$

$$\dot{X}_{dest,eva_i} = T_0 \cdot \left(\dot{m}_{LE_i} s_{LE_i} + \dot{m}_{vE_i} s_{vE_i} + \dot{m}_{vex_i} s_{vex_i} + \dot{m}_{BF_i} s_{BF_i} - \dot{m}_{vM_{i-1}} s_{vM_{i-1}} \right.$$
$$\left. - \dot{m}_{BF_i} s_{BF_i} \right) \tag{2.47}$$

where $\dot{X}_{dest,eva_i}$ is the exergy destruction rate in the evaporator. Subscripts ex and E represent the external and internal surfaces of the bundle evaporation tubes, respectively, L the fresh water saturated liquid, M the mixer, and D the demister.

C. The demister

$$\dot{m}_{vex_i} + \dot{m}_{vF_i} = \dot{m}_{vD_i} \tag{2.48}$$

$$\dot{m}_{vex_i} h_{vex_i} + \dot{m}_{vF_i} h_{vF_i} = \dot{m}_{vD_i} h_{vD_i} \tag{2.49}$$

$$\dot{X}_{dest,D_i} = T_0 \cdot \left(\dot{m}_{vD_i} s_{vD_i} - \dot{m}_{vF_i} s_{vF_i} - \dot{m}_{ex} s_{vex_i} \right) \tag{2.50}$$

where $\dot{X}_{dest,D_i}$ is the exergy destruction rate in the demister.

D. The preheater

$$\dot{m}_{vD_i} = \dot{m}_{vP_i} + \dot{m}_{LP_i} \tag{2.51}$$

$$\dot{m}_{swP_i} = \dot{m}_{swP_{i+1}} \tag{2.52}$$

$$\dot{m}_{swP_i} h_{swP_i} - \dot{m}_{swP_{i+1}} h_{swP_{i+1}} = \dot{m}_{vD_i} h_{vD_i} - \dot{m}_{vP_i} h_{vP_i} - \dot{m}_{LP_i} h_{LP_i} \tag{2.53}$$

$$\dot{X}_{dest,preh_i} = T_0 \cdot \left(\dot{m}_{swP_i} s_{swP_i} + \dot{m}_{LP_i} s_{LP_i} + \dot{m}_{vP_i} s_{vP_i} - \dot{m}_{swP_{i+1}} s_{swP_{i+1}} - \dot{m}_{vD_i} s_{vD_i} \right) \tag{2.54}$$

where $\dot{X}_{dest,preh_i}$ is the exergy destruction rate in the preheater. Subscript P represents the preheater, and sw the seawater feed.

E. The vapor mixer

$$\dot{m}_{vM_i} = \dot{m}_{vP_i} + \dot{m}_{vE_i} \tag{2.55}$$

$$\dot{m}_{vM_i} h_{vM_i} = \dot{m}_{vP_i} h_{vP_i} + \dot{m}_{vE_i} h_{vE_i} \tag{2.56}$$

$$\dot{X}_{dest,vM_i} = T_0 \cdot \left(\dot{m}_{vM_i} s_{vM_i} - \dot{m}_{vP_i} s_{vP_i} - \dot{m}_{vE_i} s_{vE_i} \right) \tag{2.57}$$

where $\dot{X}_{dest,vM_i}$ is the exergy destruction rate in the vapor mixer.

F. The liquid mixer

$$\dot{m}_{Distilled_i} = \dot{m}_{LE_i} + \dot{m}_{LP_{i-1}} + \dot{m}_{Distilled_{i-1}} \tag{2.58}$$

$$\dot{m}_{Distilled_i} h_{Distilled_i} = \dot{m}_{LE_i} h_{LE_i} + \dot{m}_{LP_{i-1}} h_{LP_i} + \dot{m}_{Distilled_{i-1}} h_{Distilled_{i-1}} \tag{2.59}$$

$$\dot{X}_{dest,LM_i} = T_0 \cdot \left(\dot{m}_{Distilled_i} s_{Distilled_i} - \dot{m}_{LE_i} s_{LE_i} - \dot{m}_{LP_{i-1}} s_{LP_i} - \dot{m}_{Distilled_{i-1}} s_{Distilled_{i-1}} \right) \tag{2.60}$$

where $\dot{X}_{dest,LM_i}$ is the exergy destruction rate in the liquid mixer. The Subscript $'Distilled'$ represents the distilled water in liquid form.

G. Effect exergy destruction

$$\dot{X}_{dest,effect_i} = \dot{X}_{dest,flash_i} + \dot{X}_{dest,eva_i} + \dot{X}_{dest,D_i} + \dot{X}_{dest,preh_i} + \dot{X}_{dest,vM_i} + \dot{X}_{dest,LM_i} \tag{2.61}$$

where $\dot{X}_{dest,effect_i}$ is the total exergy destruction rate in the effect i.

H. The MED condenser

$$\dot{m}_{vM_n} = \dot{m}_{LCon} \tag{2.62}$$

$$\dot{m}_{sw} = \dot{m}_{sw,rej} + \dot{m}_{swP_n} \tag{2.63}$$

$$\dot{m}_{vM_n}h_{vM_n} - \dot{m}_{LCon}h_{LCon} = \dot{m}_{sw,rej}h_{sw,rej} + \dot{m}_{swP_n}h_{swP_n} - \dot{m}_{sw}h_{sw} \tag{2.64}$$

$$\dot{X}_{dest,con} = T_0 \cdot \left(\dot{m}_{LCon}s_{LCon} + \dot{m}_{sw,rej}s_{sw,rej} + \dot{m}_{swP_n}s_{swP_n} - \dot{m}_{sw}s_{sw} - \dot{m}_{vM_n}s_{vM_n} \right) \tag{2.65}$$

where $\dot{X}_{dest,con}$ is the exergy destruction rate in the condenser. The subscript LCon represents the condensate water vapor in the condenser, rej the rejected seawater, and n the total number of effects.

I. MED system performance criteria

$$GOR = \frac{\dot{m}_{Distilled}}{\dot{m}_{steam}} \tag{2.66}$$

$$\dot{X}_{dest,MED} = \dot{X}_{dest,con} + \sum_{i=1}^{n} \dot{X}_{dest,effect_i} \tag{2.67}$$

where GOR is the gained output ratio, $\dot{m}_{distilled}$ the total mass flow rate of distilled water, $\dot{m}_{steam}$ the mass flow rate of steam in the first effect, and $\dot{X}_{dest,MED}$ the total exergy destruction rate in the MED subsystem. Note that thermal energy input into the MED unit at the first effect, $\dot{Q}_{effect\,1}$, is equal to the sum of the heat rejected by the rectifier and condenser in case of the combined 1s–NH$_3$H$_2$O–MED system.

The minimum separation work, or least amount of work to separate salt and water, is calculated as follows [32, 33]:

$$\dot{W}_{min} = \dot{X}_{Brine} + \dot{X}_{product} - \dot{X}_{incoming\,SW}$$

$$= \dot{X}_{BC_n} + \dot{X}_{Distilled_n} + \dot{X}_{LCon} - \dot{X}_{sw} \tag{2.68}$$

$$\eta_{II,MED} = \frac{1}{1 + \dfrac{\dot{X}_{dest,MED}}{\dot{W}_{min}}} \tag{2.69}$$

where $\eta_{II,MED}$ is the exergetic efficiency (second-law efficiency) of the MED subsystem.

The MED model was developed using the Engineering Equation Solver (EES) software [25]. The correlations of seawater properties, provided by EES, were taken in this study [37]. The thermodynamic model was validated by comparing the MED model with the related work in literature [32, 36, 38] and the obtained results were within ±5%, under the same conditions as shown in Table 7.

Table 7. Validation of MED Model

	Model	Ref.	Diff.
Fresh water production (kg/hr)	2897	2992 [36]	3.2%
Exergetic efficiency	6.2	6 [32]	3.3%
Performance ratio	9.25	9.6 [36]	3.6%
Unit product cost ($/m^3)	2.77	2.632 [38]	5.2%

The main assumptions for the reference case of the MED system are summarized in Table 8.

Table 8. Operating Condition Assumptions for MED

Parameter	Value	Unit
Mass flow rate of external heat source ($\dot{m}_A$)	1	kg/s
Specific heat input ($\dot{q}_{source}$)	1940	kJ/kg
Seawater temperature ($T_{seawater}$)	27	ºC
Top brine temperature ($T_{1st,effect}$)$^+$	66	ºC
Number of effects (n)	14	effects
Seawater salinity	35,000	ppm
Preheater temperature difference ($\Delta T_{SW,preheater}$)	2.3	ºC
Effect pressure difference (ΔP_{effect})	1	kPa

$^+$ Seawater temperature at the first effect

2.4.   Combined Ammonia-Water (NH$_3$-H$_2$O) Absorption Refrigeration and Multi Effect Distillation (MED)

In this section, we propose utilizing the heat rejection from single- and double-stage NH$_3$H$_2$O ARS to run an MED unit, with the combinations being respectively named 1s–NH$_3$H$_2$O–MED and 2s–NH$_3$H$_2$O–MED, which simultaneously produce fresh water and cooling. In the case of 1s-NH$_3$H$_2$O–MED, the rectifier and condenser operate at elevated temperatures relative to those in the standalone ARS, and reject heat to the MED unit as shown in Figure 14. Unlike the 1s–NH$_3$H$_2$O–MED, the MED unit in the 2s– NH$_3$H$_2$O–MED system only uses the heat rejected by the rectifiers,

due to the greater quantity of rejected heat associated with the rectifiers in the double-stage ARS as shown in Figure 15.
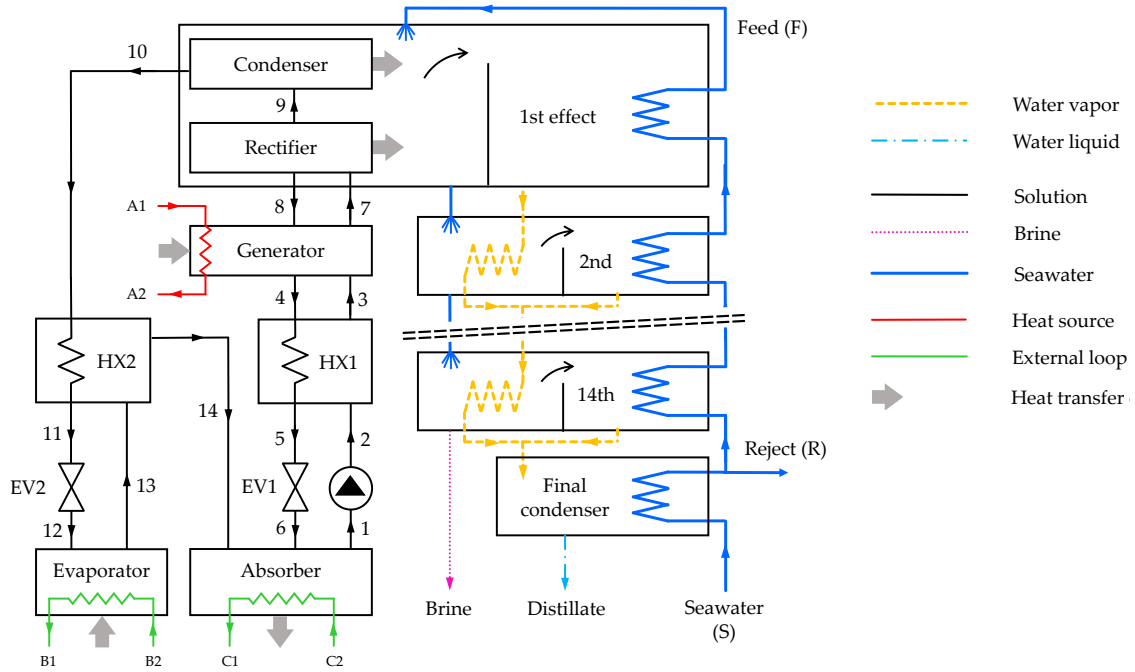
Figure 14. Schematic Diagram of the 1s– NH$_3$H$_2$O–MED Combined System
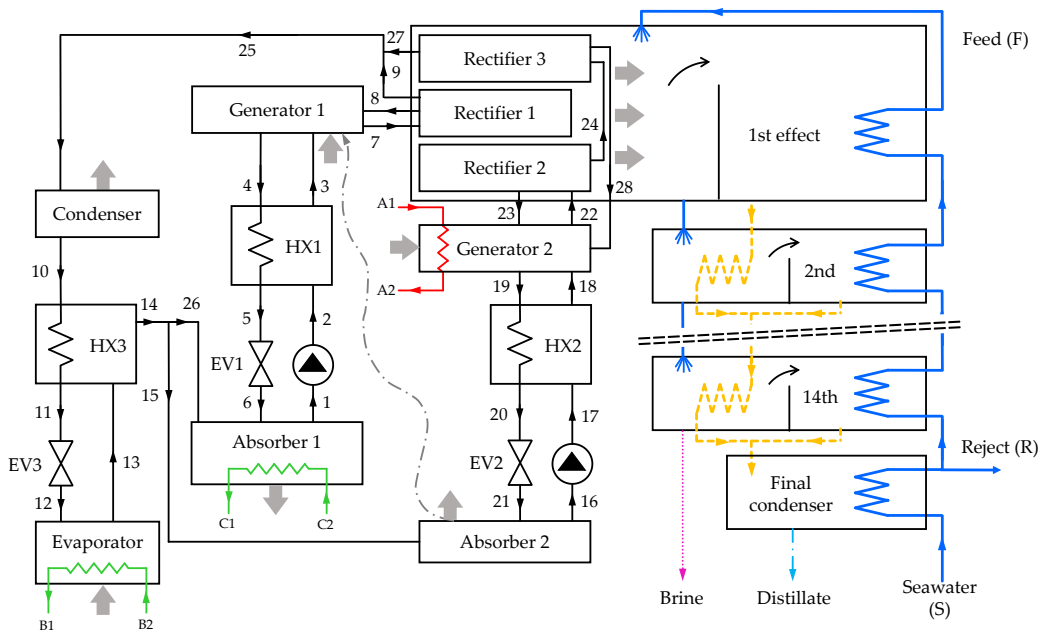
Figure 15. Schematic Diagram of the 2s– NH$_3$H$_2$O–MED Combined System

2.4.1. Thermodynamic Model

Both simulation models, developed above for ARS and MED, were combined through a heat exchanger where the mass flow rate of seawater feed into the MED first effect was calculated for single- and double– NH_3H_2O–MED, respectively, as follows:

$$\dot{m}_{F,\ 1\text{-}NH3H2O\text{-}MED} = \left(\dot{Q}_{Rectifier} + \dot{Q}_{Condenser\ @70°C}\right) \Big/ \int_{T_{SW}}^{T_{TBT}} C_{p,seawater}(T,x) \cdot dT \tag{2.70}$$

$$\dot{m}_{F,\ 2\text{-}NH3H2O\text{-}MED} = \dot{Q}_{Rectifiers} \Big/ \int_{T_{SW}}^{T_{TBT}} C_{p,seawater}(T,x) \cdot dT \tag{2.71}$$

where T_{TBT} is the top brine temperature (temperature at the first effect), x is seawater salinity, and T_{SW} is the seawater temperature.

The total combined second-law efficiency (exergetic efficiency) of the combined ARS and MED can be calculated as:

$$\eta_{II,system} = 1 - \frac{\dot{X}_{dest,ARS} + \dot{X}_{dest,MED}}{\dot{X}_{15} + \dot{W}_{p}} \tag{2.72}$$

2.4.2. Economic model

Water and cooling are two different products, which makes the comparison between them difficult, particularly when thermally driven desalination processes have relatively lower exergetic efficiency compared to ARS. The following section includes an economic evaluation of both ARS and MED subsystems from capital and operational points of view. Our economic model is based on a widely known model, Appendix A, that was developed by Farshi et al.[39], Esfahani et al. [13], and Alasfour and Bin Amer [38]. The economic model was validated by comparing the ARS and MED models individually with the related work in literature and the results were within ±5%, under similar conditions.

Natural gas and electricity prices were estimated to be $1.9/MMBtu and $0.07/kWh, respectively, with a boiler efficiency of 85% for the former.

2.5.   Results and Discussion

The main assumptions for the reference case of both single- and double-stage NH_3H_2O–MED systems are summarized in Table 4 and Table 8, except that the condenser temperature of the single-stage NH_3H_2O–MED is at 70ºC. The values of the thermodynamic parameters (temperature, pressure, mass flow rate, mass fraction, etc.) in all states of Figure 14 and Figure 15 for a fixed working condition, based on assumptions above, are shown in Appendix B. As previously stated, all studies are conducted at a fixed thermal energy input rate of 1940 kWth which is the enthalpy of vaporization of water at 200°C, for the sake of comparison, although this temperature is unnecessarily high for a single-stage system which can effectively operate at lower temperature. It is also because single-stage ARS requires a heat source at higher temperature when working at higher condenser pressure.

2.5.1.   Parametric Analysis

Figure 16 through Figure 24 show, for the proposed 1s–NH_3H_2O–MED and 2s–NH_3H_2O–MED systems, the effects of input parameter variations such as absorber outlet temperature (T_1), evaporator outlet temperature (T_{13}), ammonia mass fraction swing between weak and strong solutions (dx), and MED number of effects on the key output metrics. Exergetic efficiency (η_{II}), cooling capacity ($\dot{Q}_{eva}$), coefficient of performance (COP), gained output ratio (GOR), and freshwater mass flow rate ($\dot{V}_{distilled}$) are considered to compare the energy consumption and system productivity, while unit product cost (UPC) is used to evaluate the system unit water and cooling costs.

2.5.1.1.   Sensitivity to the absorber outlet temperature (T_1)

As shown in Figure 16, the exergetic efficiency of both systems decreases as T_1 (absorber outlet temperature) increases. This reduction is a result of a drop in the COP of the ARS system due originally to the decrease in cooling capacity, as shown in Figure 17, leading to an increase in the total exergy destruction of the system. Consequently, the ARS rectifiers' heat rejection increases resulting in an increase in the water production ($\dot{V}_{distilled}$) of the system as presented in Figure 17. It can be observed that the water production of the 2s–NH_3H_2O–MED system increases with relatively higher gradient than the 1s–NH_3H_2O–MED system. The reason is that, as T_1 increases, heat rejected by the rectifier increases, while condenser heat rejection decreases resulting in a slight rise in total heat rejection. Unit production cost of water and cooling decrease and increase, respectively, as T_1 increases as shown in Figure 18.
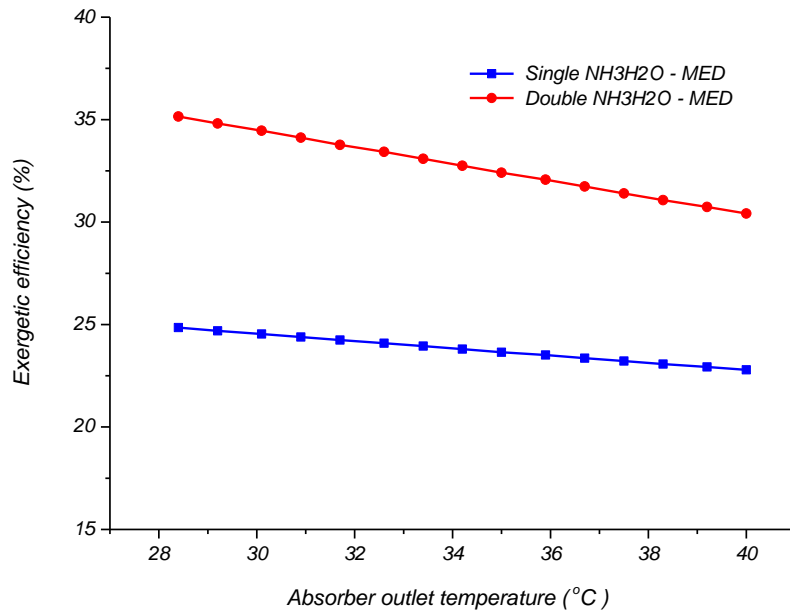
Figure 16. Effect of the Absorber Outlet Temperature (T_1) on Exergetic Efficiency for Single and Double Stage NH_3H_2O–MED
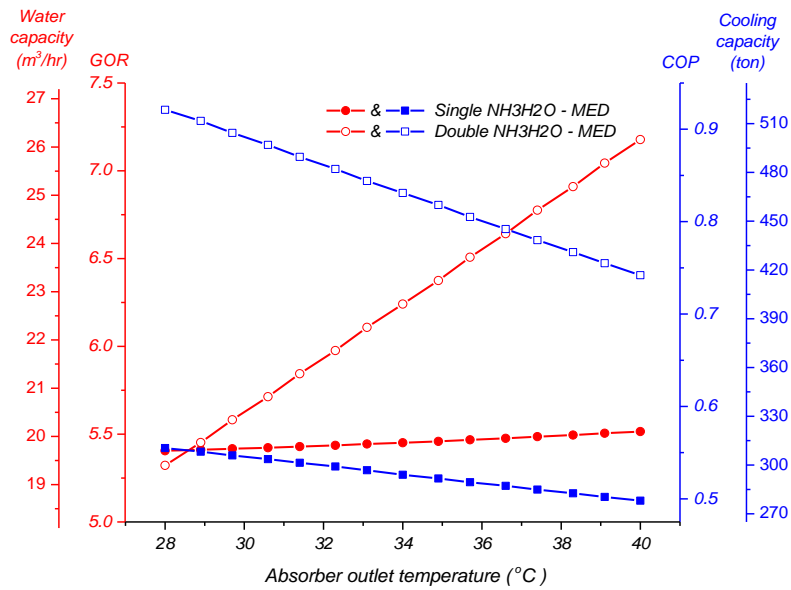
Figure 17. Effect of the Absorber Outlet Temperature (T_1) on Water Capacity, Gained Output Ratio, Coefficient of Performance and Cooling Capacity for Single and Double Stage NH_3H_2O–MED
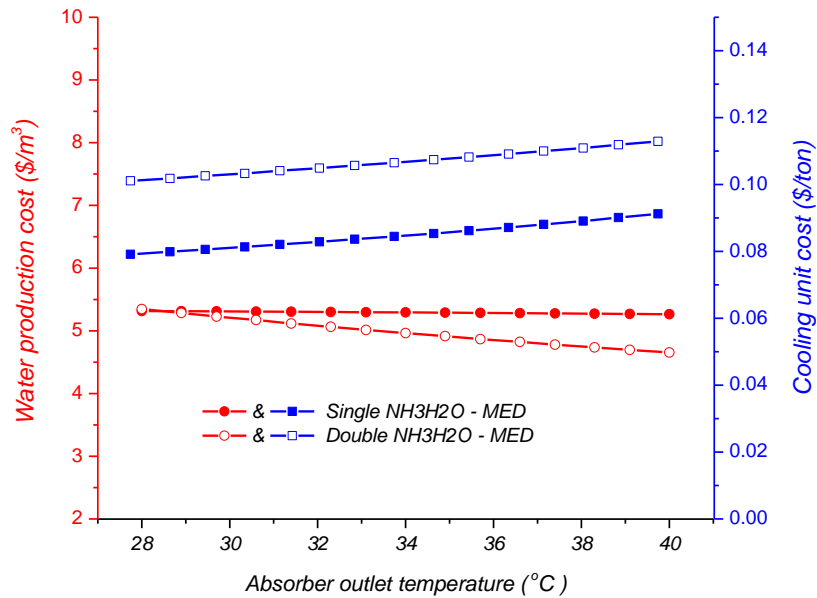
Figure 18. Effect of the Absorber Outlet Temperature (T_1) on Unit Product Costs of Water and Cooling for Single and Double Stage $NH_3H_2O–MED$

2.5.1.2.   Sensitivity to the evaporator outlet temperature (T_{13})

Figure 19 shows that the second-law efficiency increases as the evaporator outlet temperature T_{13} decreases despite the fact that the COP decreases with the evaporator temperature. The reason is that the reversible COP, which is a function of evaporator temperature [40], decreases relatively more steeply than does the actual COP. Figure 20 demonstrates that the water capacity increases considerably for the 2s–NH_3H_2O–MED system as T_{13} decreases, while the capacity of the 1s–NH_3H_2O–MED system remains constant since the increase in rectifier heat rejection nearly offsets the decrease in condenser heat rejection. Figure 21 shows a reduction in unit production cost of water as evaporator outlet temperature decreases for 2s–NH_3H_2O–MED system. This is due to the increase of the MED unit capacity as a result of the increase in the heat of rectification.
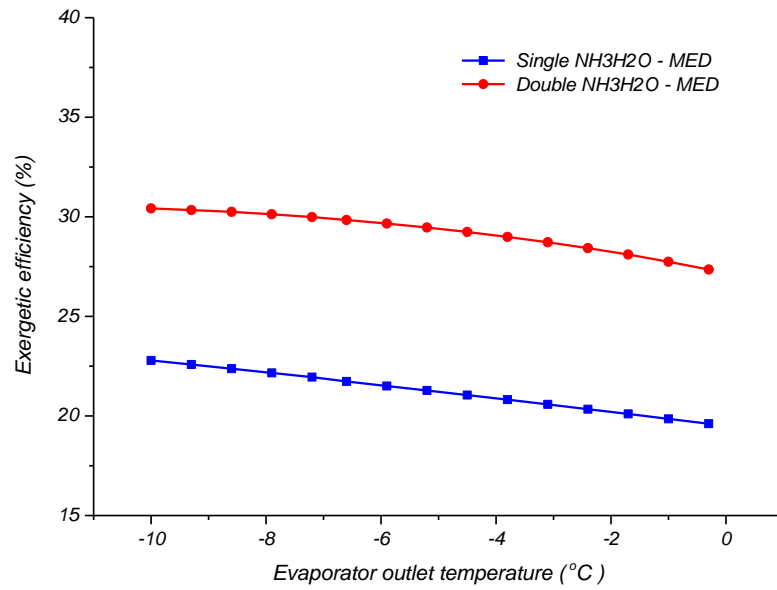
Figure 19. Effect of the Evaporator Outlet Temperature (T_{13}) on Exergetic Efficiency for Single and Double Stage NH_3H_2O–MED
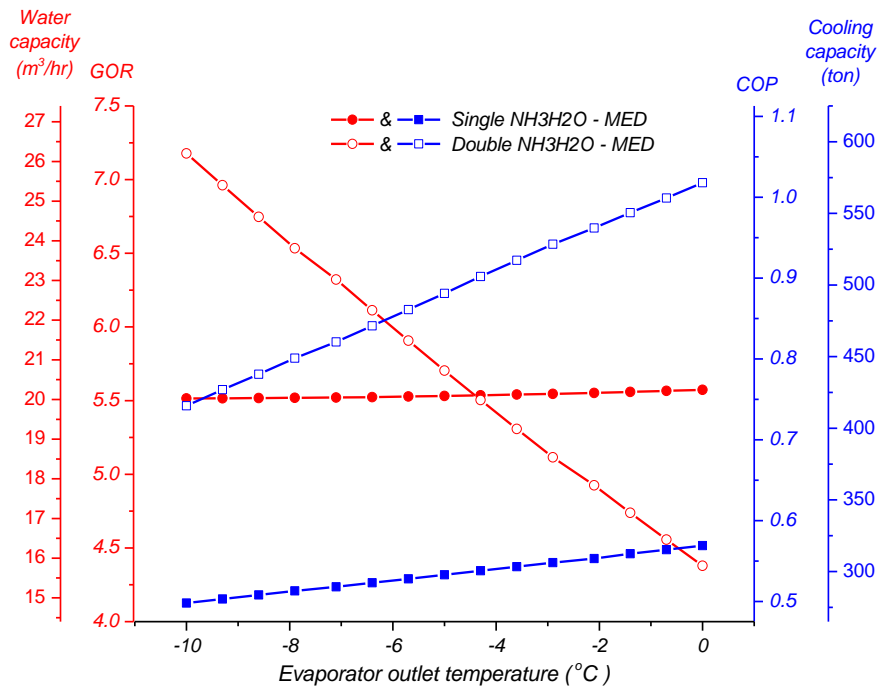
Figure 20. Effect of the Evaporator Outlet Temperature (T_{13}) on Water Capacity, Gained Output Ratio, Coefficient of Performance and Cooling Capacity for Single and Double Stage NH_3H_2O–MED
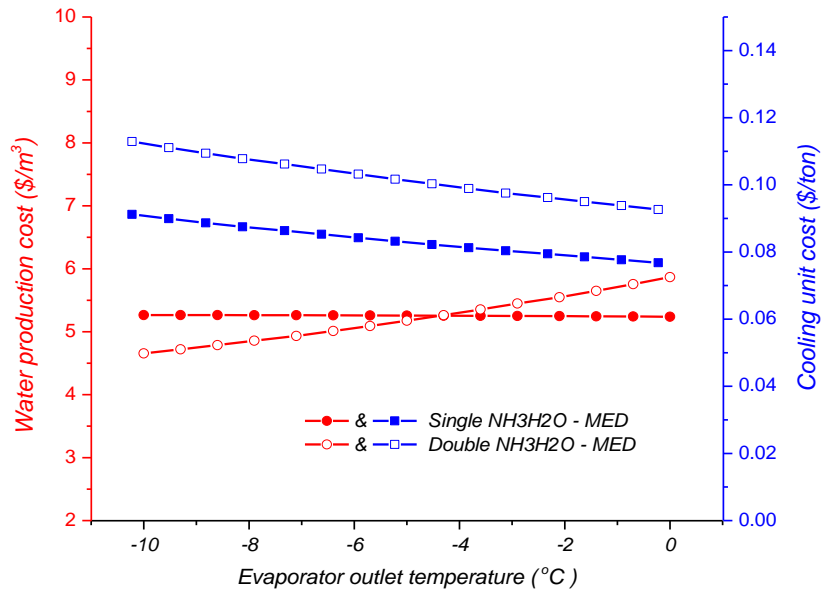
Figure 21. Effect of the Evaporator Outlet Temperature (T_{13}) on Unit Product Costs of Water and Cooling for Single and Double Stage NH_3H_2O–MED

2.5.1.3. Sensitivity to the mass concentration swing between strong-and-weak solution (dx)

Figure 22 through Figure 24 present the impact of the mass concentration swing between the strong and weak solutions on the second-law efficiency, COP, GOR, and capacity of water and cooling for a single- and double-ARS integrated with MED. Note that *dx* for a double-stage ARS system is the difference between the weak and strong solution ammonia mass fractions in HX1. It can be observed from Figure 22 and Figure 23 that for both ARS and MED systems, exergetic efficiency increases slightly with increasing *dx*, then levels off. COP of the 2s–NH_3H_2O–MED system seems to peak at about 0.78 before it starts slightly decreasing. On the other hand, the GOR of the same system keeps increasing, which results in maintaining the overall exergetic efficiency of the system fairly constant as solution concentration swing increases. The same results can be concluded for the 1s–NH_3H_2O–MED system. Figure 24 shows the costs of water and cooling decrease with the increase in ammonia mass concentration swing.

36
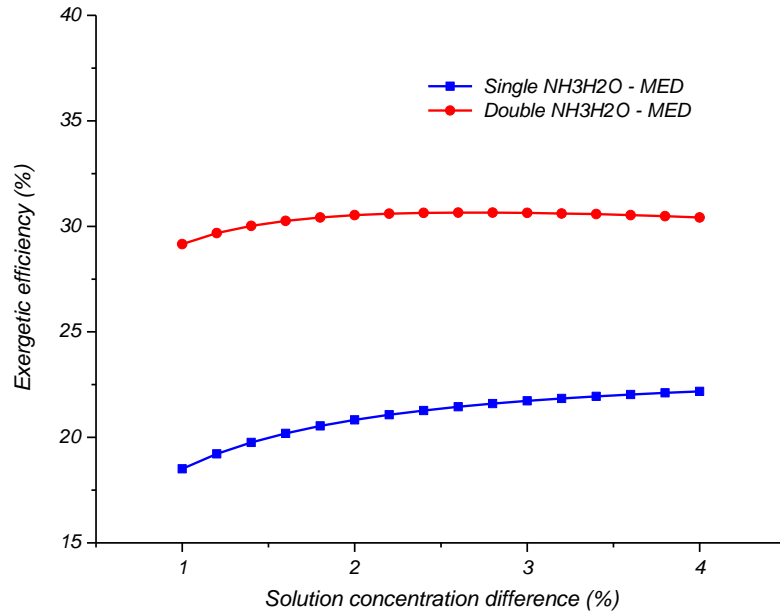
Figure 22. Effect of the Mass Concentration Swing Between Strong-And-Weak Solution (Dx) on Exergetic Efficiency for Single and Double Stage NH_3H_2O–MED
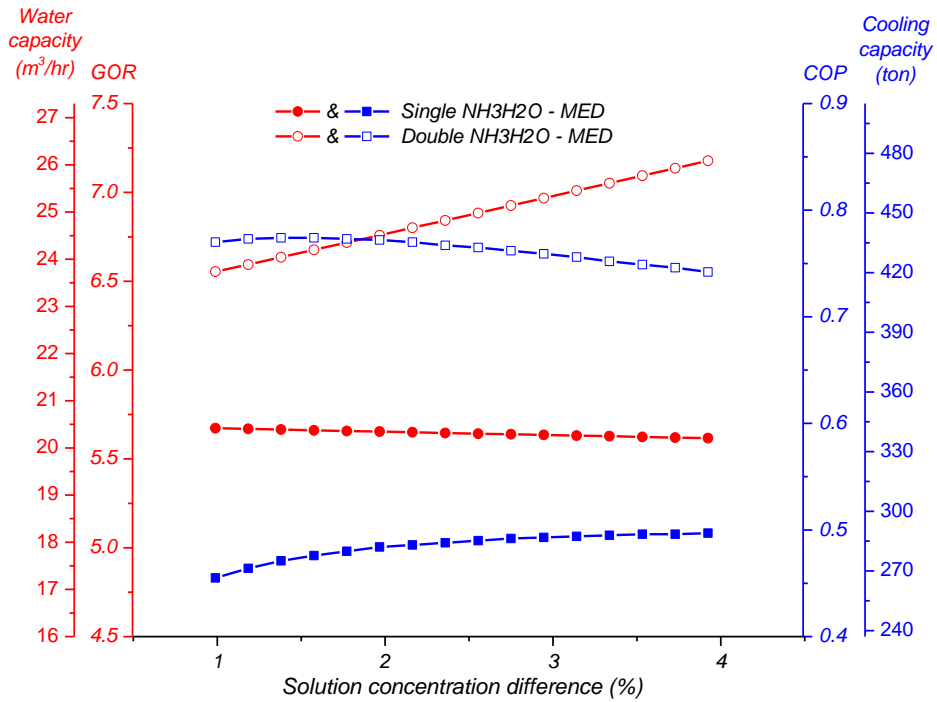
Figure 23. Effect of the Mass Concentration Swing Between Strong-and-Weak Solution (Dx) on Water Capacity, Gained Output Ratio, Coefficient of Performance and Cooling Capacity for Single and Double Stage NH_3H_2O–MED
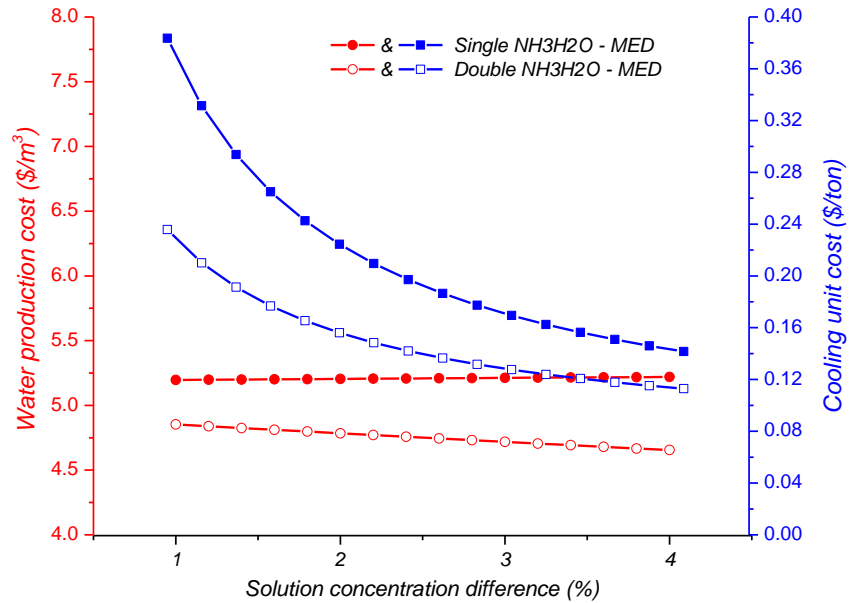
Figure 24. Effect of the Mass Concentration Swing Between Strong-and-Weak Solution (dx) on Unit Product Costs of Water and Cooling for Single and Double Stage NH_3H_2O–MED

2.5.1.4. Sensitivity to the MED's number of effects

Figure 25 through Figure 27 depict the impact of the MED unit's number of effects on the second-law efficiency, COP, GOR, and capacity of water and cooling for a single- and double-ARS integrated with MED. It can be seen clearly from Figure 26 & Figure 27 that the number of MED effects does not influence the performance of the ARS since the MED only recovers heat rejection by the ARS. Even though the overall exergetic efficiencies increase as the number of effects of the MED unit decreases, the water capacity and GOR steeply decrease. Consequently, the water production of both single- and double- NH_3H_2O–MED rises significantly compared with previous parametric analyses.
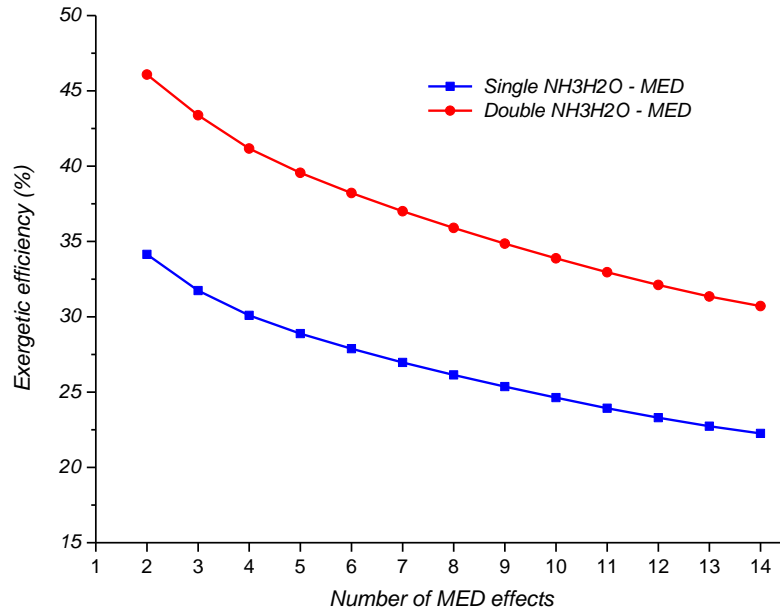
Figure 25. Effect of MED Number of Effects on Exergetic Efficiency for Single and Double Stage NH_3H_2O–MED
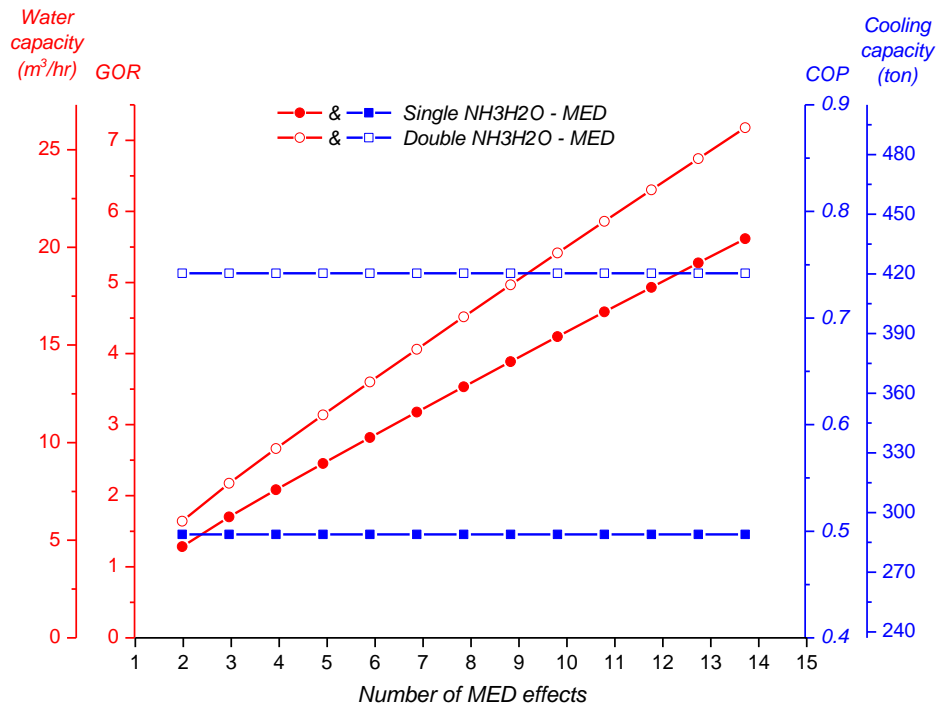
Figure 26. Effect of MED Number of Effects on Water Capacity, Gained Output Ratio, Coefficient of Performance and Cooling Capacity for Single and Double Stage NH_3H_2O–MED
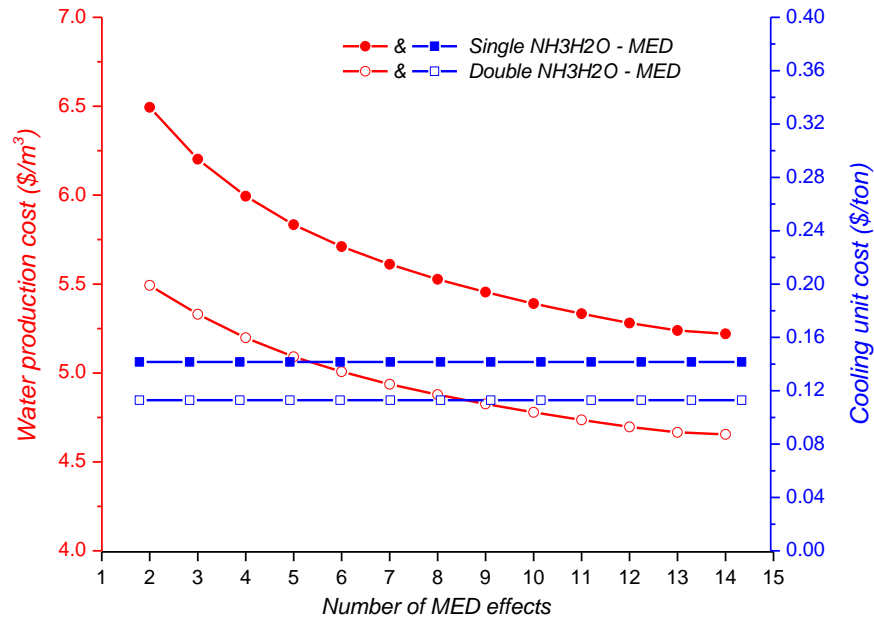
Figure 27. Effect of MED Number of Effects on Unit Product Costs of Water and Cooling for Single and Double Stage NH₃H₂O–MED

2.5.2. Comparison of all individual and combined systems

The performance of the coupled systems, 1s–NH₃H₂O–MED and 2s–NH₃H₂O–MED, were optimized using the variable metric method in the EES software. The objective function being minimized is chosen to be the unit production cost (UPC) of water. The free parameters are allowed to vary over the following intervals are shown in Table 9.

Table 9. Optimization Free Parameters

Parameter	Range	
Absorber outlet temperature	$30 \leq T_1$ (°C) ≤ 40	
Evaporator outlet temperature	$-10 \leq T_{13}$ (°C) ≤ 0	
Condenser outlet temperature	$70 \leq T_{10}$ (°C) ≤ 80	1s–NH₃H₂O–MED
	$30 \leq T_{10}$ (°C) ≤ 40	2s–NH₃H₂O–MED
Mass concentration swing between strong-and-weak solution	$1 \leq dx$ (%) ≤ 4	
Vapor mass fraction of ammonia in the evaporator	$90 \leq q_{13}$ (%) ≤ 99.8	
Temperature rise of seawater in preheater	$2 \leq dT_{sw,preheater}$ (°C) ≤ 4	
Pressure difference between each effect and its following	$0.2 \leq dP_{effect}$ (kPa) ≤ 1	

Table 10 presents the optimization results for both combined systems, 1s–NH$_3$H$_2$O–MED and 2s–NH$_3$H$_2$O–MED, at optimal operating conditions and compares them with the main three subsystems working separately at nominal operating conditions, based on assumptions in Table 4 and Table 8, at the same heat input rate of 1.94 MW$_{th}$ (enthalpy of vaporization of water at 200ºC). The 2s–NH$_3$H$_2$O–MED shows exactly the same heat rejection as the one at nominal operating conditions. Unlike that, 1s–NH$_3$H$_2$O–MED rejects more heat through the rectifier and less through the condenser due to working at double the high pressure, about 114%, than the nominal operating conditions. Consequently, the cooling capacity decreases as a result of decreasing the system efficiency as shown in Table 10. The single-stage NH$_3$-H$_2$O system's COP decreases slightly by 17% compared to the combined system, resulting in a 16% reduction in cooling capacity. On the other hand, the optimal combined system COP and cooling capacity remain unchanged compared to the double-stage NH$_3$-H$_2$O system. Relative to standalone MED, water system efficiency (GOR) decreases significantly by 30% and slightly by 9% when the MED receives its heat from the single- and double-stage NH$_3$-H$_2$O systems, respectively.

UPCs of water for the single- and double-stage NH$_3$H$_2$O–MED are 19% and 3%, respectively, more than that of the stand-alone subsystems when natural gas is used as presented in Table 10. Similarly, UPCs of water increase by 11% and 3% when exhaust heat is the heat input source. Nevertheless, the cooling unit costs for the 1s–NH$_3$H$_2$O–MED and 2s–NH$_3$H$_2$O–MED systems are 44% and 42%, respectively, *less* than that of the stand-alone subsystems because the fuel costs are exported to the water subsystem. Nonetheless, the 47% increase in the cooling cost in Table 10 is because it is compared with a cooling system that works at lower condenser pressure and operates by harnessing exhaust heat. The 2s–NH$_3$H$_2$O–MED system is able to generate 91% of water production at only 3% higher unit production cost than the MED standalone system when the same heat input is supplied to the both systems. In addition, relative to a standalone cooling system, a combined system produces the same amount of cooling resulting in decreasing the cooling costs. The 2s–NH$_3$H$_2$O-MED system is therefore competitive in thermally driven desalination plants where fossil fuel is burned to generate steam at low temperature.

Table 10. Comparison of the Single-stage NH₃-H2O, Double-stage NH₃-H2O, MED, Single-stage NH₃-H₂O+MED, and Double-stage NH₃-H₂O+MED at Optimal and Nominal Operating Conditions

		Unit	MED	Single stage NH₃-H₂O	Double stage NH₃-H₂O	Single stage NH₃-H₂O+MED		Double stage NH₃-H₂O+MED	
			Nom.	Nom.	Nom.	Opt.	diff *	Opt.	diff *
Heat input rate		kW$_{th}$	1,940	1,940	1,940	1,940	0%	1,940	0%
Rectifier(s) heat rejection rate		kW$_{th}$	−	352	1,783	525	49%	1,783	0%
Condenser heat rejection rate		kW$_{th}$	−	1,111	1,486	845	-24%	1,486	0%
Cooling capacity		Ton	−	333	418	279	-16%	418	0%
ARS high pressure		kPa	−	1,556	1,548	3,328	114%	1,548	0%
COP			−	0.60	0.74	0.50	-17%	0.74	0%
GOR			7.8	−	−	5.46	-30%	7.13	-8%
Water production capacity		m³/hr	28.3	−	−	19.3	-30%	25.8	-9%
Exergetic efficiency		%	5.0	23.5	25.8	22.8	−	30.4	−
Exergy destruction		kW	661	560	561	570	-54%	513	-57%
Natural Gas	TAC	M$/yr	1.05	0.31	0.52	1.06	-14%	1.37	-14%
	UPC Water	$/m³	4.49	−	−	5.19	19%	4.60	3%
	UPC Cooling	$/ton.hr	−	0.113	0.15	0.091	-44%	0.113	-42%
Exhaust Heat	TAC	M$/yr	0.92	0.18	0.39	0.94	0%	1.24	0%
	UPC Water	$/m³	3.94	−	−	4.40	11%	4.00	3%
	UPC Cooling	$/ton.hr	−	0.066	0.113	0.091	47%	0.113	0%

* The difference with respect to the MED, Single- and Double-stage NH₃-H₂O systems under nominal operating conditions except for the Total Annual Costs (TAC) which was compared with an MED's TAC of the same capacity size.

Figure 28 shows the effect of heat input rate, proportional to water production capacity, on the unit product cost of fresh water for the proposed systems, where the only difference here between exhaust heat and natural gas is the fuel cost (check Equation A.23 in Appendix A). Fuel cost is set to equal zero for exhaust heat and \$1.9 per MMBtu for natural gas. It can be seen from Figure 28 that water UPC reduces below a target threshold of $1/m^3$ (red horizontal line) when waste heat input of over 100 MW is available (according to our model, this is equivalent to about 31,000 m^3 per day of fresh water produced) for standalone MED, 1s–NH_3H_2O–MED, and 2s–NH_3H_2O–MED when exhaust heat is harnessed. Interestingly, 1s–NH_3H_2O–MED's (exhaust heat) UPC converges with the standalone MED as the heat input rate increases, while 2s–NH_3H_2O–MED converges with the standalone MED at about 1 MW_{th} relevant to its corresponding heat source. At this high heat input capacity, such systems are very competitive with seawater reverse osmosis (SWRO) at the same water production capacity, where SWRO water costs just about the same at the same capacity range [27]. Keep in mind that unlike standalone MED, combined systems provide two products (water and cooling).
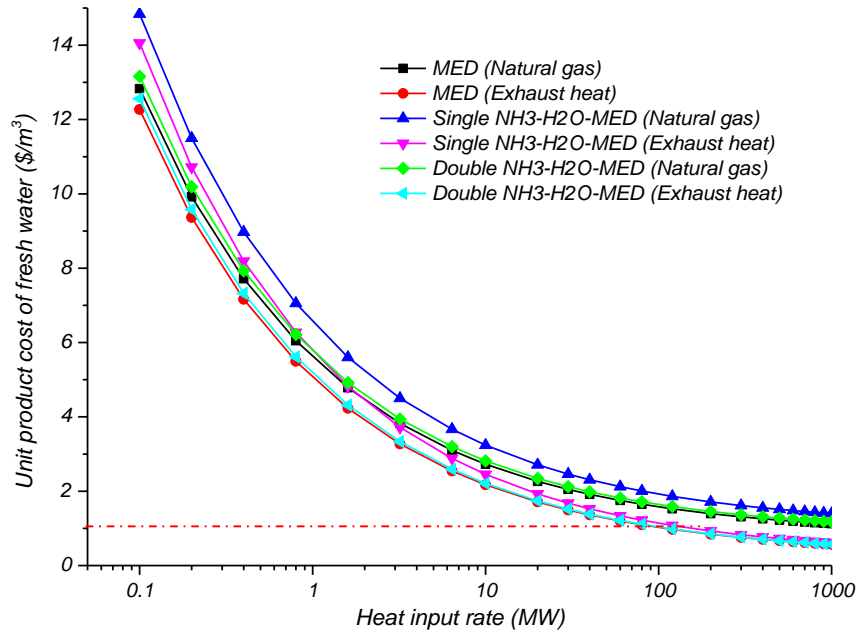
Figure 28. Effect of the Amount of Heat Input Rate (Plant Capacity) on the Unit Production Cost of Water for Standalone MED, Single- and Double stage NH_3H_2O–MED

In comparison with the results obtained from other work in the literature and in particular with the more common water-lithium bromide ARS integrated with a desalination unit, water production

per unit mass flow rate of motive steam is 5.36 kg/s for 1s–NH_3H_2O–MED and 7.16 kg/s for 2s–NH_3H_2O–MED compared to 4.016 and 9.75 kg/s as claimed by [16] and [13], respectively. Similarly, cooling capacity per unit mass of motive steam is 981 kW_{th} for 1s–NH_3H_2O–MED and 1470 for 2s–NH_3H_2O–MED compared to 1652 and 1685 kW as claimed by [1] and [13], respectively.

Darwish et al. [6] carried out a study that suggests retrofitting a combined-cycle desalination plant in Qatar to replace the inefficient multi-stage flash (MSF) desalination system with an SWRO system. They proposed to harness the latent heat coming out of the steam turbine to drive a single-stage LiBr-H_2O ARS. Table 11 shows a comparison between their proposed system with both of our proposed systems, 1s–NH_3H_2O–MED, and 2s–NH_3H_2O–MED. Note that the thermal energy supplied to the steam cycle is 866.46 MW_{th}. It can be seen from Table 11 that 2s–NH_3H_2O–MED produces more cooling and water than both the base case and proposed systems.

Table 11. A Comparison of 1s–NH_3H_2O–MED and 2s–NH_3H_2O–MED against Data from a Combined-cycle Desalination Plant [6]

	Base case	Darwish	1s–NH_3H_2O–MED	2s–NH_3H_2O–MED
Power output by steam cycle (MW_e)	215.7	243.8	226	226
Steam turbine exhaust pressure (Bar)	2.8	2.8	10	10
Water production (m^3/day)	204,570	181,843	174,048	222,432
Cooling capacity (MW_{th})	-	459	357	524

Unlike the 2s–NH_3H_2O–MED system in which its ARS requires no modification either in its operating condition, nor in its configuration design due to the abundant amount of heat rejection, the 1s–NH_3H_2O–MED system is more appealing for applications where cooling and water are not needed at the same time during the course of the day. Water and cooling production can be easily adjusted by simply controlling the condenser pressure (ARS high pressure) through the pump, and the heat source temperature. If cooling is required, for instance, the system can be operated at lower condenser pressure and lower heat source temperature, and the opposite to produce more water.

One technological difficulty related to the 1s–NH_3H_2O–MED system is the interchanging mode between cooling and desalination where it requires varying the condenser pressure. Operating the ARS system at higher pressure causes the system to act as a pressure vessel which requires high safety precautions, in fact, the double-stage NH_3H_2O ARS is not commercially available due to its high working pressure of ammonia of about 20 bar [23]. Note that our proposed systems are meant

to be operated at large cooling/desalination plants where working with high safety precautions such as high pressure, toxicity, etc. are anticipated.

One might ask about the value of generating this substantial amount of cooling. One related water application is freeze desalination (FD) where water and salt are separated based on the fact that ice crystals are pure water. FD can perhaps be aimed to distill the rejected brine from the MED desalination unit resulting not only in reducing the brine rejection rate but also possibly producing salt as a secondary product. FD involves three main processes which are ice formation, ice-salt separation, and ice melting. Note that cooling capacity can be recovered during ice melting, so there is an opportunity to store, transport, and harness that cooling for a different cooling application. Because cooling need not necessarily be consumed at the desalination plant site, district cooling is another desirable use of the large cooling capacity produced by our proposed system, particularly 2s– NH_3H_2O–MED. Regardless of the distance between the district cooling loop and the desalination plant, cooling capacity could potentially be delivered to the cooling demand sites in the form of cold fresh water, in other words, pumping two products in one.

2.6. Summary

This chapter proposes coupling absorption refrigeration systems (ARS) and multi-effect distillation (MED) with the aim of decreasing the MED's associated exergy destruction, and utilizing exhaust heat to reduce operating cost. The two proposed systems, namely 1s–NH_3H_2O–MED and 2s–NH_3H_2O–MED, recycle rejected heat from the rectifier and condenser of an NH_3–H_2O ARS to generate fresh water. Based on our thermodynamic and economic calculations, the combined 1s–NH_3H_2O–MED and 2s–NH_3H_2O–MED systems have higher heat utilization rate with a reduction in the exergy destruction by 54% and 57%, respectively, compared to the stand-alone NH_3–H_2O and MED systems. The 2s–NH_3H_2O–MED system is able to provide the same amount of cooling capacity compared to a stand-alone double-stage ARS subsystem with a 42% reduction in the unit cost of cooling. Moreover, its water production capacity only reduces by 9%, compared to a stand-alone MED unit, resulting in an increase in its unit production (water) cost by only 3%. Unlike the 2s–NH_3H_2O–MED system, the 1s–NH_3H_2O–MED system shows fewer advantages, as its water capacity decreases by 30% and cooling capacity by 16% compared to the stand-alone MED and single-stage NH_3–H_2O systems, respectively. As a result, the system unit production cost of water increases noticeably by 19%, and the unit cost of cooling decreases by 44% when natural gas is used.

3. SHERBECK CYCLE

About 85% of electricity production worldwide is generated using a Rankine power cycle [41]. However, the thermal efficiency of the Rankine cycle becomes very low and unacceptable from an economic standpoint when the steam temperature is below 371ºC [41]. Hence, at these temperatures, the key to making a Rankine cycle financially feasible is to harness the reject heat for a secondary cycle or applications. Indeed, studies show that such Rankine combined systems can be made worthwhile, and so we choose a Rankine cycle as the basis for the power generating subsystem. The Sherbeck cycle, on the other hand, exploits the condenser heat rejection to drive other thermally driven components which makes it capable to work within the full spectrum of low-grade to high-grade heat limited only by the materials available. Nevertheless, most of the system could be made out of very inexpensive parts at low temperatures through the use of plastics.

In this chapter, we investigate a novel polygeneration system to produce cooling, power, and possibly water with the intension of decreasing the overall energy consumption as well as the operating cost compared with standalone systems. Unlike other cooling and dehumidification systems available in the market, the Sherbeck cycle utilizes only air and water as working fluids, which are non-hazardous and environmentally friendly resulting in mitigating carbon emissions. Moreover, a wide variety of working fluids can be employed at the preference of the operator since the Sherbeck cycle is a closed-loop system, a key feature that distinguishes it from other systems. In practice, operational problems encountered in "open cycle" plants are owed to the simple fact that an open cycle permits fouling from dust in the air, minerals in the make-up water, and noise pollution from the inlet and exhaust.

The Sherbeck cycle, as referred to, is composed of four subsystems based on a reverse Brayton cycle (gas refrigeration cycle), a Rankine cycle, an evaporative cooling cycle, and a liquid desiccant cycle which operate internally at atmospheric and sub-atmospheric pressures. The system is potentially attractive for remote areas which require off-grid power, cooling, and freshwater. Moreover, it has the potential to be made at a modest cost, making it affordable for the developing world and in recognition that power and refrigeration systems are essential to improve the quality of life. This application is related to a utility patent that was filed on December 22, 2015 by Jonathan Sherbeck, having an application No. of 62271134 and Attorney Docket No. 10046P002Z (M16-038P) [42].

3.1. HEAT-DRIVEN CYCLE TO PRODUCE SHAFT POWER AND REFRIGERATION

Residential, commercial, and industrial buildings all over the world consume a significant fraction of energy in the form of electricity, cooling, and heating. On-site polygeneration and district systems remain atypical, perhaps due to historical, economic, or practical considerations and preferences of building managers. Consequently, fuel consumption escalates, which ultimately increases energy demand, fuel cost, air pollution, and carbon emissions [43]. Combined cooling, heating, and power (CCHP) systems have been identified as energy efficient and an effective strategy in the face of rising fuel costs with less negative environmental impact compared to conventional stand-alone systems [7, 11, 44-46].

In this section, we propose a novel cooling, dehumidification, and power cycle that is composed of four subsystems based on a gas refrigeration cycle (reverse Brayton cycle), a Rankine power cycle, an evaporative cooling cycle, an ejector, and a liquid desiccant cycle that operates internally at atmospheric and sub-atmospheric pressures. Unlike other cooling and dehumidification systems available in the market, the proposed cycle utilizes only air and water as working fluids, which are non-hazardous and environmentally friendly. The proposed cycle exploits the heat rejection by the Rankine cycle condenser to drive other thermally driven components. Such a system is designed for a hot and humid climate with high water scarcity, thus, it is critical to make it a closed-loop system.

3.1.1. Literature Review

Cho et al. [47] presented a broad review of performance improvement methodology for combined cooling, heating, and power (CCHP) systems using energy and exergy analyses. They found that CCHP systems are usually analyzed and optimized in a wider context using various techniques and criteria such as primary energy savings, total cost rate, greenhouse gas emissions, and energetic and exergetic efficiencies. They concluded that major trends in recent literature regarding CCHP systems are utilizing alternative power sources, applying novel thermodynamic techniques, and improving system selection with new working schemes.

Demirkaya et al. [41] explored in a review paper the feasibility of improving the overall energy conversion efficiency of different combined power and refrigeration cycles, in which heat rejected by the power cycles can be recovered to provide refrigeration. They concluded that, in most applications, refrigeration is a more expensive product than power since it requires purchasing both

power and equipment to produce. Consequently, the extra refrigeration reduced by the combined power and refrigeration cycles is more beneficial than standalone conventional power plants.

Liu et al. [48] surveyed state-of-the-art CCHP systems in which the survey was divided into three parts. In the first part, they presented the development and operation strategies of CCHP systems. Secondly, they introduced prime movers (steam turbines, reciprocating internal combustion (IC) engines, and fuel cells) that provide reject heat and thermally activated cooling technologies (absorption and adsorption chillers, and desiccant dehumidifiers) that can utilize that heat. In the third part, they presented the recent research progress on the management, control, optimization, and sizing of CCHP systems.

In a similar work, Al Moussawi et al. [49] classified different types of trigeneration systems based on the prime mover, size, and energy sequence usage. They showed in detail a methodology for selecting the optimum heat recovery equipment (cooling or heating) that is suitable and compatible with a given prime mover. Additionally, they considered various thermal energy storage systems and heat transfer fluids to be employed in order to reduce the trigeneration system's size and capital cost. In their detailed review, they found that CCHP systems often have positive performance impacts compared with separate systems that provide the same services.

Because cooling demand varies frequently, Han et al. [50] compared two operating strategies of small-scale gas turbines, namely turbine inlet temperature (TIT) and compressor inlet air throttling (IAT), to improve the overall performance of combined cooling and power (CCP) systems. A single-effect LiBr-H_2O absorption refrigeration system was considered to harness the high-temperature exhaust of the gas turbine in order to meet the cooling demand. The result showed that, when the gas turbine is operated at 50% rated power output, the IAT operating strategy can increase the overall system performance by 10% compared with the TIT strategy.

Rostamzadeh et al. [51] presented energy and exergy analyses of a combined cooling and power (CCP) cycle based on a combination of the organic Rankine cycle (ORC) and ejector refrigeration cycle (ERC). In three different configurations of the ORC, the ORC reject heat was harnessed to drive the ERC. Aiming to identify the best configuration based on energy and exergy performances, they selected (1) isobutene as the refrigerant for the ERC, (2) R123 as the ORC working fluid for the ORC, and (3) a configuration with recuperation and turbine bleeding.

Kang et al. [52] proposed a coupled combined heat and power and heat pump (CHP-HP) system of which a domestic hot water heater utilizes the waste heat from a ground source heat pump (GSHP)

condenser and exhaust heat of a gas turbine engine. The result indicated that the proposed system can generate more power compared to the reference system. In a recent work by the same authors [53], the proposed system was optimized by a genetic algorithm based on several parameters such as primary energy saving ratio (PESR), CO_2 emission reduction ratio (CER), and annual total expense saving ratio (ATESR). The result showed that the comprehensive performance (CP) metric of the proposed system reached a maximum of 26.76% when the prime mover capacity was 1.136 MW_e, where the corresponding PESR, CER, and ATESR were 23.24%, 35.13%, and 21.93%, respectively.

3.1.2. System Configuration

The original cycle (OC) is a closed, low-grade heat-driven Rankine cycle driving a reverse Brayton cycle (gas refrigeration cycle) using an ejector as the expansion element with a liquid desiccant loop to produce shaft power and refrigeration by adiabatic expansion and evaporation. A schematic diagram of the original cycle, also referred to as "Configuration 1", is shown in Figure 29. The OC operates at three different pressure levels. First, a high pressure is generated by a boiler feed water pump (BFWP) that provides the inlet motive steam into the ejector. Second, there is a medium pressure at the ejector outlet (discharge), which is maintained at atmospheric pressure as dictated by the ambient condition of the separating tank and desiccant cycle. The third pressure is a low (vacuum) pressure that exists between the turbine outlet and ejector suction.

Since the cool air produced by the gas refrigeration cycle (at turbine outlet, point 9) is dry, we chose to add an evaporative cooling section in order to enhance the cooling effect and to provide chilled water instead of air to the heat exchanger (HX1). In conventional air conditioner technologies, the cooling coil has to be cooled down below the corresponding dew point temperature in order to remove moisture by condensation. There is no longer a need to do this in the proposed cycle, thus leaving the cooling coil responsible only for the sensible cooling loads while the desiccant solution cycle handles the latent cooling load from the air conditioned space. Consequently, the cooling coil may operate at higher temperatures in the OC compared with conventional AC systems and yet achieve the same comfort levels.
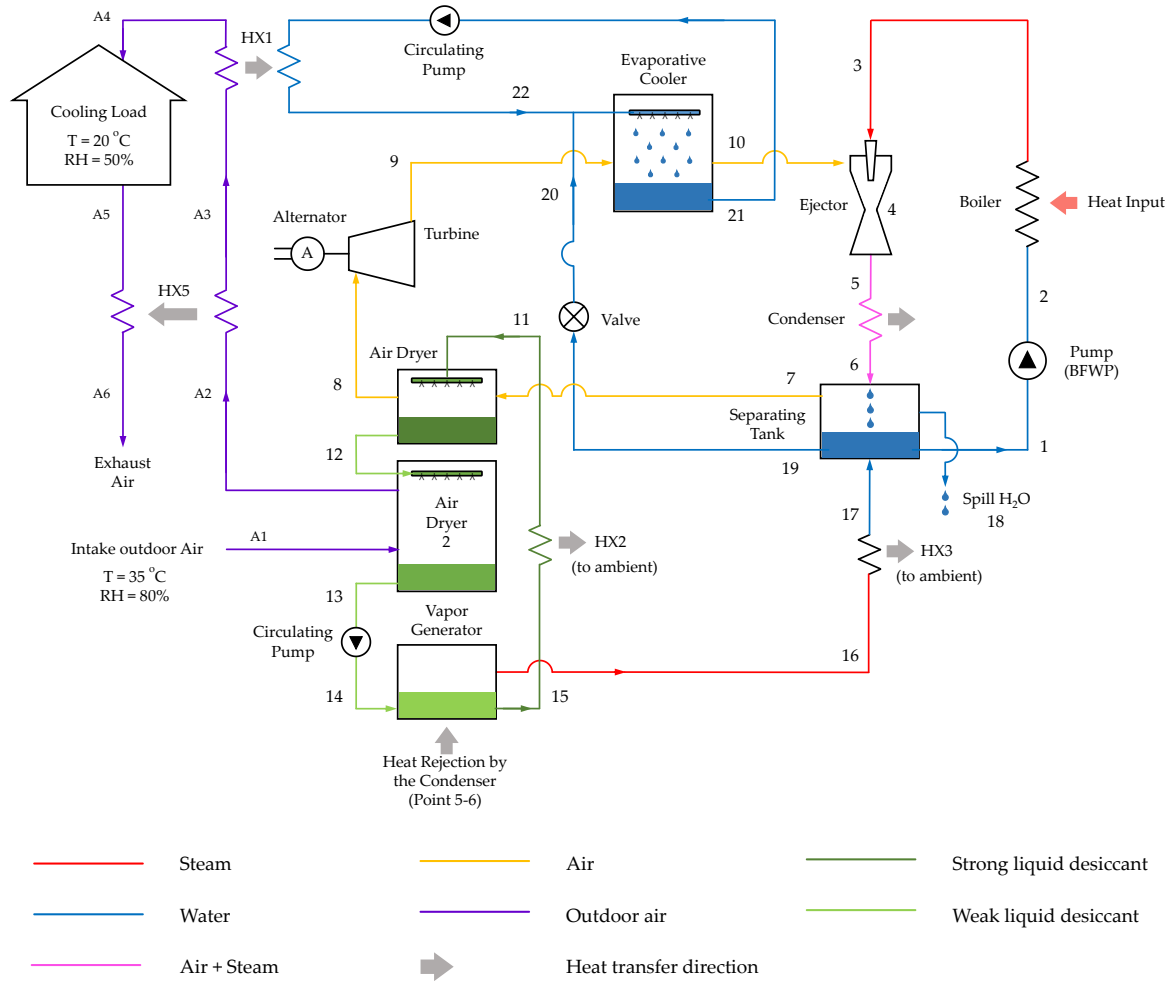
Figure 29. Schematic diagram of the proposed original cycle (OC) (Configuration 1)

Following the state point numbering in Figure 29, liquid water coming out of the separating tank and condenser are brought to a higher pressure using a boiler feedwater pump (BFWP, points 1→2). In the boiler, the heat input, e.g. steam at 210ºC, heats up the liquid water and converts it into saturated steam, which enters the steam ejector (point 3). Driven by high pressure steam (point 3) as a motive gas, the ejector draws a low pressure at point 10. This low-pressure suction drives the turbine to produce shaft power and cold air (point 9) via expansion. This air transfers its cooling capacity to water in the evaporative cooler. The mixture of steam and moisture-saturated air (point 5) is cooled through the condenser into a mixture of water and saturated air (point 6), which is separated in the tank by gravity. Some of the water in the separating tank is used to make up water in the evaporative cooler, which is connected to the separating tank through a thermal expansion valve (TXV) (between points 19 & 20). The rest of the water in the separating tank is then mixed

50

with condensed water from the desiccant cycle (point 17) before entering the BFWP again. Using a spill-to-fill tank (separating tank) allows the collected moisture from the air conditioned space to spill out of the system as fresh water if it exceeds the required amount of water (point 18). Saturated air coming out of the separating tank (point 7), at atmospheric (medium) pressure, enters the desiccant system dryer heading to the turbine where the strong solution of the sorbent is sprayed to dry the air in order to reduce the erosion rate of the turbine blades in and thus increase the turbine life time. Dry air (point 8) is then expanded in a gas turbine in which mechanical work is converted into electrical power using a generator. Low-pressure dry air (point 9) becomes saturated as water is sprayed in the evaporative cooler between points 9 and 10. As the desiccant system dryer acts to dry the air by absorbing the water vapor, medium strength solution (point 12) handles the latent heat load of the process air, becoming a weak solution (point 13) that is sent to a vapor generator where the heat rejection by the condenser (between points 5 & 6) is used to regenerate the desiccant. The generated water vapor (point 16) is released from the sorbent by heating and then condensed at the heat exchanger 3 (HX 3 between points 16 and 17). Strong solution (point 15) is cooled down in a liquid desiccant cooler (between points 15 and 11) before it is circulated back to repeat the desiccant cycle (point 11). Note that HX2, HX3, HX4 reject heat to the environment.

Unlike the original cycle (Configuration 1 in Figure 29), the steam ejector in the *enhanced cycle* (EC), as shown in Figure 30 (Configuration 2), is replaced with a steam turbine (Rankine cycle) and a compressor for a gas refrigeration cycle (reverse Brayton cycle). It can be observed from Figure 30 that the Rankine cycle turbine, compressor, and turbine of the gas refrigeration cycle are connected with the same shaft to avoid the unnecessary irreversibility associated with the electric generator. Nevertheless, connecting both cycles via an electric generator can be very advantageous from an operational viewpoint to control power/cooling production, especially considering that air conditioning systems are often operated in on/off mode.

A steam Rankine cycle is inefficient at converting low-grade heat to shaft work, however, the EC system exploits both the shaft work to drive the gas refrigeration cycle and the rejected latent heat to drive the liquid desiccant solution cycle. Therefore, the EC is anticipated to obtain a higher overall conversion efficiency than the OC.
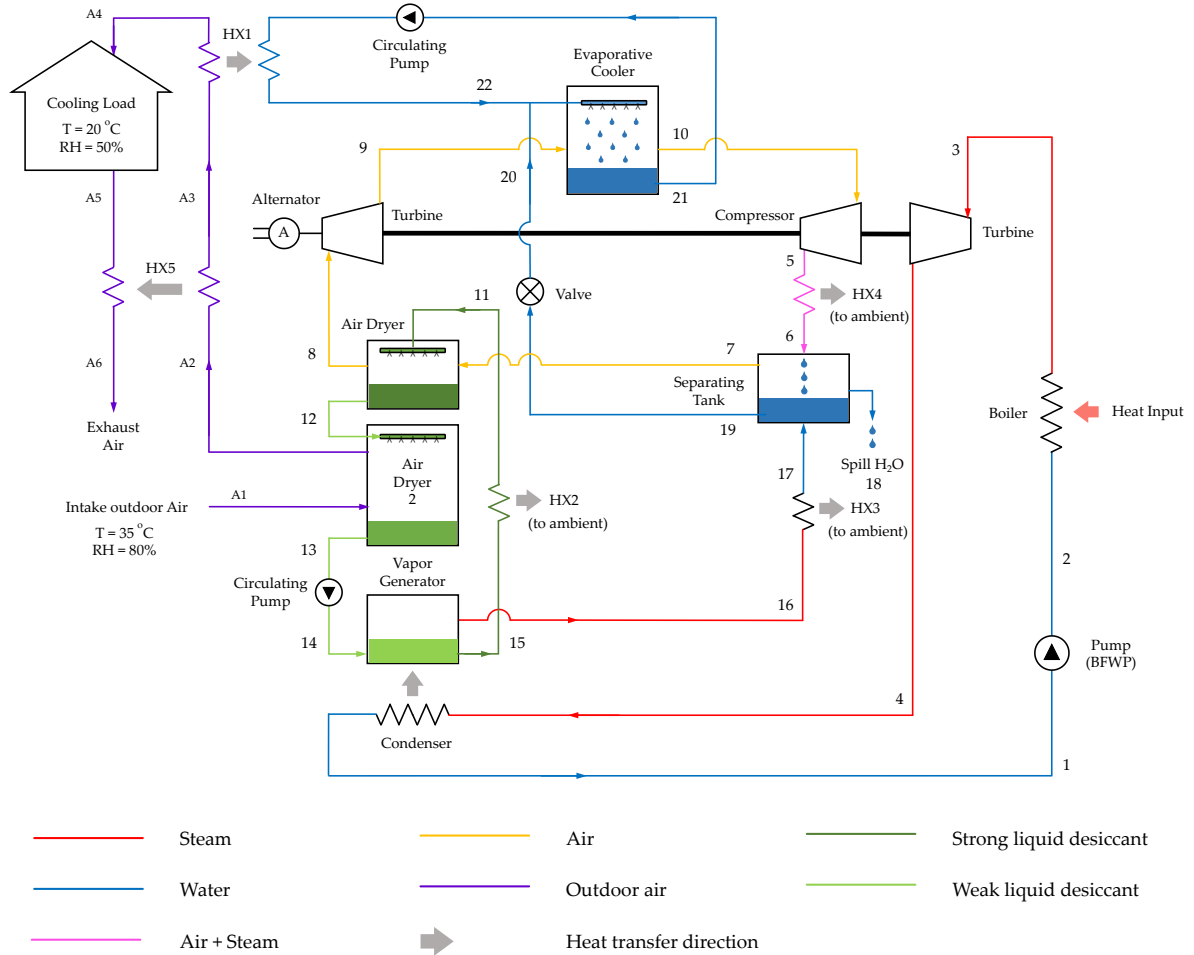
Figure 30. Schematic diagram of the enhanced cycle (EC) (Configuration 2)

For the sake of simplicity, Figure 31 illustrates a block diagram for the cascaded heat flow of the enhanced cycle that demonstrates the various inter-relationships among all four subsystems in terms of their inputs and outputs. In Figure 31, the only heat input into the system is supplied to the steam Rankine cycle boiler (points 2→3) where part of the shaft work done by the steam turbine drives the reverse Brayton cycle compressor. Meanwhile, the latent heat rejection by the Rankine cycle (points 4→1), at about 80ºC, is utilized to regenerate the liquid desiccant solution in the vapor generator (points 14→15). Cold dry air proceeds to the evaporative cooler (points 9→10) where it provides cold water at about 13ºC that is used to handle the sensible cooling load. Warm humid air exiting the compressor of the reverse Brayton cycle (point 5) needs to first be cooled in the separating tank then dehumidified using the desiccant solution cycle before it enters the gas refrigeration cycle's turbine (point 8) in order to avoid erosion of the turbine blades. Warm and humid air coming from outdoors dissipates its latent heat by dehumidification in the air dryer 2

52

before it enters the cooling coil (between points 21 and 22 in Figure 29 & Figure 30) where it rejects its sensible heat to provide cool air at about 18ºC and 40% relative humidity to the cooling load.
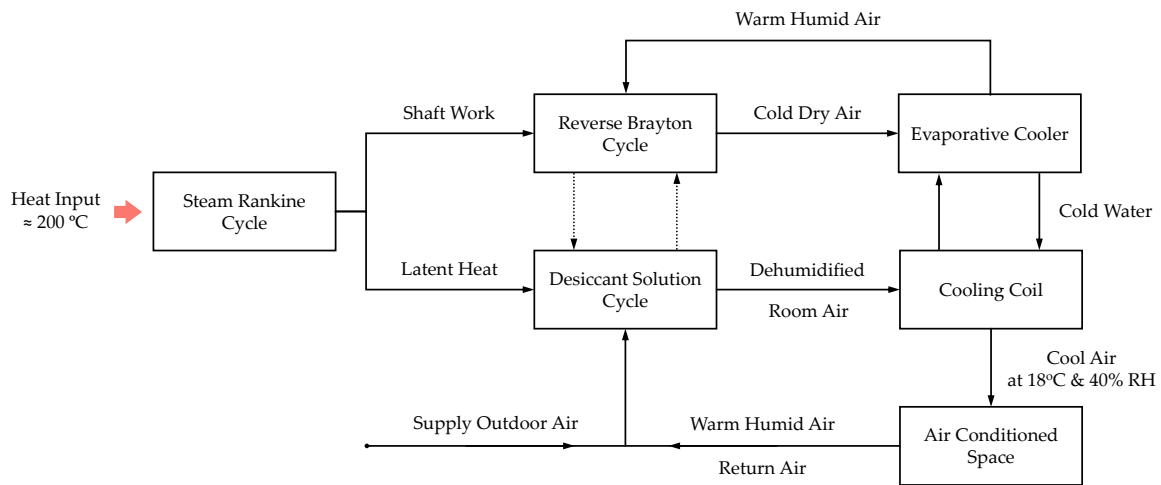
Figure 31. Block diagram for the cascaded heat flow of the enhanced cycle (Configuration 2)

Since integrating the evaporative cooling, liquid desiccant, and gas refrigeration subsystems is a key feature that distinguishes our proposed cycle from other systems, we present the T-s diagram of this subsystem in Figure 32. Furthermore, the evaporative cooling, liquid desiccant, and gas refrigeration cycles are visualized on an h-s diagram and psychrometric chart for both the OC and EC as depicted in Figure 33 and Figure 34, respectively. It is worth noting that the evaporative cooler is divided into multiple stages to ensure heat absorption and humidification at the same time in order to increase the cooling capacity as illustrated in Figure 34.
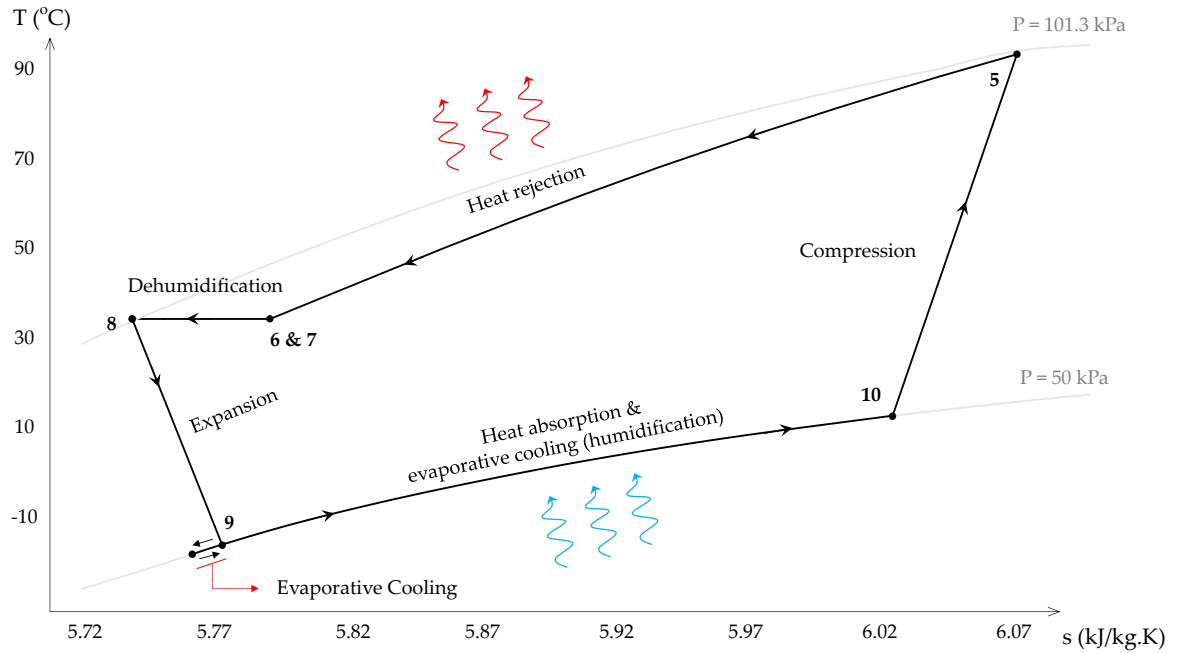
Figure 32. T-s diagram of the evaporative cooling, liquid desiccant, and gas refrigeration subsystems
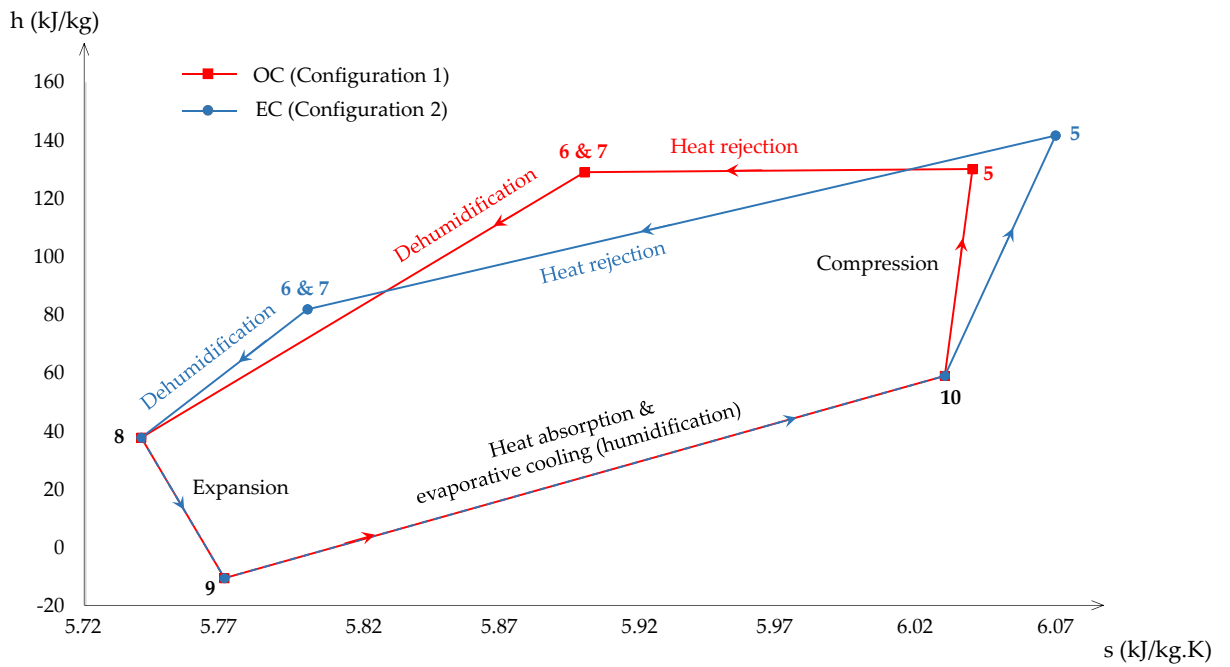
Figure 33. h-s diagram of the evaporative cooling, liquid desiccant, and gas refrigeration subsystems for the original and enhanced cycles
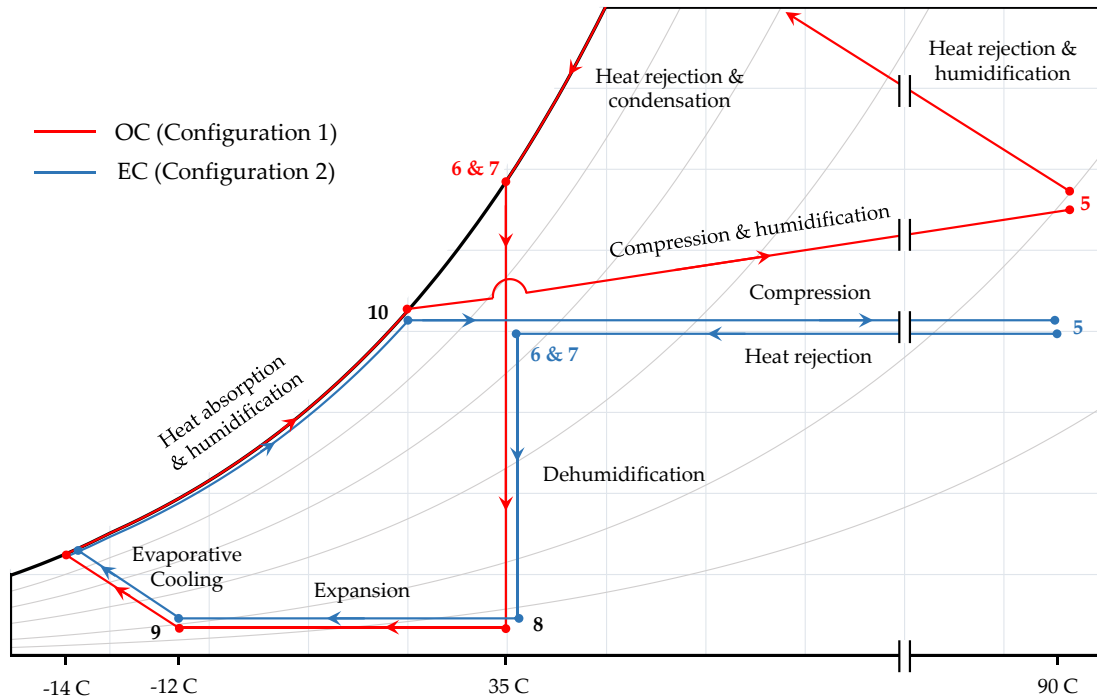
Figure 34. Psychrometric chart showing the evaporative cooling, liquid desiccant, and gas refrigeration subsystems for the original and enhanced cycles

3.1.3. Mathematical Modelling

The mathematical model of the OC and EC are composed of multiple subsystems (sub-cycles) based on a gas refrigeration cycle, Rankine cycle, evaporative cooling cycle, ejector refrigeration cycle, and liquid desiccant cycle, as appropriate. Initially, each subsystem was modelled and validated separately before they were integrated with each other to form both the original cycle (configuration 1) and the enhanced cycle (configuration 2).

In order to simplify the complexity of these cycles, the following assumptions were applied for the thermodynamic models:

i. Heat losses and pressure drops in all components and piping are not considered.

ii. Steady-state operation with negligible potential and kinetic energy, especially for the ejector inlet and outlet velocities.

iii. Irreversibilities in the primary nozzle, mixing chamber, and diffuser of the ejector were considered by applying different efficiency coefficients.

iv.   The mixing of motive fluid (steam) and entrained fluid (saturated air) takes place in the mixing chamber at constant pressure equal to the evaporative cooler pressure (point 4 of Figure 29).

v.   The desiccant solution properties are calculated at the interface with air at average conditions.

vi.   The air is dry (3% relative humidity) at point 8 and almost saturated (95% relative humidity) at point 10 (Figure 29 & Figure 30).

Based on the above-mentioned assumptions, the mass balance (continuity), energy balance (the first law of thermodynamics), and exergy balance (the second law of thermodynamics) are performed for each component of the system. The Rankine, gas refrigeration, and evaporative cooling cycles are modelled straightforwardly based on widely known thermodynamic models by Cengel and Moran [54, 55]. Therefore, in this paper, we present only the ejector and liquid desiccant cycle mathematical models, in addition to the chief parameters describing the overall system performance.

It is worth mentioning that the sensible cooling capacity in the gas refrigeration subsystem of the OC, configuration 1, is restricted by the desired vacuum (refrigeration temperature) that needs to be achieved by the ejector. In other words, the lower the desirable refrigeration temperature, the less air mass flow rate can be drawn into the ejector or turbo-compressor which plays a role in limiting the operating range of the OC. Unlike the OC, sensible and latent cooling capacities in the enhanced cycle (EC) are restricted by the heat rejection of the Rankine cycle condenser, since it determines the size and mass flow rate of the liquid desiccant cycle that can be regenerated (recharged).

3.1.3.1.   Ejector thermodynamic model

The ejector in the original cycle (Figure 29) is responsible for generating the low pressure of the air refrigeration subsystem (evaporative cooler). In our case, the motive fluid (steam) and entrained fluid (humid air) are clearly different fluids, which is accounted for by assuming that the air inlet and outlet specific humidity difference is negligible. A steady-state mathematical model of the ejector based on a simplified model was applied as recommended by [56, 57]. The energy balance across the ejector can then be written as

$$\dot{m}_3 h_3 + \dot{m}_{10} h_{10} = \dot{m}_3 h_{5,steam} + \dot{m}_{10} h_{5,Air} \qquad (3.1)$$

where $\dot{m}$ is the mass flow rate in (kg s^{-1}) and h the specific enthalpy in (kJ kg^{-1}).

As the motive steam (point 3) adiabatically expands in the primary nozzle, it experiences an increase in its velocity resulting in a significant reduction in its pressure at the nozzle exit. Therefore, the motive steam exit enthalpy of the primary nozzle (point 3e) can be calculated by assuming a nozzle isentropic efficiency (η_{nozz}):

$$\eta_{nozz} = \frac{h_3 - h_{3e}}{h_3 - h_{3e,s}}$$

(3.2)

where the subscript e is the nozzle exit and s the isentropic process.

As the motive steam exiting the primary nozzle is mixed with the secondary saturated air, it partially gives its kinetic energy to the secondary saturated air thus generating a low pressure across the evaporative cooler. The entrainment efficiency (η_{entr}) is defined in order to impose a constraint needed to solve the energy balance at the mixing chamber which can be written as follows:

$$\eta_{entr} = \frac{\dot{m}_3\left(h_{5,steam} - h_{4,steam}\right) + \dot{m}_{10}(h_{5,air} - h_{4,air})}{\dot{m}_3(h_3 - h_{3e})}$$

(3.3)

By assuming that steam and humid air are in thermal equilibrium at the ejector exit, their enthalpies can be calculated by assuming a diffuser isentropic efficiency (η_{diff}):

$$\eta_{diff} = \frac{\dot{m}_3\left(h_{s5,steam} - h_{s4,steam}\right) + \dot{m}_{10}\left(h_{s5,air} - h_{s4,air}\right)}{\dot{m}_3\left(h_{5,steam} - h_{4,steam}\right) + \dot{m}_{10}(h_{5,air} - h_{4,air})}$$

(3.4)

The above-mentioned equations are solved simultaneously in order to determine the mass flow rate $\dot{m}_{10}$ of the gas refrigeration subsystem for the original cycle (Figure 29) at a specified desirable pressure.

3.1.3.2. Liquid desiccant thermodynamic model

The liquid desiccant subsystem, based on Lithium Chloride (LiCl) in both the original (OC) and enhanced cycles (EC), is responsible for dehumidifying the humid air before it enters the gas refrigeration (reverse Brayton) turbine and for handling the latent cooling load. The liquid desiccant subsystem consists of a dehumidifier (air dryer), vapor generator, and circulating pump. A simplified mathematical model based on energy and mass balances is adapted from Gandhidasan [58, 59]. The energy balance across the dehumidifier (dryer) can be written as

$$\dot{m}_{a,7}c_{p,a}(T_7 - T_8) + \dot{m}_{a,7}h_{fg}(\omega_7 - \omega_8) = \dot{m}_{11}c_{p,s}(T_{12} - T_{11}) \qquad (3.5)$$

where T is temperature in (°C), ω humidity ratio of air in (kg water/kg dry air), and $c_{p,a}$ and $c_{p,s}$ the specific heats of the air and desiccant solution (LiCl) in (kJ kg^{-1} K^{-1}), respectively.

The moisture removal effectiveness α can be written as a function of the air humidity ratio or of the partial pressure of water vapor in the air, as the former is a function of the latter:

$$\alpha = \frac{\omega_7 - \omega_8}{\omega_7 - \omega_{8,min}} = \frac{P_{a,7} - P_{a,8}}{P_{a,7} - P_{a,8,min}} \qquad (3.6)$$

where P_a is the partial pressure of water vapor in the air in (kPa), and $P_{a,8,min} = P_{s,11}$ since the dehumidification process takes place as long as the partial pressure of water vapor in the air is higher than the solution vapor pressure.

Also, the dehumidifier (dryer) thermal effectiveness β, which accounts for the air temperature change across the dryer, can be written as

$$\beta = \frac{T_7 - T_8}{T_7 - T_{11}} \qquad (3.7)$$

From Eqs. (6) and (7), Eq. (5) can be rewritten as

$$\dot{m}_{a,7}c_{p,a}\,\beta(T_7 - T_{11}) + \dot{m}_{a,7}y\alpha(P_{a,7} - P_{s,11}) = \dot{m}_{11}c_{p,s}(T_{12} - T_{11}) \qquad (3.8)$$

where for small partial pressures of water vapor, y can be defined as

$$y = \frac{M_w}{M_a}\frac{h_{fg}}{P_{atm}} = 0.622\frac{h_{fg}}{P_{atm}} \qquad (3.9)$$

where M is the molar mass in (kg mol^{-1}), h_{fg} the enthalpy of vaporization in (kJ kg^{-1}), and $P_{atm} = P_7$ the atmospheric pressure in (kPa).

The vapor pressure of the strong inlet desiccant solution ($P_{s,11}$) and specific heat ($c_{p,s}$) of the LiCl solution are calculated in terms of the desiccant solution concentration (χ) and temperature as introduced by Conde [60], and is shown in Appendix C. The temperature of the weak desiccant solution (T_{12}) and the air exiting the dryer (T_8) can be found through Eqs. (8) and (7), respectively. It is worth remarking that the moist air dehumidification (point 7-8) does not occur at constant

temperature, however, we assumed so for the sake of simplicity. In fact, we abandoned the idea of harnessing the cooling potential leaving the evaporative cooler (point 10) with the purpose of achieving dehumidification at constant temperature.

The condensation rate ($\dot{m}_{cond}$) and humidity ratio of the air leaving the dryer (ω_8) can then be calculated from

$$\dot{m}_{cond} = \frac{\dot{m}_{a,7} \, y\alpha}{h_{fg}}(P_{a,7} - P_{s,11}) \tag{3.10}$$

$$\dot{m}_{cond} = \dot{m}_{a,7}(\omega_7 - \omega_8) \tag{3.11}$$

The outlet desiccant solution concentration ($\chi_{s,12}$) can be found by the following relationship:

$$\frac{1}{\chi_{s,12}} = \frac{1}{\chi_{s,11}}\left(1 + \frac{\dot{m}_{cond}}{\dot{m}_{11}}\right) \tag{3.12}$$

Equations (5) to (12) are applied on dryer 2 (Figure 29 & Figure 30) to predict the additional moisture removal rate in dryer 2, the humidity ratio of air leaving dryer 2 (ω_{A2}), the desiccant solution concentration entering the vapor generator ($\chi_{s,13}$), etc. The required heat input rate in order to regenerate the liquid desiccant of LiCl solution is calculated from

$$\dot{Q}_{reg} = \dot{m}_{14}c_{p,s,14}(T_{15} - T_{14}) \tag{3.13}$$

where T_{15} is the regeneration temperature and is assumed to equal the condenser temperature of the Rankine cycle. Note that the specific heat of the LiCl solution ($c_{p,s,14}$) is a function of both temperature and concentration.

For the enhanced cycle, Eqs. (5) to (12) are solved backwards in order to determine the maximum flow rate of the gas refrigeration (reverse Brayton) subsystem since the liquid desiccant subsystem is restricted by the required heat input from the Rankine sub-cycle condenser to regenerate the desiccant.

3.1.3.3. System performance indicator

For CCHP systems, Rosen and Le [61] recommended the use of exergy (second law) efficiency rather than energy (first law) efficiency since the latter is quite misleading. Unlike energy efficiency, the exergy efficiency takes into account the quality of heat and energy, which can be

defined as the fraction of the useful exergy to the total exergy input. The energy (first law) and exergy (second law) efficiencies can be expressed as:

$$\eta_{energy} = \frac{\dot{W}_{ele} + \dot{Q}_{sen} + \dot{Q}_{lat}}{\dot{Q}_{hs}} \qquad (3.14)$$

$$\eta_{exergy} = \frac{\dot{W}_{ele} + \dot{E}_{sen} + \dot{E}_{lat}}{\dot{E}_{hs}} \qquad (3.15)$$

where $\dot{Q}$ and $\dot{E}$ are the energy and exergy rates associated with the sensible ($\dot{Q}_{sen}$, $\dot{E}_{sen}$) and latent cooling outputs ($\dot{Q}_{lat}$, $\dot{E}_{lat}$) and heat input ($\dot{Q}_{hs}$, $\dot{E}_{hs}$), in which $\dot{Q}_{sen}$, $\dot{Q}_{lat}$, and $\dot{E}$ can be calculated as

$$\dot{Q}_{sen} = \dot{m}_A \cdot c_{p,A} \cdot (T_{A1} - T_{A3}) \qquad (3.16)$$

$$\dot{Q}_{lat} = \dot{m}_A \cdot h_{fg} \cdot (\omega_{A1} - \omega_{A3}) \qquad (3.17)$$

$$\dot{E} = \dot{m} \cdot [(h_{in} - h_{out}) - T_o(s_{in} - s_{out})] \qquad (3.18)$$

where T_o and s are the dead state temperature and entropy, and the subscripts *in* and *out* refer to the inlet and outlet values. Note that the total exergy input is estimated as the change in exergy flow rate across the boiler (points 2→3). The coefficient of performance (COP) of the sensible refrigeration sub-cycle for EC configuration can be calculated as:

$$COP_{config,2} = \frac{\dot{Q}_{sen}}{\dot{Q}_{hs}} \qquad \textit{for EC (configuration 2)} \qquad (3.19)$$

Since our proposed system suggests decoupling the sensible and latent cooling loads, the sensible heat ratio *SHR* is used which can be defined as the ratio of sensible heat to total heat load:

$$SHR = \frac{\dot{Q}_{sen}}{\dot{Q}_{sen} + \dot{Q}_{lat}} \qquad (3.20)$$

In order to compare the above proposed cooling and power configurations with conventional stand-alone cooling and power systems from an energy savings perspective, the primary energy saving ratio *PESR* can be applied. Principally, *PESR* is the ratio of the energy savings amount of the combined system compared with the energy consumption of the reference separate systems [50, 52, 53], and is expressed as

$$PESR = \left(\frac{F_s - F_c}{F_s}\right) \times 100\% = \left(1 - \frac{F_c}{F_s}\right) \times 100\% \qquad (3.21)$$

where F_s and F_c are the fuel energy consumption for the separate reference and combined systems, respectively.

Figure 35 depicts the energy flow of the proposed original and enhanced cycles, while Figure 36 shows the reference standalone cooling and power systems. Thus, the fuel energy consumptions F_s and F_c can be expressed as
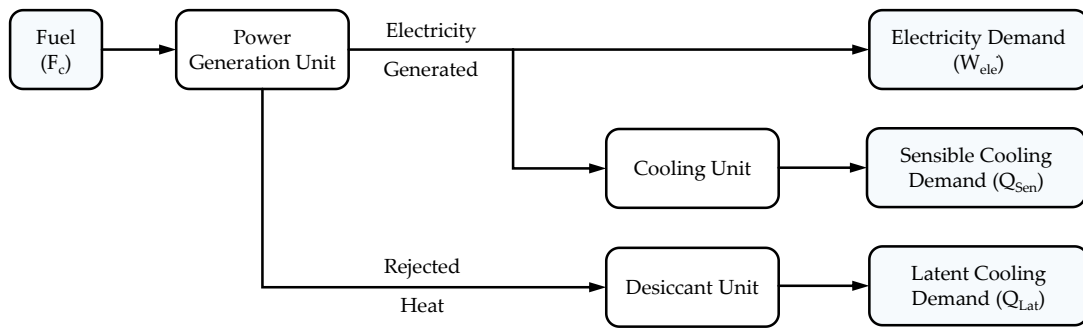
Figure 35. Energy flows of the proposed combined cooling and power system (both configurations)
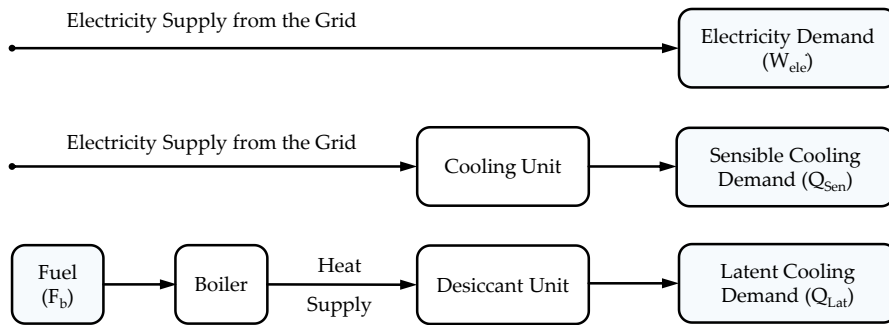
Figure 36. Energy flows of the reference separate cooling and power systems

$$F_c = \frac{\dot{Q}_{hs}}{\eta_b} \qquad (3.22)$$

$$F_s = F_{grid} + F_b \qquad (3.23)$$

where η_b is the boiler efficiency, which is assumed to equal 80%; F_b the fuel consumption associated with the standalone liquid desiccant boiler; and F_{grid} the electricity consumed from the electrical grid. These can be calculated based on Figure 36 as follows:

$$F_{grid} = \frac{\dot{W}_{ele}}{\eta_{grid}} + \frac{\dot{Q}_{sen}}{COP_{sen} \cdot \eta_{grid}} \tag{3.24}$$

$$F_b = \frac{\dot{Q}_{lat}}{COP_{lat} \cdot \eta_b} \tag{3.25}$$

where η_{grid} and COP_{sen} represent the average power plant efficiency with a constant value of 33% and sensible cooling COP with a value of 4.5 as in large-capacity vapor-compression chillers at standard conditions, respectively [50]. COP_{lat} represents the coefficient of performance of the liquid desiccant unit with a constant value of 70% [62]. It is worth noting that the proposed combined cooling and power system cannot save energy when the *PESR* value is negative compared with the stand-alone reference systems.

The aforementioned equations are solved simultaneously for steady operating conditions (fluid states and mass, energy, and exergy flows) based on the assumptions shown in Table 1. Thermodynamic properties of air-water vapor mixtures, water and steam at each point in the system are calculated by calling on Engineering Equation Solver (EES) routines, while LiCl-H$_2$O solution properties are calculated using the model developed by Conde [60].

Table 12. Main operation condition assumptions for the original and enhanced cycles

Parameter	Value	Unit
$\dot{m}_1$	1	kg s^{-1}
$\dot{q}_{hs}$ (Steam at 210 ºC)	2.4	MJ kg^{-1}
T_3	210	ºC
T_1 for configuration 1	100	ºC
T_1 for configuration 2	90	ºC
T_{10}	13	ºC
Turbine isentropic efficiency (η_T)	85	%
Pump isentropic efficiency (η_P)	85	%
Compressor isentropic efficiency (η_C)	80	%
Ambient relative humidity (RH_∞)	80	%
Ambient temperature (T_o)	35	ºC
$P_5 = P_8$	101.325	kPa
$P_9 = P_{10}$	50	kPa
RH_8	3	%
RH_{10}	95	%
Desiccant solution concentration (χ_{11})	38	%
Moisture removal effectiveness (α)	80	%
Entrainment efficiency (η_{entr})	70	%
Diffuser isentropic efficiency (η_{diff})	70	%
Nozzle isentropic efficiency (η_{nozz})	85	%

3.1.3.4.   Model validation

The mathematical model was validated by comparing the Rankine cycle, gas refrigeration cycle, desiccant cycle, evaporative cooling cycle, and ejector refrigeration cycle individually and independently with the related work in the literature [54-59]. The obtained results of all individual models were within $\pm 2\%$ under the same reference conditions. Figure 37 demonstrates the single model validation by showing a good agreement between our liquid desiccant sub-model and the experimental results by Mohamed et al. [63] under the same operating conditions.
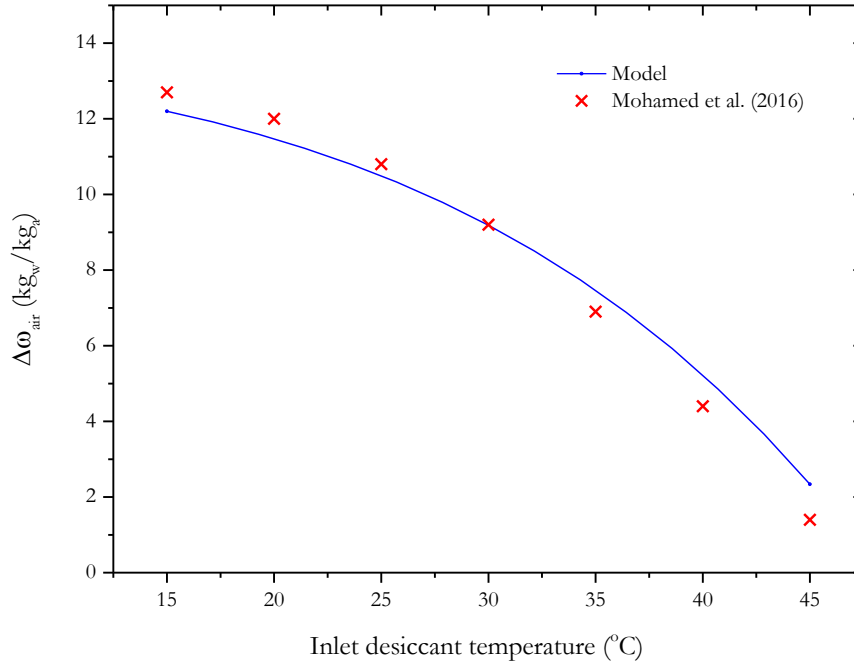
Figure 37. Comparison of the desiccant model with experimental results from the literature [63]

3.1.4. Results and Discussion

The values of the thermodynamic parameters (temperature, pressure, mass flow rate, humidity ratio, etc.) in all states of Figure 29 and Figure 30 for a fixed working condition, based on Table 1, are shown in Appendix D. All studies are conducted at a fixed thermal energy input rate of 2.4 MW$_{th}$ of steam leaving the boiler at 210 ℃ and 1 kg/s mass flow rate.

Figure 38 – Figure 53 depict the influence of input parameter variations such as evaporative cooler pressure (P_{10}) and outlet air relative humidity (RH_{10}) on the key output metrics at different sensible heat ratios (*SHR*). Exergy efficiency (η_{exergy}), electrical power, sensible and latent cooling capacities, and primary energy saving ratio (*PESR*) are considered to compare the energy consumption and system productivity, while *PESR* is used to compare the proposed OC and EC with the standalone reference systems from an energy savings point of view. Our results show that the original cycle (OC), under no circumstances, is more promising than the enhanced cycle (EC) since it has much lower efficiency. In fact, the OC uses more energy than the standalone conventional systems it replaces unless SHR is below 14%.

3.1.4.1. Sensitivity to the evaporative cooler pressure (P_{10})

Figure 38 depicts that the exergy efficiency of the original Sherbeck cycle (configuration 1) increases as the evaporative cooler pressure (P_{10}) increases, due to the reduction in the mass flow rate of humid air sucked by the ejector when P_{10} decreases. Consequently, both the sensible cooling capacity and electrical power generation reduces considerably as P_{10} decrease as shown in Figure 39. Although the PERS increase as P_{10} increases for configuration 1, the OC system is not feasible at sensible heat ratio (SHR) equal to 0.25, 0.35, or 0.45 compared to the standalone system since it has a negative PESR's values as shown in Figure 40.
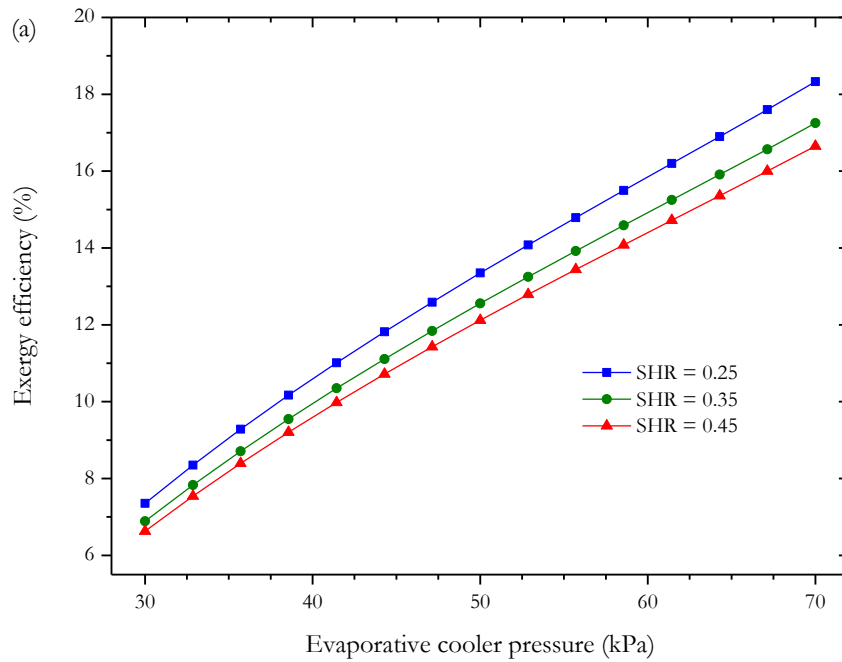
Figure 38. Effect of the evaporative cooler pressure (P_{12}) on exergy efficiency of the original cycle (configuration 1) at different sensible heat ratios (SHR)
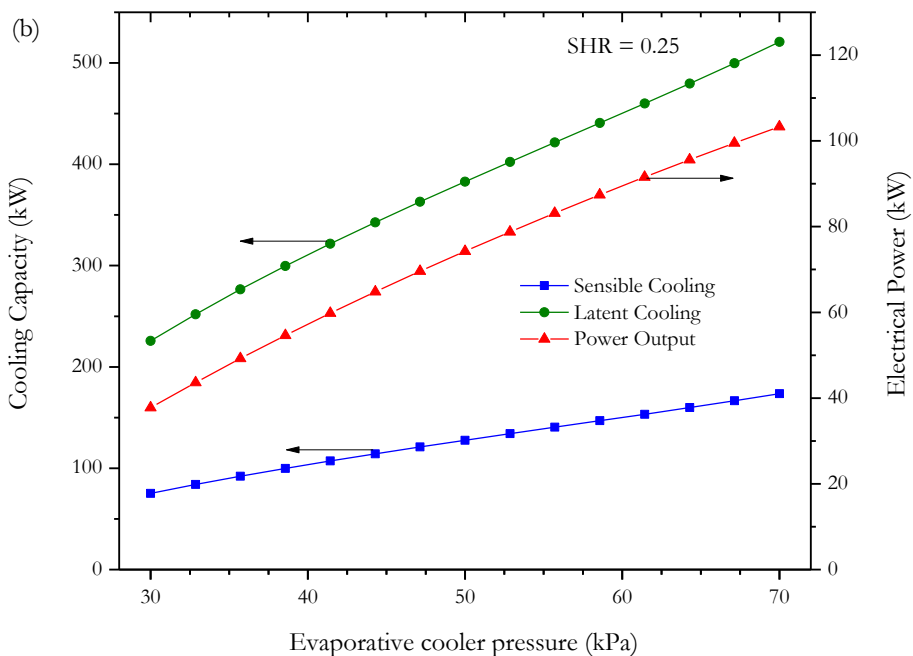
Figure 39. Effect of the evaporative cooler pressure (P_{12}) on electrical power, and sensible & latent cooling capacities at SHR = 0.25 of the original cycle (configuration 1)
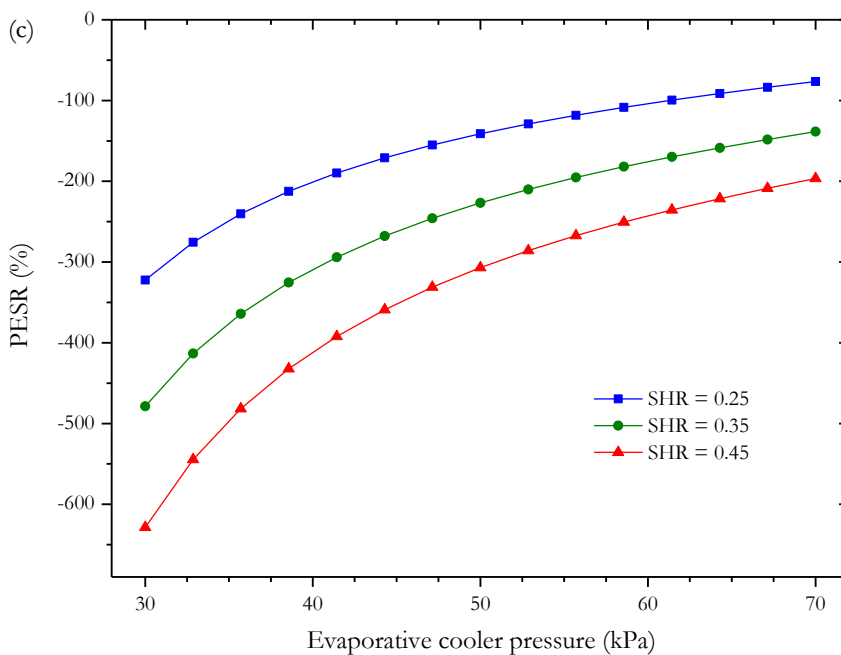
Figure 40. Effect of the evaporative cooler pressure (P_{12}) on primary energy saving ratio (PESR) of the original cycle (configuration 1) at different sensible heat ratios (SHR)

Similarly, the exergy efficiency of the enhanced cycle (configuration 2) increases as the evaporative cooler pressure (P_{10}) increases as presented in Figure 41. Furthermore, the exergy efficiency increases as the sensible heat ratio (SHR) decreases. However, at constant SHR, as P_{10} decreases, the sensible cooling capacity increases while electrical power generation decreases significantly since more shaft power is consumed internally in order to generate more cooling, as shown in Figure 42. It can be clearly seen from Figure 43 that compared to the OC, the EC is more practicable as P_{10} decreases even more so at lower SHR since *PESR* is largely a function of the latent cooling capacity.
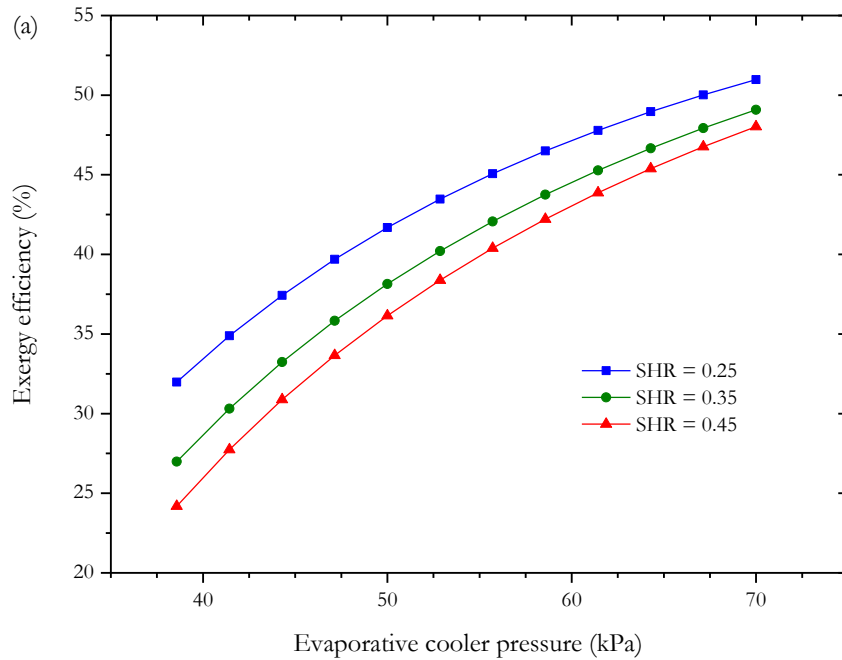
Figure 41. Effect of the evaporative cooler pressure (P_{10}) on exergy efficiency of the enhanced cycle (configuration 2) at different sensible heat ratios (SHR)
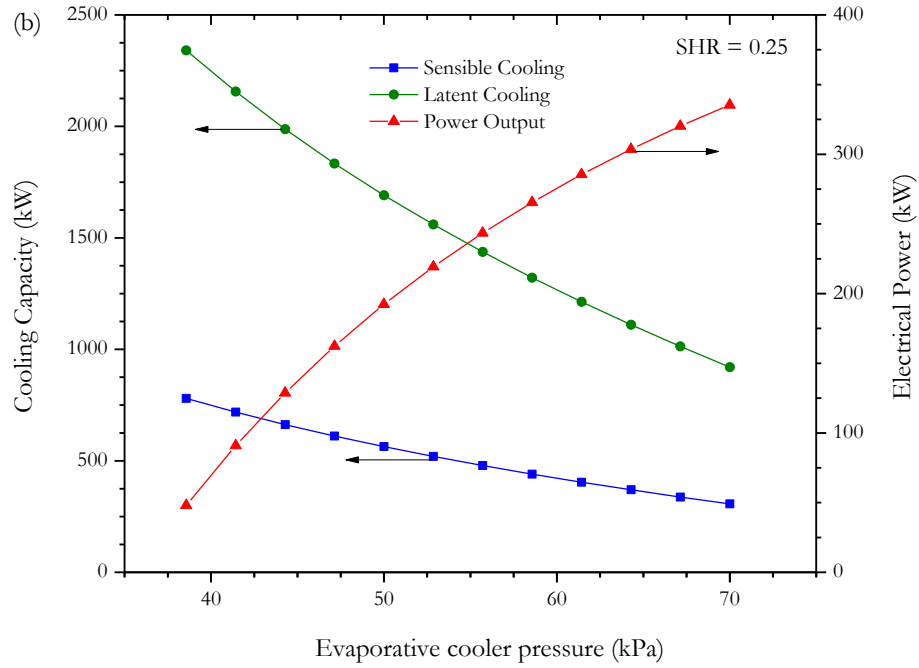
Figure 42. Effect of the evaporative cooler pressure (P_{10}) on electrical power, and sensible & latent cooling capacities at SHR = 0.25 of the enhanced cycle (configuration 2)
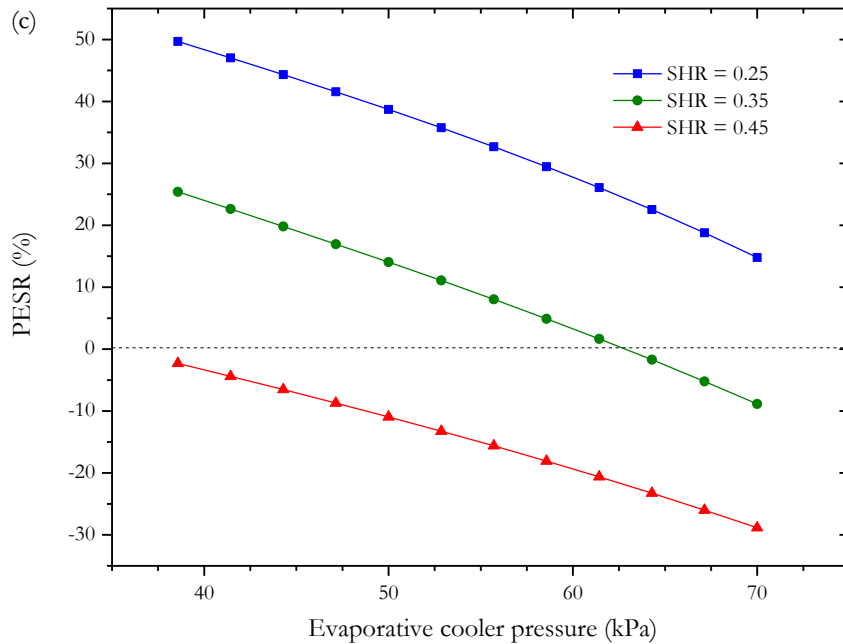
Figure 43. Effect of the evaporative cooler pressure (P_{10}) on primary energy saving ratio (PESR) of the enhanced cycle (configuration 2) at different sensible heat ratios (SHR)

3.1.4.2.   Sensitivity to the evaporative cooler outlet relative humidity (RH_{10})

Both original and enhanced cycle configurations follow the exact pattern for the exergy efficiency, electrical power, cooling capacity, and PESR as the evaporative cooler outlet relative humidity varies as shown in Figure 44 – Figure 49. The exergy efficiency of the cycle increases as RH_{10} increases owing to the substantial rise of sensible and latent cooling capacities despite the minimal reduction in the electrical power capacity as shown in Figure 44 and Figure 45. The *PESR* of the EC increases with increasing evaporative cooler outlet relative humidity as shown in Figure 46. Unlike OC system, it can be seen that the EC system becomes more efficient and feasible compared to the standalone reference systems at certain SHR. For instance, at SHR = 35%, the evaporative cooler outlet relative humidity must be more than 70% to justify the EC system from an energy point of view compared to separate systems. It is worth mentioning that the increase in the sensible cooling capacity of the EC, in Figure 50, is attributed to the incorporation of the evaporative cooling subsystem.
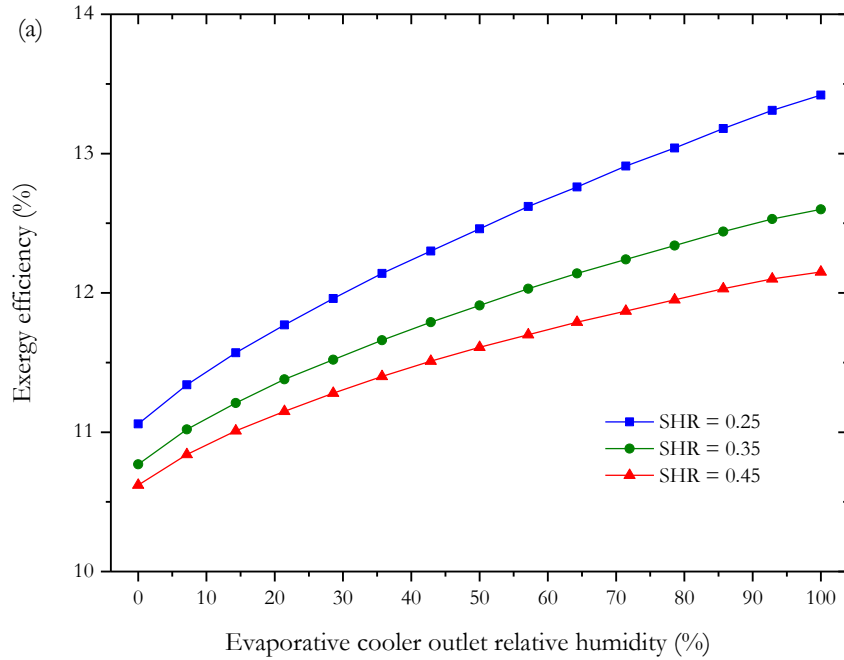
Figure 44. Effect of the evaporative cooler outlet relative humidity (RH_{12}) on exergy efficiency of the original cycle (configuration 1) at different sensible heat ratios (SHR)

69
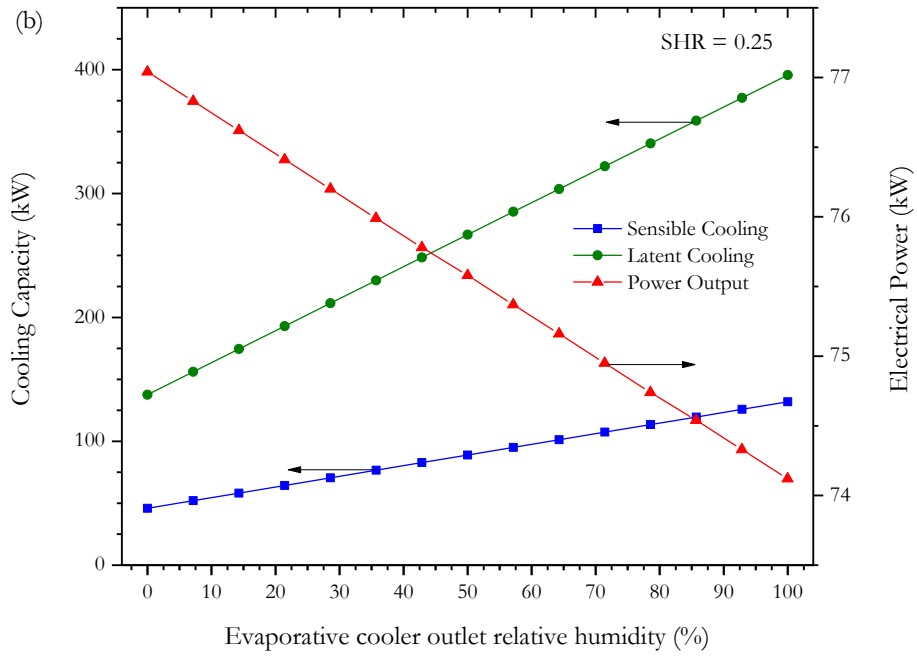
Figure 45. Effect of the evaporative cooler outlet relative humidity (RH_{12}) on electrical power, and sensible & latent cooling capacities at SHR = 0.25 of the original cycle (configuration 1)
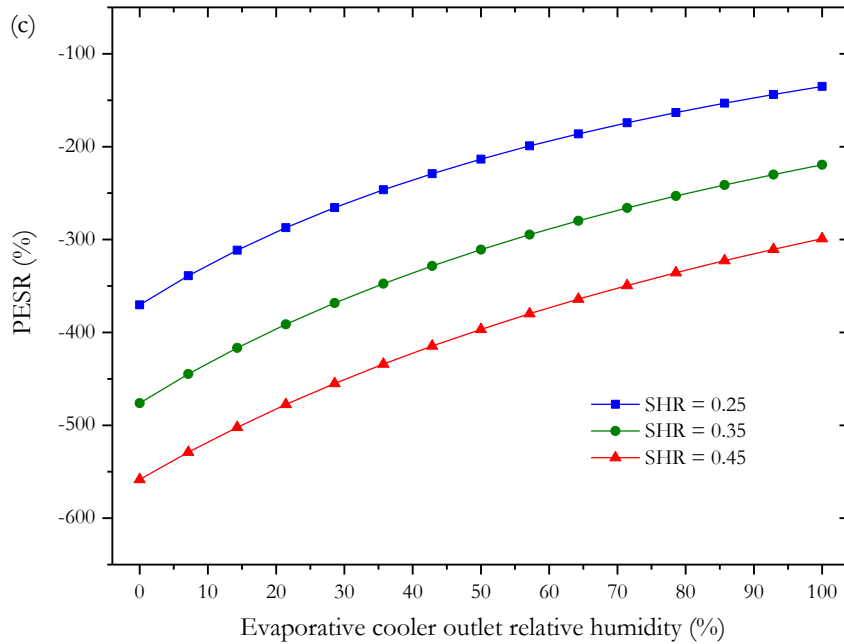
Figure 46. Effect of the evaporative cooler outlet relative humidity (RH_{12}) on primary energy saving ratio (PESR) of the original cycle (configuration 1) at different sensible heat ratios (SHR)
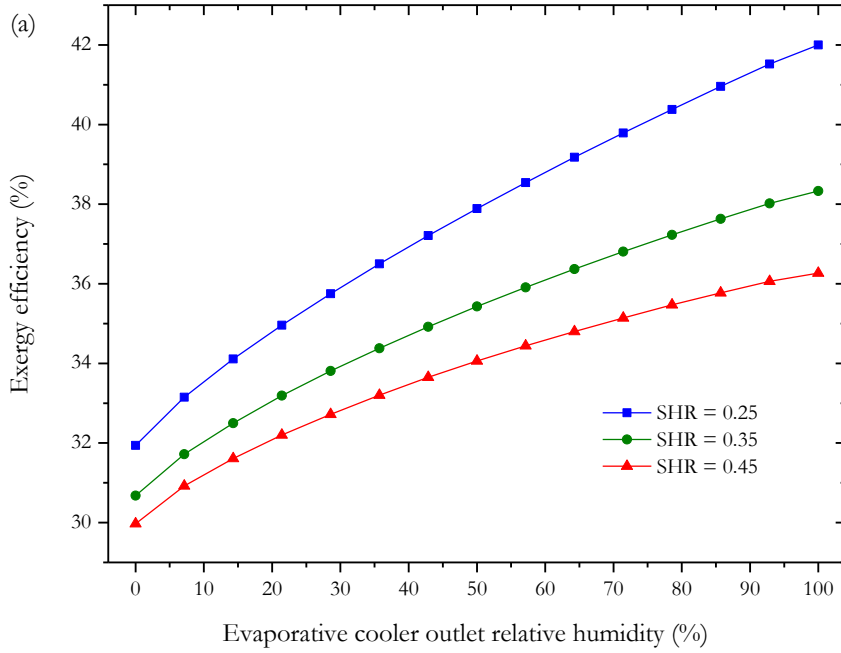
Figure 47. Effect of the evaporative cooler outlet relative humidity (RH_{10}) on exergy efficiency of the enhanced cycle (configuration 2) at different sensible heat ratios (SHR)
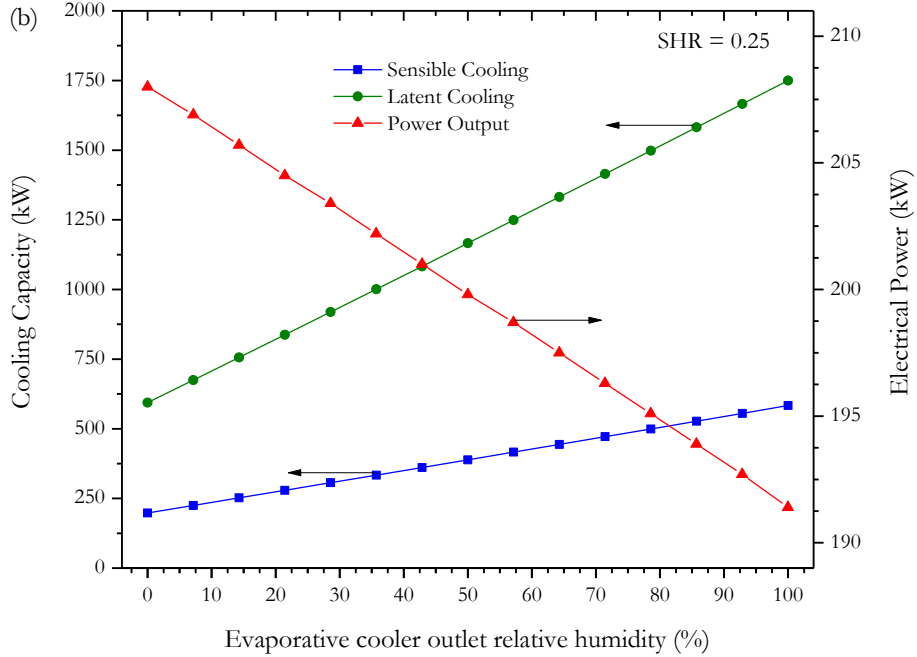
Figure 48. Effect of the evaporative cooler outlet relative humidity (RH_{10}) on electrical power, and sensible & latent cooling capacities at SHR = 0.25 of the enhanced cycle (configuration 2)
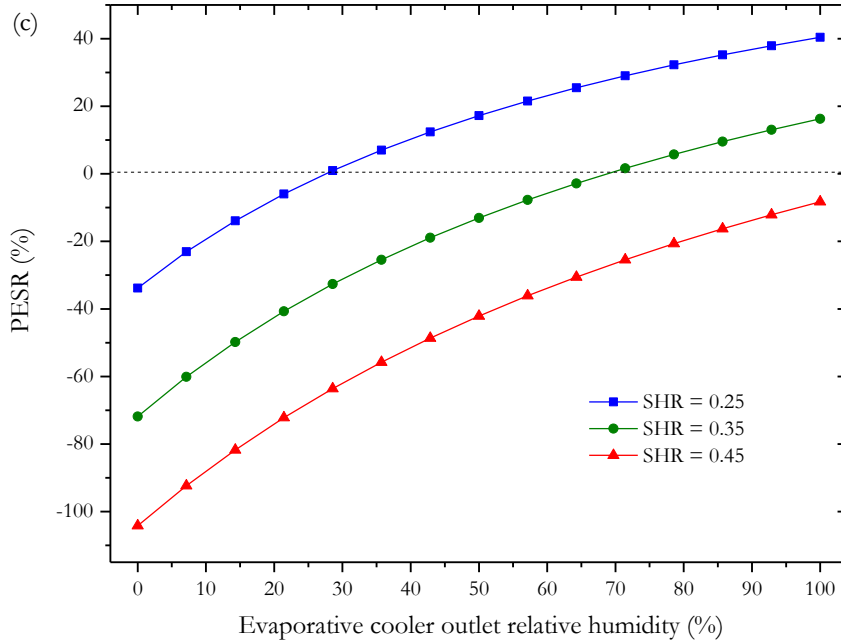
Figure 49. Effect of the evaporative cooler outlet relative humidity (RH_{10}) on primary energy saving ratio (PESR) of the enhanced cycle (configuration 2) at different sensible heat ratios (SHR)
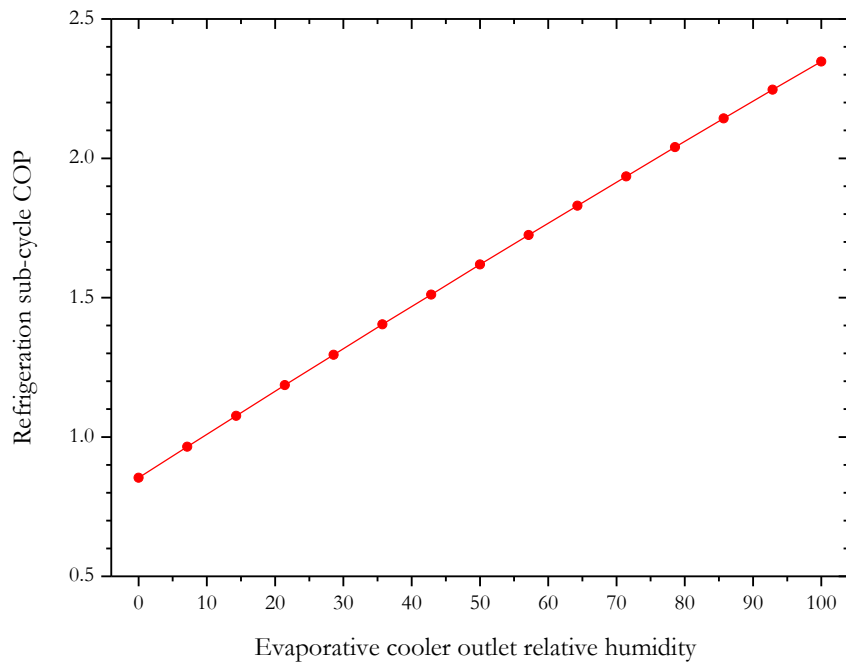
Figure 50. Effect of the evaporative cooler outlet relative humidity (RH_{10}) on the gas refrigeration sub-cycle COP in the enhanced cycle (configuration 2)

3.1.4.3.   Sensitivity to the condenser temperature (T_1)

Figure 51 shows that, as the condenser temperature decreases, the exergy efficiency of the EC (configuration 2) increases slightly until it peaks at about 73ºC (at SHR=0.25) before it starts decreasing rapidly. Moreover, it can be observed that the location of the exergy efficiency peak shifts to the right as SHR increases. The peak point occurs as a result of an increase in the heat rejection by the condenser as the condenser temperature decreases, resulting in an increase in the liquid desiccant capacity, which in turn leads to an increase in the mass flow rate of the gas refrigeration sub-cycle. (Recall that the liquid desiccant unit in this case is designed to harness all heat rejection by the condenser). Consequently, the sensible cooling capacity increases with a relatively higher gradient than the power production, causing the refrigeration subsystem to draw more power than produced as shown in Figure 52. Note that power capacity is supposed to increase as T_1 decreases. On the other hand, the primary energy saving ratio (*PESR*) increases as T_1 decreases due to the increase of the latent cooling capacity as shown in Figure 53.
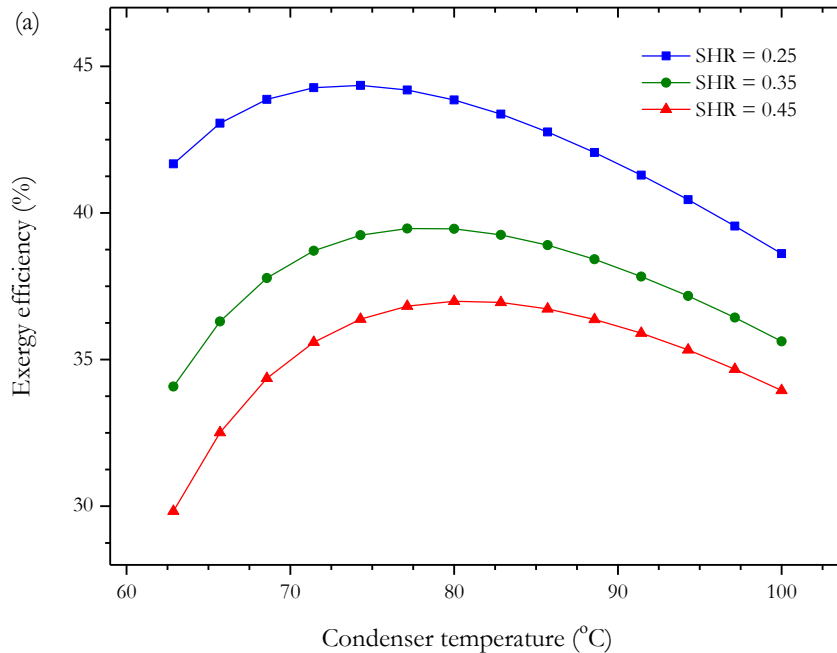
Figure 51. Effect of the condenser temperature (T_1) on exergy efficiency of the enhanced cycle (configuration 2) at different sensible heat ratios (SHR)
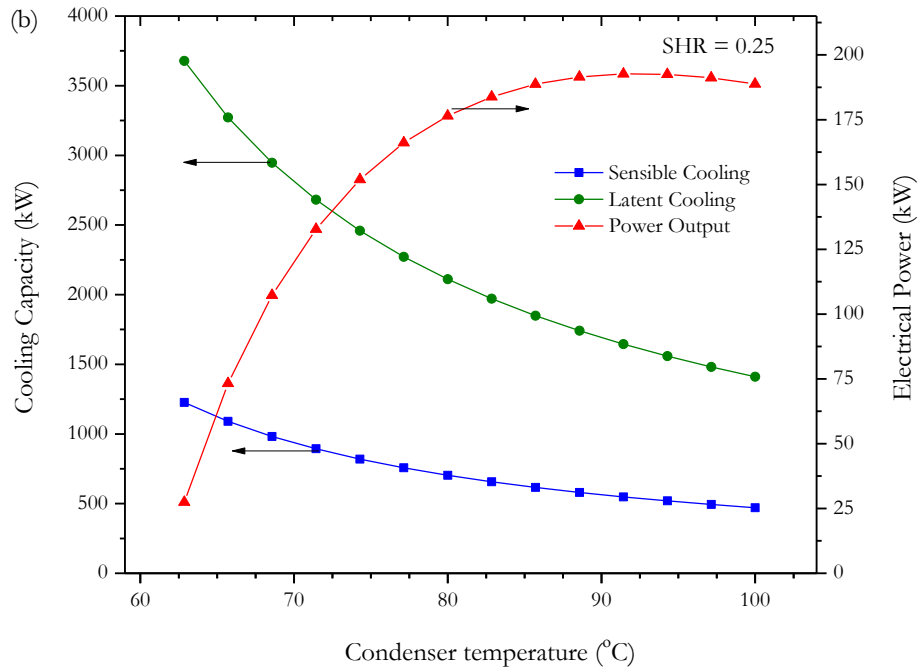
Figure 52. Effect of the condenser temperature (T_1) on electrical power, and sensible & latent cooling capacities at SHR = 0.25 of the enhanced cycle (configuration 2)
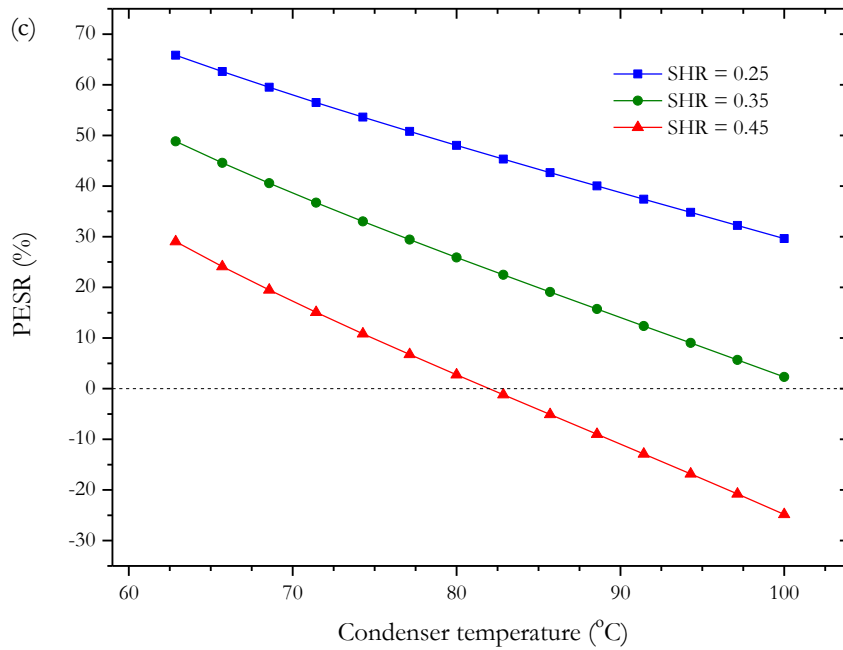
Figure 53. Effect of the condenser temperature (T_1) on primary energy saving ratio (PESR) of the enhanced cycle (configuration 2) at different sensible heat ratios (SHR)

3.1.4.4.   Sensitivity to the sensible heat ratio (SHR) at optimal operating conditions

Based on previous sensitivity analysis, the latent cooling capacity particularly played a decisive role on all system performance indicators, especially the *PESR*. Both the proposed OC and EC configurations were optimized using the Conjugate Directions method in EES software, wherein the objective function being maximized was the exergy efficiency. Figure 54a depicts the optimal exergy efficiency of both the OC (configuration 1) and EC (configuration 2) systems in which the exergy efficiency increases slightly as SHR decreases before it starts growing exponentially at lower SHR. At the optimal operating conditions, Figure 54b shows that the OC and EC do not make sense from an energy-savings perspective until *SHR* becomes less than 0.14 and 0.39, respectively. In other words, the OC and EC are not recommended from an energy-saving viewpoint compared to the separate systems unless the cooling load is 14% sensible and 86% latent for the OC or 39% sensible and 61% latent for the EC. Nevertheless, the EC is superior to the OC since the energy of steam is better harnessed in the turbine expansion rather than driving the ejector of the gas refrigeration cycle. This is not solely due to the ejector inefficiency but also attributable to the low mass flow rate of humid air entrained by the ejector.
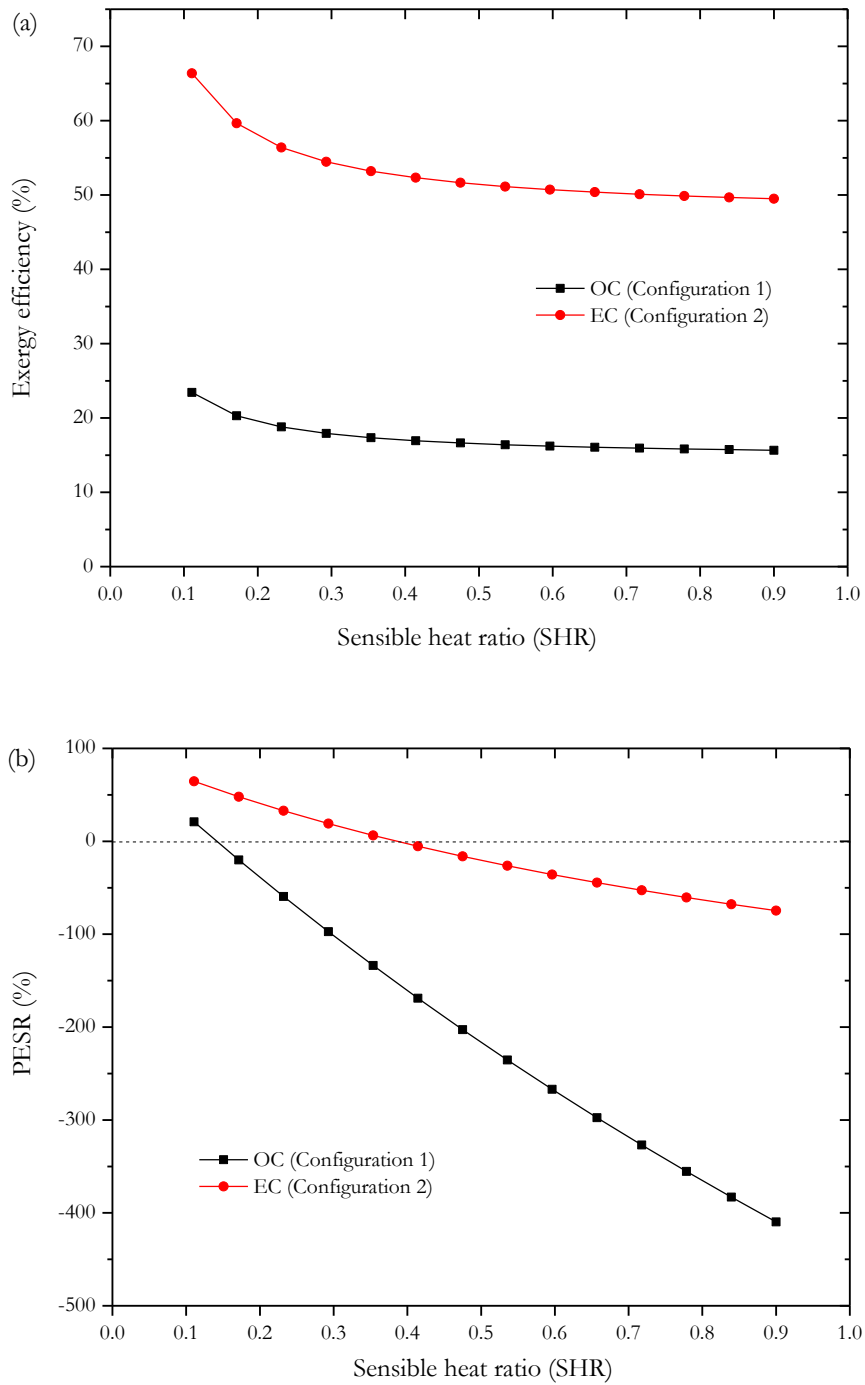
Figure 54. Optimal (a) exergy efficiency and (b) primary energy saving ratio (PESR) of both the original (OC) and enhanced cycles (EC) at varying sensible heat ratios (SHR)

Under the optimal operating conditions, the *PESR*, energy (first law) efficiency, exergy efficiency, electrical power, sensible cooling capacity, latent cooling capacity, and water production capacity

were calculated at different sensible heat ratio (*SHR*) for the original (OC) and enhanced cycles (EC) as summarized in Table 13. It can be noted from Table 13 that the OC at *SHR* = 0.10 is 28.3% more efficient compared with standalone systems with an electrical power output of 103.2 kW$_e$ and a sensible cooling capacity of 181.2 kW$_{th}$ at an exergy efficiency of 24.4% (energy efficiency of 54.7%). Additionally, the OC system is capable of producing fresh water at 2.7 m^3 per hour due to the high latent heat capacity of 1631 kW$_{th}$.

At almost the same *PESR* of 28.8% (*SHR* = 0.25), the EC is cable of generating 354.6 kW$_e$ and 399.7 kW$_{th}$ of electrical power and sensible cooling capacity, respectively, at an exergy efficiency of 54.6% and first law efficiency of 78.7%. Because the latent cooling capacity (1199 kW$_{th}$) of the EC is less than that of OC, the EC's water production capacity is 0.9 m^3/hr less than that of the OC. Evidently, either cycle could be attractive in places and applications where latent heat cooling is more dominant than sensible cooling.

Table 13. Comparison of the original (OC) and enhanced cycles (EC) at optimal operating conditions

		OC	EC		
Sensible Heat Ratio (SHR)	-	0.10	0.25	0.30	0.35
Primary Energy Saving Ratio (*PESR*)	%	28.3	28.8	17.6	7.1
Energy efficiency	%	54.7	78.7	68.0	60.4
Exergy efficiency	%	24.4	55.7	54.3	53.3
Electrical Power output	kW$_e$	103.2	354.6	354.3	354.2
Sensible cooling capacity	kW$_{th}$	181.2	399.7	400.5	401.0
Latent cooling capacity	kW$_{th}$	1631	1199	935	745
Water production capacity	m^3/hr	2.7	1.8	1.4	1.1

Based on the above findings, the proposed OC and EC configurations are only feasible from an energy-saving perspective compared to the standalone systems at low sensible heat ratio (high latent load 86% for OC and 61% for EC). Therefore, this makes both systems very sensitive to the environmental conditions and relative humidity, particularly when the dehumidification system is used to dehumidify the outdoor air. Nonetheless, the latent load is not limited to air conditioning applications but rather can be used for other applications such as food drying, electronics moisture control, hygroscopic chemicals, etc.

3.1.5. Summary

This study explores the opportunities of a novel combined cooling and power (CCHP) system that is thermally driven using low- to mid-grade heat. The proposed cycle is comprised of a Rankine cycle that drives a gas refrigeration (reverse Brayton) cycle directly and indirectly, with liquid desiccant and evaporative cooling cycles, to produce shaft power and refrigeration by adiabatic expansion and evaporation. Two configurations are proposed, namely the original cycle (OC) and the enhanced cycle (EC), with the goal of increasing the CCHP system's primary energy saving ratio (*PESR*) compared with stand-alone systems with minimal to zero water consumption. The study is conducted at a fixed thermal energy input rate of 2.4 MW_{th} of steam at 210°C. Our thermodynamic model shows that the OC performs better than standalone systems from an energy savings perspective as long as the sensible heat ratio (SHR) is less than 14%. The OC is capable of generating 103 kW_e of electrical power, 181 kW_{th} of sensible cooling, 1631 kW_{th} of latent cooling capacity, and 2.7 m^3/hr of fresh water at 24% exergy efficiency and *PESR* of 28%. On the other hand, the EC is more efficient than both the OC and standalone conventional systems with a minimum exergy efficiency of 52.7%, as long as the *SHR* is less than 39%. At the optimal operating condition and SHR of 25%, the EC can obtain an electrical power, sensible, and latent cooling capacity of 354 kW_e, 400 kW_{th}, and 1199 kW_{th}, respectively, at *PESR* of 29% and fresh water capacity of 1.8 m^3/hr.

3.2. AN INTEGRATED ORGANIC RANKINE/REVERSE BRAYTON REFRIGERATION CYCLE AND MULTIPLE EFFECT DESALINATION UNIT

In this section, we propose a combined cooling, desalination, and power (CCDP) system that is comprised of Rankine power and gas refrigeration (reverse Brayton) cycles, plus a thermally driven desalination unit. This extends our previous introduction of a unit that produces shaft power and refrigeration, but not desalination [64]. The heat rejection from the condenser of the Rankine cycle is exploited to drive the desalination unit which is based on multiple effect distillation (MED) technology. Primarily, our proposed CCDP system utilizes water and air as the working fluid and refrigerant, respectively, which are non-hazardous and environmentally friendly with the aim of minimizing carbon emissions. The combined system is designed to be located by a large body of saltwater such as the ocean and to provide fresh water, refrigeration, and power on demand which makes it potentially attractive to remote and off-grid areas.

3.2.1. Literature Review

Murugan and Horak [65] discussed in a recent review paper the research efforts and developments that have been conducted regarding poly and trigeneration, a subset of polygeneration in which three outputs are generated. They concluded that the selection of the energy conversion device, such as gas turbines and organic Rankine cycles (ORCs), and its size are extremely important for residential and industrial applications. The location of the polygeneration plant is a significant factor to determine the most desirable products. For instance, local climate would play a role in determining the plant configuration and its possible products for an off-grid plant. Thus, they recommended feasibility studies should be carried out for the installation of a polygeneration system, since every system is different.

Anvari et al. [66] performed a thermoeconomical study on a combined cooling, heating, and power (CCHP) system that consists of three sections, namely, gas turbine and heat recovery steam generator (GT-HRSG), regenerative organic Rankine cycle (RORC), and absorption refrigeration cycle based on LiBr-H_2O. The result showed that adding an RORC and absorption refrigeration cycle to the GT-HRSG cycle increases the overall exergetic efficiency of the CCHP system by 2.5% and 0.75%, respectively, with a 5.5% and 0.45% increase in the total investment cost of the trigeneration cycle.

Ortega-Delgado et al. [67] performed a parametric study of a multiple effect distillation unit with a steam ejector –widely known as multiple effect distillation with thermal vapor compression (MED-TVC)– coupled with a Rankine cycle power block. They studied the effect of the motive and suction steam pressures on the MED-TVC performance, fresh water capacity, and other key variables. They concluded that there is an optimum value of the heat transfer area of the evaporator after the suction point and optimum position of the steam ejector for every suction and motive steam pressure, respectively. When electricity demand is high, it was recommended to extract low-pressure motive steam and place the steam ejector close to the 5th effect in order to maximize the electric power production at the expense of the MED-TVC efficiency. On the other hand, extracting high pressure motive steam from the Rankine cycle turbine and locating the thermocompressor closer to the last effect are desirable when electricity demand is low to enhance the MED-TVC performance.

Mohan et al. [68] examined technically and economically the advantages of harnessing the excess waste heat from a gas turbine and rejected heat from a steam Rankine cycle condenser in a combined power plant in the United Arab Emirates. The trigeneration system was optimized based on the cooling demands of the neighboring community to simultaneously produce electricity, fresh water using air gap membrane distillation, and cooling using LiBr-H_2O absorption refrigeration system. The proposed trigeneration system was projected to have an energy conversion efficiency of about 83% compared to 51% for the combined cycle power plant with a payback period of only 1.4 years with cumulative net present value of $66 million over the project life time.

Akbari et al. [69] analyzed the effect of the turbine inlet pressure and evaporator outlet temperature on a Combined Cooling Clean Water and Power (CCCWP) system from energy and exergy perspectives. The polygeneration system consists of a Kalina cycle[†], a LiBr-H_2O heat transformer, and a water desalination system using a geothermal hot water heat source at 124 ºC. The energy and exergy efficiencies of the system were found to be about 17% and 65%, respectively, with a maximum fresh water production of 1.32 m^3 per hour. Sahoo et al. [70] studied the viability of coupling a hybrid solar-biomass power plant with cooling using a LiBr-H_2O absorption system, and desalination using an MED system in a polygeneration process in India. It was found that the net equivalent power for a polygeneration system increases by 18.2% compared to a conventional power plant with standalone cooling and desalination systems.

[†] The Kalina cycle is a thermodynamic process that converts thermal energy into mechanical power. It uses a mixture of two fluids as the working fluid in order to extract more heat from the heat source than conventional Rankine cycle since heat addition takes place at varying temperature even during phase change.

Ameri and Jorjani [71] conducted exergy and economic analyses on an integrated system comprised of a Brayton cycle with a heat recovery steam generator (HRSG), an ORC, and an MED unit. The gas turbine exhaust energy is initially harnessed by the MED unit by means of employing a single-pressure HRSG before it then drives the ORC. It was concluded that the optimum power and fresh water capacities are very sensitive to the MED evaporator approach temperature. Among three organic working fluids, R134a achieved the highest exergy efficiency.

Recently, Salimi and Amidpour [72] investigated the effect of the integration of different desalination systems on cogeneration system performance by utilizing the R-curve tool in order to identify the most effective way to decrease the operating cost. They found that the integration of thermally and electrically driven desalination units can result in either the improvement or impairment of the overall cogeneration efficiency based on the operating conditions of the cogeneration system. In particular, they demonstrated that the integration of a 17.8 MW_{th} multiple effect distillation (MED) unit can either provide 28.97 MW_{th} fuel savings or cause 47.84 MW_{th} excess fuel consumption.

3.2.2. System Configuration

A schematic diagram of the proposed CCDP system is shown in Figure 55. It can be observed from Figure 55 that the Rankine cycle's turbine is connected with the compressor, the turbine of the gas refrigeration cycle, and the generator through the same shaft in order to maximize the shaft power output. Nevertheless, this might not always be the case especially if the required cooling (refrigeration) load is irregular in which the gas refrigeration sub-cycle is preferably fed by electrical power via a generator that produces electricity from the Rankine power sub-cycle.
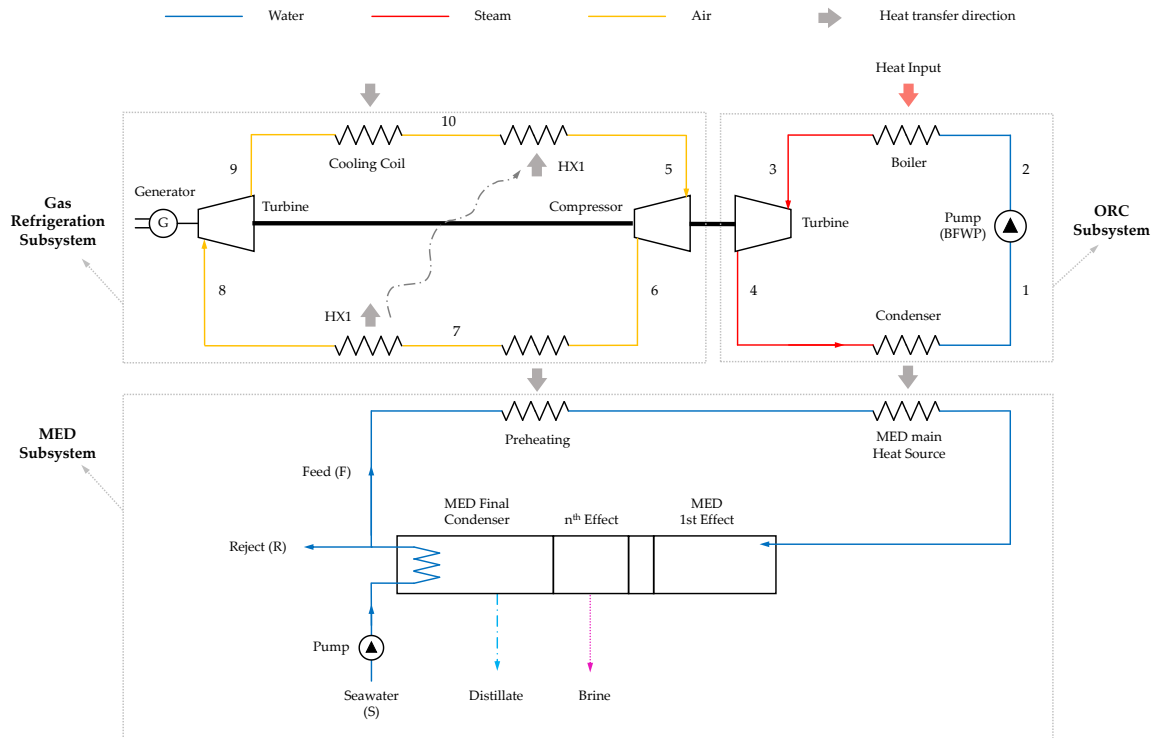
Figure 55. Schematic diagram of the combined cooling, desalination, and power (CCDP) system

Rejected heat via the Rankine cycle's condenser is proposed to provide the required heat to the first effect of the MED desalination system. Incoming seawater is first introduced to the MED subsystem (stream S) by condensing the steam in a final condenser, which is produced by the last effect. Over 60% of incoming saltwater gets rejected back to the source (stream R) after exchanging heat with the MED's condenser, while the rest is pumped to the first effect (stream F). On its way to the first effect, saltwater gets preheated by the gas refrigeration cycle (between points 7 & 8) and partially condenses the steam generated in each effect.

3.2.3. Mathematical Modelling

The mathematical model of our proposed CCDP system is based on a combined model of three separate thermodynamic models, namely, the Rankine power cycle, the gas refrigeration (reverse Brayton) cycle, and the MED desalination unit. Initially, each subsystem was modelled and validated separately before integrating them to each other to form our proposed CCDP system in Figure 55. The following assumptions are applied for the thermodynamic mathematical model:

i. Steady-state operation with negligible kinetic and potential energy.

82

ii.   Heat losses and pressure drops in the components and piping are not considered.

iii.   The distilled fresh water is salt free.

iv.   During phase change processes, the bulk liquid and vapor flows are at equilibrium in each cross section.

The mass balance (continuity), energy balance (the first law of thermodynamics), and exergy balance (the second law of thermodynamics) are performed for each component of the system based on the above-mentioned assumptions. The Rankine power and gas refrigeration cycles can be directly modelled using widely known models as presented by Cengel and Moran [54, 55]. The mass and energy balance equations of the MED unit are derived above (Check Chapter 2.3.2.1.)

3.2.3.1.   System performance indicator

For polygeneration systems, Rosen and Le [61] recommended the use of exergy (second law) efficiency as a system performance indicator. Unlike energy (first law) efficiency, the exergy efficiency takes into account the quality of heat and energy, and can be defined as the fraction of the useful exergy to the total exergy input:

$$\eta_{exergy} = \frac{\dot{W}_{ele} + \dot{E}_{cool} + \dot{W}_{MED,min}}{\dot{E}_{hs}} \tag{1}$$

where $\dot{W}_{ele}$ is the electrical power output and $\dot{W}_{MED,min}$ the least amount of required work to separate salt and water as calculated in appendix A. $\dot{E}_{cool}$ and $\dot{E}_{hs}$ are the exergy rates associated with the cooling capacity and heat source input, respectively, in kW, in which $\dot{E}$ can generally be calculated as

$$\dot{E} = \dot{m} \cdot [(h_{in} - h_{out}) - T_o(s_{in} - s_{out})] \tag{2}$$

where $\dot{m}$, h, and s are mass flow rate, specific enthalpy, and specific entropy, respectively, and T_o is the temperature at the dead state. In order to compare the proposed CCDP system with conventional stand-alone cooling, desalination, and power systems from an energy savings perspective, the primary energy saving ratio *PESR* can be applied. Principally, the *PESR* is the ratio of the amount of energy savings of the combined system compared with the energy consumption of the reference separate systems [50, 52, 53], and is expressed as

$$PESR = \left(\frac{F_s - F_c}{F_s}\right) \times 100\% = \left(1 - \frac{F_c}{F_s}\right) \times 100\% \qquad (3)$$

where F_s and F_c are the fuel energy consumption for the separate reference and combined systems, respectively.

Figure 56 depicts the energy flows of the proposed combined cooling, desalination, and power (CCDP) system, while Figure 57 shows the reference standalone cooling, desalination, and power systems. Thus, the fuel energy consumptions F_s and F_c can be expressed as

$$F_c = \frac{\dot{Q}_{hs}}{\eta_b} \qquad (4)$$

$$F_s = F_{grid} + F_b \qquad (5)$$

where η_b is the boiler efficiency, F_{grid} the electricity consumed from the electrical grid, and F_b the fuel consumption associated with the standalone MED unit, and can be calculated based on Figure 56 as follows:

$$F_{grid} = \frac{\dot{W}_{ele}}{\eta_{grid}} + \frac{\dot{Q}_{cool}}{COP_{ref} \cdot \eta_{grid}} \qquad (6)$$

where η_{grid} and COP_{ref} represent an average power plant efficiency with a constant value of 33% and cooling COP with a value of 4.5 as in large-capacity vapor-compression chillers at standard conditions, respectively [50]:

$$F_b = \frac{\dot{Q}_{MED,input}}{\eta_b} \cdot \frac{PR}{PR_{ref}} \qquad (7)$$

$$PR = \frac{\dot{m}_{Distilled} \cdot h_{fg}}{\dot{Q}_{MED,input}} \qquad (8)$$

where PR is the performance ratio of the multiple effect distillation (MED) unit which is defined as the mass of desalinated water produced ($\dot{m}_{distilled}$ in kg s^{-1}) per thermal energy input ($\dot{Q}_{MED,input}$ in kW) which is equal to the heat rejected by the Rankine cycle's condenser. h_{fg} is the enthalpy of vaporization of H$_2$O at 73°C which corresponds to 2326 kJ kg^{-1} and PR_{ref} represents the performance ratio reference with a constant value of 10 [27, 28]. It is worth noting that the

proposed CCDP system cannot save energy when the *PESR* value is negative compared with the stand-alone reference systems.

The Rankine power, gas refrigeration cycles, MED unit, and aforementioned equations are solved simultaneously for steady operating conditions (fluid states and mass, energy, and exergy flows) based on the assumptions shown in Table 14. The thermodynamic properties of water, air, helium, carbon dioxide, etc. are calculated at each point in the system by calling on Engineering Equation Solver (EES) routines.
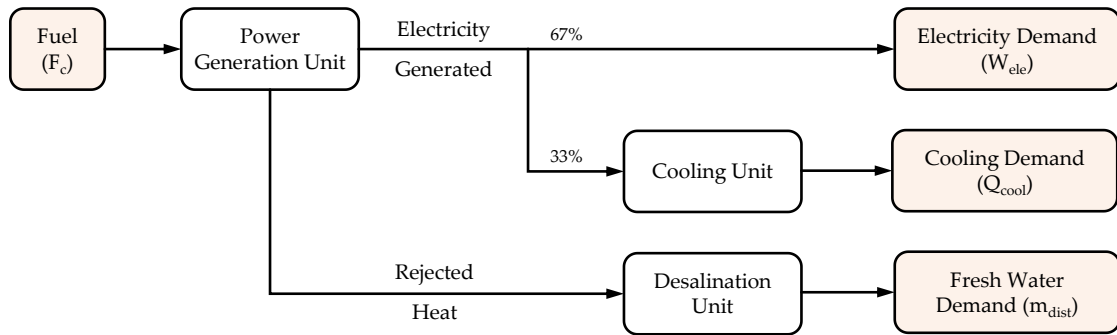
Figure 56. Energy flows of the proposed combined cooling, desalination, and power (CCDP) system
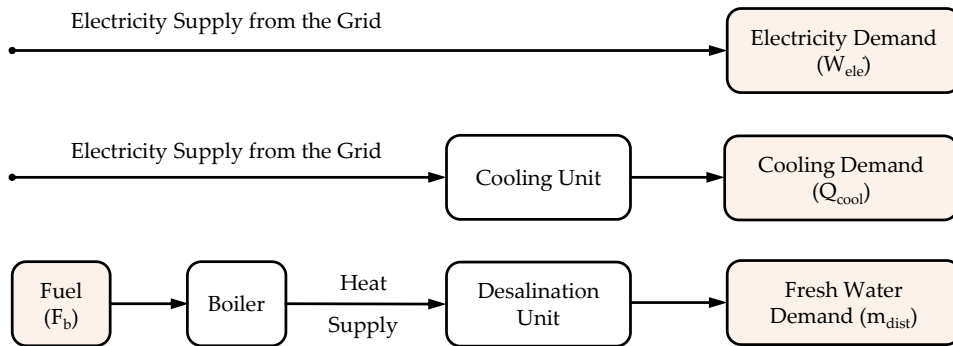
Figure 57. Energy flows of the reference separate cooling, desalination, and power (CCDP) systems

Table 14. Main operation condition assumptions for the combined cooling, desalination, and power (CCDP) system

Parameter	Value	Unit
Rankine cycle		
Temperature (T_3)	200	°C
Boiler saturation temperature	170	°C
Condenser saturation temperature	70	°C
Gas Refrigeration cycle		
Low pressure	70	kPa
Pressure ratio	2.5	
Heat exchanger 1 (Regenerator) effectiveness	60	%
Temperature (T_{10})	15	°C
MED	35	%
MED number of effects	14	effects
Top brine (First effect) temperature (TBT)	66	°C
Temperature rise of seawater in preheater (dT)	2.3	°C
Pressure difference between the effects of MED (dP)	1	kPa
Seawater temperature	27	°C
Seawater salinity	35000	ppm
Others		
$\dot{m}_{hs}$	1	kg/s
$\dot{q}_{hs}$ (Steam at 200 °C)	1940	kJ/kg
Cooling ratio	33	%
Shaft efficiency	95	%
Turbine isentropic efficiency (η_T)	85	%
Pump isentropic efficiency (η_P)	85	%
Compressor isentropic efficiency (η_C)	80	%
Boiler efficiency (η_b)	85	%
Ambient temperature (T_o)	35	°C
Natural gas price	1.9	$/MMBtu

3.2.3.2.   Model validation

The mathematical model was validated by comparing the Rankine cycle, organic Rankine cycle, and gas refrigeration cycles individually and independently with the related work in the literature [54-59]. The obtained results of all individual models were within $\pm 0.5\%$ under the same reference conditions. Table 15 demonstrates the multiple effect distillation (MED) single model validation by showing good agreement with the related work in literature [13, 33, 36, 38] under the same operating conditions.

Table 15. Validation of the multiple effect distillation (MED) model

	Current Model	Reference	Difference
Fresh water production (kg/hr) [36]	2897	2992	3.2%
Exergy efficiency [32]	6.2	6.0	3.3%
Performance ratio [36]	9.25	9.6	3.6%

3.2.4.   Results and Discussion

Figure 58 – Figure 73 depict the impact of input parameter variations such as the gas refrigeration sub-cycle's pressure ratio, the Rankine sub-cycle's condenser temperature (T_1), the heat exchanger (regenerator) effectiveness (ε_{HX1}), and the MED number of effects. Exergy efficiency (η_{exergy}), electrical power, cooling capacity, fresh water capacity, and primary energy saving ratio (*PESR*) are considered to compare the energy consumption and system productivity. *PESR* is used to compare the proposed CCDP system with the standalone reference systems from an energy savings point of view. Although the results discuss three different refrigerants, namely air, helium, and carbon dioxide, the electrical power output, cooling capacity, and water production are only shown for air since the same pattern is anticipated. It is worth noting that the study is conducted at a fixed thermal energy input rate of 1940 kW$_{th}$ which corresponds to the value of enthalpy of vaporization of water at 200ºC at 1 kg/s mass flow rate.

3.2.4.1.   Sensitivity to the pressure ratio (r_p)

Figure 58 shows that the exergy efficiency of the CCDP system increases significantly before it levels off as the pressure ratio increases. It can be observed that the exergy efficiency of the combined system only peaks when helium (He) is used as a refrigerant at a pressure ratio of 3.5. Figure 59 demonstrates the effect of pressure ratio on electrical power output, cooling capacity, and water production when air is used as a refrigerant. At a pressure ratio of about 1.5, the gas

refrigeration sub-cycle reaches its optimum operating point (maximum COP) as reflected by the cooling capacity in Figure 59 with only a negligible decrease in the electrical power capacity (to the point that can't be observed in the figure). Consequently, the rise in the rejected heat by the gas refrigeration sub-cycle leads to an increase in the heat absorption by the MED unit which increases the fresh water production capacity. Because the electrical power output is constant with respect to the pressure ratio, the primary energy saving ratio (*PESR*) is directly dependent on the cooling capacity. Figure 60 shows that the *PESR* of the CCDP system peaks where the gas refrigeration sub-cycle COP peaks for different refrigerants. Unlike a conventional stand-alone cooling cycle, such a combined system is potentially attractive for industrial applications that require fresh water, power, and refrigeration (cryogenics) where very low temperatures are desirable, as shown in Figure 61, without sacrificing the overall system performance and productivity.
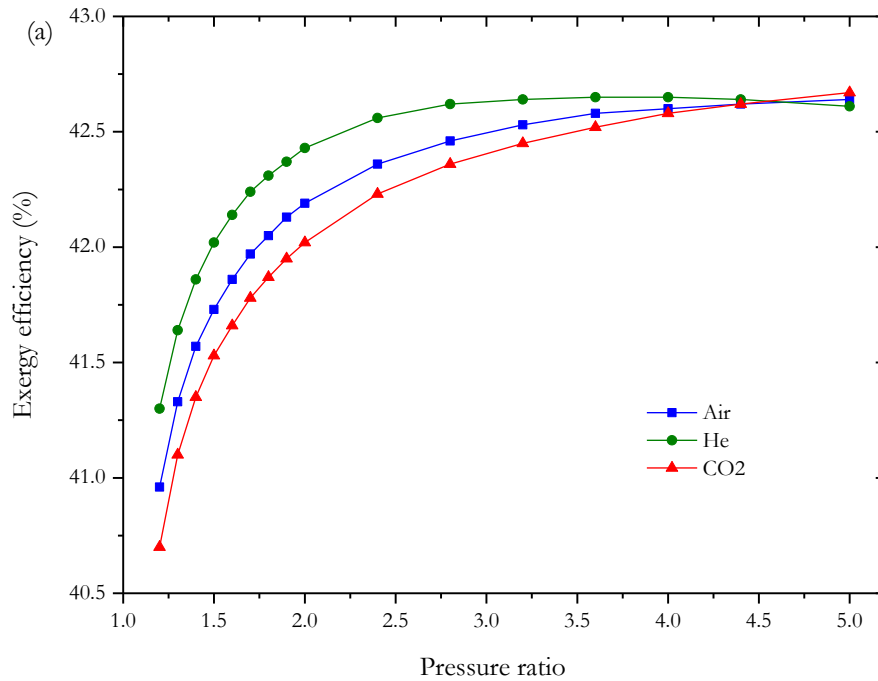
Figure 58. Effect of the pressure ratio (r_p) of the gas refrigeration sub-cycle on exergy efficiency of the proposed CCDP system at different refrigerants (Air, He, CO_2)
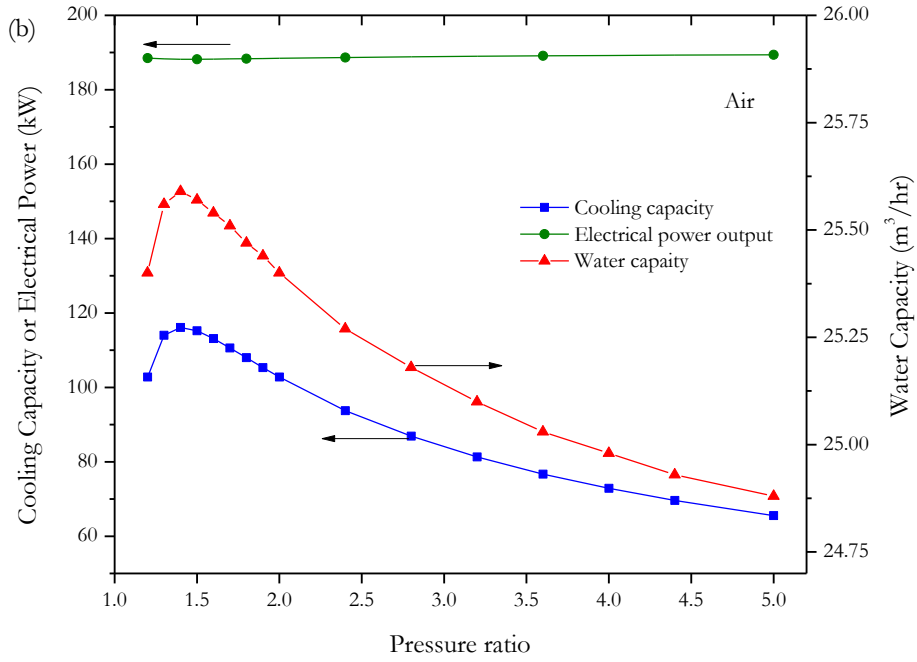
Figure 59. Effect of the pressure ratio (r_p) of the gas refrigeration sub-cycle on electrical power, cooling capacity, and water production of the proposed CCDP system at different refrigerants (Air, He, CO_2)
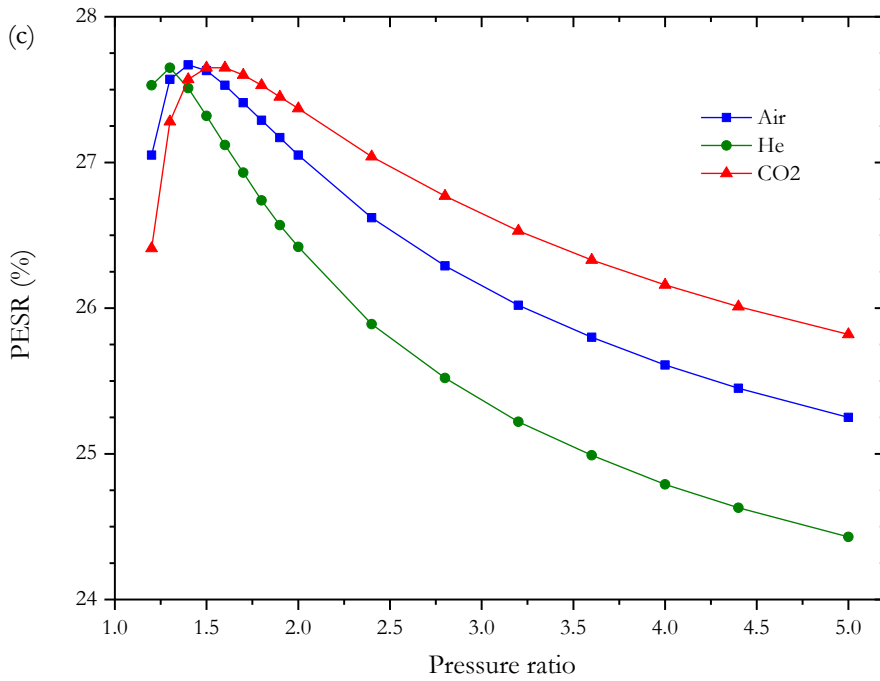
Figure 60. Effect of the pressure ratio (r_p) of the gas refrigeration sub-cycle on primary energy saving ratio (PESR) of the proposed CCDP system at different refrigerants (Air, He, CO_2)

(d)
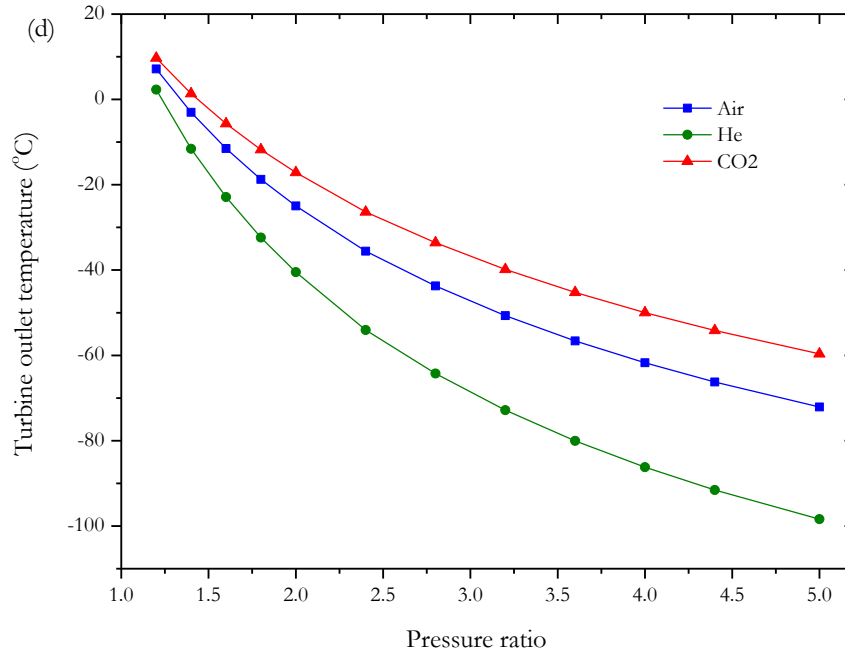
Figure 61. Effect of the pressure ratio (r_p) of the gas refrigeration sub-cycle on gas turbine outlet temperature (T_9) of the proposed CCDP system at different refrigerants (Air, He, CO_2)

3.2.4.2. Sensitivity to the Rankine sub-cycle condenser temperature (T_1)

The exergy efficiency of the CCDP system decreases significantly as condenser temperature (T_1) of the Rankine sub-cycle increases as shown in Figure 62. When air is employed as a refrigerant, the electrical power output increases remarkably as condenser temperature decreases as depicted in Figure 63. Moreover, since our model assumes that one third of the produced shaft power is used to drive the gas refrigeration cycle, the cooling capacity increases as the electrical power output increases (condenser temperature decreases). Thus, the *PESR* rises notably as the electrical power output and cooling capacity increases (condenser temperature decreases) as shown in Figure 64. At the same condenser temperature and pressure ratio, the *PESR* associated with helium is the lowest due to the low output gas turbine temperature. The fresh water production increases marginally with increasing condenser temperature.

(a)
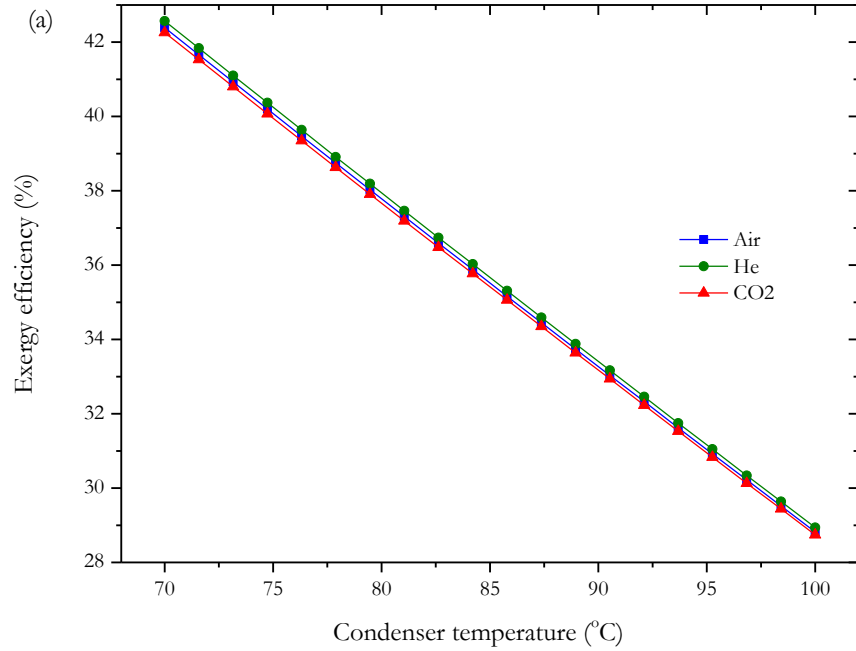
Figure 62. Effect of the Rankine sub-cycle condenser temperature (T_1) on exergy efficiency of the proposed CCDP system for different refrigerants (Air, He, CO_2)

(b)
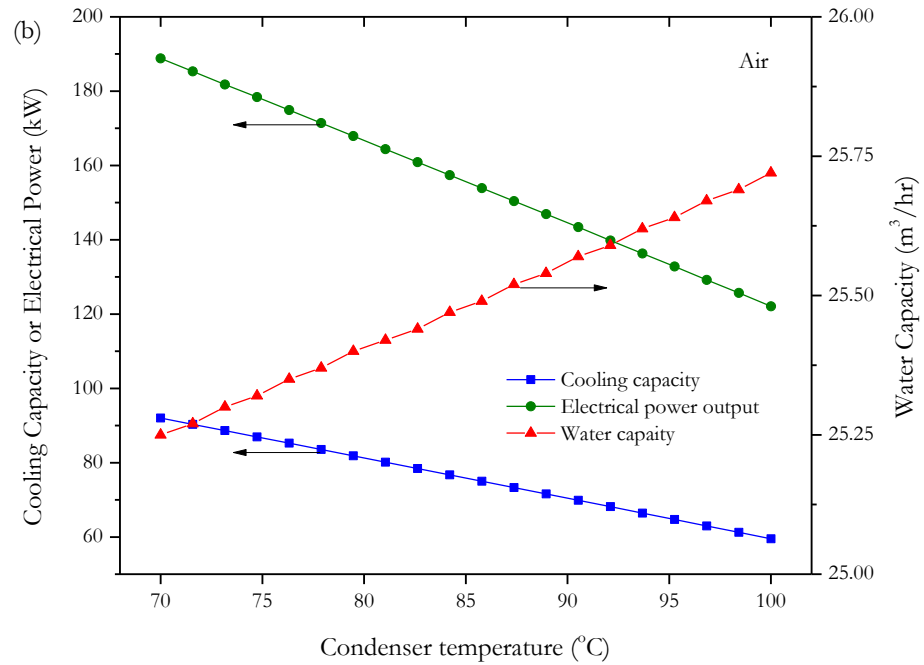
Figure 63. Effect of the Rankine sub-cycle condenser temperature (T_1) on electrical power, cooling capacity, and water production of the proposed CCDP system for Air

91
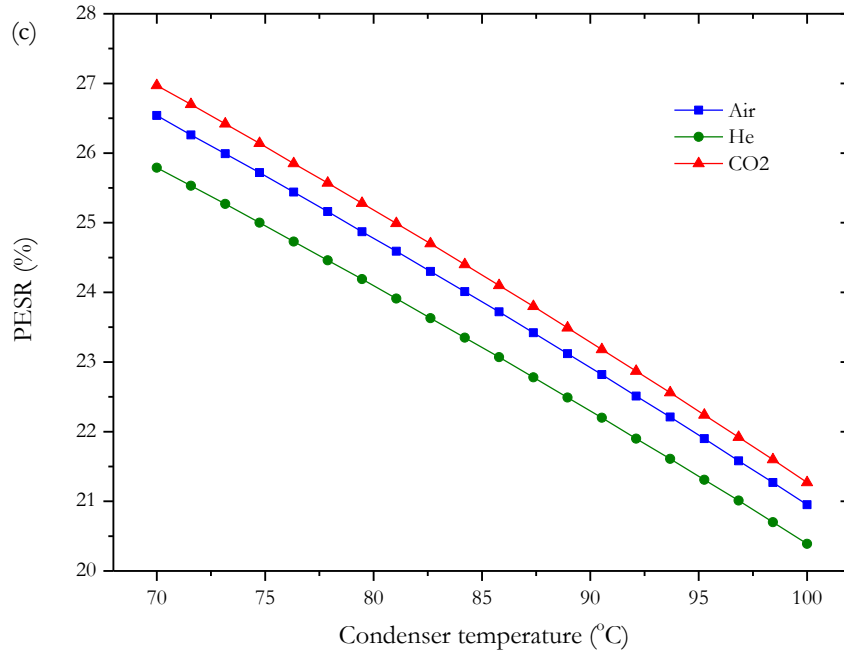
Figure 64. Effect of the Rankine sub-cycle condenser temperature (T_1) on primary energy saving ratio (*PESR*) of the proposed CCDP system for different refrigerants (Air, He, CO_2)

3.2.4.3. Sensitivity to the reverse Brayton cycle regenerator effectiveness (ε_{HX1})

For the reason that the refrigerant leaves the cooling coil at relatively low temperature and is highly desirable to enter the gas turbine at low temperature, a heat exchanger (regenerator) is vital to recover the cool refrigerant internally. Figure 66 shows that as the regenerator effectiveness increases, the exergy efficiency slightly increases. It can be observed that the exergy efficiencies for different refrigerants are larger at lower regenerator effectiveness, then converge as ε_{HX1} increases. As the regenerator effectiveness rises, the electrical power output remains constant, while cooling and fresh water capacities increase slightly as shown in Figure 67. Likewise, the *PESR* increases with increasing regenerator effectiveness in which the growth differs from only a minor effect when CO_2 is employed to none when He is used as shown in Figure 68. Even though the regenerator effectiveness has a slight effect on cooling capacity regardless of the refrigerant type, the *PERS* is more sensitive to the water production which is the case when carbon dioxide is used due to the higher heat rejected which is eventually absorbed by the MED unit.
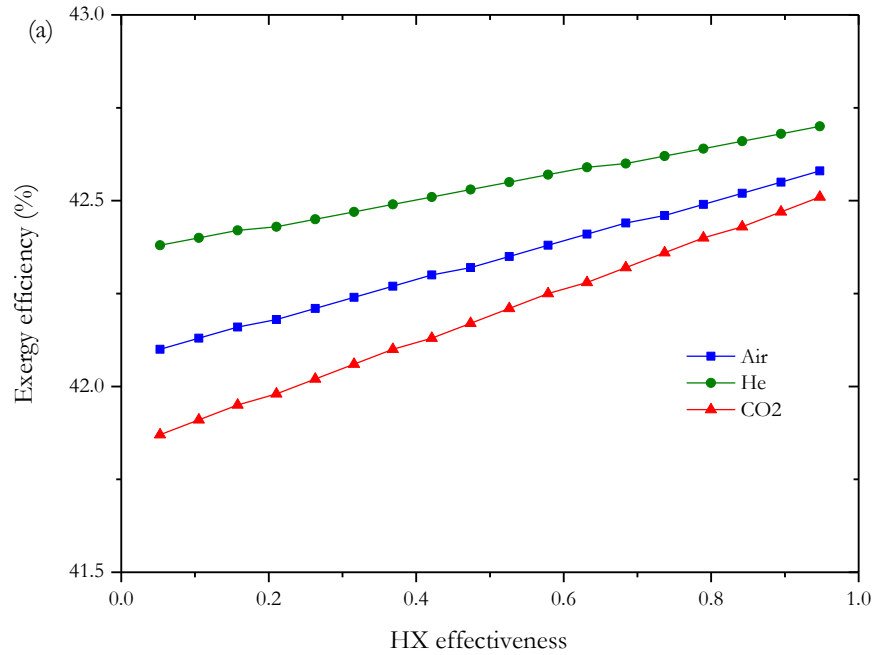
Figure 65. Effect of the reverse Brayton cycle heat exchanger (regenerator) effectiveness (ε_{HX1}) on exergy efficiency of the proposed CCDP system for different refrigerants (Air, He, CO_2)
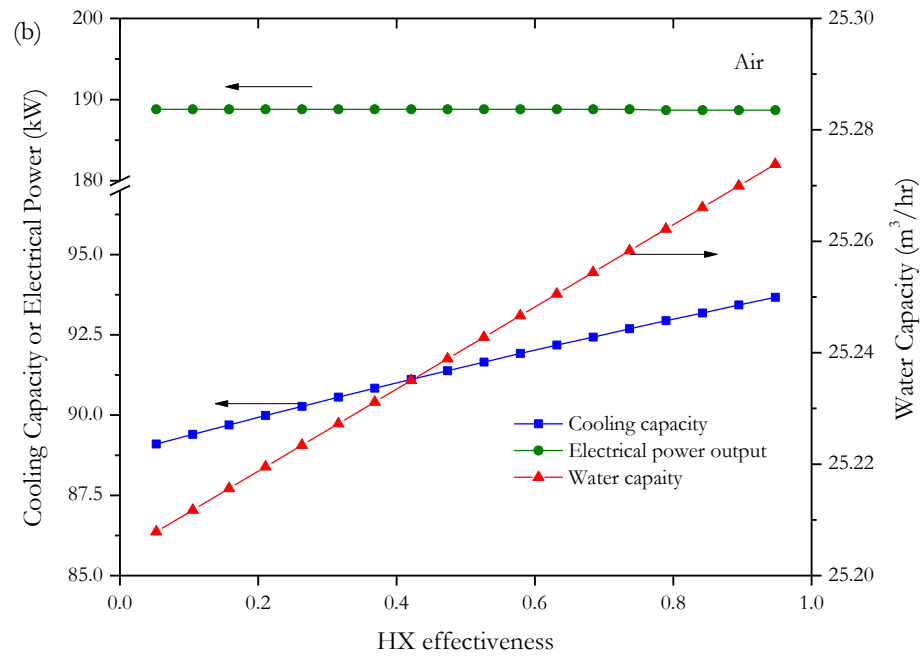
Figure 66. Effect of the reverse Brayton cycle heat exchanger (regenerator) effectiveness (ε_{HX1}) on electrical power, cooling capacity, and water production of the proposed CCDP system for Air
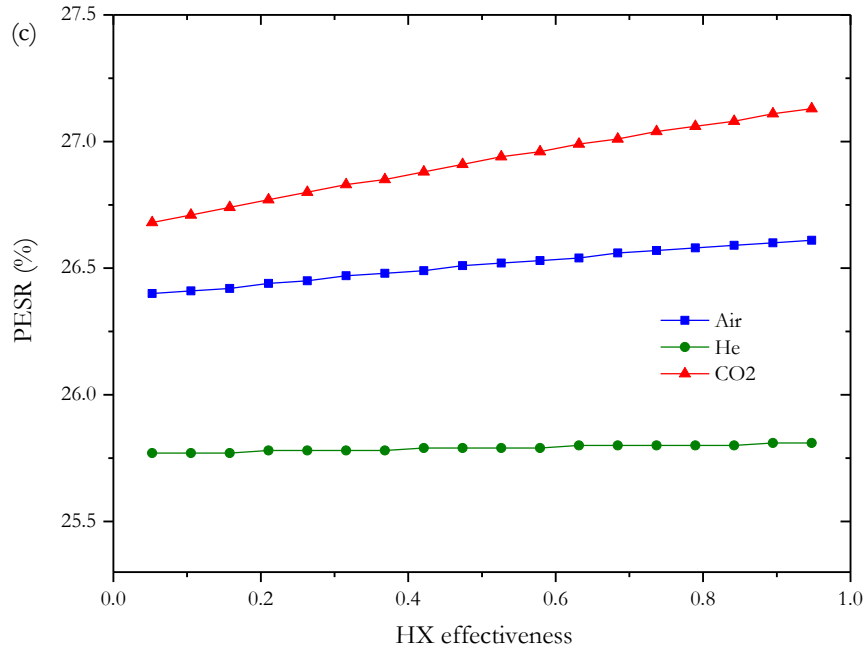
Figure 67. Effect of the reverse Brayton cycle heat exchanger (regenerator) effectiveness (ε_{HX1}) on primary energy saving ratio (PESR) of the proposed CCDP system for different refrigerants (Air, He, CO_2)

3.2.4.4. Sensitivity to the cooling ratio

Based on the application, electrical power and cooling demands fluctuate during the day and time of the year which makes control of any polygeneration system very important. Our proposed CCDP system allows the cooling subsystem (gas refrigeration sub-cycle) to be connected or disconnected easily. Therefore, we define the cooling ratio as the fraction of the electrical power consumed by the gas refrigeration sub-cycle to the total electrical power produced by the Rankine power sub-cycle. Figure 68 shows that the exergy efficiency decreases steeply from about 55% when zero cooling is generated to about 15% when zero electrical power is generated. When air is employed as a refrigerant, the CCDP system is capable of generating between 290 kW_e of electrical power output and 22 m^3/hr of fresh water production at a cooling ratio = 0. On the other hand, the CCDP system can produce about 275 kW_{th} of cooling and 30 m^3/hr of fresh water at a cooling ratio = 1, as shown in Figure 69. Furthermore, the *PESR* decreases as the cooling ratio increases, as shown in Figure 70, at different decreasing (negative) rates of change based on the type of refrigerant. Similar to the last case, the *PESR* is a strong function of water capacity which changes as rejected heat by the gas refrigeration sub-system absorbed by the MED preheating process.
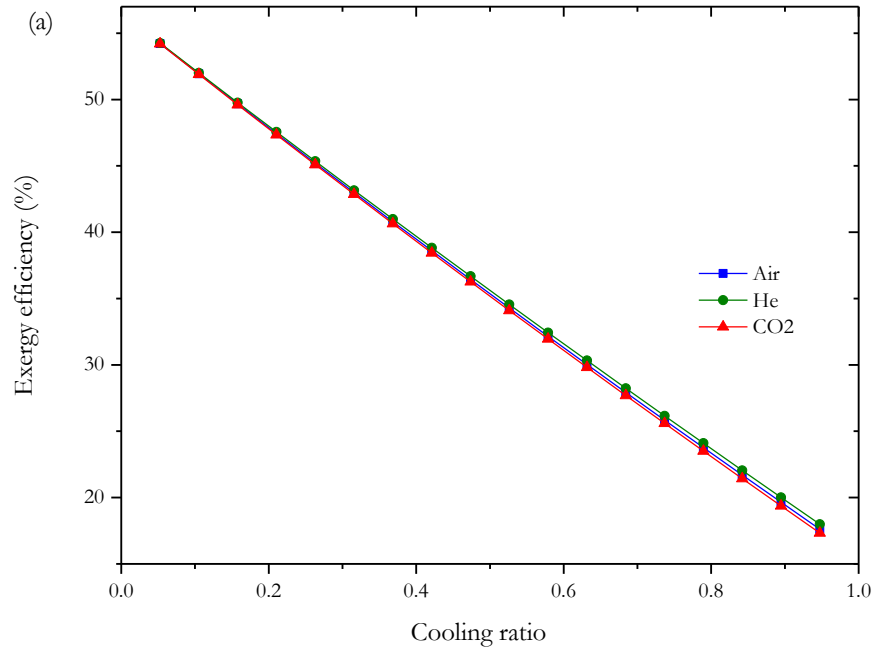
Figure 68. Effect of the cooling ratio on exergy efficiency of the proposed CCDP system for different refrigerants (Air, He, CO_2)
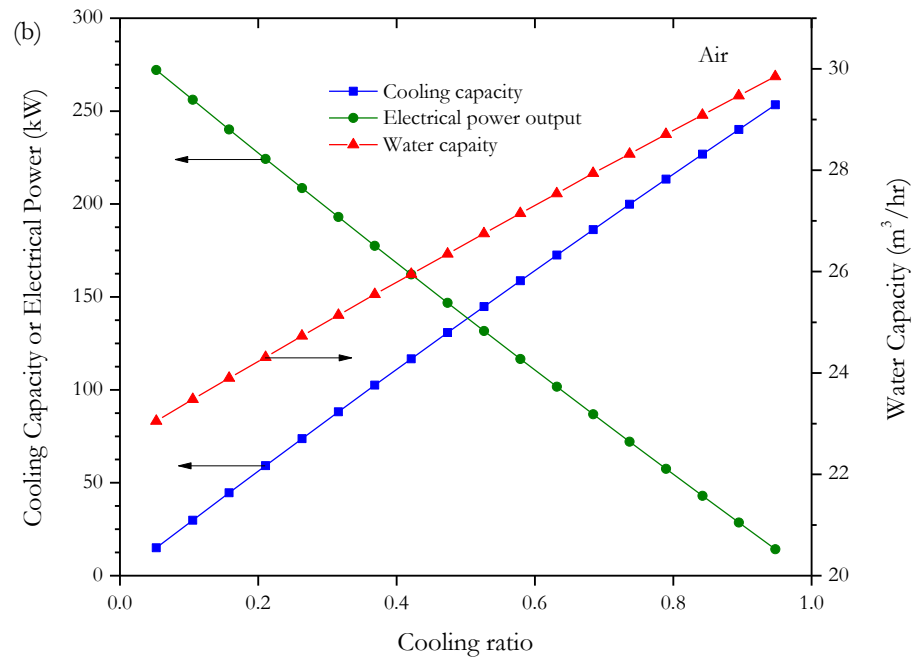
Figure 69. Effect of the cooling ratio on electrical power, cooling capacity, and water production of the proposed CCDP system for Air
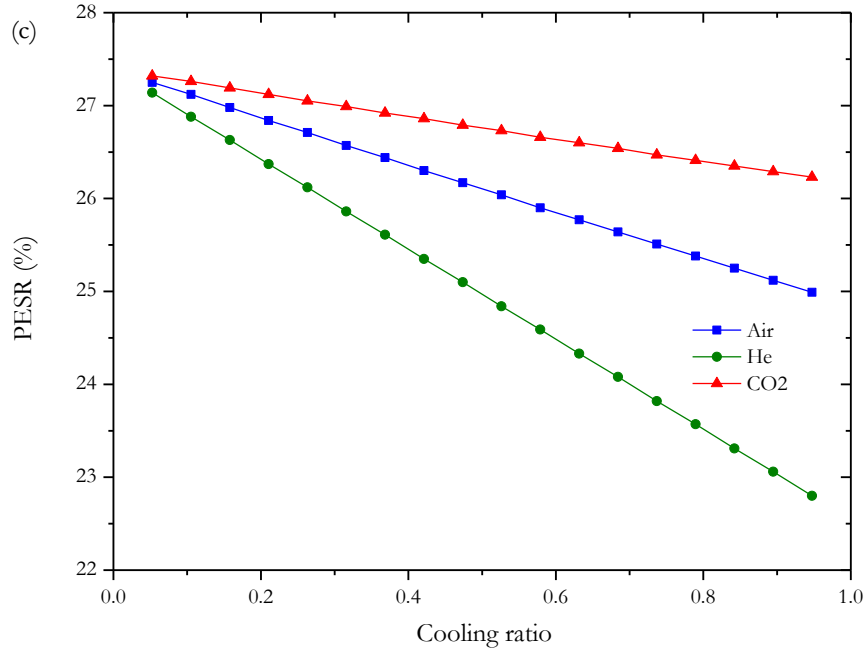
Figure 70. Effect of the cooling ratio on primary energy saving ratio (PESR) of the proposed
CCDP system for different refrigerants (Air, He, CO_2)

3.2.4.5. Sensitivity to the MED number of effects

Figure 71 depicts that the exergy efficiency sharply decreases as the multiple effect distillation
(MED) number of effects increases. Nevertheless, the fresh water capacity increases significantly
as the MED number of effects increases as shown in Figure 72. Consequently, the *PESR* increases
as the fresh water production increases (MED number of effects increases) as shown in Figure 73.
The CCDP system becomes feasible from an energy perspective when the MED number of effects
exceeds 8 effects (units) which proves that the PESR is a strong function of water production by
the MED unit. The reduction of the electrical power output, as the MED number of effects
increases, is due to the electrical power consumption associated with the required pumping system,
which leads to a reduction in the cooling capacity as well.
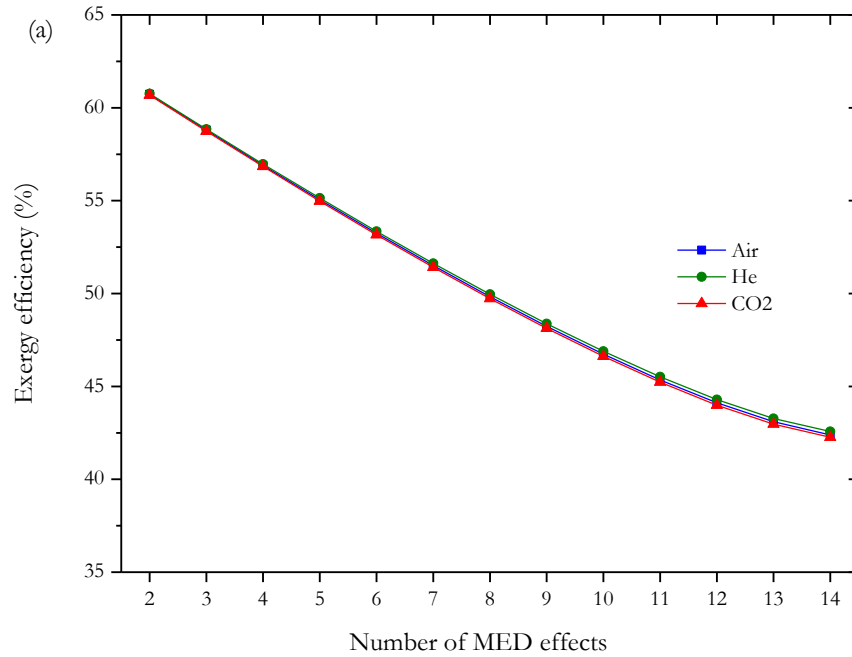
Figure 71. Effect of the MED number of effects on exergy efficiency of the proposed CCDP system for different refrigerants (Air, He, CO_2)
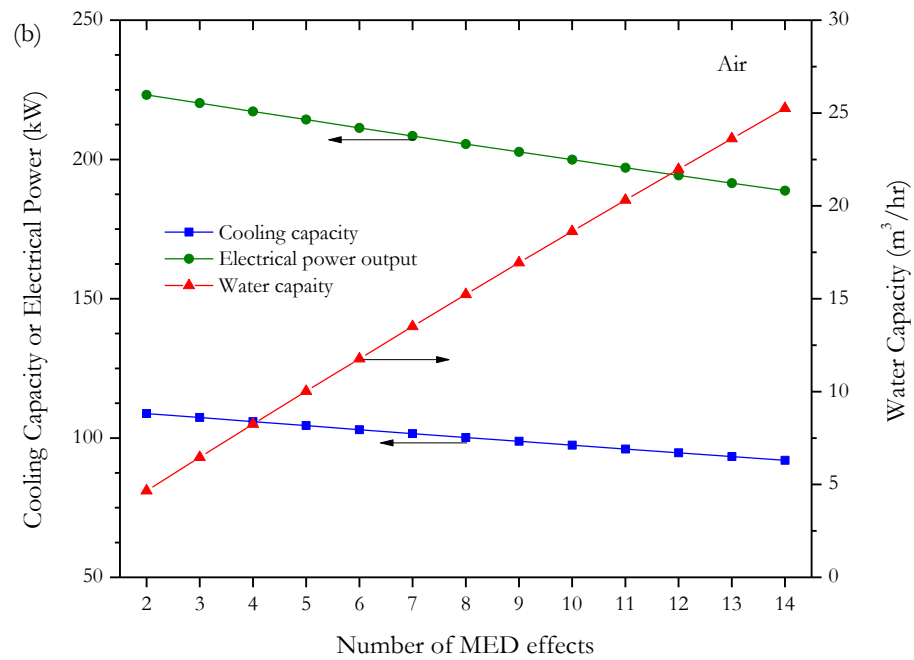
Figure 72. Effect of the MED number of effects on electrical power, cooling capacity, and water production of the proposed CCDP system for Air
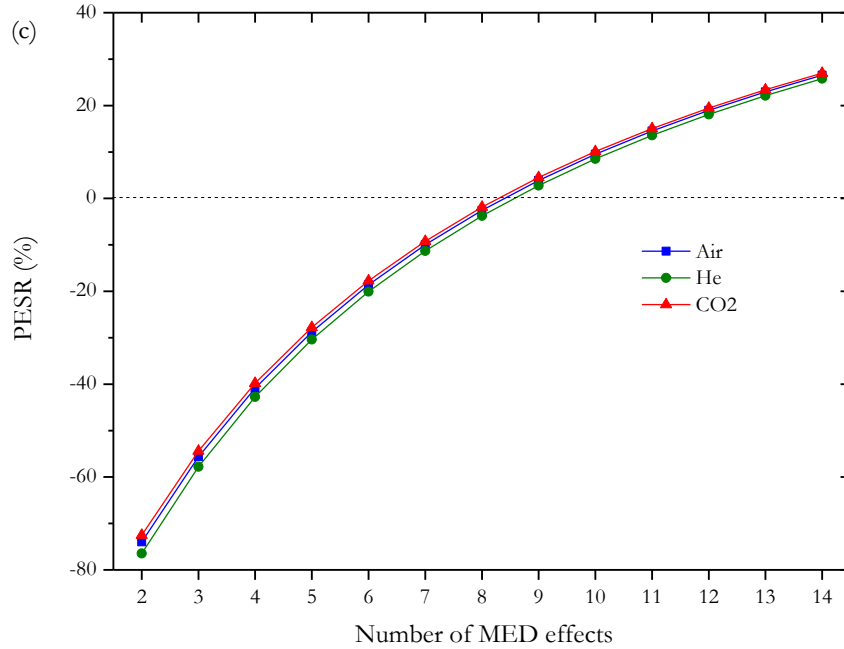
Figure 73. Effect of the MED number of effects on primary energy saving ratio (PESR) of the proposed CCDP system for different refrigerants (Air, He, CO_2)

3.2.4.6.   Sensitivity to the Rankine sub-cycle working fluid

Unlike the conventional steam Rankine cycle (RC), an organic Rankine cycle (ORC) uses working fluids that are suitable for converting low-temperature heat into electricity [73]. In our case, using an ORC instead of a conventional steam RC is more desirable due to one major advantage: the slope of the saturated vapor curve (right curve of the dome) is almost vertical. Consequently, there is no need for superheating or reheating the vapor before the turbine inlet since the vapor quality problem at the turbine outlet does not exist in the ORC [74]. Under the main assumptions listed in Table 14 (except pressure ratio = 1.4), Table 16 shows a comparison of our proposed CCDP system using different combinations of working fluids and refrigerants for the Rankine sub-cycle and gas refrigeration sub-cycle, respectively. It can be observed from Table 16 that the CCDP system that employs water and air as working fluid and refrigerant, respectively, attains the highest cooling capacity of 116.1 kW_{th} and PESR of 27.7%. Similarly, the CCDP system with water and helium (He) produces the maximum electrical power output of 188.3 kW_e with a maximum exergy efficiency of 41.9%. In the same way, the highest water production of 26.6 m^3/hr is achieved by the CCDP system that uses propane as the ORC working fluid due to the low ORC efficiency (highest heat rejection by the condenser).

Table 16. Comparison of the proposed CCDP system using different working fluid combinations

Power cycle working fluid	Cooling cycle refrigerant	Power cycle efficiency (%)	Cooling cycle COP	Exergy efficiency (%)	Power capacity (kW$_e$)	Cooling capacity (kW$_{th}$)	Water capacity (m^3/hr)	PESR (%)	Annual fuel savings (k$/yr)
Water*	Air	17.8	1.25	41.6	188.2	116.1	25.6	27.7	973
Water*	CO$_2$	17.8	1.23	41.4	188.3	114.0	25.6	27.6	970
Water*	He	17.8	1.22	41.9	188.3	112.8	25.5	27.5	966
R123*	Air	14.1	1.25	35.3	139.9	86.3	25.8	23.5	826
R123*	CO$_2$	14.1	1.23	35.1	139.9	84.8	25.8	23.4	822
R123*	He	14.1	1.22	35.5	140.0	83.9	25.8	23.4	822
Isopentane*	Air	12.7	1.25	32.0	121.5	75.0	25.9	21.8	766
Isopentane*	CO$_2$	12.7	1.23	31.9	121.5	73.6	25.9	21.7	763
Isopentane*	He	12.7	1.22	32.2	121.6	72.8	25.9	21.7	763
R245fa	Air	11.8	1.25	30.9	109.6	67.6	26.0	20.6	724
R245fa	CO$_2$	11.8	1.23	30.7	109.6	66.4	26.0	20.6	724
R245fa	He	11.8	1.22	31.1	109.6	65.7	26.0	20.5	720
Isobutene	Air	11.2	1.25	29.6	101.6	62.7	26.0	19.8	696
Isobutene	CO$_2$	11.2	1.23	29.4	101.7	61.6	26.0	19.8	696
Isobutene	He	11.2	1.22	29.8	101.7	60.9	26.0	19.7	692
R134a	Air	5.9	1.25	16.5	32.6	20.1	26.4	12.2	428
R134a	CO$_2$	5.9	1.23	16.4	32.6	19.8	26.4	12.2	428
R134a	He	5.9	1.22	16.5	32.6	19.5	26.4	12.2	428
Propane	Air	5.0	1.25	13.6	21.1	13.0	26.5	10.8	389
Propane	CO$_2$	5.0	1.23	13.6	21.1	12.8	26.5	10.8	389
Propane	He	5.0	1.22	13.7	21.1	12.6	26.5	10.8	389
* ORC boiler pressure is at critical pressure									

3.2.4.7.   Economic impact of the polygeneration system

For the sake of a simple economic analysis, thermal energy is assumed to be supplied to both the combined and standalone systems by burning natural gas. The annual fuel savings (AFS) is

calculated as follows and results for different working fluids are shown in the last column of Table 16:

$$AFS = \frac{C_f \cdot \text{PSRE} \cdot F_s \cdot \text{AOH} \cdot (3600 \text{ s/hr})}{\text{HHV} \cdot \rho_{\text{fuel}}} \tag{9}$$

where C_f is the fuel specific cost in ($/m³), AOH annual operation hours (assuming 24 hours per day, and 345 days per year), HHV the higher heating value in (kJ/kg), and ρ_{fuel} the fuel density in (kg/m³) [75]. It can be seen from Table 13 that when water and air are used as working fluids, for instance, the proposed CCDP system can save $973,000/year compared to standalone systems. Alelyani et al. [46] estimated that the total annual costs (TAC) of an MED unit with matching water capacity to be $1.05M/year. Accordingly, our proposed CCDP system is capable of cutting the total annual cost most by almost 93% compared to a standalone MED unit when water and air are used as a working fluid and refrigerant, respectively.

3.2.5. Summary

This chapter proposes the opportunity of a combined cooling, desalination, and power (CCDP) system based on the Rankine and gas refrigeration (reverse Brayton) cycles, and multiple effect distillation (MED) water desalination unit. The proposed CCDP system harnesses heat rejection by the Rankine cycle condenser to drive the desalination unit and part of the shaft work to drive the gas refrigeration cycle. At a fixed thermal energy input of 1940 kW$_{th}$ (via steam at 200ºC), our thermodynamic model shows that the proposed CCDP system is more feasible from an energy-saving perspective when the MED number of effects is more than eight effects (units) compared to separate systems that provide the same services. When water and air are utilized as a working fluid and refrigerant, respectively, the CCDP system is capable of generating around 188 kW$_e$ of electrical power output, 116 kW$_{th}$ of cooling capacity, and 26 m³/hr fresh water capacity. Additionally, the polygeneration system can achieve an exergy efficiency and primary energy saving ratio (*PESR*) of approximately 42% and 28%, respectively. Furthermore, we also explored replacing the conventional steam Rankine sub-cycle with an organic Rankine cycle (ORC) with the aim of using other working fluids that are suitable for converting low-temperature heat into electricity. The results show that working fluids with the lowest ORC energy efficiency produce slightly more fresh water due to the high heat rejection rate. Additionally, employing helium as a refrigerant instead of air allows the CCDP system to achieve the lowest turbine outlet temperature and highest exergy efficiency.

100

4. SINGLE-BED ADSORPTION SYSTEM

Similar to absorption, adsorption is based on the interaction between gases (refrigerant) and solid (adsorbent) as shown schematically in Figure 74. It can be also defined as the adhesion of molecules of the working fluid to a surface.
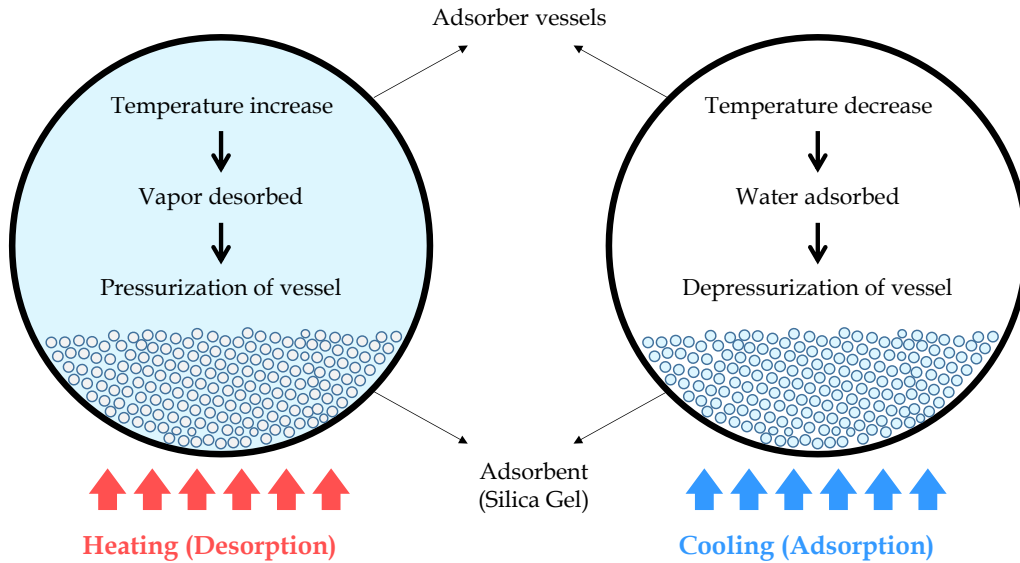
Figure 74. Desorption and adsorption processes in a typical adsorption heat pump

Some examples of the most commonly used working pairs including their regenerative temperatures are silica gel-water (85ºC), zeolite-water (200ºC), activated carbon-methanol (100ºC), activated carbon-ammonia (160ºC), zeolite-methanol (155ºC), and activated carbon-water (250ºC) [76].

Table 17. Advantages and Disadvantages of Adsorption over Vapor Compression System [77-79]

	Advantages	Disadvantages
1	Requires low-grade heat source	Low COP
2	No moving parts (no noise or vibration)	Large volume and weight
3	Long life time	Required the system to maintain high vacuum
4	Simple working principle	Intermittently working principle
5	Very low maintenance	Commercial products are expensive
6	No corrosion and crystallization problems	Poor mass and heat transfer rate
7	Environmentally friendly	
8	Very low operating cost	

Adsorption heat pumps are considered a promising alternative to the mechanical vapor-compression heat pump as the latter faces serious ecological problems associated with its working fluids and high energy consumption [79]. However, adsorption heat pump systems are presently not cost competitive and still have some serious technical weaknesses. The advantages and disadvantages of adsorption refrigeration systems over other conventional systems, such as vapor and absorption compression refrigeration systems, are listed in Table 17 [77-79].

In this chapter, we investigate the possibility of eliminating the major disadvantages listed above in Table 17 by proposing a new design based on adsorption cooling system with the intension of decreasing the system capital cost and increasing the system performance from energy and mass transfer standpoints. Moreover, we estimate the proposed system capital cost in order to compare it with solar PV and other thermally driven cooling systems such as absorption, desiccant, etc. based on the total capital cost per unit watt of cooling.

4.1. Review of Literature

Al-Alili et al. [78] provided an overview for improvements of solar thermally driven cooling technologies from recent publications. The research activities, as they presented, were intended to enhance adsorption cooling systems COP by testing various adsorbent-adsorbate pairs, improving heat and mass transfer, and optimizing the cycle time. They concluded that further improvements in the COP of all solar thermal cooling cycles are critical in order for these systems to compete with vapor compression systems and penetrate the market. They also highlighted that long-term data for some of these systems, such as an adsorption system, are important to prove the system feasibility.

Demir et al. [79] presented a review that covered studies on advanced adsorption cycles, enhancement in adsorbent beds, and improvements in adsorbent-refrigerant pairs. They emphasized studies that focused on solving high vacuum and linked leakages in the adsorption system since a consistent operation pressure is required to repeat the cycle. They predicted the adsorption cooling system will become very popular in the near future.

Sah et al. [80] presented a review on adsorption cooling systems driven by low-grade heat sources with silica gel and activated carbon as adsorbents. The study revealed that the silica gel and activated carbon-based adsorption refrigeration systems are still in the prototype stage due to their low performance. They concluded that integrating modern solar energy collecting and transferring technologies, and advanced design simulation and optimization models with adsorption

102

refrigeration system are promising and a research area of interest. Recently, the same research group, in another review paper [81], presented mathematical and experimental models for previous work in the literature related to adsorption refrigeration systems for ice production. They arrived at the same previous conclusion that adsorption cooling systems suffer primarily from their low COP, even with their remarkable environmental benefits.

Younes et al. [77] recently reviewed various types of physical adsorbent-adsorbate pairs for adsorption cooling applications. They concluded that significant research and development are still needed to deliver a compact commercial adsorption refrigeration system. They pointed out four major drawbacks of adsorption systems to be tackled: (a) high vacuum tightness is necessary, (b) low COP, (c) large specific mass and volume, and (d) commercial systems are expensive. In fact, we believe that the key feature of adsorption systems that distinguishes them from other refrigeration systems is their design and operating simplicity which is supposed to make them inexpensive, nevertheless, the last drawback clearly contradicts that. Unfortunately, the system simplicity has been sacrificed so as to enhance the system overall COP which results in a corresponding increase in its cost.

Fernandes et al. [76] provided a thorough review paper about the current status of single-bed (also called basic cycle) solar adsorption refrigeration systems. They identified new approaches, such as developing hybrid or thermal energy storage systems, in order to overcome the related difficulties and limitations to the single-bed intermittent system. They concluded that an attractive alternative cooling system based on a simple single-bed adsorption system is very promising not only for air-conditioning, refrigeration, or ice production purposes but also to meet and shape the summer peak demand.

Even though peak electrical demand lasts only for a short time during the summer as a result of cooling demand, it is very expensive for power utilities to meet that electrical demand. Photovoltaic (PV) specifically still struggles to solve the peak demand problem without storage for the reason that the non-tracking solar PV output peak is approximately three hours ahead of the electrical peak demand [82]. Intermittency and variability of renewable energy, particularly in solar energy, has been the cause of significant logistical problems and complications with these energy sources [83]. Adsorption refrigeration system performance is not sensitive to the short-term intermittency of solar energy which makes it very attractive to be powered by solar thermal energy [77].

4.2. Single-bed (Basic) Adsorption Heat Pump Cycle

The basic adsorption refrigeration cycle consists of four main components: a condenser, an evaporator, an expansion valve, and an adsorbent bed (adsorber) which is simply a vessel filled with an adsorbent (e.g. silica gel, activated carbon, zeolite, etc.). In other words, an adsorption heat pump has the same working principle as a mechanical vapor compression cycle, except that the compressor is replaced by a thermal compressor that works according to the phenomenon of adsorption.

The adsorption cooling cycle can be considered as two independent processes wherein each process consists of two steps. The first process is the adsorption process which is schematically shown in Figure 75 and consists of two steps: (i) cooling and depressurization (isosteric cooling) where the adsorbent bed releases heat while being closed until the pressure inside the adsorbent bed equals the evaporator pressure as a result of a reduction in the temperature of the absorbent bed. The second step is (ii) cooling, adsorption, and evaporation (isobaric adsorption) in which the adsorbent bed is connected to the evaporator so that the refrigerant is vaporized in the evaporator by absorbing heat (Q_L) from the cooling load and releasing heat, the heat of adsorption, to the ambient.
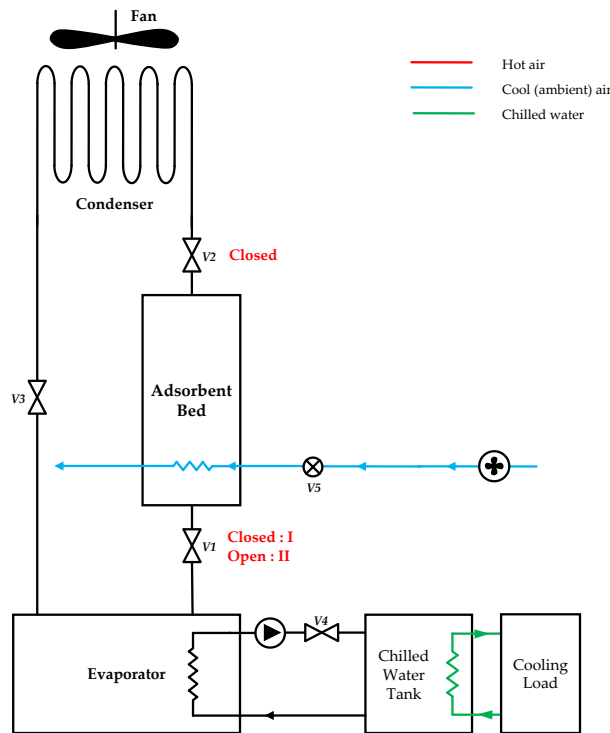
Figure 75. Adsorption Process of the Adsorption Heat Pump Cycle

The second process of the adsorption heat pump cycle is the desorption process, shown in Figure 76, which also consists of two steps. The first step (iii) is heating and pressurization (isosteric heating) in which the adsorbent bed receives low-grade heat while isolated from both the condenser and evaporator. As the temperature of the bed increases, the pressure also increases until it reaches the condenser pressure. Directly after this, the second step (iv), heating desorption and condensation (isobaric desorption), starts by opening the adsorbent bed to the condenser. As the temperature of the bed increases, the adsorbent releases the refrigerant vapor which is then condensed in the condenser.
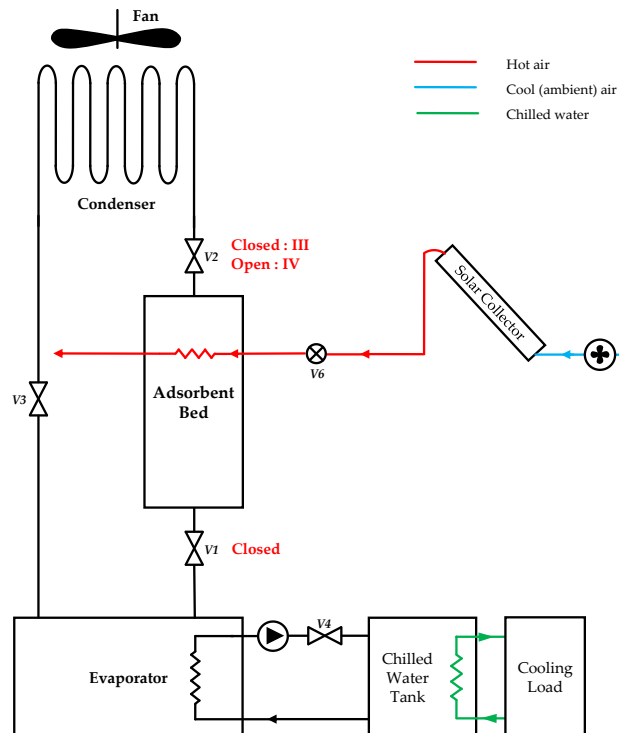
Figure 76. Desorption Process of the Adsorption Heat Pump Cycle

4.3.   Evacuated Tube Adsorption Heat Pump System

Reverse Osmosis (RO) has separated itself from all other standalone desalination technologies due to its simplicity, scalability, and relatively high performance. Similarly, evacuated tube solar collectors have also proven their maturity in the field of solar thermal energy transfer due to their moderate temperature, scalability, and ability to maintain vacuum over 15-20 years (according to Apricus.com). Inspired by both RO and solar evacuated tubes, we propose a novel design based on a single tube adsorption refrigeration system that is simple, easily scalable, potentially inexpensive,

able to operate continuously, and capable of holding and maintaining high vacuum with no leak problems.

According to the literature, a simple tube adsorption module has been proposed only by Critoph [84] in several similar works between 1998–2005. His design was based on a number of simple tubular adsorption modules, where each module consists of a generator (adsorbent bed), and evaporator/condenser as shown in Figure 77.
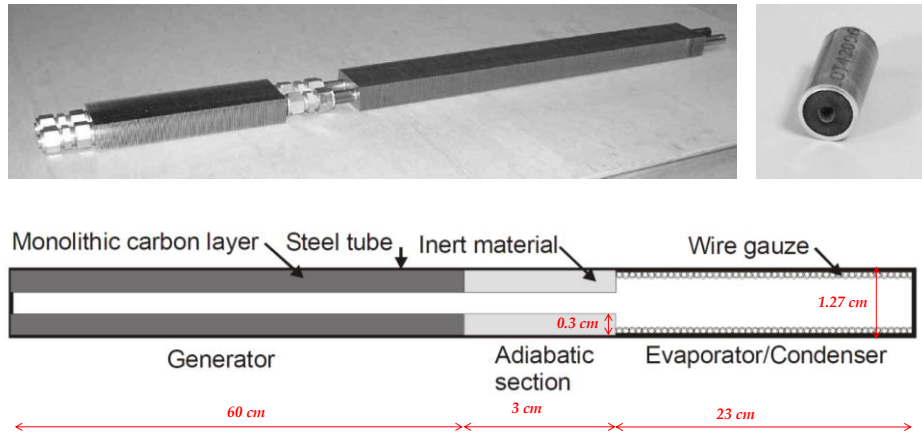
Figure 77. A Schematic Diagram of a Simple Tubular Adsorption Module by Critoph [84]

The top left picture in Figure 77 shows a double module with aluminum fins in order to enhance the heat transfer of the system, while the top right corner shows a picture of the cross section of the generator with monolithic carbon fixed in a cylindrical shape inside the tube wall. Monolithic carbon and ammonia were the only adsorbent and refrigerant, respectively, used by Critoph in all his presented work [84-88]. Monolithic carbon was chosen due to its ability to adhere strongly to the tube wall besides its favorability to withstand extensive thermal cycling. In his final adsorption system design, he arranged 16 modules in a cylindrical shell in which they rotate about the central axis completing one revolution in about 10 minutes. The working procedures of Critoph's multiple bed regenerative adsorption system are illustrated in Figure 78.
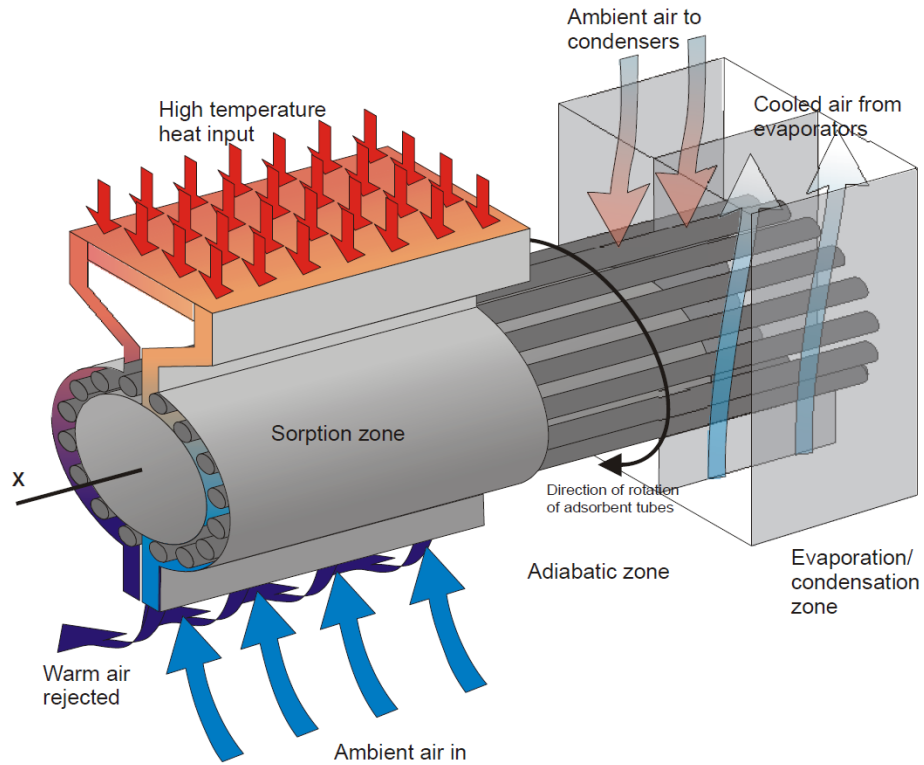
Figure 78. Schematic Diagram of Multiple-bed Regenerative Adsorption Cycle by Critoph
[84]

4.3.1. Evacuated Tube Adsorption Heat Pump Module Design

In our novel evacuated tube module design, we propose using a tube that is made of glass like in an evacuated tube solar collector as shown in Figure 79. The top part of the module shows the adsorbent bed section which contains the adsorbent (e.g., silica gel), while the bottom part of the module (glass) shows the evaporator/condenser section which contains the refrigerant (e.g., water).
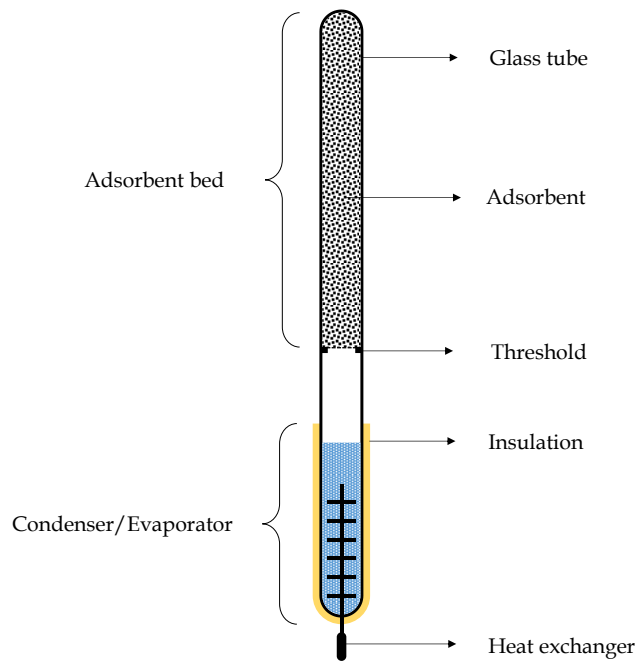
Figure 79. Schematic Diagram of Evacuated Tube Adsorption Module

During the desorption process, the top of the glass tube (adsorbent bed) is heated using solar energy (let's say during the day). Meanwhile, the refrigerant is condensed with the help of a small fan or domestic water system at the bottom of the glass tube (acting as a condenser). As the sun sets or as the module gets shaded, the adsorbent bed starts cooling down and the adsorption process takes place. During the adsorption process, refrigerant at the bottom of the glass (acting as an evaporator) generates a cooling effect as the temperature-dependent pressure inside the tube reaches the refrigerant temperature at the end of the adsorption process. For instance, if the water at the condenser is at 30ºC at the end of the desorption process (sunset), then the pressure inside the tube is above the water vapor pressure. As the temperature of the adsorbent bed cools down, the temperature-dependent pressure inside the tube decreases until it reaches the vapor pressure at the condenser temperature of 30ºC. Directly after the completion of this process, the adsorption process starts as evaporation starts.

4.4. Experiments of the Evacuated Tube Adsorption Heat Pump System and their Assessment

In this section, we examine the evacuated tube adsorption heat pump module experimentally in order to evaluate its actual performance under different conditions. All experimental runs were performed in a laboratory using a solar simulator with the aim of minimizing the irregular fluctuations associated with daily and hourly variation of solar radiation.

4.4.1. Experimental Setup

Our experimental apparatus, illustrated in Figure 80 and Figure 81, is comprised of three main elements, namely the evacuated tube adsorption heat pump, the insulated box, and the solar simulator.
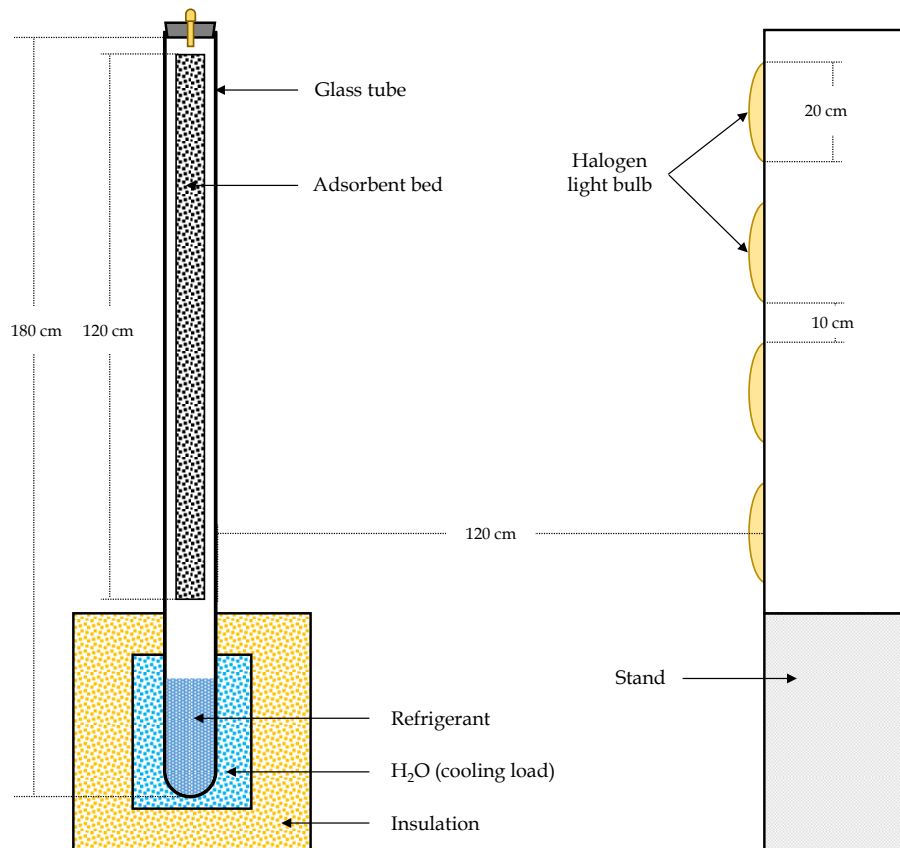
Figure 80. Schematic diagram of the evacuated tube adsorption heat pump module experimental apparatus

Figure 81. The experimental apparatus of the evacuated tube adsorption heat pump module during adsorption process (left) and desorption process (right)

The evacuated tube adsorption heat pump module is made out of a single-wall glass tube with a length of 180 cm, outer diameter of 55 mm, and inner diameter of 51.2 mm. The adsorbent bed cage is placed inside the glass tube which is made of perforated stainless steel with 0.64 mm thickness, and 3.18 mm diameter holes on 4.76 mm staggered centers (40% open area) as shown in Figure 82 in order to act as an absorber yet allow mass transfer freely into and out of the adsorbent. The adsorbent bed cage was then coated with a selective absorber paint which was selected among three different paints as shown in Figure 83. Zeolite 13X was mostly used during the experimental runs as the adsorbent before testing other adsorbents such as silica gel type-A, type-RD, type-N, as it will be explained later in this chapter. 350 g of distilled water was used as a refrigerant (adsorbate) for each experimental run.

Figure 82. Perforated stainless steel adsorbent bed cage with 3.18 mm diameter holes on 4.76 mm staggered centers (40% open area)

Figure 83. Flat protective enamel by Rust-Oleum black paint was used as a selective absorber due to its high performance under solar radiation

Seven 30-gauge OMEGA type-K thermocouples were introduced into the system through a rubber stopper as shown in Figure 84 (note that there was no leakage into the tube with this method). Five thermocouples were distributed vertically on the back of the adsorbent bed cage in order to measure the temperature gradient during the adsorption process. Additionally, the five thermocouples were

distributed horizontally in a radial direction to study the temperature gradient during the desorption process. The remaining two thermocouples were placed inside the evaporator/condenser at two different levels. A Campbell Scientific CR23X micrologger was used to monitor and read temperature values every second and record the average over 60 seconds. The temperature measurement system was calibrated and its mean relative error was estimated to be around ±0.5ºC.
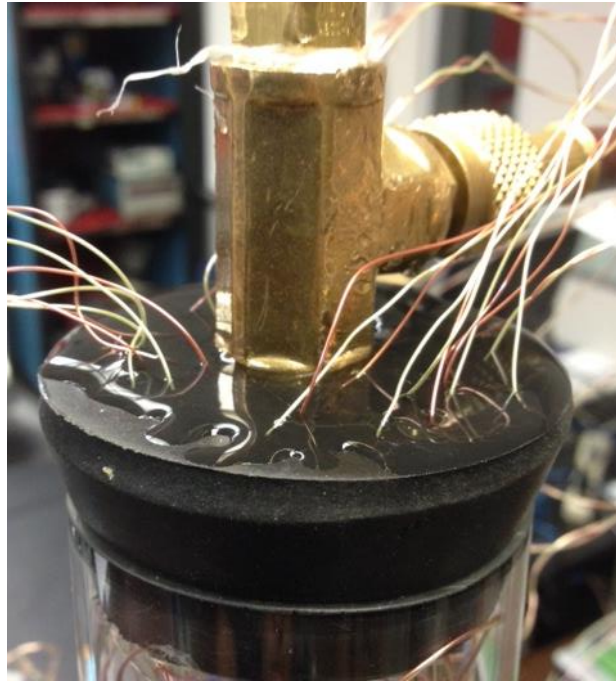
Figure 84. 30-gauge OMEGA type-K thermocouples were introduced to the tube through the rubber stopper

The vacuum pressure was measured using an OMEGA vacuum pressure transducer (Model no. PX480A-060CV) which was excited using a Keithley 6517B electrometer. The pressure measurements were read and recorded using a Fluke 8846A Digital Mustimeter every second.

Even though multiple attempts were carried out to measure the evaporation and condensation rates in the evaporator/condenser during the adsorption and desorption processes, respectively, these methods failed mainly due to the system operating under vacuum. At the end and after many failures, we decided to measure the water level in the evaporator/condenser with the naked eye using a ruler as shown in Figure 85. It is worth noting that measurements were recorded mostly every 30 minutes which minimizes the human error associate with these readings. I must say that I was extremely thoughtful when I took those readings.
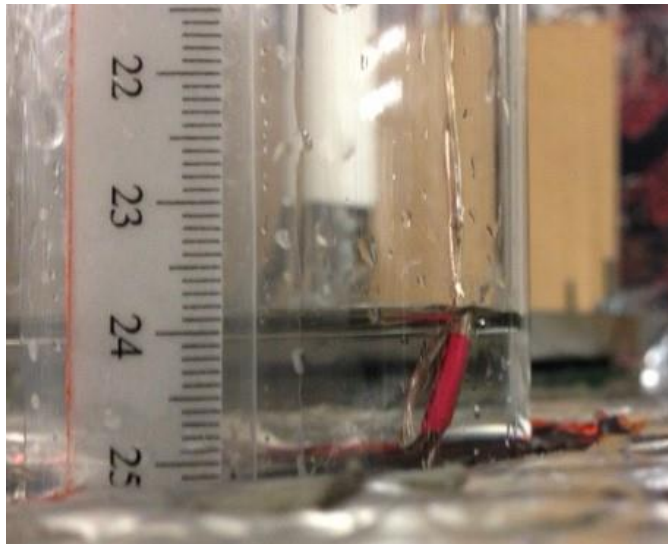
Figure 85. Naked eye and a ruler were used to measure the adsorption and desorption rates

The second element of the evacuated tube adsorption heat pump was the insulated box. With the intension of measuring the cooling effect by the evaporator during the adsorption process and rejected heat by the condenser during desorption, we submerged the lower part of the glass tube inside a water bath as shown in Figure 80. 4.45 kg (about 4.45 liter) of freshwater was insulated using insulating foam and then placed inside a 52 Quart Xtreme® 5 cooler by Coleman. The R-value was estimated to be about 7.92 ℃/W. The whole cooler was then put inside an insulated box as shown in Figure 86.

Figure 86. The insulated box that contained the 52 Quart Xtreme® by Coleman

Two additional 30-gauge OMEGA type-K thermocouples were placed inside the water bath which was connected as well to the Campbell Scientific CR23X micrologger. The following simple energy equation was used to calculate the (adsorbed heat) cooling effect at any time interval:

$$Q_{absorbed} = m_{H2O} \cdot C_{p,H2O} \cdot (T_i - T_f) \tag{4.1}$$

where m_{H2O} is the mass of water bath which equals 4.45 kg, $C_{p,H2O}$ is the specific heat at constant pressure which equals 4.18 kJ kg^{-1}K^{-1}, and T is the temperature at the initial and final point of the time interval.

The third element of the evacuated tube adsorption heat pump setup was the solar simulator. Four General Electric 1000W PAR64 halogen light bulbs were placed 120 cm away from the evacuated glass tube. The four light bulbs were distributed vertically as illustrated in Figure 80 with 30 cm between centers.

2700 W

1700 W

1000 W

700 W
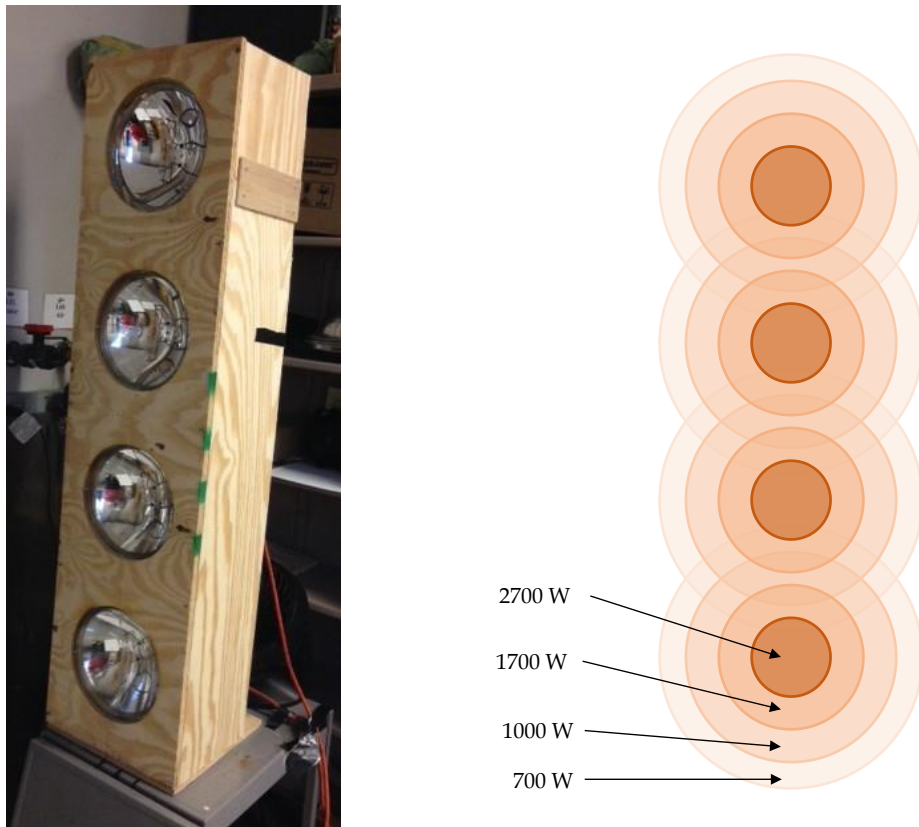
Figure 87. (a) Solar simulator made out of four 1000W halogen light bulbs, (b) illustration of the very narrow spot and heat flux control

It was observed on the preliminary experimental runs that the light bulbs produce very narrow light spots as illustrated in Figure 87 which created nonuniform radiation leading to very hot spots on the adsorbent bed at very high radiation intensity. In order to mitigate such a problem and control the amount of input heat flux, the solar simulator was moved a few centimeters (3-6 cm) to obtain the desirable heat flux. A 4-component net radiometer (NR01 Net Radiometer by Hukesflux) was used to measure the net radiation at different points in the axial direction until the desirable average heat flux was obtained, for instance 700W, 1000W, and 1700W in our case. Note that during the experimental runs, the radiometer was placed as close as possible to the glass tube and measurements were read every second and 60-second averages recorded using the Campbell Scientific CR23X micrologger.

4.4.2. Uncertainty Analysis

The total uncertainty analysis in the experimental efficiency calculations of the evacuated tube adsorption heat pump module were calculated based on Gauss' error propagation as shown below. The precision (P_{cop}) and bias (B_{cop}) uncertainties come from the evaporator temperature, adsorbed mass (water level), and heat flux measurements.

$$COP_{solar} = \frac{\dot{m}_{ref,exp} \cdot h_{fg}}{\dot{q}_{input} \cdot A_c} = \frac{\rho \cdot (\pi \cdot r^2) \cdot L_{H2O} \cdot h_{fg}}{\dot{q}_{input} \cdot A_c} \tag{4.2}$$

$$P_{cop} = \sqrt{\left(\frac{\partial COP_{solar}}{\partial L_{H2O}} \cdot P_L\right)^2 + \left(\frac{\partial COP_{solar}}{\partial \dot{q}_{solar}} \cdot P_q\right)^2} \tag{4.3}$$

$$P_{Q,absorbed} = \sqrt{\left(\frac{\partial Q_{absorbed}}{\partial T_f} \cdot P_T\right)^2} \tag{4.4}$$

where P_L, P_T, and P_q are the precision uncertainty due to the adsorbed mass (water level), evaporator temperature, and heat flux measurements, respectively, assuming normal precision error which means 95% of data fall within ±2σ (standard deviation):

$$P_L = 2 \cdot \sigma\left(L_{H2O,avg}\right) \tag{4.5}$$

$$P_T = 2 \cdot \sigma\left(T_{evap,avg}\right) \tag{4.6}$$

$$P_q = 2 \cdot \sigma\left(\dot{q}_{solar,avg}\right) \tag{4.7}$$

Similarly, the total bias uncertainty and its relevant uncertainties due to the adsorbed mass (water level) (P_L), evaporator temperature (P_T), and heat flux (P_q) measurements are calculated as follow:

$$B_{cop} = \sqrt{\left(\frac{\partial COP_{solar}}{\partial L_{H2O}} \cdot B_L\right)^2 + \left(\frac{\partial COP_{solar}}{\partial \dot{q}_{solar}} \cdot B_q\right)^2} \qquad (4.8)$$

$$B_{Q,absorbed} = \sqrt{\left(\frac{\partial Q_{absorbed}}{\partial T_f} \cdot B_T\right)^2} \qquad (4.9)$$

$$B_L = \pm\, 0.05 \; cm \qquad\qquad\qquad\qquad\qquad\qquad\qquad (4.10)$$
$$B_T = \pm\, 0.5 \;°C \qquad\qquad\qquad\qquad\qquad\qquad\qquad (4.11)$$
$$B_q = \pm\, 30 \; W/m^2 \qquad\qquad\qquad\qquad\qquad\qquad\quad (4.12)$$

The total uncertainty (U) of a measurement is the magnitude of the precision and bias uncertainties and can be calculated as follow:

$$U = \sqrt{B^2 + P^2} \qquad (4.13)$$

4.4.3. Experimental Procedure

At the beginning of each experimental run associated with adsorption, the adsorbent is added to the adsorbent bed cage and placed inside the tube as soon as possible, particularly for zeolite, in order to avoid any water vapor adsorption especially since the adsorbent is completely dry (based on the manufacturer's description). The vacuum pump is then turned on for 3 minutes, then it will be turned on for one minute every 20 minutes. The reason is not only to ensure there is no leakage (due to the thermocouple wires) but also because of the trapped air inside the adsorbent pores. As the adsorbent adsorbs water vapor, the trapped air inside its pores is released which affects the system pressure. This issue is noticeable for zeolite because of its high adsorption rate. Mass balance was performed for adsorbate (refrigerant) and adsorbent before and after the experiment to account for mass loss through the vacuum pump. In all cases, the lost water was less than 2%.

4.4.4. Experimental Results and Discussion

In this section, several experimental runs were carried out with the intention of evaluating and further understanding the performance of the evacuated tube adsorption heat pump module. It was essential for us to answer questions such as; what is the best adsorbent bed shape from heat addition and rejection viewpoints? What is the minimum required energy input to regenerate the system?

What adsorbent is more preferable for such a system? It is worth mentioning that Zeolite 13X was largely used for all preliminary experimental runs due to its high adsorption capacity at low relative humidity.

4.4.4.1.   Impact of the adsorbent bed design

In this section, we investigate five different adsorbent bed designs, namely the single small bed, double small bed, concentric bed, skewed bed, and big bed. The shapes and dimensions of the top view for these designs are shown in Figure 88 below.
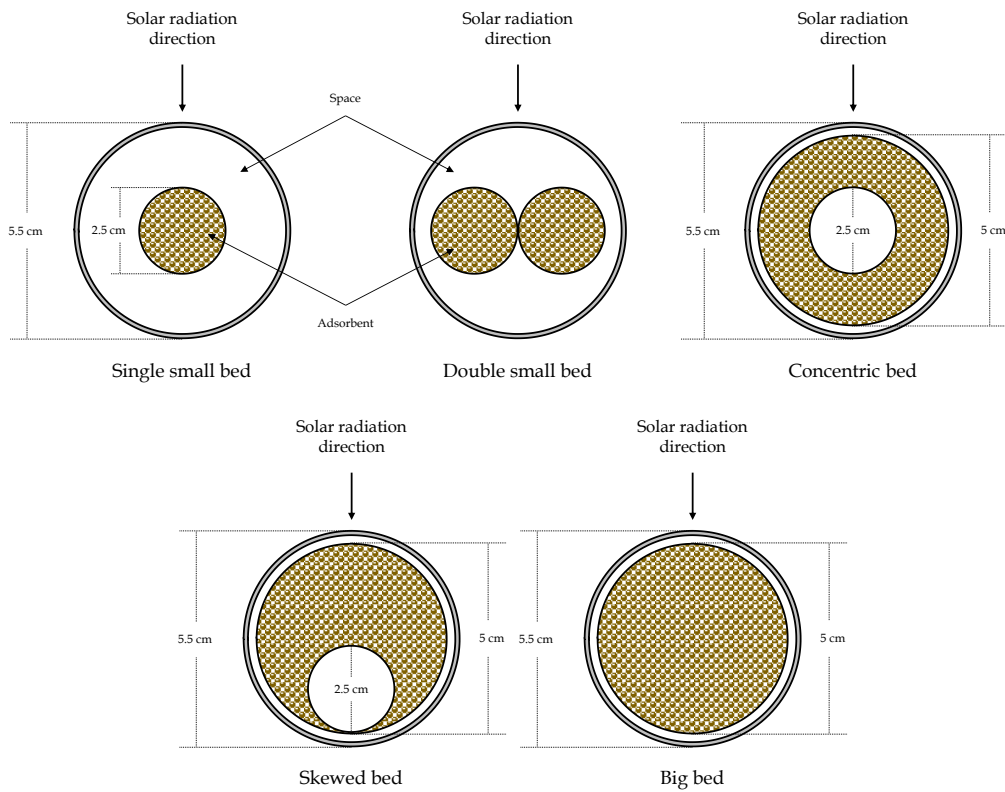
Figure 88. The five adsorbent bed designs and their dimensions

It is worth discussing the reasons behind such designs. In all designs, generally, there is a trade-off between the adsorbent amount, the distance (between the selective absorber and the farthest point) in which the heat must travel due to the low thermal conductivity of such adsorbents, and the space between the glass tube and the adsorbent bed cage to allow condensation on the inner wall of the glass. Most importantly, it is important to leave enough space to allow vapor (refrigerant) to move smoothly and make a direct contact with the adsorbent bed.

117

It can be clearly seen from Figure 89 that the single small bed has that highest adsorption rate due to its low mass (quantity) compared to other designs and secondly due to the large space between the glass tube and the adsorbent bed cage which allows refrigerant to move freely. This can also be seen from Figure 90 as the adsorbent bed average temperature peaks as early as five minutes after starting the system which reflects the highest adsorption rate (highest cooling capacity). Keep in mind that the zeolite in these runs was initially completely dry.
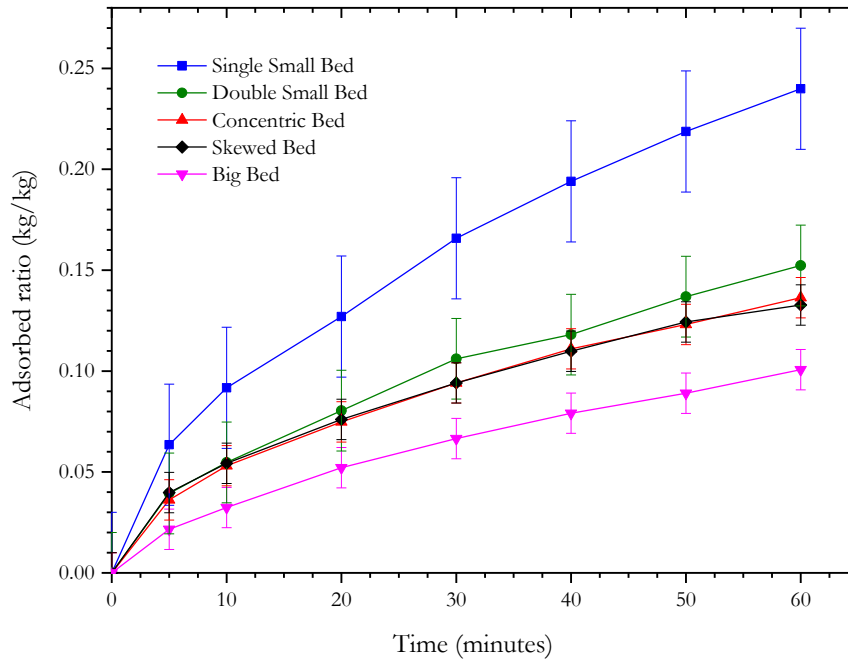
Figure 89. Adsorption rate for different adsorbent bed designs (Zeolite 13X)
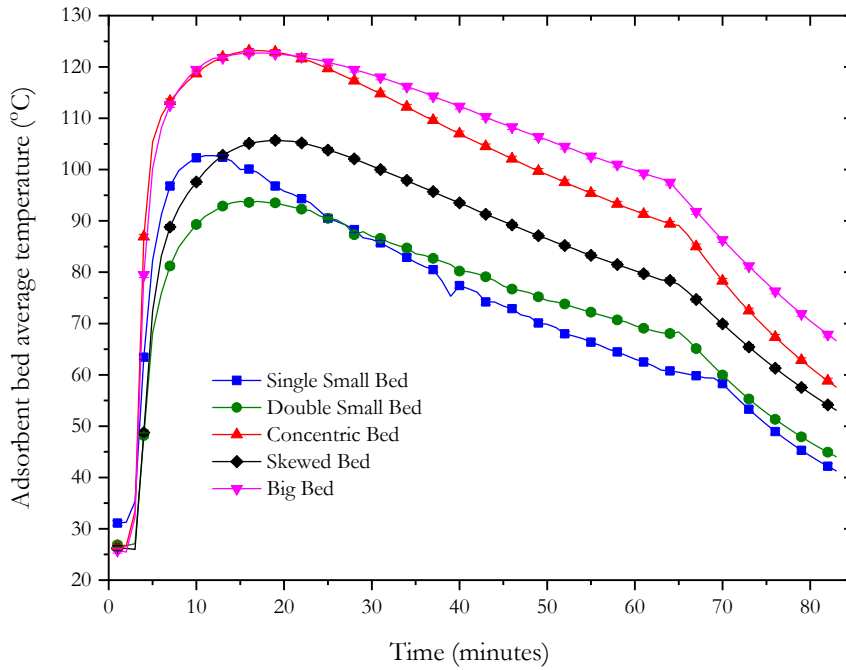
Figure 90. Adsorbent bed average temperature for different adsorbent bed designs during the adsorption process (Zeolite 13X) (the error bars are too small to be observed)
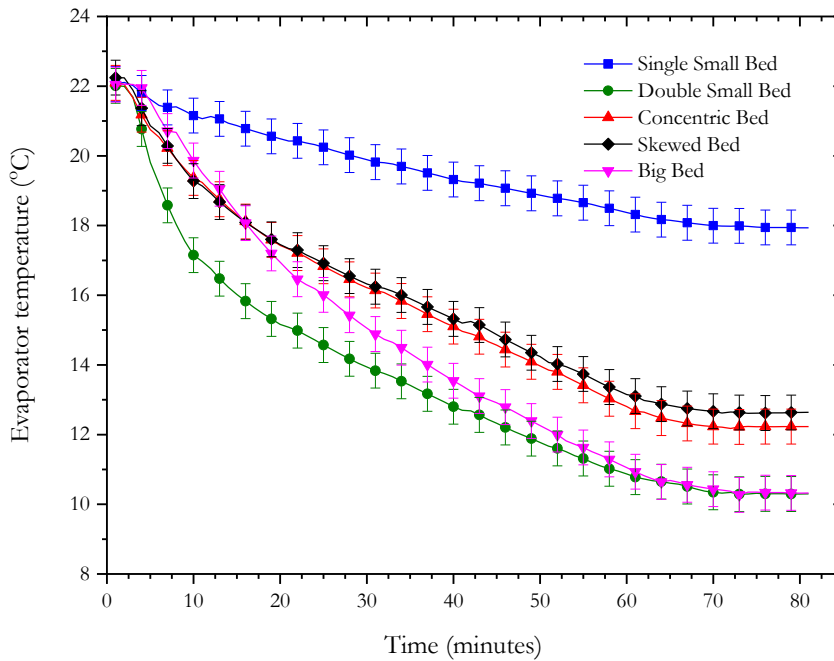
Figure 91. Evaporator temperature for different adsorbent bed designs during the adsorption process (Zeolite 13X)

Figure 91 and Figure 92a show that the double-small-bed is more effective than other adsorbent bed designs as it achieves low temperature (cooling capacity) faster than other designs. This demonstrates that the double-small-bed design balances the adsorbent amount, space with the glass tube, and contact surface with the adsorbent. Note that the pressure inside the glass was kept at atmospheric pressure for all experimental runs.

Figure 92b shows that the double-small-bed design delivers the highest cooling effect (adsorbed heat by the evaporator per unit mass of the adsorbent) among all other designs while the big-bed design has the lowest. It was observed during the experimental run that the adsorbent bed of the big-bed design does not adsorb at the same time but rather only the lower part of the adsorbent bed starts adsorbing due to the small gap between the adsorbent bed and the glass tube as shown in Figure 93. Consequently, the big-bed design was dropped out as well as the small-bed design which had low cooling effect capability.
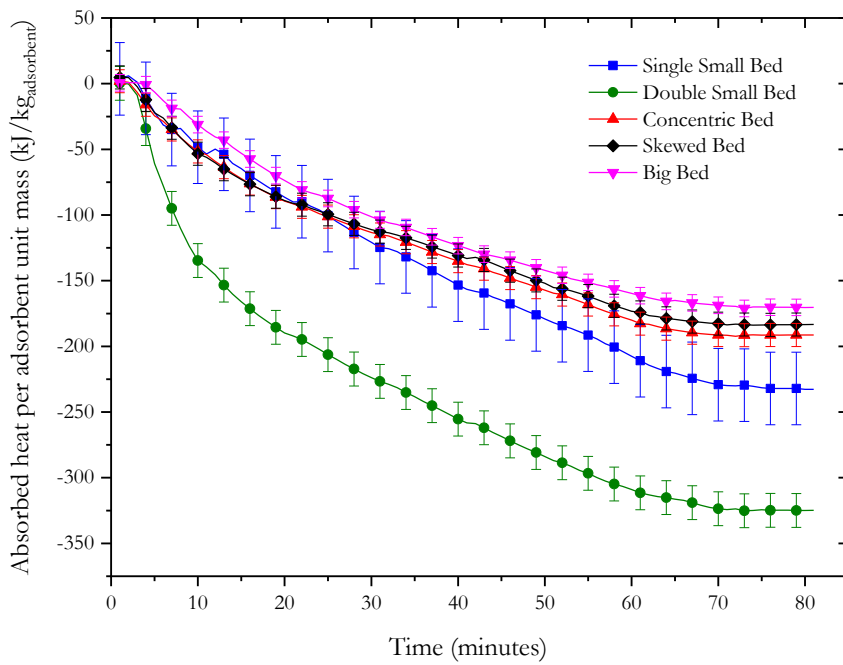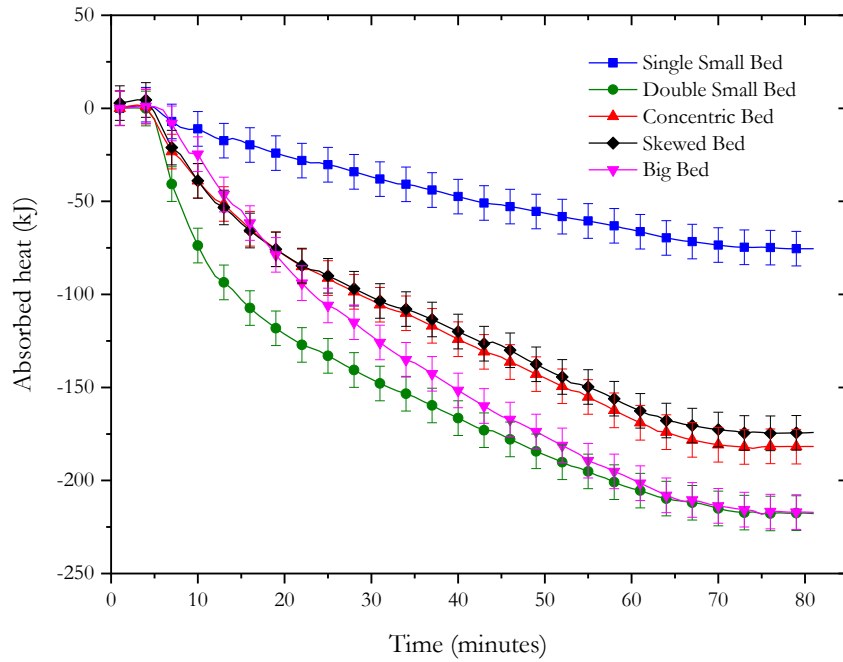
Figure 92. (a) Adsorbed heat in the evaporator for different adsorbent bed designs (b) Adsorbed heat per adsorbent mass in the evaporator for different adsorbent bed designs (Zeolite 13X)
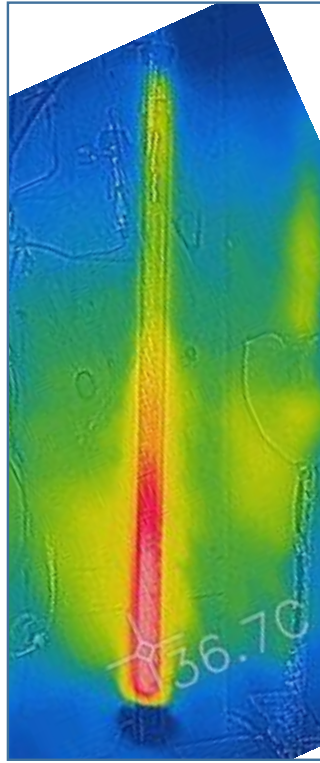
Figure 93. Thermal image of the big-bed design showing non-uniform adsorption

4.4.4.1.2. Desorption process

Among the five adsorbent bed designs, only three designs, namely the double-small-bed, concentric-bed, and skewed bed, were examined in this section of the experiment as justified in the previous section. In this section, we investigate the remaining adsorbent bed designs from a desorption point of view. Note that the experimental runs in this section were performed under atmospheric pressure, however, only a small hole was left open to ensure only minimal water vapor escapes the tube. Figure 94 shows that the double-small-bed design is capable of achieving a faster and greater desorption rate than the concentric and skewed bed designs even though the error bars are slightly overlapped. This is because the (depth) distance from the selective absorber to the farthest point in the adsorbent bed is very small compared to other designs. For the same reason, the concentric-bed design has a slightly better desorption rate than the skewed-bed design.
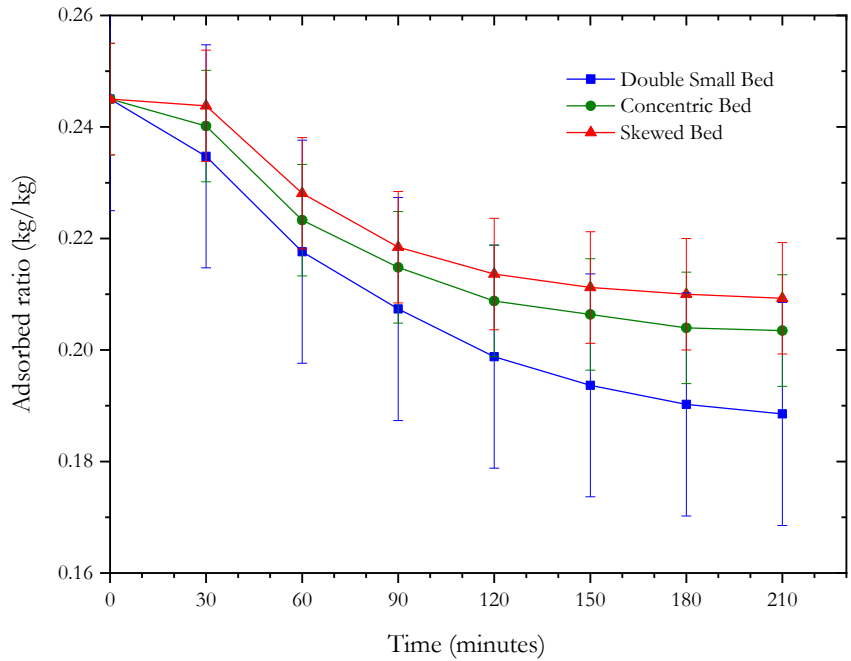
Figure 94. Desorption rate for different adsorbent bed designs at 1000 W/m² radiation input (Zeolite 13X)
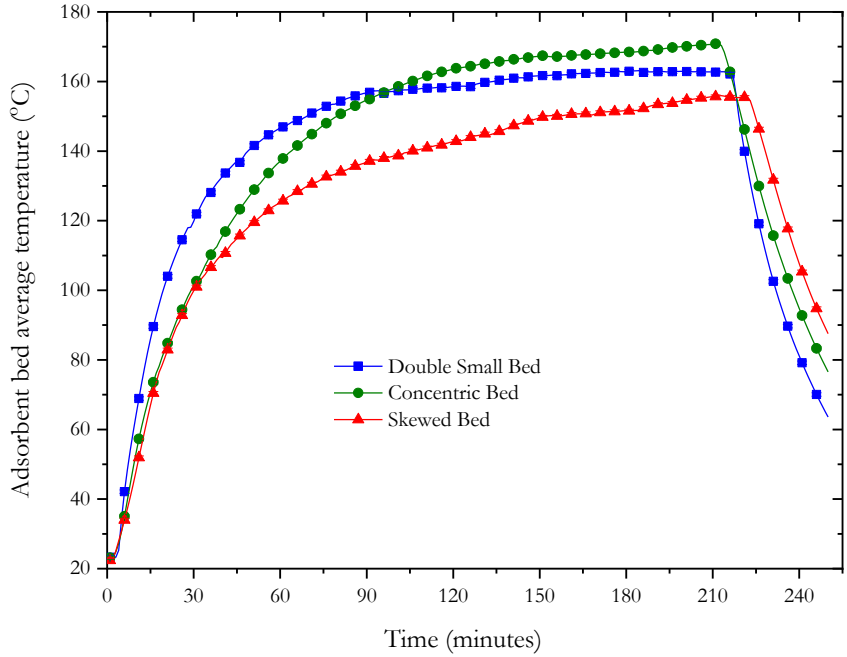
Figure 95. Adsorbent bed average temperature for different adsorbent bed designs during the adsorption process at 1000 W/m² radiation input (Zeolite 13X) (the error bars are too small to be observed)

Figure 95 displays the same behavior in the form of a dramatic increase in the adsorbent bed average temperature with time. The solar simulator was turned off after 3.5 hours (210 minutes) which explains the drop in temperature in Figure 95. One of the major advantages of our evacuated tube adsorption heat pump system is that during the desorption process, the condensation (latent heat) occurs on the inner glass of the tube as shown in Figure 96.

Figure 96. Condensation on the inner glass is one of the major advantages of our evacuated tube adsorption heat pump module

Even though the error bars in Figure 97 are relatively large, it can be clearly observed that the condenser temperature only increased by 1°C (sensible heat). It is worth mentioning that the reduction in the condenser temperature at the beginning of the desorption process occurred for all experimental runs and the reason behind that reduction is not known. Based on the obtained results in this section, we decided to proceed with our experiment work with only the double-small-bed design due to its cooling capacity, adsorption and desorption rate, and cooling-to-weight ratio.
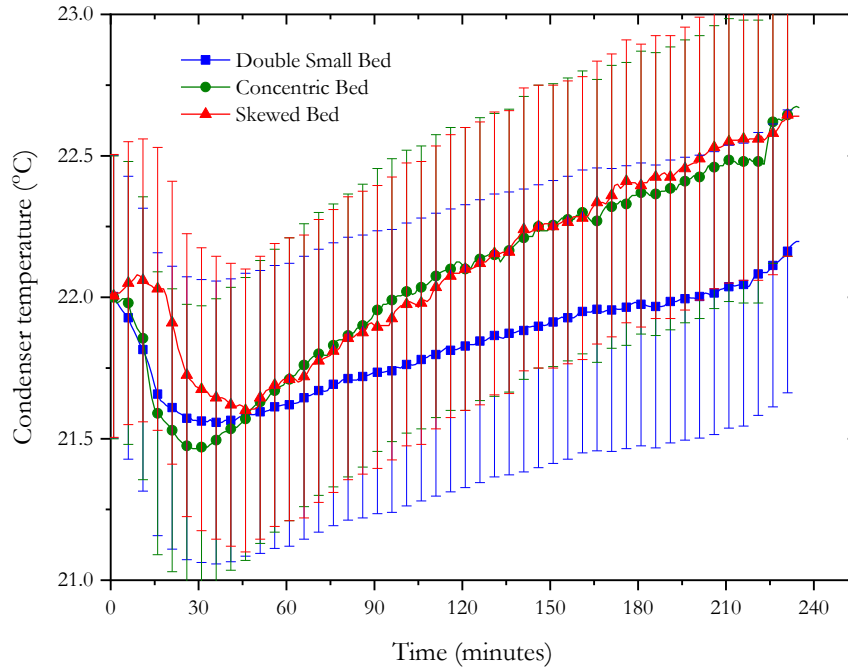
Figure 97. Condenser temperature for different adsorbent bed designs during the desorption process at 1000 W/m² radiation input (Zeolite 13X)

4.4.4.2. Impact of the heat input during desorption process

In this section, we investigate the effect of the radiation heat flux input on the desorption process in order to identify the minimum adsorbed ratio. Note that the zeolite (same for silica gel) for all experimental runs in this section was saturated together to ensure that all batches start with the same water (refrigerant) content. Again, the experimental runs in this section were performed under atmospheric pressure, however, only a tiny hole was left open to make sure minimal vapor leaves the tube. Figure 98 and Figure 99 show that significant desorption is attainable by increasing the radiation heat flux which directly increases the adsorbent bed average temperature. It can be observed that zeolite 13X requires very high temperature to achieve a low adsorbent ratio. The rapid drop in the adsorbent bed average temperature in Figure 99 is due to turning off the solar simulator.
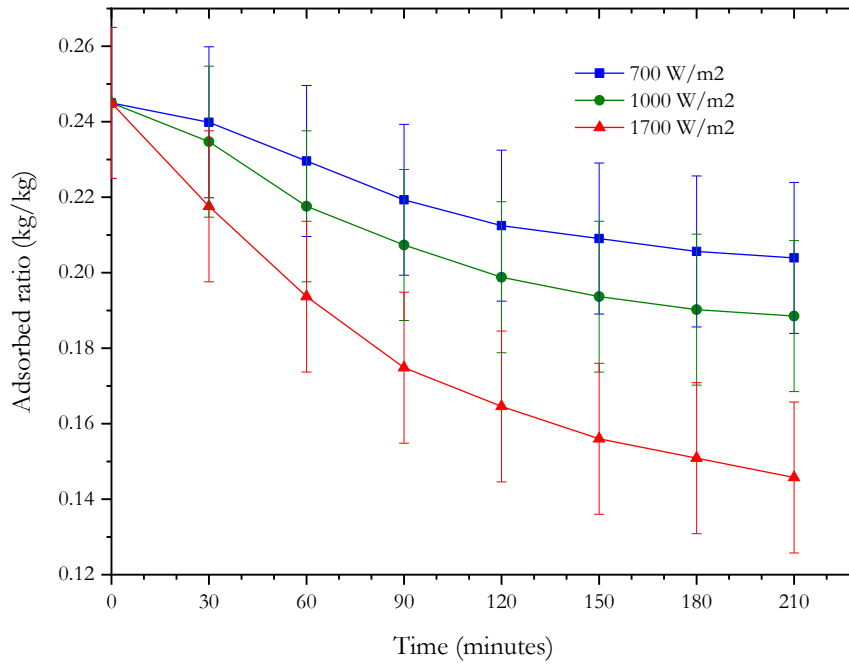
Figure 98. Desorption rate for different radiation heat flux using the double small bed design (Zeolite 13X)
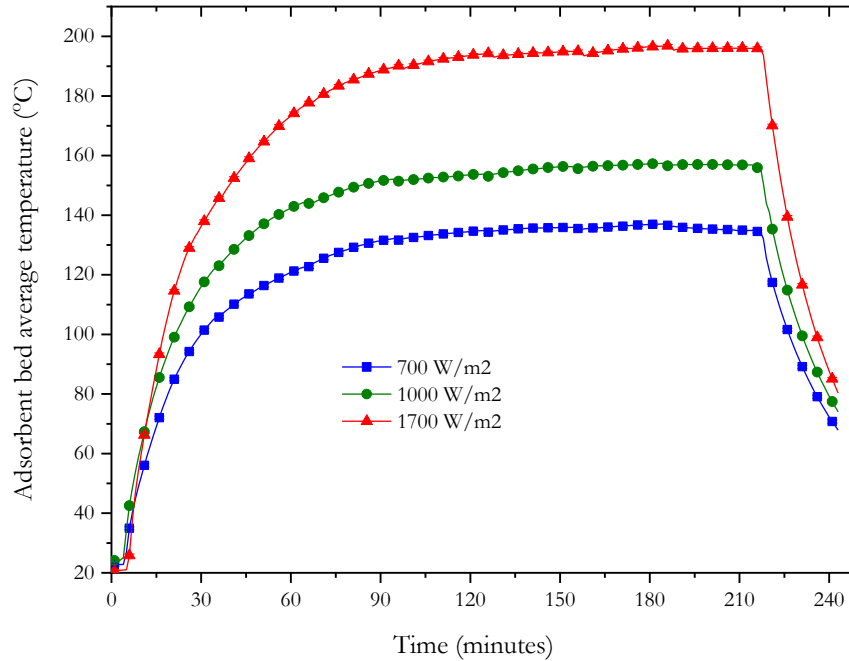
Figure 99. Adsorbent bed average temperature for different radiation heat flux using the double small bed design (Zeolite 13X) (the error bars are too small to be observed)

126

Unlike zeolite 13X, silica gel can desorb substantially when its temperature exceeds 100ºC as shown in Figure 100 and Figure 101. Remember that these experimental runs were performed under atmospheric pressure, otherwise, 100ºC can obtain very low adsorbed ratio.
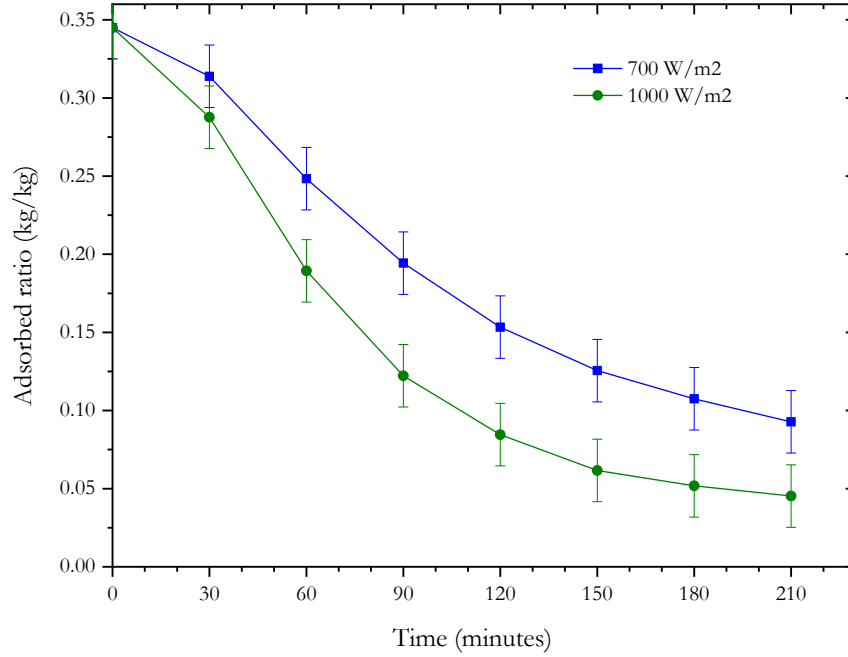
Figure 100. Desorption rate at different radiation heat flux using the double small bed design (Silica Gel)
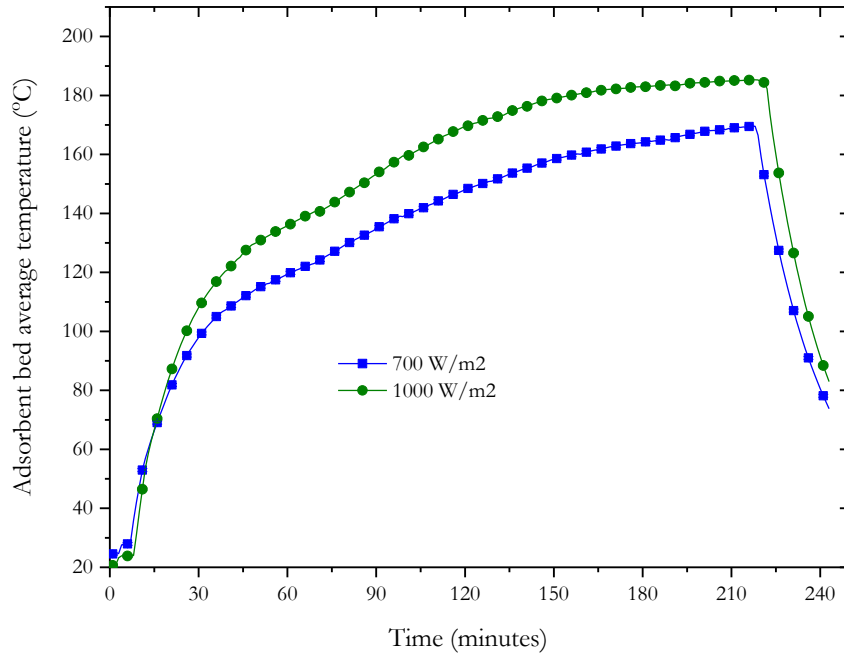
Figure 101. Adsorbent bed average temperature for different radiation heat flux using the double small bed design (Silica Gel) (the error bars are too small to be observed)

4.4.4.3. Impact of the pressure during the desorption process

In this section, we show the effect of the pressure on the evacuated tube adsorption heat pump module during the desorption process for zeolite 13X. Even though the adsorbent bed average temperature slightly increased (due to the reduction in the heat loss), the adsorbed ratio increased almost by two times as shown in Figure 102 and Figure 103. This demonstrates the important role that the pressure plays during the desorption process.
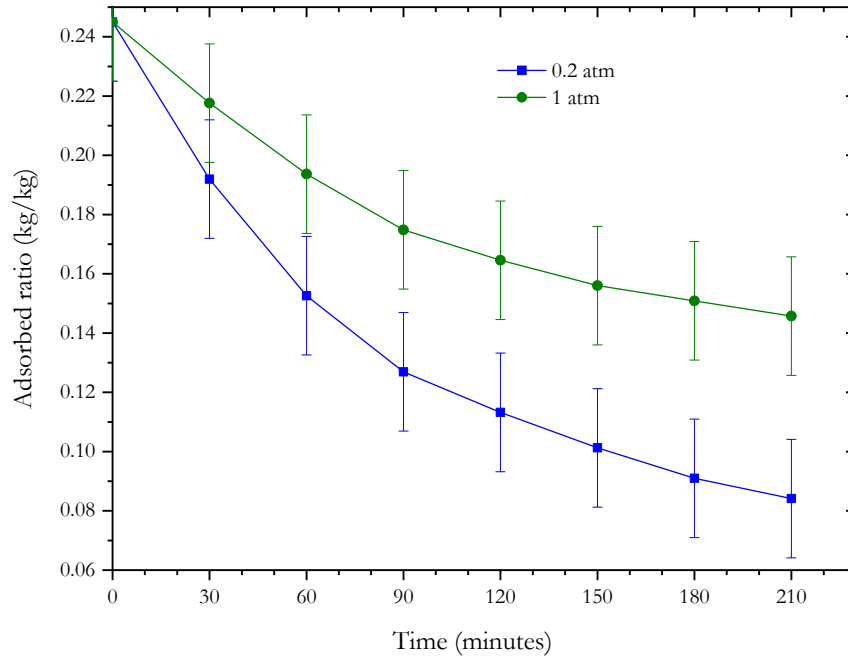
Figure 102. Desorption rate at different pressures using the double small bed design and at 1700 W/m² (Zeolite 13X)
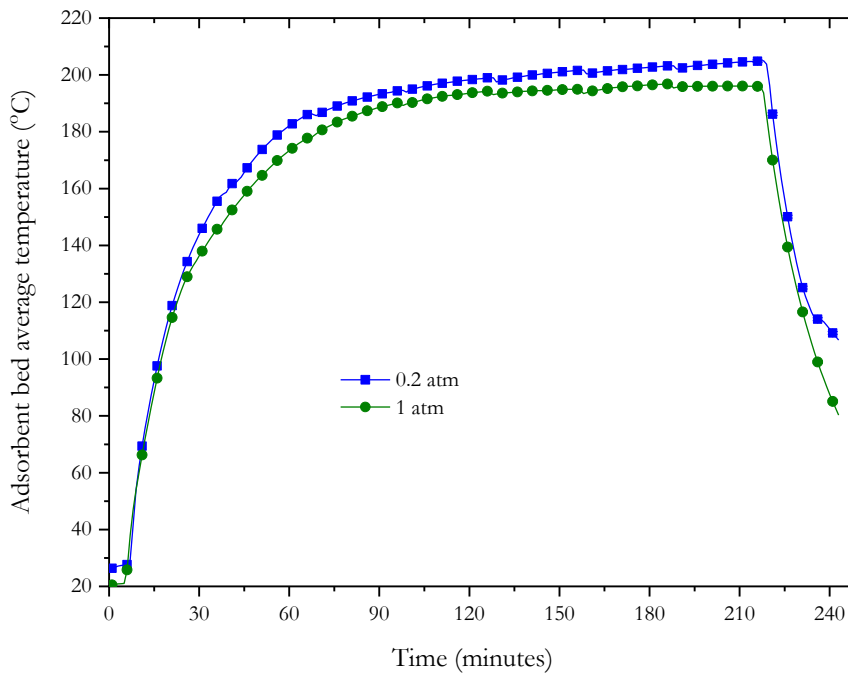
Figure 103. Adsorbent bed average temperature at different pressures using the double small bed design and 1700 W/m² (Zeolite 13X) (the error bars are too small to be observed)

4.4.4.4. Impact of the adsorbent type

In the past few sections, we have chosen an adsorbent bed design based on its performance during both the adsorption and desorption processes. We also investigated the desirable amount of incident radiation heat flux (temperature) for both zeolite 13X and silica gel, then lastly, the effect of the working pressure on the desorption process. In this section, we examine how the system performs using different adsorbents, namely silica gel Type-A, silica gel Type-RD, silica gel Type-N, and Zeolite 13X using the double-small-bed design and working under high vacuum. The thermophysical properties of the used adsorbent are summarized in Table 18.

Table 18. Thermophysical properties of different adsorbents

Adsorbent	Silica Gel			Zeolite
Type	A	RD	N	13X
Grade	Beads	Beads	Beads	Beads
Avg. pore diameter (nm)	2.2	2.2	2.2	1.3
Particle size (mm)	4-6	4-6	4-6	3-5
Density (kg/m3)	730	700	780	689
Specific surface area (m2/g)	650	720	600	726
Porous volume (ml/g)	0.36	0.32	0.40	0.25
Specific heat capacity (kJ/kgK)	0.920	0.920	-	0.795
Manufacturer	Fuji Silysia Chemical, Ltd	Fuji Silysia Chemical, Ltd	Fuji Silysia Chemical, Ltd	SORBENT SYSTEMS (IMPAK Inc.)

4.4.4.4.1. Adsorption

Due to the many thermocouples inside the evacuated tube adsorption heat pump module and to guarantee no leakage occurs during the adsorption process for all four runs (over 12 hours' experiment for silica gel), the vacuum pump was automated to operate for one minute every 20 minutes. It can be observed clearly from Figure 104 and Figure 105 that zeolite 13X has an excellent adsorption rate compared to other silica gel types as it almost reaches its absorptive capacity in less than three hours (this is why zeolite curve ends earlier than silica gel). It basically can deliver the same cooling capacity within 3 hours compared to an average of 20 hours for silica gel as shown

in Figure 106 and Figure 107. Among all silica gel types, the Type-RD has a better performance that Type-A and Type-N.
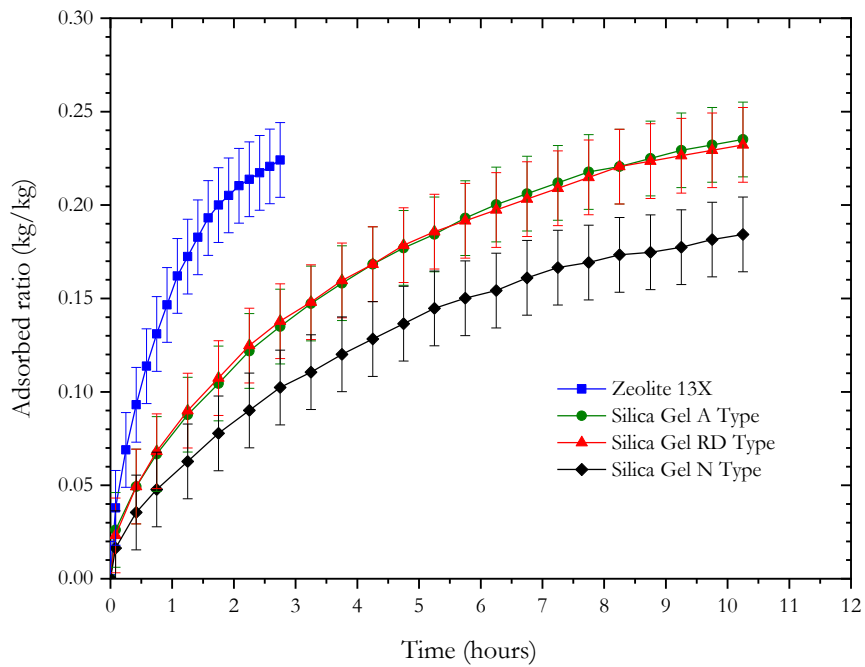
Figure 104. Adsorption rate for different adsorbents (using the double small bed design)
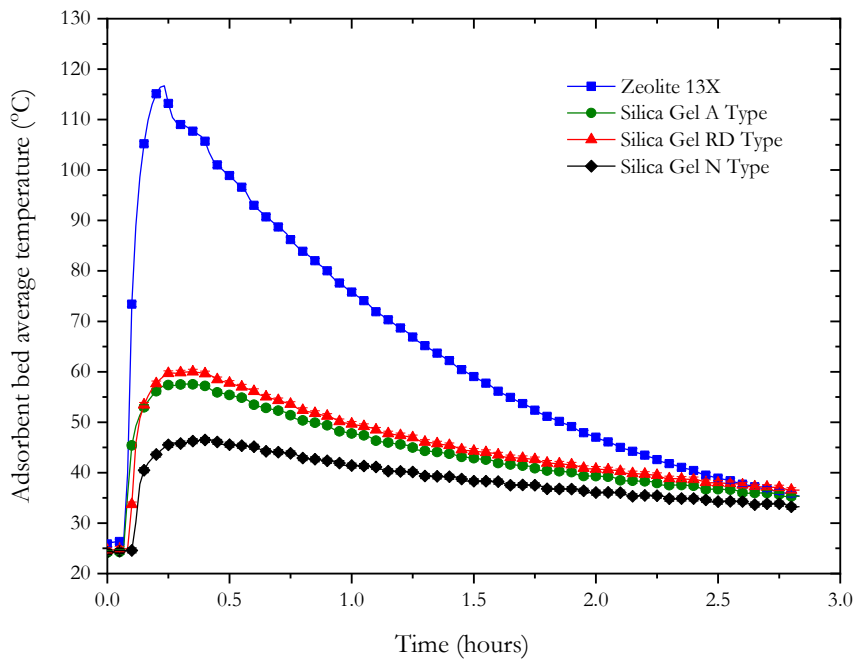
Figure 105. Adsorbent bed average temperature for different adsorbents during the adsorption process (using the double small bed design) (the error bars are too small to be observed)
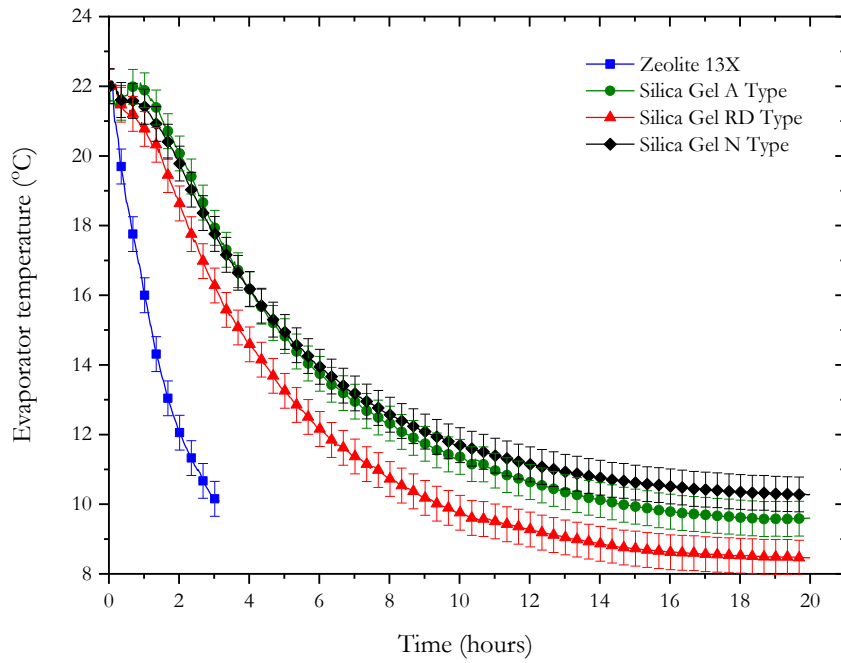
Figure 106. Evaporator temperature for different adsorbents (using the double small bed design)
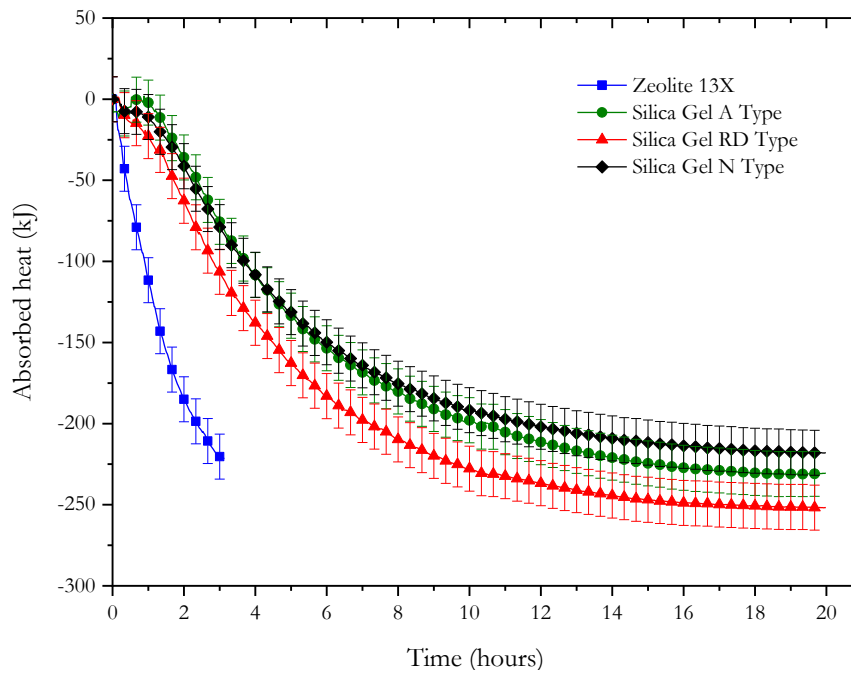
Figure 107. Adsorbed heat in the evaporator for different adsorbents

132

The rate of absorbed heat ($\dot{Q}_{ref,exp}$) with respect to time can be calculated based on equation (4.1) for every time interval for these experimental runs and the results are shown in Figure 108. It can be observed that Zeolite 13X reaches its cooling capacity peak in less than 30 minutes while Silica gel requires three times that. The minus sign (negative numbers) in Figure 108 is used to indicate the heat absorbed by the system. It is very important to point out that Zeolite 13X seems more desirable to provide cooling instantly especially if the system is to be regenerated frequently.
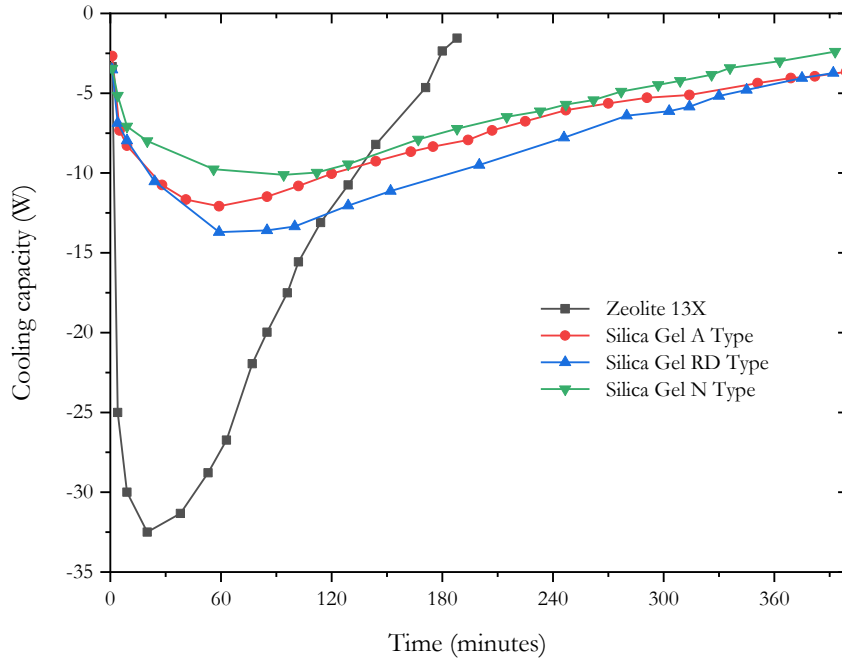
Figure 108. Calculated cooling capacity (rate of absorbed heat, $\dot{Q}_{ref,exp}$) with respect to cycle time for all adsorbents

4.4.4.4.2.   Desorption

After 12 hours of every experimental run, the last reading of the adsorption process was recorded before starting the desorption process. Note that for these 12 hours the vacuum pump was not operating and vacuum was maintained below 0.67 kPa. The updated version of Figure 104 including the last reading is shown in Figure 109 below.
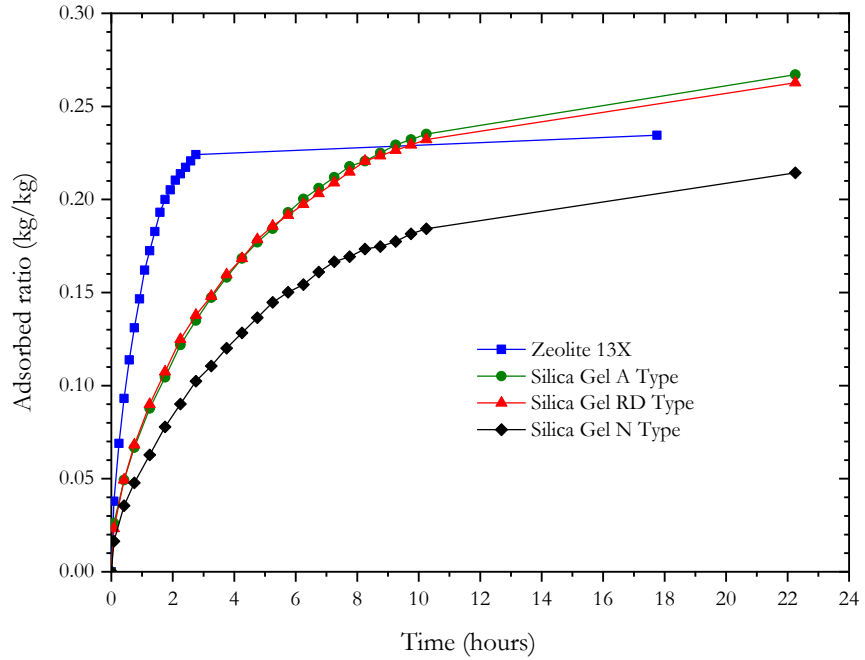
Figure 109. Adsorption rate for different adsorbents (same as Figure 104)

The solar simulator was then turned on to begin the desorption rates as shown in Figure 110. Note that the radiation heat input was set at 1000 W/m² for all silica gel types and at 1700 W/m² for zeolite 13X. The silica gel types were almost able to return to the starting point, on the other hand, zeolite 13X is still a bit far from the point in which it starts the adsorption process even with using higher heat flux. Figure 111 shows that the adsorbent bed average temperatures of the silica gel types level off as they reach the lowest adsorbed ratio.
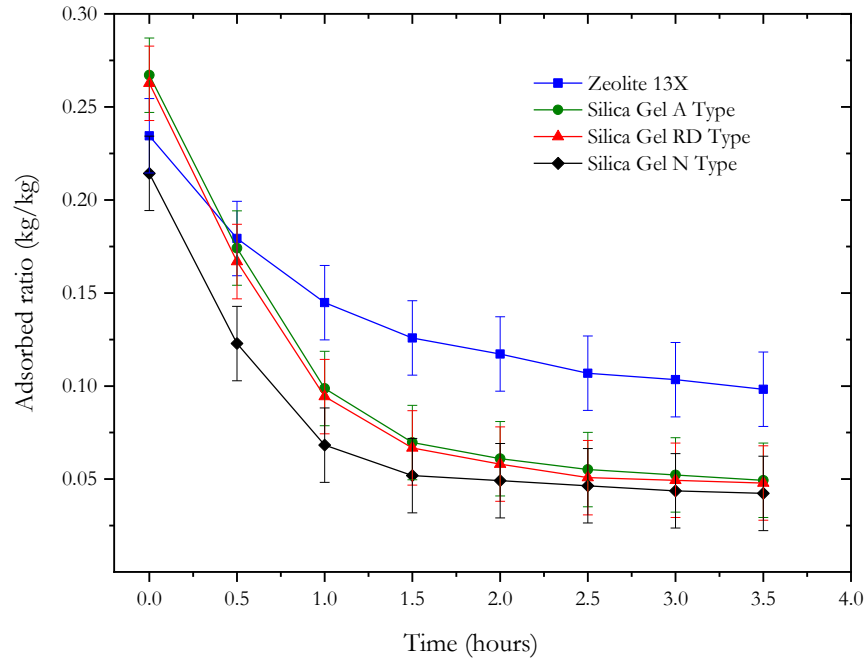
Figure 110. Desorption rate for different adsorbents (using the double small bed design)
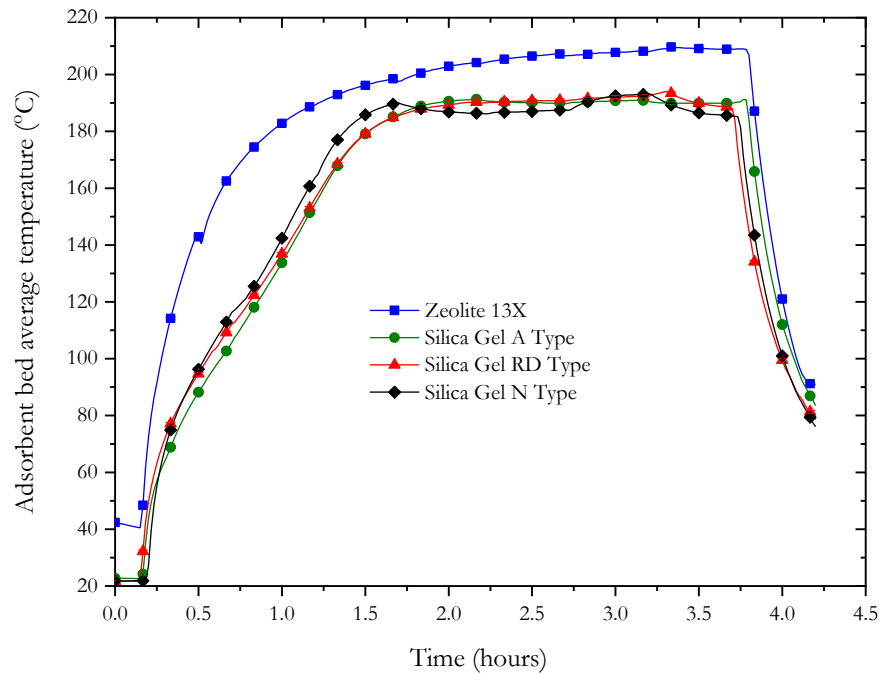
Figure 111. Adsorbent bed average temperature for different adsorbents (using the double small bed design) (the error bars are too small to be observed)

135

4.4.4.4.3.   Assessment of system performance

Based on the above results from Figure 104, Figure 108, and Figure 111, we can estimate the system performance of the evacuated tube adsorption heat pump module. Firstly, we assume, based on Figure 111, that Zeolite 13X can only be desorbed to 0.10 kg/kg while all silica gel types can be completely desorbed. Second, we assume, based on Figure 104, Figure 108, and Figure 111, that the cycle time is three hours even though it can be much less for zeolite. Lastly, we assume an average cooling capacity for each adsorbent. The solar coefficient of performance (COP$_{solar}$) can be calculated as follows:

$$COP_{solar} = \frac{\dot{Q}_{ref,exp}}{\dot{q}_{input} \cdot A_c} \tag{4.14}$$

Table 19 below shows the evacuated tube adsorption heat pump module performance for four different adsorbents. It can be seen that the heat pump performs best when Zeolite 13X or Silica gel Type-RD are used.

Table 19. Experimental evacuated tube adsorption heat pump module performance results

Adsorbent	Average cooling capacity, $\dot{Q}_{ref,exp}$ (W)	Heat flux, $\dot{q}_{input}$ (W/m^2)	Collector area A_c, (m^2)	COP_{solar}
Zeolite 13X	15	1700	0.06	0.15 ± 0.05
Silica gel Type-A	8	1000	0.06	0.13 ± 0.06
Silica gel Type-RD	10	1000	0.06	0.17 ± 0.06
Silica gel Type-N	6	1000	0.06	0.10 ± 0.06

4.5. Dynamic Simulation of the Evacuated Tube Adsorption Heat Pump System

Several studies on theoretical modeling of adsorption-based heat pump have been carried out [89-93]. Likewise, the evacuated tube solar collector has been mathematically modeled by many researchers [94-96]. In this section, a mathematical model based on a dynamic adsorption heat pump and evacuated tube solar collector was developed to simulate the transient behavior of the evacuated tube adsorption heat pump.

4.5.1. Physical Model

The physical model for the evacuated tube adsorption heat pump uses the following assumptions:

- The heat and mass transfer processes are transient (time-dependent).
- The mass transfer inside the adsorbent bed takes place only in the radial direction.
- The temperature gradients in the longitudinal and rotational directions are insignificant.
- Heat losses from the adsorbent bed to the surroundings are only in the radial direction and are negligible in the axial direction.
- Temperature, pressure, and concentration are uniform during each time interval.
- Adsorption and desorption processes run for the same time with zero switching time.
- The condenser and evaporator are characterized by their saturation temperatures T_c and T_e, respectively.
- Latent heat of condensation during the desorption occurs on the inner wall of the glass tube and not inside the condenser. Only sensible heat is rejected inside the condenser.

Similar to the experimental setup, the evacuated tube is a single-glass tube with a cylindrical adsorbent bed as illustrated in Figure 112.
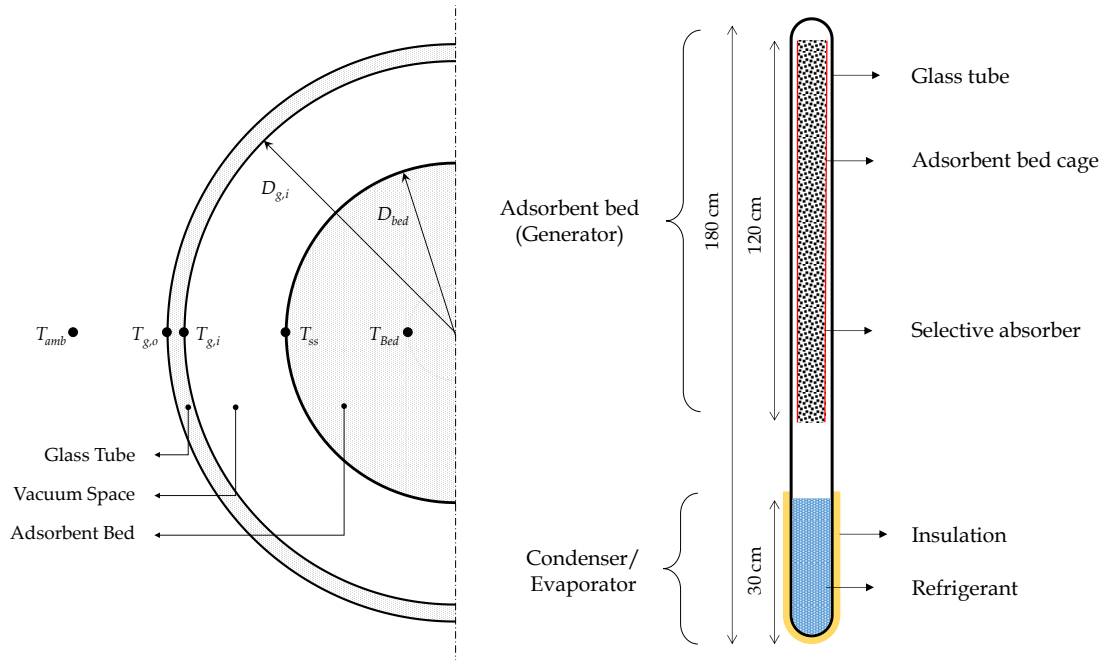
Figure 112. Physical Theoretical Model of the Evacuated Tube Adsorption Heat Pump
Module (left) Top view, (right) Side view

4.5.2.   Mathematical Description

In order to analyze the transient behavior of the evacuated tube adsorption heat pump, we used the
thermal network analysis due to its simplicity. Using the analogy between thermal and electrical
systems, the incident solar energy is distributed into useful energy, heat losses, and optical losses.
The thermal network (electrical analogy) of the evacuated tube adsorption heat pump is illustrated
in Figure 113 which is linked with Figure 112. Note that C and R represent the thermal capacitance
(heat storage) and resistance, respectively.
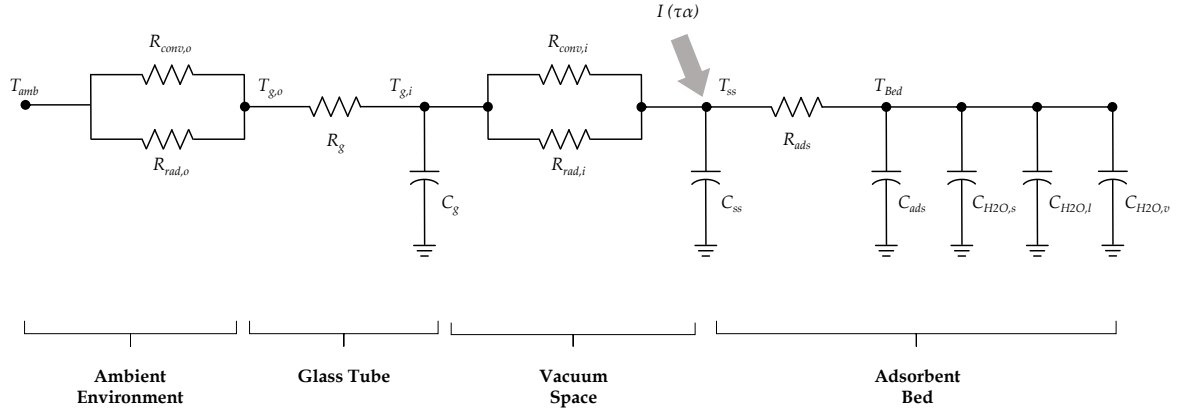
Figure 113. Electrical Analogy for the Evacuated Tube Adsorption Heat Pump Model

4.5.2.1.   Incident Solar Radiation and Optical Losses

In reference to Figure 113 and Figure 112, the incident solar radiation absorbed by the selective absorber per unit area (input heat flux) $\dot{q}_{input}$ can be calculated as follows:

$$\dot{q}_{input} = I \cdot (\tau\alpha) \tag{4.15}$$

where I is the incident solar radiation per unit area (W/m^2), and $(\tau\alpha)$ is the transmittance-absorptance product which represents the optical loss when solar radiation passes through the collector (glass tube).

The transmittance-absorptance product $(\tau\alpha)$ can be calculated in a collection of equations as extensively described by Duffie & Beckman [96]. Here, we are going to cover these equations broadly.

$$(\tau\alpha) \cong 1.01\,\tau \cdot \alpha \tag{4.16}$$

where τ is the transmittance of the cover (glass) system at the desired angle and α the angular absorptance of the absorber plate (selective absorber). The angular solar absorptance (α) can be calculated as follows:

$$\begin{aligned}
\frac{\alpha}{\alpha_n} = {}& 1 - 1.5879 \times 10^{-3}\,\theta_b + 2.7314 \times 10^{-4}\,\theta_b^2 - 2.3026 \times 10^{-5}\,\theta_b^3 + 9.0244 \\
& \times 10^{-7}\,\theta_b^4 - 1.8000 \times 10^{-8}\,\theta_b^5 + 1.7734 \times 10^{-10}\,\theta_b^6 - 6.9937 \\
& \times 10^{-13}\,\theta_b^7
\end{aligned} \tag{4.17}$$

139

where α_n is the solar absorptance at normal incidence. θ_b the angle of incidence of the radiation which is initially equal zero (perpendicular to the selective absorber).

On the other hand, the transmittance of the cover (glass) system at the desired angle (τ) can be calculated as follows:

$$\tau = \tau_{rN} \cdot \tau_{aN}$$

(4.18)

where τ_{rN} is the cover transmittance due to reflection (only reflection losses are considered) while τ_{aN} cover transmittance due to absorption (only absorption losses are considered). τ_{rN} and τ_{aN} can be calculated as follows:

$$\tau_{aN} = \exp(-N \cdot \frac{K \cdot L}{\cos \theta_2})$$

(4.19)

where N represents the number of glass covers (one cover in our case), K is extinction coefficient which is assumed to be constant in the solar spectrum and equal to 32 m^{-1} [96], L is the glass cover thickness in (m). θ_2 is the angle of reflection which can be calculated from Snell's law as follows:

$$n_1 \cdot \sin \theta_b = n_2 \cdot \sin \theta_2$$

(4.20)

where n_1 and n_2 are the refractive indices for air and glass, respectively, which are equal to 1 for air and 1.526 for glass.

$$\tau_{rN} = \frac{1}{2} \left(\frac{1 - r_\parallel}{1 + (2N - 1) r_\parallel} + \frac{1 - r_\perp}{1 + (2N - 1) r_\perp} \right)$$

(4.21)

where $r_\parallel$ and $r_\perp$ represent parallel and perpendicular component of unpolarized radiation (Fresnel coefficients), respectively, and can be calculated as follows:

$$r_\perp = \left[\frac{\sin(\theta_2 - \theta_b)}{\sin(\theta_2 + \theta_b)} \right]^2$$

(4.22)

$$r_\parallel = \left[\frac{\tan(\theta_2 - \theta_b)}{\tan(\theta_2 + \theta_b)} \right]^2$$

(4.23)

4.5.2.2. Thermal Losses to the Environment

In reference to the thermal network in Figure 113, thermal losses from the adsorbent bed to the ambient consider the convection and radiation through the vacuum space, conduction through the

glass tube, and convection and radiation through the ambient [96, 97]. Note that the heat losses through the vacuum space and glass tube, during the adsorption process, are desirable as it enhances the heat rejection process. Similarly, the heat losses through the glass tube during the desorption process is also needed as it improves the film condensation on the inner surface of the glass tube. In contrast, the heat losses through the vacuum space is rather kept as low as possible during the desorption process.

4.5.2.2.1.   Heat Loss through the Vacuum Space (Annulus)

The thermal losses through vacuum space by convection and radiation can be calculated using thermal resistance concept as follows:

$$\dot{Q}_{loss,total} = \dot{Q}_{conv,i} + \dot{Q}_{rad,i} = \frac{(T_{ss} - T_{g,i})}{R_{conv,i}} + \frac{(T_{ss} - T_{g,i})}{R_{rad,i}} \tag{4.25}$$

where $\dot{Q}$ is the thermal loss in (W) and R the thermal resistance. The subscript ss represents the stainless steel selective absorber, g, i the inner surface of the glass tube, $conv, i$ and rad, i are related to convection and radiation, respectively, associated with the area between selective absorber and glass tube. Thermal resistance by convection can be calculated as follows:

$$R_{conv,i} = \frac{\ln(D_{g,i}/D_{bed,o})}{2\pi \cdot k_{eff} \cdot L_{bed}} \tag{4.26}$$

where D is the diameter in (m), L_{bed} the length of the adsorbent bed in (m), k_{eff} the effective thermal conductivity in the annual (vacuum space) at low pressure in (W m^{-1}K^{-1}) which can be calculated from Ratzel et al. (1979) [98] as follows:

$$\frac{k_{eff}}{k} = \left[1 + \frac{9 \cdot c_p/c_v - 5}{c_p/c_v + 1} \cdot \frac{b \cdot \gamma}{\ln(D_{g,i}/D_{bed,o})} \left(\frac{1}{D_{g,i}} + \frac{1}{D_{bed,o}}\right)\right]^{-1} \tag{4.27}$$

where k is the thermal conductivity of the annulus gas in (W m^{-1}K^{-1}). Note that when $k = k_{eff}$, the free convection is suppressed and the heat transfer is by conduction. γ is the mean free path of the gas molecules given by [98]:

$$\gamma = \frac{K.T}{\sqrt{2}\pi.P\delta^2} \tag{4.28}$$

where K is Boltzmann's constant, P the pressure in (Pa), and δ the molecular diameter of the gas inside the annulus (3×10^{-10} m for air). It is worth noting that when pressure in the annulus is

141

reduced towards ultra-high vacuum, the heat transfer moves from free convection heat transfer to free molecular heat transfer.

Thermal resistance by radiation between the selective absorber and glass tube can be calculated as follows:

$$R_{rad,i} = \frac{\dfrac{1}{\varepsilon_{ss}} - \dfrac{1-\varepsilon_g}{\varepsilon_g} \cdot \dfrac{D_{bed}}{D_{g,i}}}{\pi \cdot D_{bed,o} \cdot L_{bed} \cdot \sigma \cdot \left(T_{ss} + T_{g,i}\right) \cdot \left(T_{ss}^{\;2} + T_{g,i}^{\;2}\right)} \tag{4.29}$$

where ε represents the emissivity of the selective absorber (ss) and glass tube (g).

4.5.2.2.2. Heat Loss through the Glass Tube

Thermal loss through the glass tube to the ambient is solely by conduction, and can be calculated using the thermal resistance concept as follows:

$$\dot{Q}_{loss,total} = \dot{Q}_{cond} = \frac{\left(T_{g,i} - T_{g,o}\right)}{R_{cond}} \tag{4.30}$$

$$R_{cond} = \frac{\ln(D_{g,o}/D_{g,i})}{2\pi \cdot k_g \cdot L_{bed}} \tag{4.31}$$

where subscripts g and g,o refer to the glass and outer surface of the glass, respectively.

4.5.2.2.3. Heat Loss to the Environment

Thermal losses from the glass tube to the environment considers heat transfer by convection and radiation which can be calculated as follows:

$$\dot{Q}_{loss,total} = \dot{Q}_{conv,o} + \dot{Q}_{rad,o} = \frac{\left(T_{g,o} - T_{amb}\right)}{R_{conv,o}} + \frac{\left(T_{g,o} - T_{sky}\right)}{R_{rad,o}} \tag{4.32}$$

Subscripts $conv,o$ and rad,o are related to convection and radiation, respectively, associated with the area between the glass tube and the environment.

Thermal resistance by convection of the outer surface of glass tube can be calculated as:

$$R_{conv,o} = \pi \cdot D_{g,o} \cdot h_o \cdot L_{bed} \tag{4.33}$$

Convection heat transfer coefficient of the outer glass of the tube (h_o) and its associated Nusselt and Reynolds numbers are calculated as given by Duffie & Beckman [96]:

$$h_o = \frac{k_a \cdot Nu}{D_{g,o}} \tag{4.34}$$

$$Nu = \begin{cases} 0.4 + 0.54 \cdot Re^{0.52}, & 0.1 < Re < 1000 \\ 0.3 \cdot Re^{0.6} & , \quad 1000 < Re < 50000 \end{cases} \tag{4.35}$$

$$Re = \frac{\rho_a \cdot V_a \cdot D_{g,o}}{\mu_a} \tag{4.36}$$

where k_a, ρ_a, V_a and μ_a are the thermal conductivity in (W/m-K), density (kg/m^3), wind speed in (m/s), and dynamic viscosity in (kg/m.s) for air.

Thermal resistance by radiation between the glass tube and the surroundings can be calculated as follows:

$$R_{rad,o} = \frac{1}{\varepsilon_g \cdot \pi \cdot D_{g,o} \cdot L_{bed} \cdot \sigma \cdot \left(T_{g,o} + T_{sky}\right) \cdot \left(T_{g,o}{}^2 + T_{sky}{}^2\right)} \tag{4.37}$$

where T_{sky} is the sky temperature in (K) and can be calculated as a function of ambient temperature T_{amb} in (K) and dew-point temperature T_{dp} in (°C) as follows [96]:

$$T_{sky} = T_a \cdot \left[0.711 + 0.0056 \cdot T_{dp} + 0.000073 \cdot T_{dp}{}^2 + 0.013 \cdot \cos(15 \cdot t)\right]^{1/4} \tag{4.38}$$

where t is the hour from midnight.

4.5.2.3.   Conservation of Energy

The energy conservation equation of the evacuated tube adsorption heat pump can generally be written as follows:

$$\text{Heat Input} \left(\dot{q}_{\text{input}} \cdot A_c\right) = \text{Useful heat input} \left(\dot{Q}_{\text{useful}}\right) - \text{Total heat loss} \left(\dot{Q}_{\text{loss,total}}\right) \tag{4.39}$$

In the previous two sections, we have determined both the total heat input and total heat loss. In this section, we will analyze the transient behavior of the evacuated tube adsorption heat pump based on thermal network analysis in Figure 113 (for the sake of convenience, Figure 112 and Figure 113 are shown below).
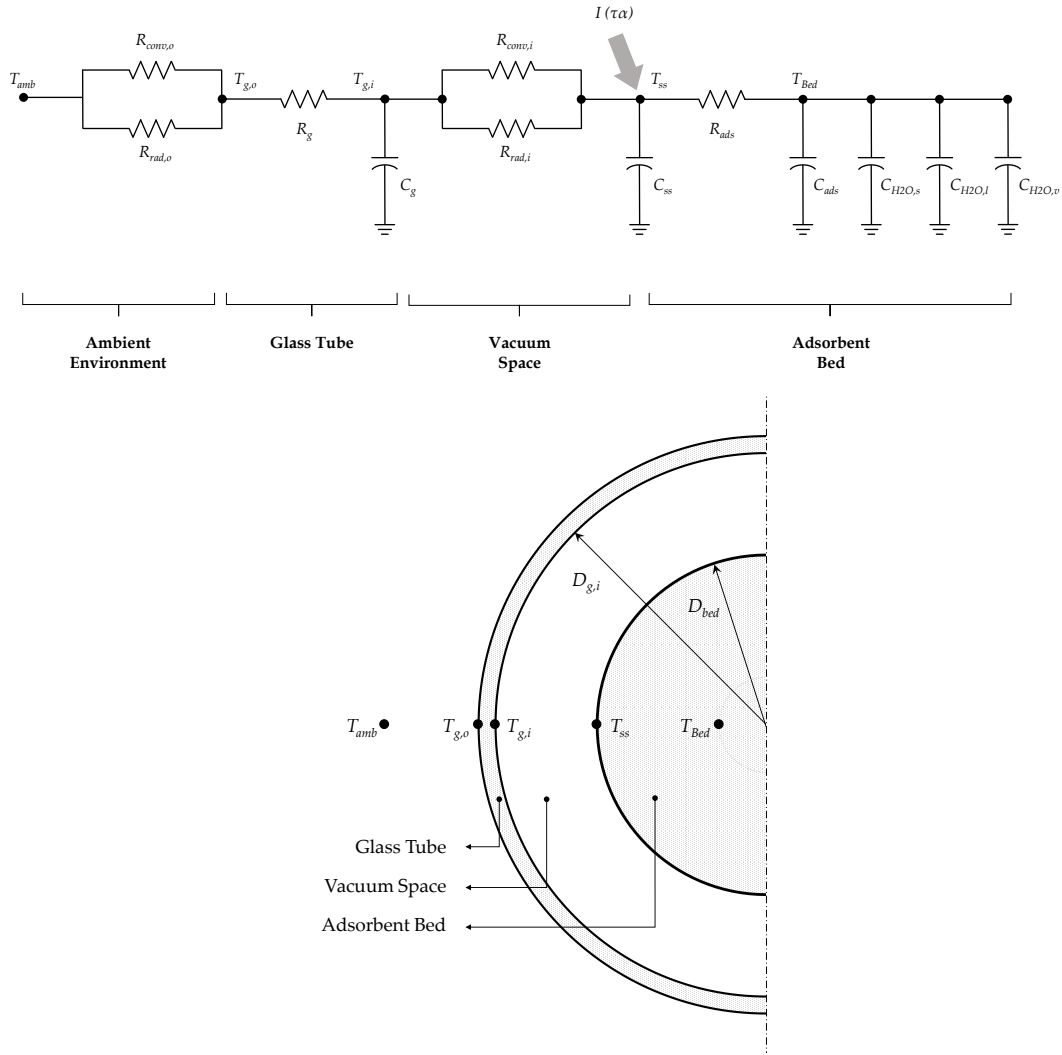
Figure 114. Electrical Analogy for the Evacuated Tube Adsorption Heat Pump Model (same as Figure 112 and Figure 113)

- *Energy balance at node (T_{ss})*

$$\dot{Q}_{useful} = m_{ss} \cdot C_{ss} \cdot \frac{dT_{ss}}{dt} + \frac{T_{ss} - T_{Bed}}{R_{ads}} \tag{4.40}$$

where m and C are the mass and specific heat of the stainless steel adsorbent bed in (kg) and (kJ/kg-K), respectively. R_{ads} is the thermal resistance between the stainless steel adsorbent bed and the adsorbent which can be calculated as follows:

$$R_{ads} = \frac{\ln(D_{ss}/D_{bed,x})}{2\pi \cdot k_{ads} \cdot L_{bed}} \tag{4.41}$$

where k_{ads} represents the thermal conductivity of the adsorbent, and $D_{bed,x}$ refers to the distance between the stainless steel adsorbent bed and the adsorbent. Note that the $D_{bed,x}$ is an imaginary circle that represents the average temperature of the total adsorbent bed in the radial direction.

- *Energy balance at node* (T_{Bed})

$$\frac{T_{ss} - T_{bed}}{R_{ads}} = m_{ad} \cdot C_{ad} \cdot \frac{dT_{Bed}}{dt} + m_{ad} \cdot q \cdot C_{H2O,s} \cdot \frac{dT_{Bed}}{dt} - m_{ads} \cdot H_{ads} \cdot \frac{dq}{dt}$$
$$+ (1 - \delta) \cdot m_{ads} \cdot C_{H2O,v} \cdot (T_e - T_{Bed}) \cdot \frac{dq}{dt} \tag{4.42}$$

$$\delta = \begin{cases} 1, & desorption\ process \\ 0, & adsorption\ process \end{cases} \tag{4.43}$$

where q, H_{ads}, and T_e are the absolute amount adsorbed, heat of adsorption, and evaporator temperature, respectively. Note that the first term of the R.H.S represents the sensible heat of the adsorbent, the second term represents the sensible heat of the adsorbate (refrigerant), the third term represents the latent heat of the adsorbate (refrigerant), and the fourth term represents the sensible heat of saturation water vapor. It is worth noting that the T_{bed} node means a particular axial location within the bed and not the entire bed.

- *Energy balance at node* ($T_{g,i}$)

Due to the importance of the glass tube temperature for the heat loss and condensation process, we consider in this section the transient temperature of the glass tube. The energy balance equation at node $T_{g,i}$ can be written as follows:

$$\dot{Q}_{loss,total} + I \cdot (1 - \tau_{aN}) = m_g \cdot C_g \cdot \frac{dT_{g,i}}{dt} + \frac{T_{g,i} - T_{g,o}}{R_g} \tag{4.44}$$

where the second term of the L.H.S. represents the amount of the incident solar radiation absorbed by the glass tube and can be calculated as shown in equation (4.19) above.

- *Heat transfer of film condensation*

The heat transfer of film condensation inside an inclined tube during the desorption process is given for low vapor velocities by [97, 99]:

$$Q_{con} = h_{con}A_c\left(T_{sat} - T_{g,i}\right) \tag{4.45}$$

$$h_{con} = 0.555\left[\frac{g \cdot \cos\theta \cdot \rho_l\,(\rho_l - \rho_v) \cdot k_l^3}{\mu_l \cdot \left(T_{sat} - T_{g,i}\right) \cdot D_{g,i}} \cdot \left(h_{fg} + \frac{3}{8} \cdot c_{p,l}\left(T_{sat} - T_{g,i}\right)\right)\right]^{1/4} \tag{4.46}$$

where θ is the collector inclination angle, ρ is the density in (kg/m3), and subscripts l and v stands for liquid and vapor, respectively.

4.5.2.4. Mass Conservation (Adsorption Equilibrium)

In the present analysis, the Toth isotherm equation [100, 101], which is based on an empirical model and developed to improve the Langmuir and Freundlich isotherm models [102-106], is used to model the adsorption equilibrium. Unlike other adsorption equilibrium models, the Toth model is relatively simple and effectively describes various heterogeneous adsorption systems at low and high pressures:

$$q = q^{\infty} \cdot \frac{K \cdot P}{[1 + (K \cdot P)^n]^{1/n}} \tag{4.47}$$

$$K = K^{\infty} \cdot \exp\left[\frac{-\Delta H}{R \cdot T_{Bed}}\right] \tag{4.48}$$

where q and q^{∞} are the absolute amount adsorbed and the limiting (maximum) amount adsorbed of the refrigerant (adsorbate) in (kg of adsorbate per kg of adsorbent), and P is the equilibrium pressure in (kPa) which equals the saturation pressure at condenser and evaporator temperatures during the desorption and adsorption process, respectively. K^{∞} is the infinite adsorption constant, ΔH is the isosteric heat of adsorption at zero loading, and n is the heterogeneity parameter and can be calculated from the heterogeneity coefficients a and b related to the thermal variation as follows:

$$n = a + b \cdot T_{Bed} \tag{4.49}$$

The above coefficient values are listed in Table 20 for Zeolite13X–H_2O and Silica Gel RD–H_2O.

Table 20. Toth Equation Parameters for Different Systems [100, 101]

	q^∞	K^∞	$-\Delta H$	a	b
	$kg. kg^{-1}$	kPa^{-1}	$kJ. kmol^{-1}$	$-$	K^{-1}
Zeolite13X–H_2O	0.2719	1577	56.97	0.3974	0.00004569
Silica Gel RD–H_2O	114220	0.001026	9.088	-0.00119	0.0002408

4.5.2.5.   System Performance Parameters

For our proposed evacuated tube adsorption heat pump module, the cooling capacity and coefficient of performance (COP) are considered to evaluate the overall module performance. The cooling capacity can be simply calculated as follows:

$$\dot{Q}_{ref} = \dot{m}_{ref} \cdot (h_v - h_f)$$ (4.50)

where h_v and h_f are the specific enthalpy of vapor at the evaporator temperature and liquid at the condenser temperature, respectively. $\dot{m}_{ref}$ represents the mass flow rate of the refrigerant (adsorbate) and can be calculated as follows:

$$\dot{m}_{ref} = \frac{m_{ads} \cdot (q_{conc} - q_{dil})}{t_{cycle}}$$ (4.51)

where q_{conc} is the amount adsorbed (adsorbed ratio) at the end of the adsorption process, q_{dil} is the adsorbed ratio at the end of the desorption process, and t_{cycle} is the cycle time.

Coefficient of performance (COP) of the system can simply be defined as the ratio of cooling capacity to the heat input. However, the heat input can arguably be defined in two different ways as illustrated in Figure 115. It can be clearly seen from Figure 115 that the total heat input is depicted as a straight line during the desorption process (area under the red line represents the total heat input (solar radiation)). As time goes on, the useful heat (area under the blue curve) starts significantly decreasing while the heat loss increases up to the point where heat input is completely useless and no more refrigerant can be desorbed.
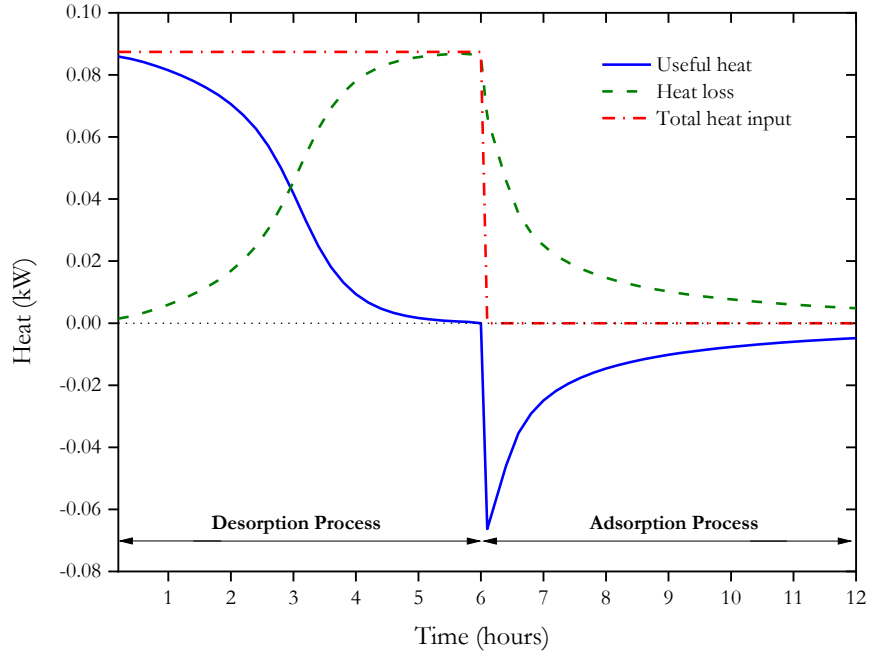
Figure 115. Heat flow for a typical adsorption heat pump system

Accordingly, the coefficient of performance (COP) can be defined with respect to the useful heat input ($\dot{Q}_{useful}$) and can be calculated as follows:

$$COP = \frac{\dot{Q}_{ref}}{\dot{Q}_{useful}} \tag{4.52}$$

$$\dot{Q}_{useful} = \dot{m}_{ref} \cdot H_{ads} + \left[\frac{m_{ss} \cdot C_{ss} + m_{ad} \cdot C_{ad} + m_{ad} \cdot q_{conc} \cdot C_{H2O,s}}{\frac{t_{cycle}}{2}} \right] \times \left(T_{Bed,f} - T_{Bed,i} \right) \tag{4.53}$$

where $T_{Bed,i}$ and $T_{Bed,f}$ are the adsorbent bed temperature at the end of the adsorption process and the adsorbent bed temperature at the end of the desorption process.

Additionally, the coefficient of performance (COP) can be defined based on the total heat input ($\dot{q}_{input}$) as follows:

$$COP_{solar} = \frac{\dot{Q}_{ref}}{\dot{q}_{input} \cdot A_c} \tag{4.54}$$

Note that we will be using the latter definition of the COP for the rest of this chapter (not COP_{solar}), however, COP_{solar} can be easily calculated from the results of the cooling capacity since COP_{solar} changes linearly with the cooling capacity based on equation (4.54).

4.5.2.6. Assumptions and Initial Conditions

The detailed assumptions and initial conditions of the theoretical model of the evacuated tube adsorption heat pump module are summarized in Table 21.

Table 21. Assumptions and initial conditions of the theoretical model of the evacuated tube adsorption heat pump model

Single-glass Tube	
Glass outer diameter ($D_{g,o}$)	55 mm
Glass inner diameter ($D_{g,i}$)	51.2 mm
Length (L_{glass})	1.8 m
Emissivity of glass (ε_{glass})	88 %
Thermal conductivity of glass	1.4 W/m-K
Specific heat of glass	0.835 kJ/kg-K
Density of glass	2225 kg/m^3
Adsorbent Bed	
Outer diameter ($D_{bed,o}$)	35 mm
Inner diameter ($D_{bed,i}$)	33 mm
Length (L_{bed})	1.2 m
Emissivity (ε_{bed})	20 %
Absorptivity (α_{bed})	95%
Specific heat of stainless steel	0.460 kJ/kg-K
Density of stainless steel	7700 kg/m^3
Adsorbent	Zeolite 13X, Silica gel RD
Specific heat – Zeolite 13X	0.795 kJ/kg-K

Heat of adsorption – Zeolite 13X	3852 kJ/kg
Thermal conductivity – Zeolite 13X	0.13 W/m-K
Density (including air gaps) – Zeolite 13X*	585.3 kg/m^3
Specific heat – Silica gel type-RD	0.920 kJ/kg-K
Heat of adsorption – Silica gel type-RD	2800 kJ/kg
Thermal conductivity – Silica gel type-RD	0.15 W/m-K
Density (including air gaps) – Silica gel type-RD*	644.2 kg/m^3
Adsorbate (Refrigerant)	H_2O
Specific heat of liquid water	4.18 kJ/kg-K
Specific heat of water vapor	1.866 kJ/kg-K
Additional Parameters	
Ambient temperature (T_{amb})	30 ºC
Air speed (V_a)	0.1 m/s
Evaporator temperature (T_{eva})	5 ºC
Condenser temperature (T_{cond})	30 ºC
Cycle Parameters	
Heat flux ($\dot{q}_{input}$)	1000 W/m^2
Cycle time (t_{cycle})	6 hours for Silica gel 3 hours for Zeolite

* It was measured in the laboratory

4.5.2.7. Model Validation

The simulation model was developed using the Python programming language (Python Software Foundation[‡]). The correlations of the water, steam, and air properties, provided by CoolProp[§], were used in this study. The dynamic mathematical model was validated with our experimental data

---

[‡] https://www.python.org/
[§] www.coolprop.org/

under the same reference conditions. Figure 116 to Figure 118 show that the obtained results were within ±5% for both silica gel RD type and Zeolite 13X.
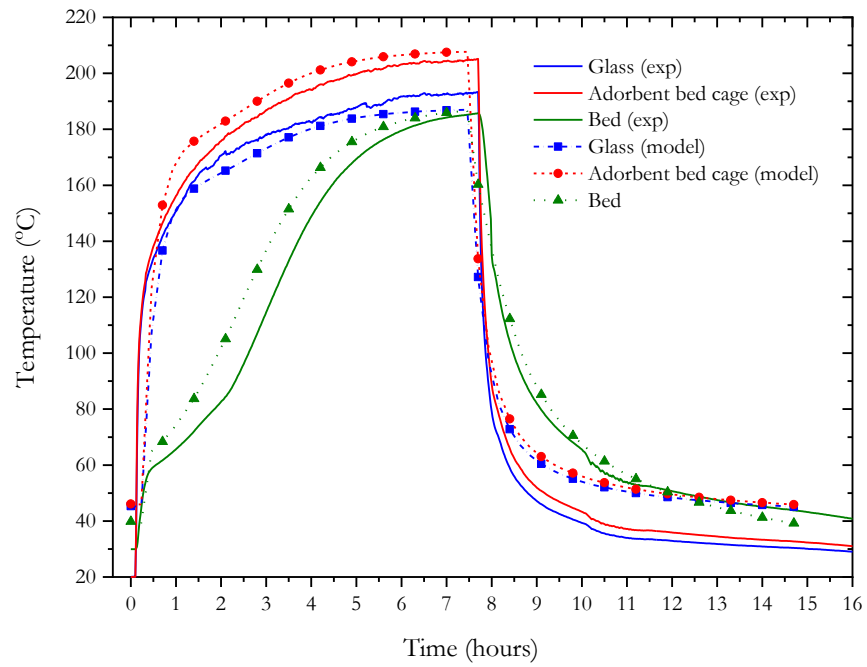
Figure 116. Comparison of the adsorbent bed temperatures of the mathematical model with the experimental results for Silica Gel (RD type)
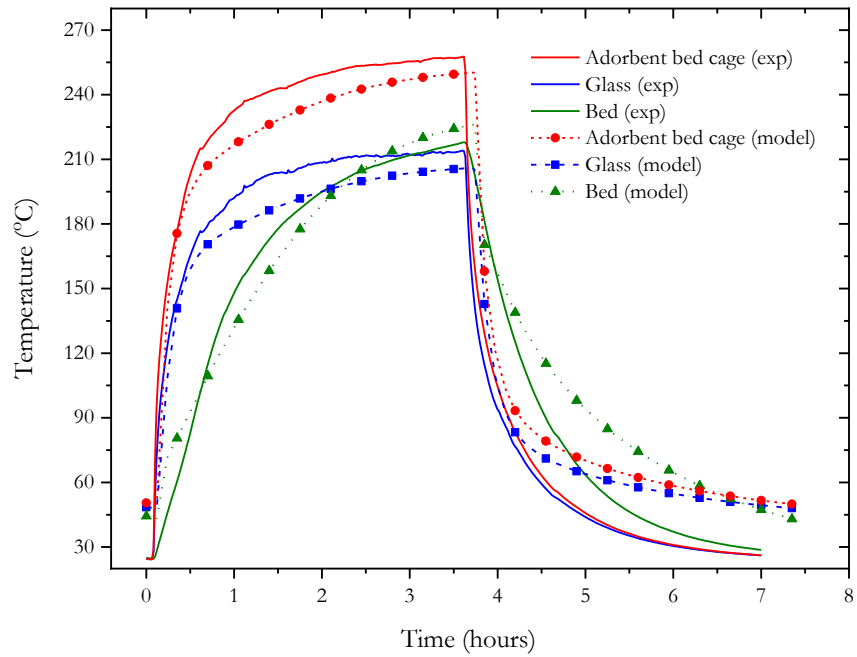
Figure 117. comparison of the adsorbent bed temperatures of the mathematical model with the experimental results for Zeolite 13X
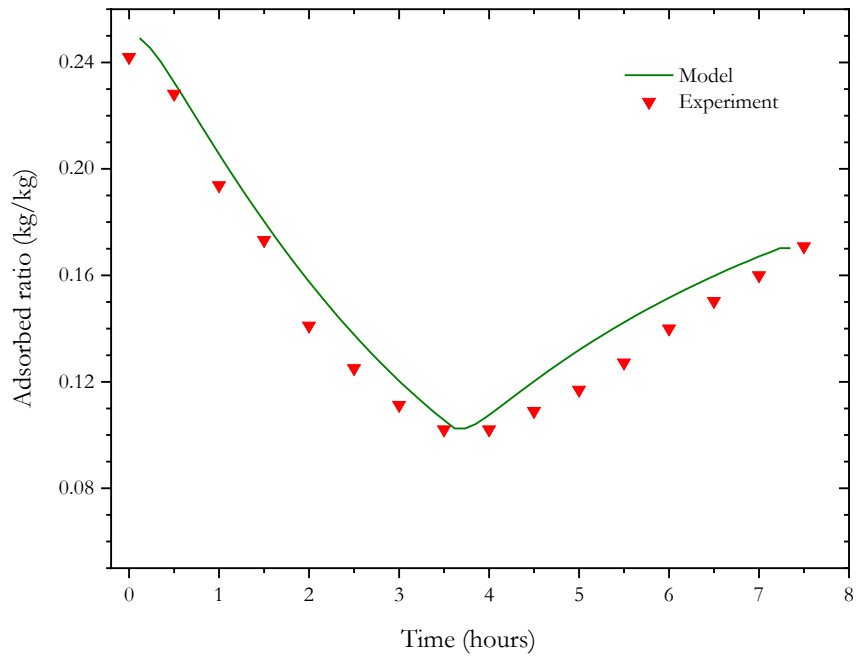
Figure 118. Comparison of the adsorbed ratio of the mathematical model with the experimental results for Zeolite 13X

4.5.3. Simulation Results and Discussion

Figure 119 to Figure 132 show, for the evacuated tube adsorption heat pump, the influence of input parameters such as the input solar radiation (heat flux, $\dot{q}$), adsorbent bed diameter (D_{bed}), glass tube diameter (D_{glass}), adsorbent bed cage (absorber) emissivity (ε_{ss}), cycle time for both adsorption and desorption processes (t_{cycle}), wind speed (air speed around the tube) (V_a), and ambient temperature (T_{amb}) for both Silica gel and Zeolite. The average cooling capacity and coefficient of performance are considered to evaluate the evacuated tube adsorption heat pump system productivity, while the adsorbed ratio-adsorbent bed average temperature diagram is plotted to illustrate the cycle performance.

4.5.3.1. Sensitivity to the heat flux (solar radiation, $\dot{q}$)

Figure 119 and Figure 120 display the effect of the heat flux (solar radiation) on the adsorbed ratio, adsorbent bed average temperature, cooling capacity, and coefficient of performance for silica gel and zeolite, respectively. It can be observed from both Figure 119a and Figure 120a that as the heat flux increases, the adsorbent ratio (during the desorption process) becomes lower (i.e., improves) due to the increase in the average temperature of the adsorbent bed. Clearly, at about 160 °C adsorbent bed temperature, the silica gel is almost dry, on the other hand, zeolite still requires higher temperature to reach dryness (over 300 °C). Even though the cycle time of the silica gel system is twice the cycle time of zeolite, the rate of adsorption of the silica gel is poor compared to zeolite. This can clearly be seen at the end of the adsorption process for zeolite in which the cycle associated with 1300 W/m² was able to catch and make an equal gap between the other two cycles (700 and 1000 W/m²). Therefore, zeolite is a better choice if the evacuated tube heat pump model is to be absorbed/desorbed multiple times during the day. Figure 119b and Figure 120b demonstrate that the COP peaks at about 600 W/m² for silica gel and at about 1600 W/m² for zeolite. In other words, adding excessive heat flux will desorb the silica gel system completely before starting to waste additional heat input. For this reason, the cooling capacity starts decreasing as heat flux increases since there is no additional desorption. Unlike silica gel, zeolite COP is almost flat as the heat flux increases because it continues generating a cooling affect even after passing the peak point since more refrigerant is desorbed.
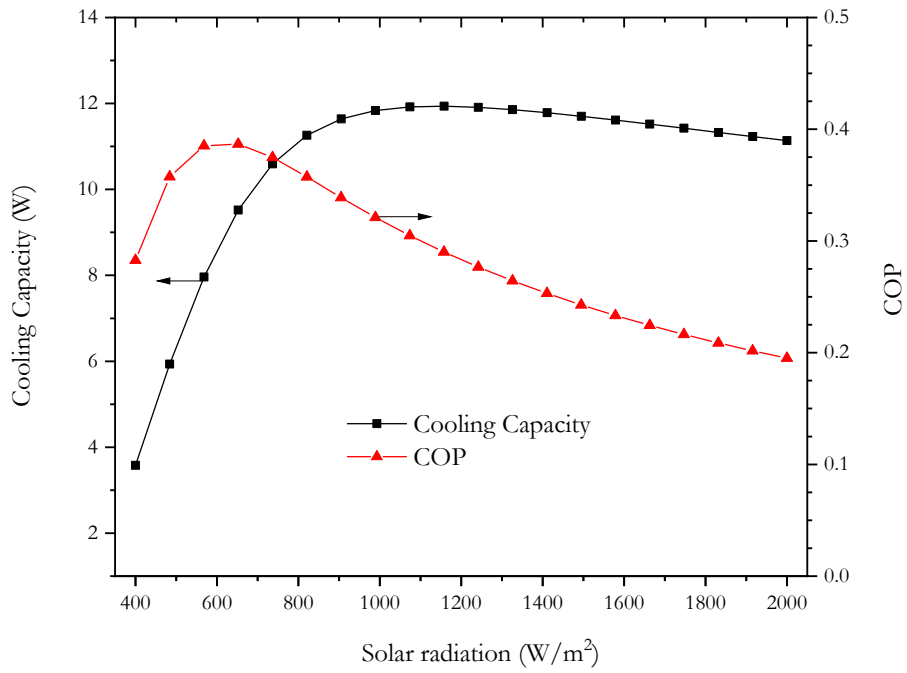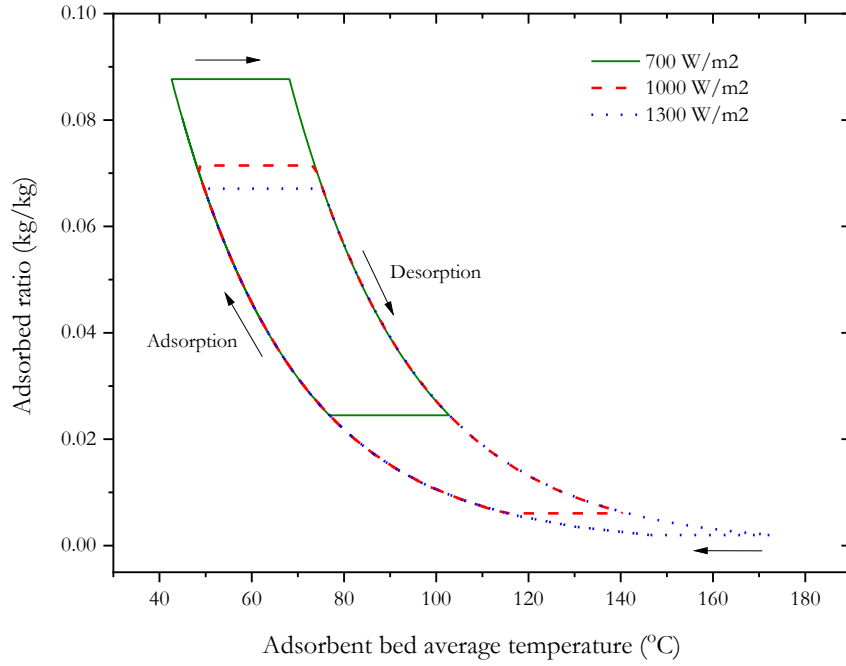
Figure 119. Effect of the heat flux (solar radiation, $\dot{q}$) on (a) adsorbed ratio with respect to the average temperature of the adsorbent bed (b) cooling capacity and COP (Silica gel RD type)

Figure 120. Effect of the heat flux (solar radiation, $\dot{q}$) on (a) adsorbed ratio with respect to the average temperature of the adsorbent bed (b) cooling capacity and COP (Zeolite 13X)

4.5.3.2. Sensitivity to the adsorbent bed diameter (D_{bed})

Similarly, Figure 121 and Figure 122 depict the effect of the adsorbent bed diameter on the adsorbed ratio, adsorbent bed temperature, cooling capacity, and COP for both silica gel RD type and zeolite 13X. It is extremely important to point out that as the adsorbent bed diameter decreases, the adsorbent mass (and adsorbate/adsorbent ratio) inside the adsorbent bed decreases and vice versa. For this reason, it can be observed from Figure 121a and Figure 122a that as the adsorbent bed diameter decreases (adsorbent mass decreases), the temperature of the adsorbent bed increases as a result of decreasing the radius between the selective absorber and center of the adsorbent bed. However, decreasing the adsorbent bed diameter leads to minimizing the amount of refrigerant that can be absorbed. A trade-off between achieving higher average adsorbent bed temperature and high absorbed refrigerant (cooling capacity) leads to an optimal COP and cooling capacity for both silica gel and zeolite as shown in Figure 121b and Figure 122b.

Figure 121. Effect of the adsorbent bed diameter (D_{bed}) on (a) adsorbed ratio with respect to the average temperature of the adsorbent bed (b) cooling capacity and COP (Silica gel RD type)

Figure 122. Effect of the adsorbent bed diameter (D_{bed}) on (a) adsorbed ratio with respect to the average temperature of the adsorbent bed (b) cooling capacity and COP (Zeolite 13X)

Sensitivity to the glass tube diameter (D_{glass})

Figure 123 and Figure 124 show the effect of the glass tube diameter on the adsorbed ratio, adsorbent bed temperature, cooling capacity, and COP for both silica gel RD type and zeolite 13X. Unlike adsorbent bed diameter, varying the glass tube diameter does not change the adsorbent mass inside the adsorbent bed. Instead, the glass tube diameter plays an important role in increasing/decreasing the heat loss associated with radiation and convection from the glass wall to the environment during both desorption and adsorption processes. It also decreases/increases the convective heat transfer coefficient between the selective absorber and inner wall of glass tube. It can be observed from Figure 123a and Figure 124a that as the glass tube diameter increases the convective heat transfer coefficient between the selective absorber and inner wall of glass tube decreases during desorption process allowing adsorbent bed temperature to reach high temperature (low adsorbent ratio). Nevertheless, this additional heat becomes excessive resulting in undesirable thermal resistance during the adsorption process as shown in Figure 123b. For that reason, an optimal COP exists for silica gel RD type. Unlike silica gel, the COP of the zeolite 13X system does not peak (at least not in Figure 124b) because the heat flux in this case is relatively low (1000 W/m^2), thus, achieving high temperature by increasing the glass tube diameter is desirable. A similar graph to Figure 123b can be obtained for zeolite when the heat flux is around 1600 W/m^2.

Figure 123. Effect of the glass tube diameter (D_{glass}) on (a) adsorbed ratio with respect to the average temperature of the adsorbent bed (b) cooling capacity and COP (Silica gel RD type)

Figure 124. Effect of the adsorbent bed diameter (D_{glass}) on (a) adsorbed ratio with respect to the average temperature of the adsorbent bed (b) cooling capacity and COP (Zeolite 13X)

4.5.3.4.   Sensitivity to the adsorbent bed cage (absorber) emissivity (ε_{ss})

Figure 125 and Figure 126 show the effect of the adsorbent bed cage (selective absorber) on the adsorbed ratio, adsorbent bed temperature, cooling capacity, and COP for both silica gel RD type and zeolite 13X. Similar to the previous sections, increasing the adsorbent bed temperature is always advantageous during the desorption process (as long as the adsorbent has not reached dryness). On the other hand, heat rejection is desirable during the adsorption process to cool down the adsorbent bed. In this case, low emissivity selective absorber allows the evacuated tube adsorption heat pump to reach high temperature and consequently lower adsorbent ratio. As one may expect, there is an optimal operating point to achieve maximum cooling capacity when silica gel is used. Nonetheless, the variation of the cooling capacity is minor which can be illustrated clearly in Figure 125a where the enclosed cycle is identical. The increase of COP with the selective absorber emissivity reflects the important role of heat rejection during the adsorption process. Figure 126b shows that at this stage, minimizing any heat loss during the desorption process for zeolite is still vital to the system performance. As heat flux increases, zeolite starts behaving like silica gel.
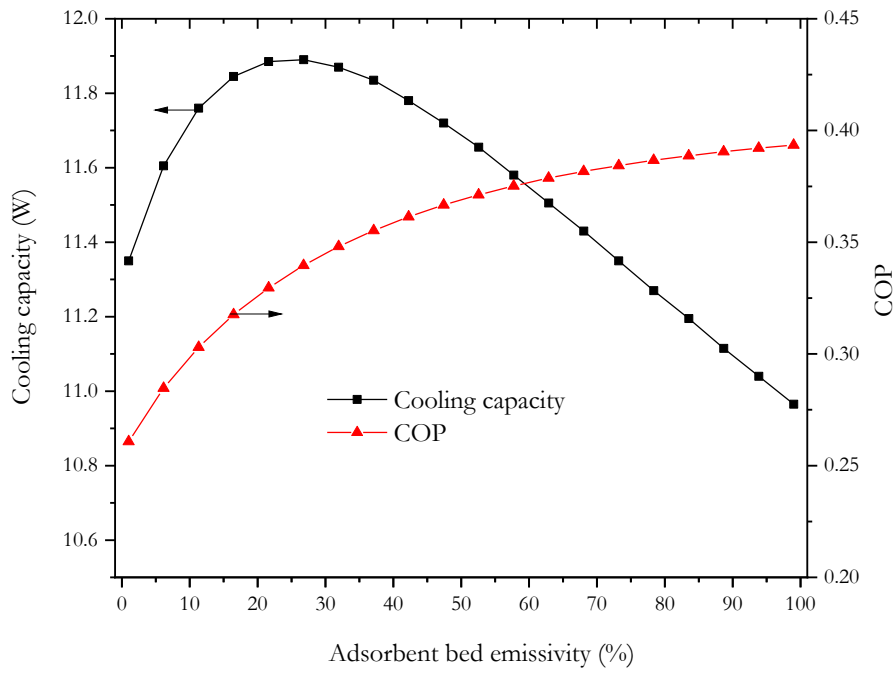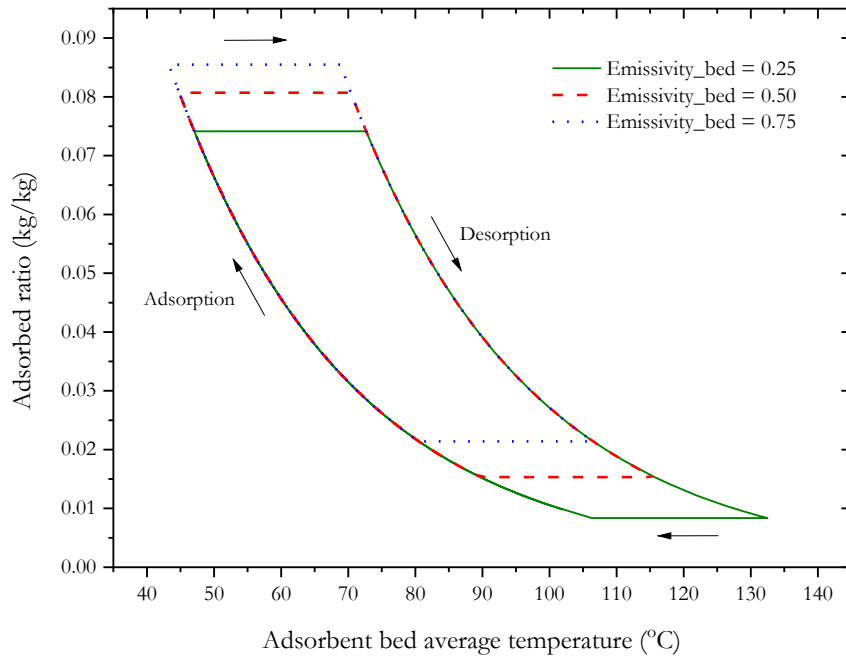
Figure 125. Effect of the adsorbent bed cage emissivity (ε_{ss}) on (a) adsorbed ratio with respect to the average temperature of the adsorbent bed (b) cooling capacity and COP (Silica gel RD type)
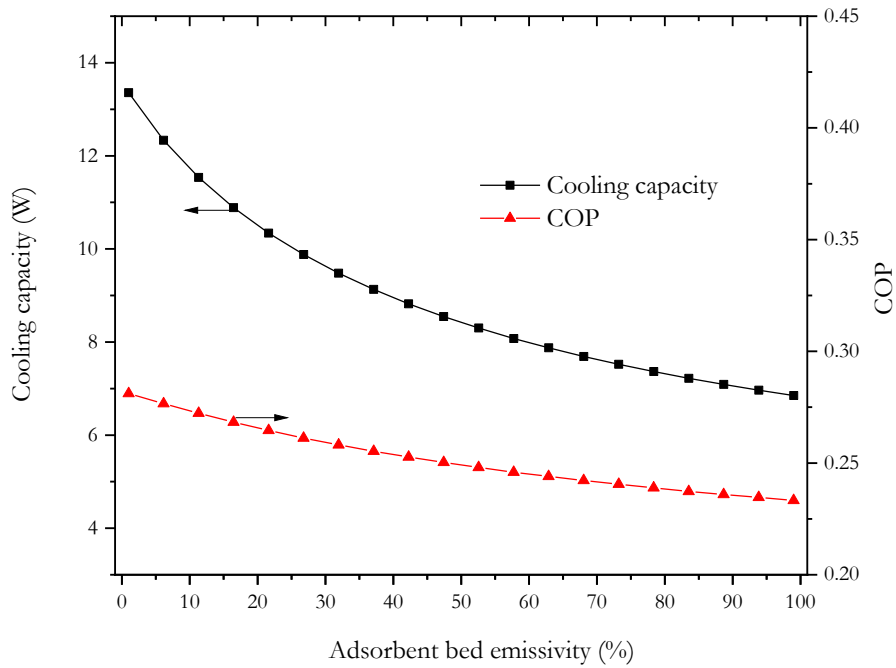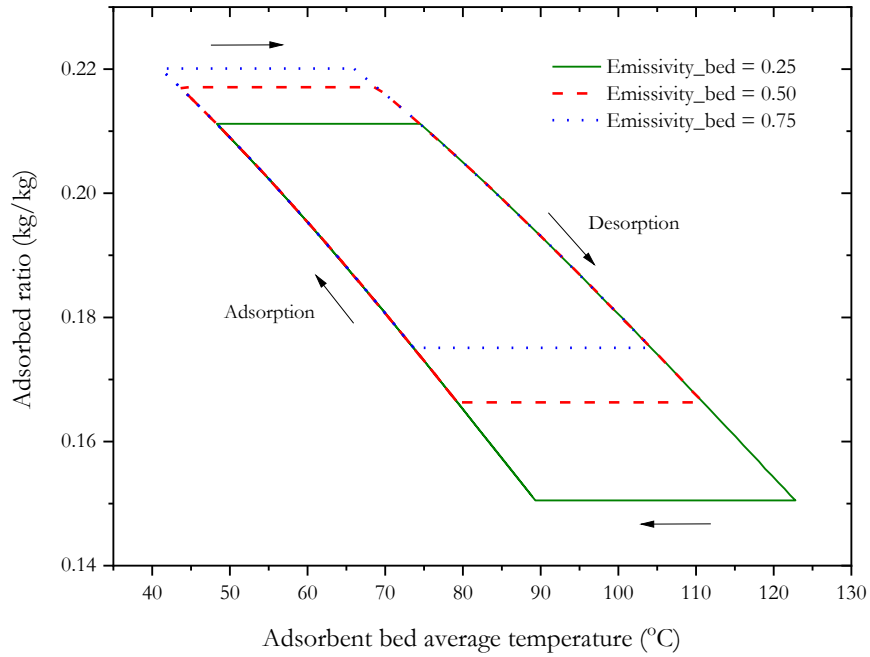
Figure 126. Effect of the adsorbent bed cage emissivity (ε_{ss}) on (a) adsorbed ratio with respect to the average temperature of the adsorbent bed (b) cooling capacity and COP (Zeolite 13X)

4.5.3.5. Sensitivity to the air speed around the glass tube (V_a)

Figure 127 and Figure 128 show the effect of the air speed around the glass tube on the adsorbed ratio, adsorbent bed temperature, cooling capacity, and COP for both silica gel RD type and zeolite 13X. Based on equation (4.36), the air velocity plays apart in the calculation of the heat transfer coefficient between the outer surface of the glass tube and the environment. In other words, when wind speed is very low, convective heat transfer coefficient can be modeled as a natural convection, while can be treated as a forced convection when wind speed increases (note that average wind speed on a typical day is about 5 m/s). Similar to previous cases, Figure 127 shows clearly that high adsorbent bed temperature can be achieved when wind speed is negligible. It can also be observed that high wind speed helps the system to cool down resulting in increasing its ability to adsorb as illustrated by reaching an optima cooling capacity at about 1 m/s for silica gel. Minimizing heat loss by Zeolite (increasing heat input) still at this phase very important as both COP and cooling capacity decrease dramatically.
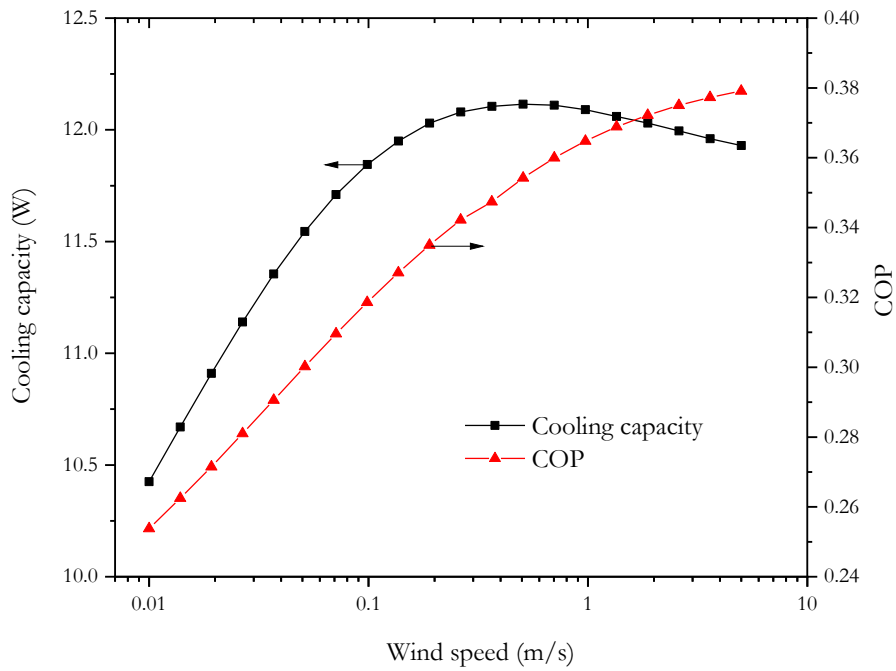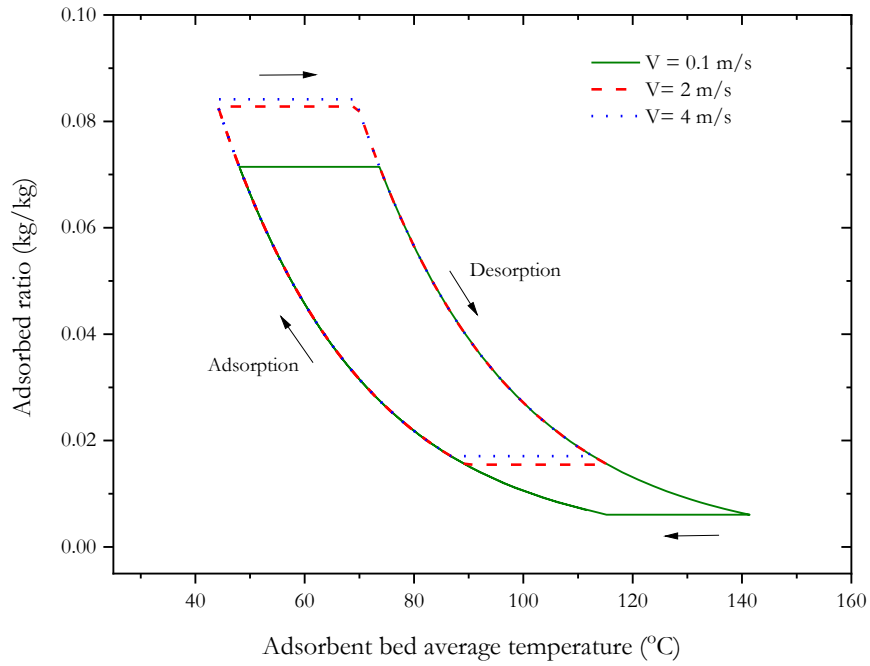
Figure 127. Effect of the air speed around glass tube (V_a) on (a) adsorbed ratio with respect to the average temperature of the adsorbent bed (b) cooling capacity and COP (Silica gel RD type)
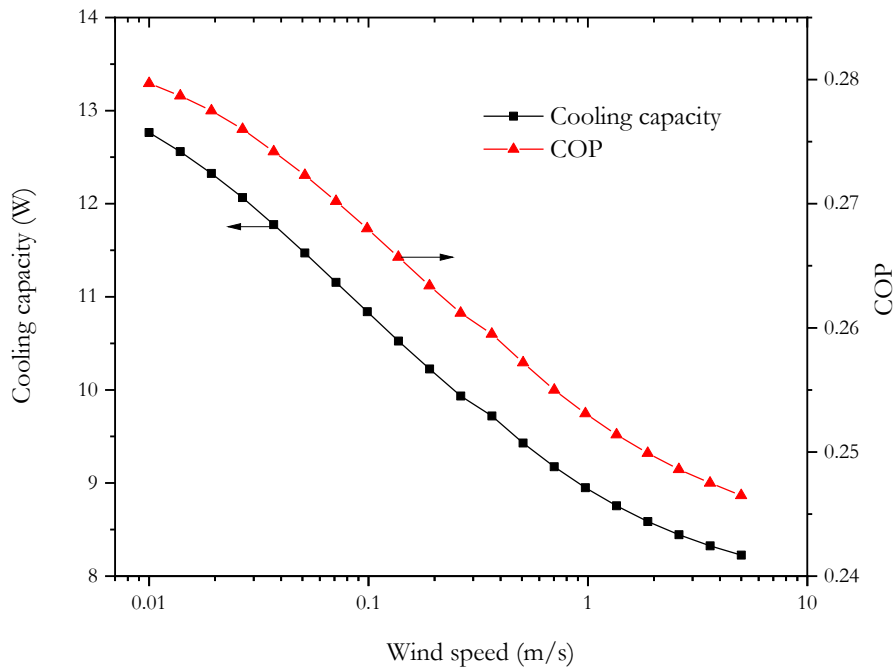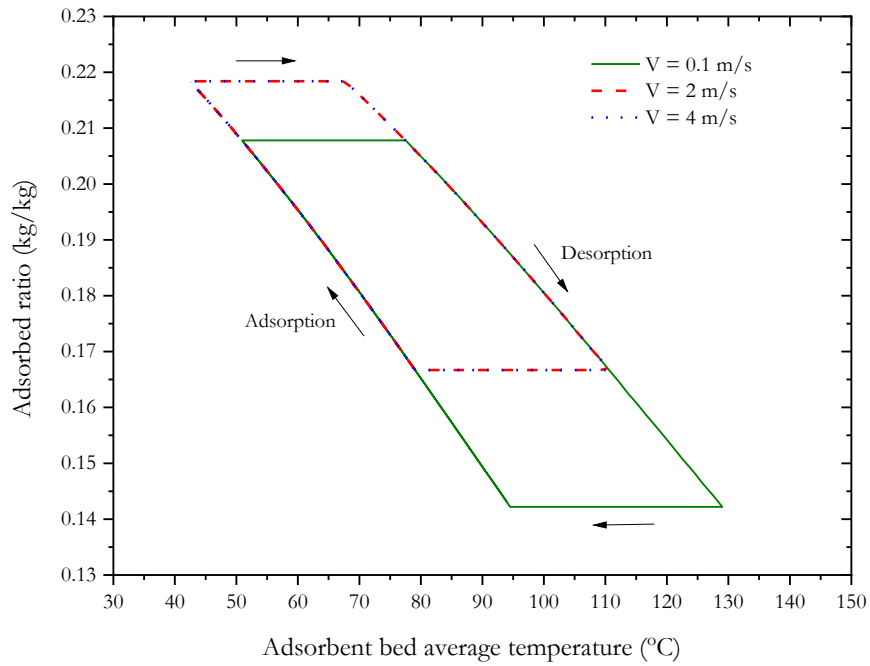
Figure 128. Effect of the air speed around glass tube (V_a) on (a) adsorbed ratio with respect to the average temperature of the adsorbent bed (b) cooling capacity and COP (Zeolite 13X)

4.5.3.6.   Sensitivity to the ambient temperature (T_{amb})

There is no better way to demonstrate the importance of cooling the adsorbent bed during the adsorption process than ambient temperature. Figure 129 and Figure 130 show the effect of the ambient temperature on the adsorbed ratio, adsorbent bed temperature, cooling capacity, and COP for both silica gel RD type and zeolite 13X. It can be seen from Figure 129a the huge difference in the adsorbed ratio during the adsorption process compared with desorption process as the ambient temperature increases for the silica gel based system. The COP and cooling capacity fall significantly as the ambient temperature increases as shown in Figure 129b. Interestingly, zeolite does not dramatically lose its ability as the ambient temperature varies as shown in Figure 130. This advantage may give the zeolite the upper hand over silica gel since cooling is mostly desirable when ambient temperature is high.
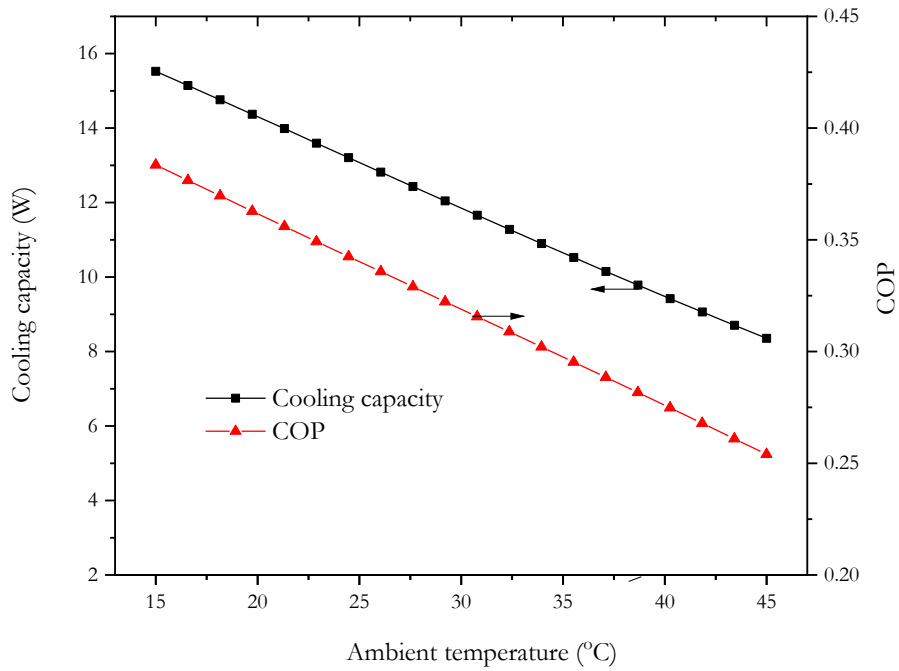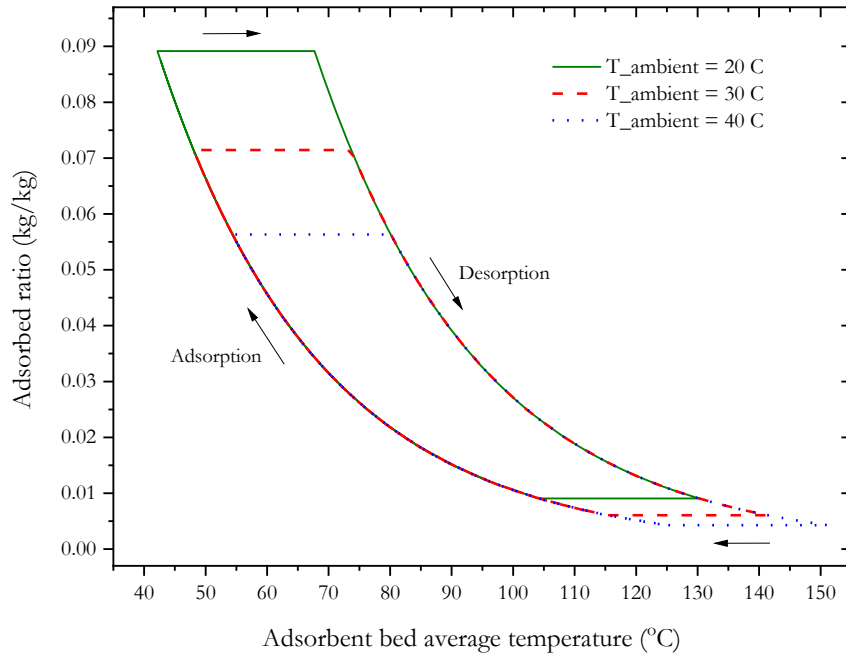
Figure 129. Effect of the ambient temperature (T_{amb}) on (a) adsorbed ratio with respect to the average temperature of the adsorbent bed (b) cooling capacity and COP (Silica gel RD type)
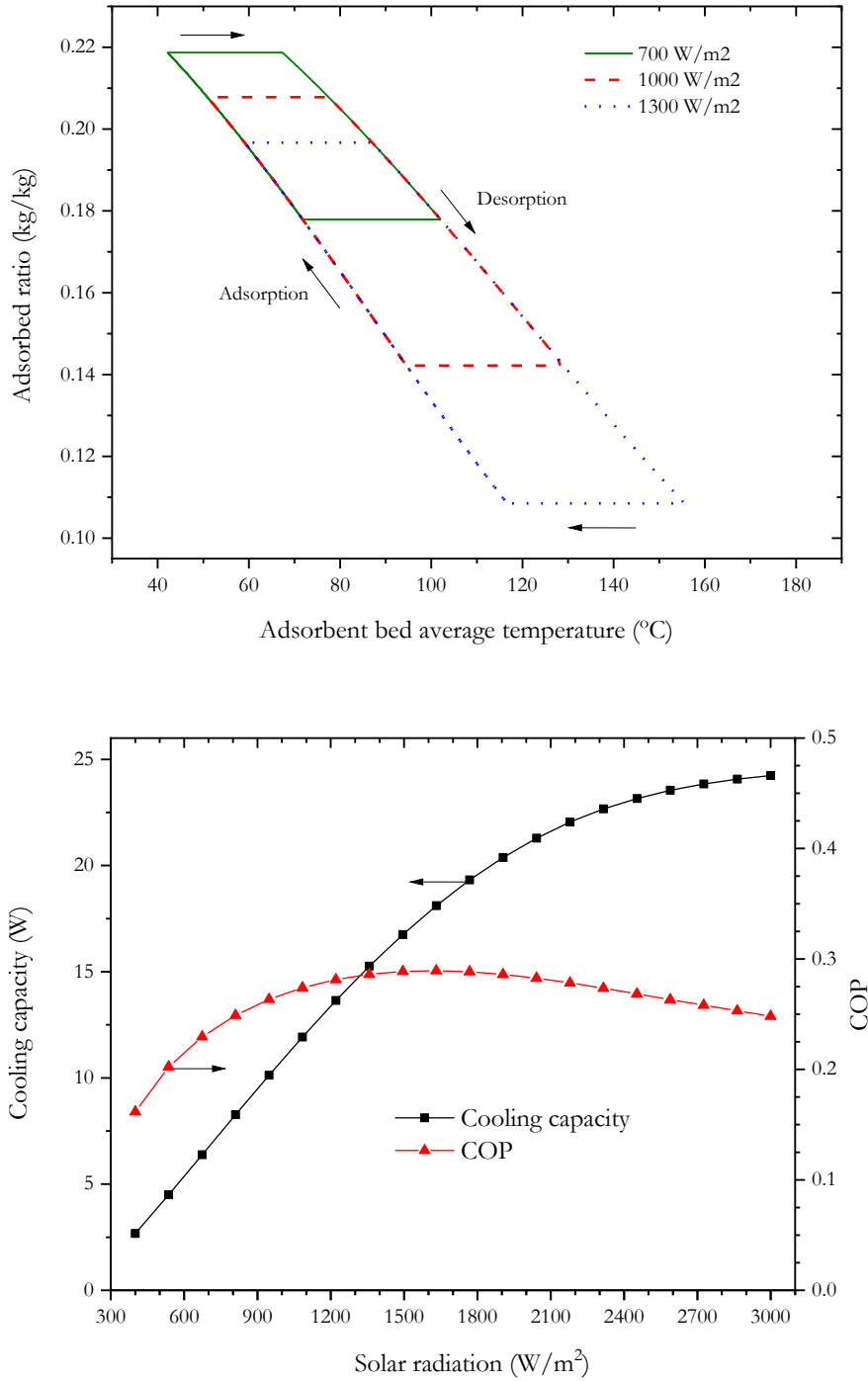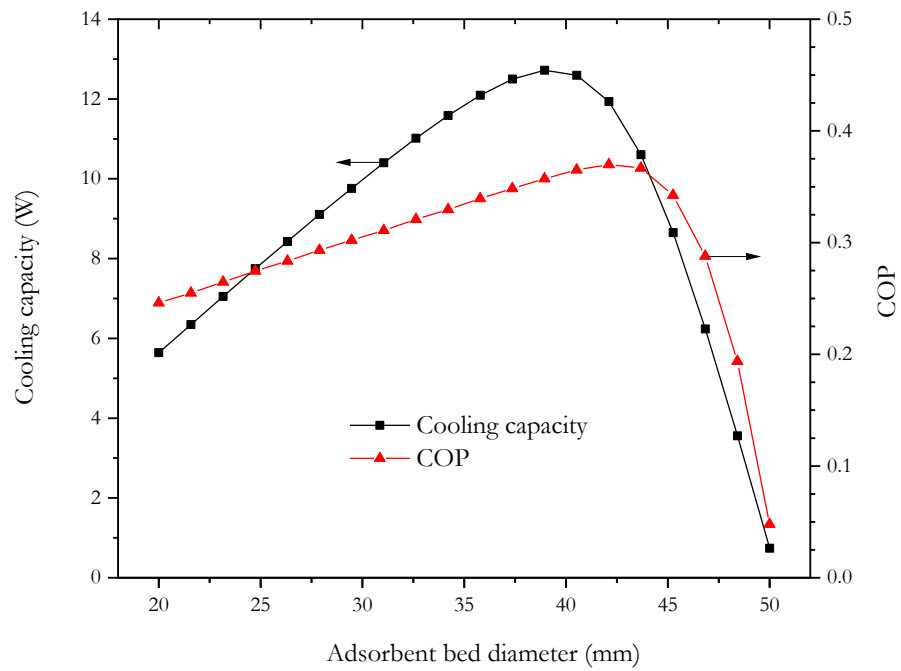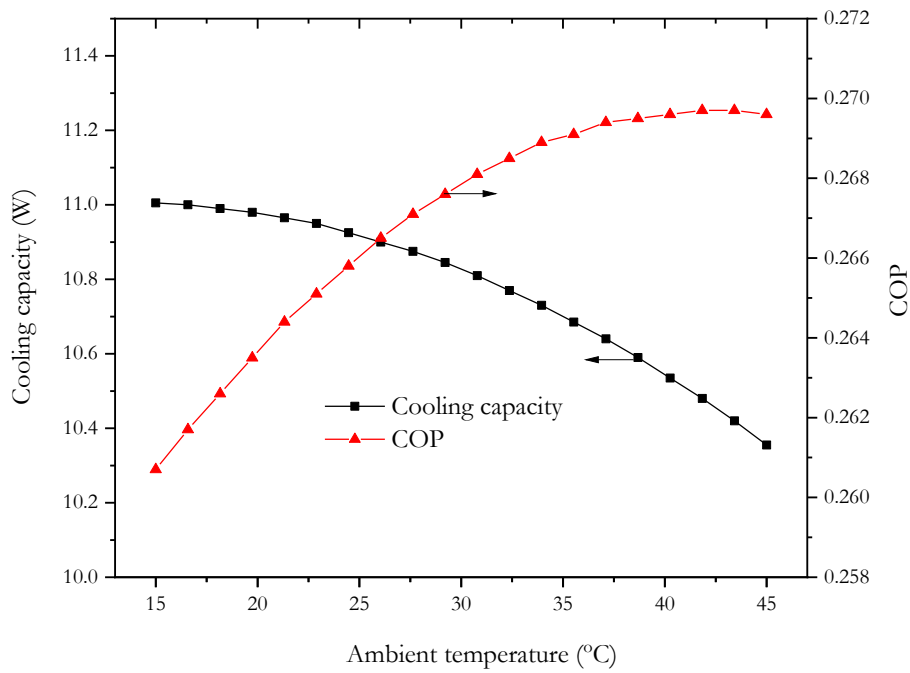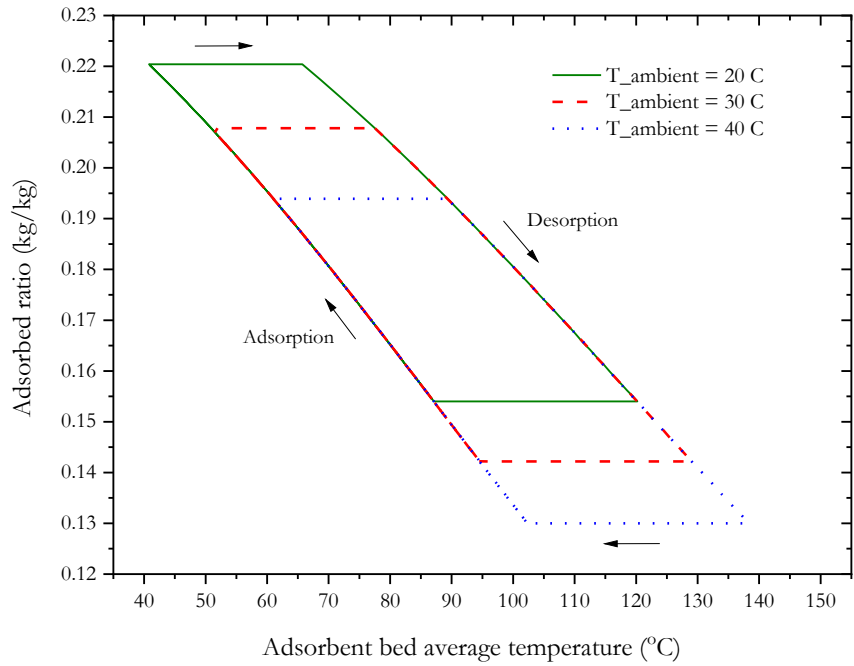
Figure 130. Effect of the ambient temperature (T_{amb}) on (a) adsorbed ratio with respect to the average temperature of the adsorbent bed (b) cooling capacity and COP (Zeolite 13X)

4.5.3.7. Sensitivity to the cycle time (t_{cycle})

Probably one of the most important questions for an intermittent heat driven cooling system is when do we start the desorption process, especially since the adsorption rate decreases as the adsorbent ration increases. It is worth noting that in this study we are assuming that the desorption and adsorption time is equal. Therefore, increasing cycle time will achieve lower adsorbent ratio during the desorption process and higher adsorbent ratio during the adsorption process. However, the question still stands: when should we stop? Figure 131 and Figure 132 show the effect of cycle time on the adsorbed ratio, adsorbent bed temperature, cooling capacity, and COP for both silica gel RD type and zeolite 13X. Figure 131b and Figure 132b show clearly that under our main assumptions, silica gel and zeolite-based cooling capacity peaks at about 2.5 hours and 1.25 hours, respectively. After that point, the cooling capacity decreases slightly for silica gel due to its adsorption capacity and steeply for zeolite due to its excellent adsorption rate.
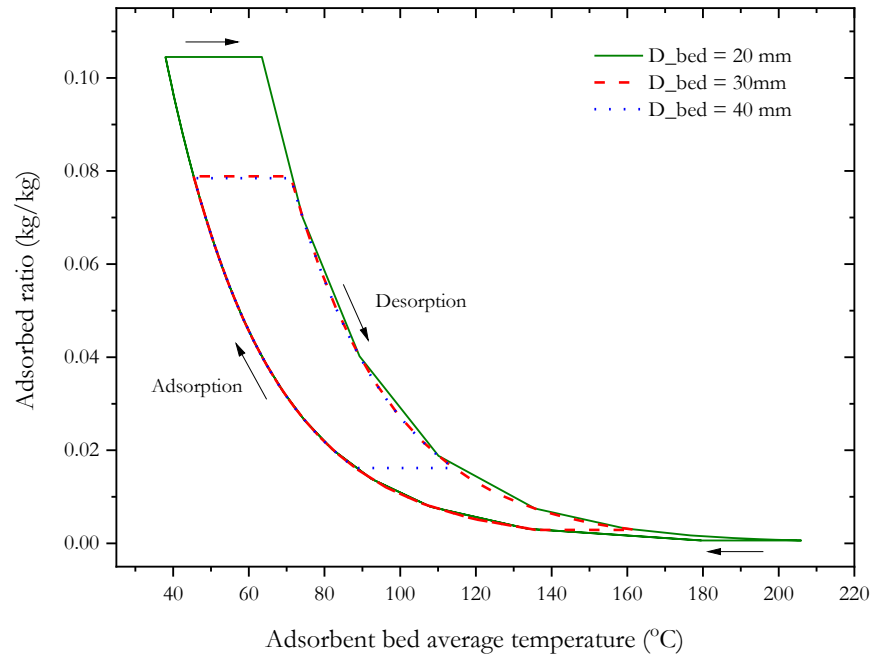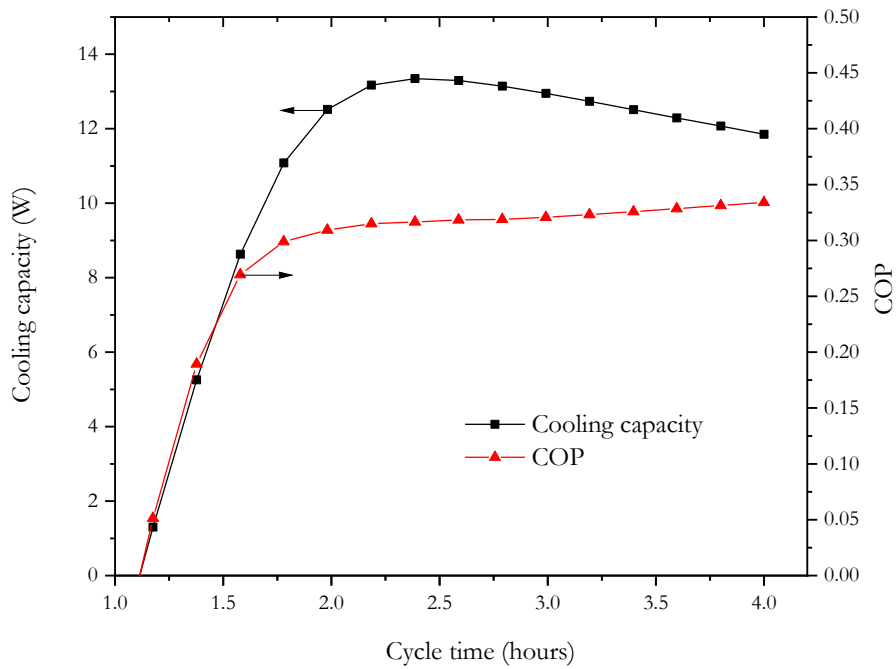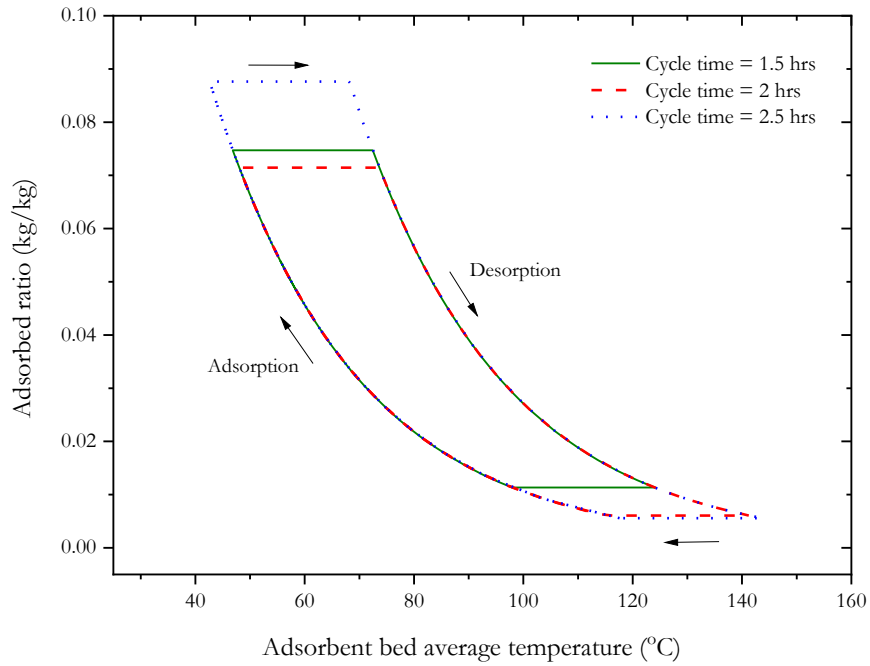
Figure 131. Effect of the cycle time (t_{cycle}) on (a) adsorbed ratio with respect to the average temperature of the adsorbent bed (b) cooling capacity and COP (Silica gel RD type)
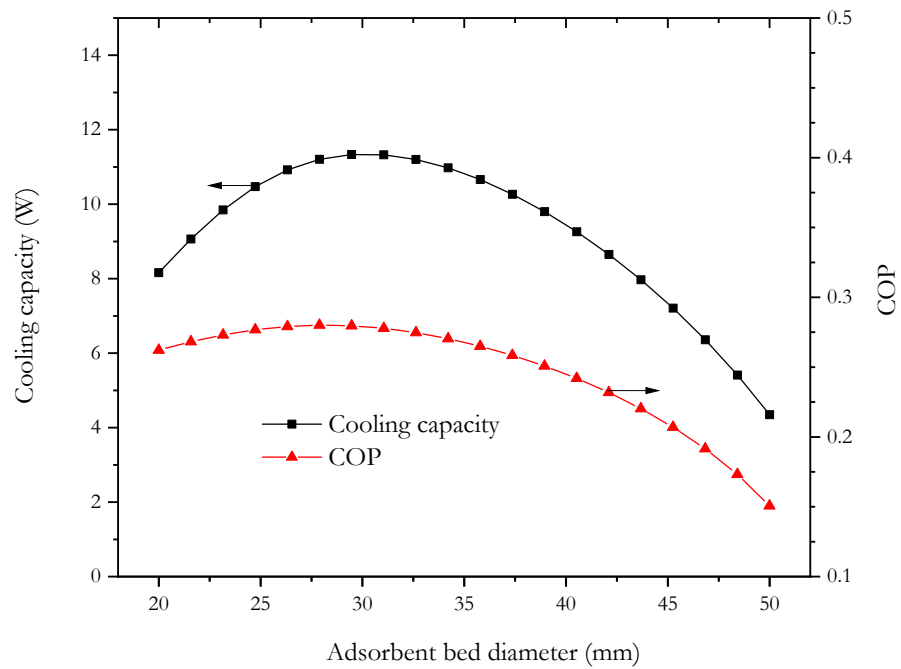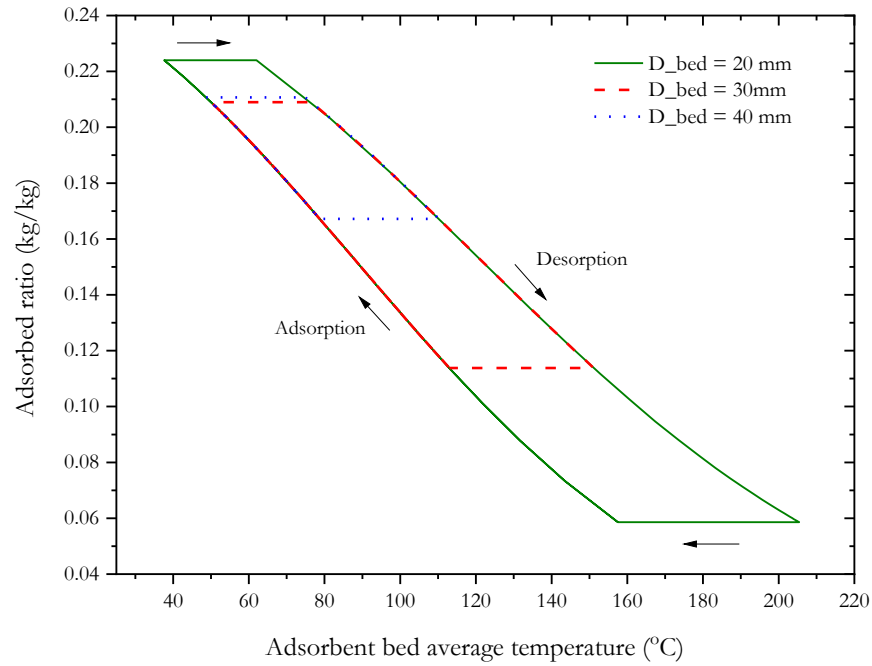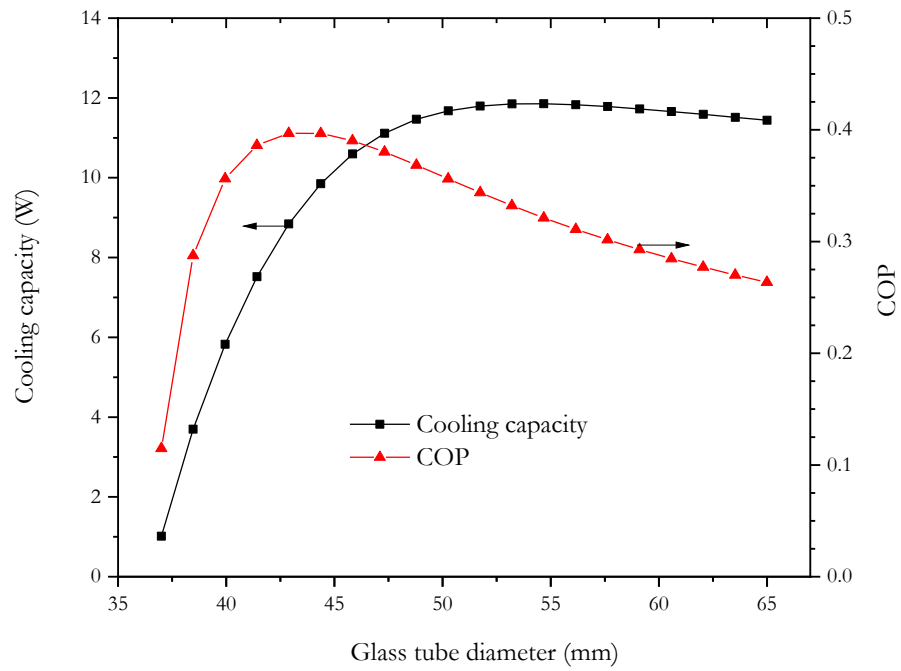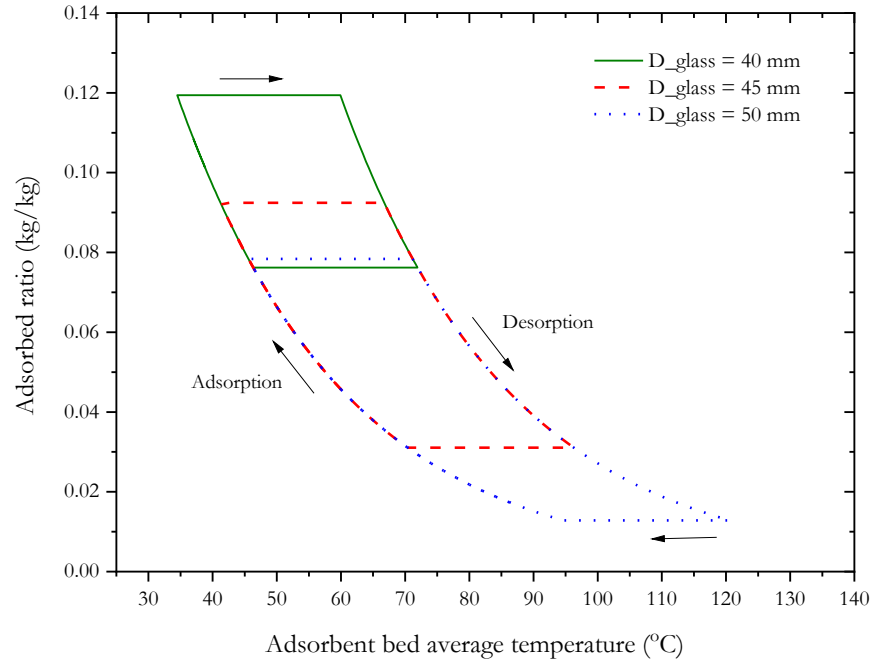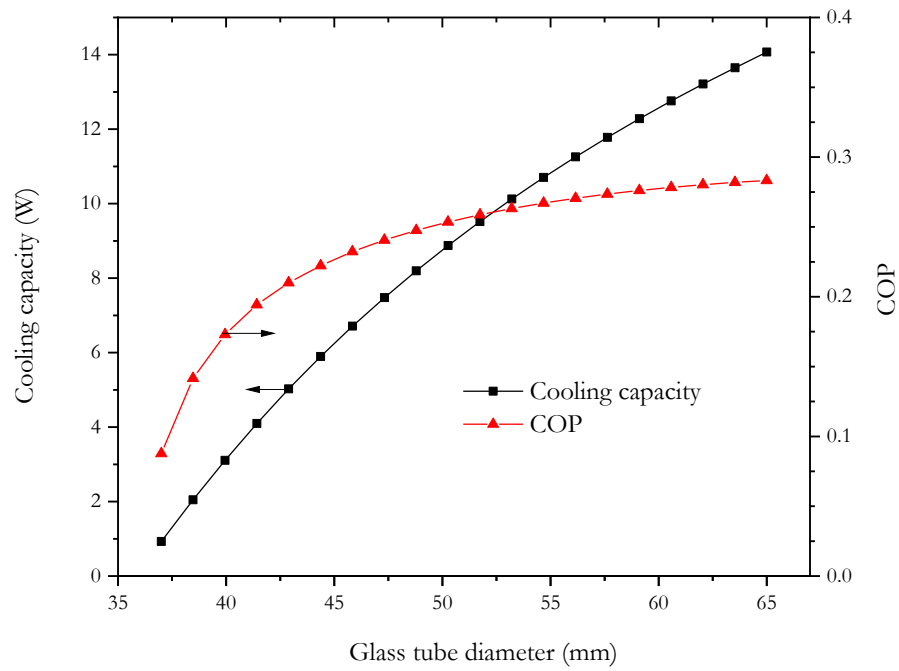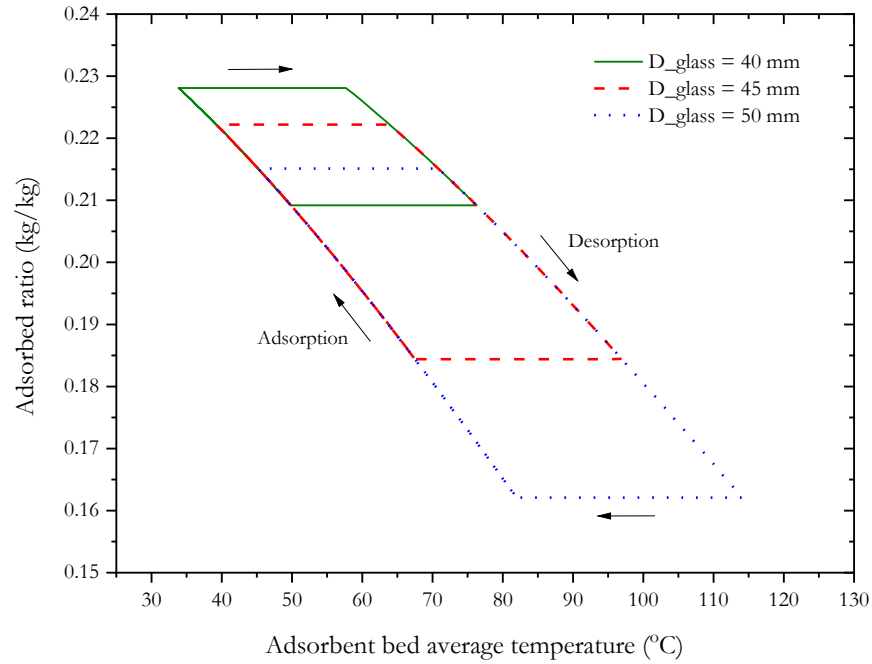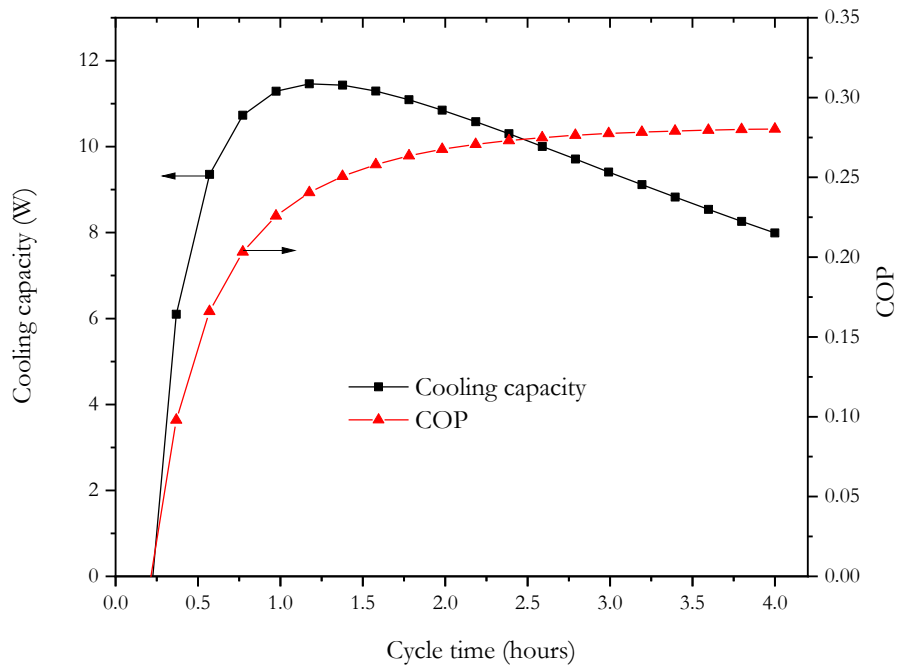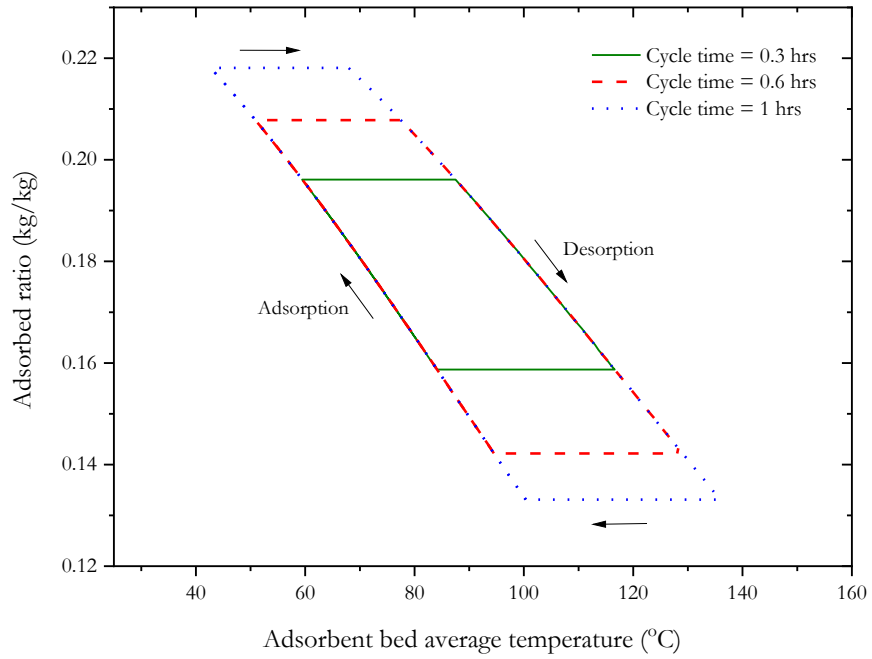
Figure 132. Effect of the cycle time (t_{cycle}) on (a) adsorbed ratio with respect to the average temperature of the adsorbent bed (b) cooling capacity and COP (Zeolite 13X)

Based on the obtained experimental results in Table 19 and simulation results based on Table 21, Table 22 shows a comparison between the solar coefficient of performance for both Zeolite 13X and Silica gel Type-RD. Note that solar COP for the simulation can easily be derived from the cooling capacity values and heat input using equation (4.54).

Table 22. Comparison between experiments and simulations of the evacuated tube adsorption heat pump module performance

Adsorbent	Simulation			Experimental	
	COP_{sim}	$COP_{solar,sim}$	Avg. cooling capacity (W)	$COP_{solar,exp}$	Avg. cooling capacity (W)
Zeolite 13X	0.27	0.11	10.8	0.15 ± 0.05	15
Silica gel Type-RD	0.31	0.20	11.8	0.17 ± 0.06	10

Based on the results obtained above and the major disadvantages listed in Table 17, our proposed evacuated tube adsorption heat pump module has demonstrated its ability to overcome those drawbacks (problems). Unlike existing adsorption systems, our proposed system is capable of maintaining high vacuum with no leakage problems, simplifying the continuous working principle of the system more effectively in form of operating modules out of phase, improving mass and heat transfers within the system and with the environment, and most importantly reducing the system capital and operating costs mainly due to the elimination of fitting and material used.

Otanicar et al. [107] performed an economic comparison between solar thermal and solar PV cooling systems with the intension of answering the question: is it better to use a solar thermal cooling system, or one driven by solar PV panel (based on vapor compression cycle). They took into account the initial cost of the cooling system, electrical/thermal storage cost, and PV/thermal collector cost. A summary of their result (based on 2020) compared with a similar economic evaluation of our proposed evacuated tube adsorption heat pump system are listed in Table 23. It can be clearly seen that our proposed evacuated tube adsorption heat pump system required the lowest capital cost compared to other thermally driven solar cooling systems and very comparative with solar PV cooling system at low COP. Our capital cost estimate for ONE evacuated tube adsorption heat pump module is based on $17.04 per a glass tube including the manifold, $1.36 per

adsorbent (Zeolite) in one glass tube, $3 per one adsorbent bed cage, and $3.41 per thermal storage tank for one module.

Table 23. An economic comparison between solar thermal and solar PV cooling system

System	System total cost ($/W$_{th}$ cooling)	Reference
PV – electric (vapor compression at COP = 3)	1.94	[107]
PV – electric (vapor compression at COP = 6)	1.43	[107]
Evacuated tube – thermal (NH$_3$ Absorption)	3.77	[107]
Flat plate – thermal (Desiccant)	3.09	[107]
Flat plate – thermal (Adsorption)	4.57	[107]
Evacuated tube adsorption heat pump system (*our proposed system*)	2.08	–

4.6. Summary

A new novel design is proposed that couples an evacuated tube solar collector and adsorption heat pump system in one module, namely, an evacuated tube solar adsorption heat pump module. The module is comprised of an evacuated single-wall glass tube in which one side (top section of the tube) represents the adsorbent bed (generator) and contains the adsorbent, while the other side (bottom section of the tube) represents the condenser/evaporator and contains the refrigerant. The module was investigated experimentally and theoretically and results show that the system is promising from energy point of views. Various adsorbents, such as Zeolite 13X and Silica gel Type-RD, were examined and it was observed that even though Silica gel has higher adsorptive capacity compared to Zeolite, the latter shows an excellent adsorption rate which gives it the advantage over silica gel for cooling applications. The solar COP of the evacuated tube adsorption heat pump module was experimentally and theoretically evaluated, and was found as 0.15 and 0.11 for Zeolite, respectively, and 0.17 and 0.2 for silica gel Type-RD. Our mathematical analysis showed that an optimal design point exists with respect to the radiation heat flux, adsorbent bed diameter, and glass tube diameter for both Zeolite and Silica gel.

5. CONCLUSION

Three different heat-driven cooling systems were examined mathematically and experimentally with the intension of enhancing these existing systems not only from energy conservation viewpoint but also from techno-economic analysis prospective. Our first proposed system investigates (Chapter 2) the opportunities for integrating single- and double-stage ammonia-water (NH_3–H_2O) absorption refrigeration systems with multi-effect distillation (MED) via cascade of rejected heat. Cooling capacity and hourly water production are calculated from thermodynamic properties of the working fluids at different operating conditions using simple models for each of the constituent systems. Additionally, the second law of thermodynamics is applied with the aim of examining the total exergy destruction of the entire stand-alone and combined systems. A cost model is developed as well in order to estimate the total annual cost of the system and the unit production cost (UPC) of both fresh water and cooling. The results indicate that the total exergy destruction of the combined systems, which consist of an MED unit driven by either a single- or double-stage NH_3–H2O refrigeration system, decreases by an average of 55% compared to stand-alone NH_3–H_2O and MED systems. Relative to stand-alone systems, although water production decreases by 30% and 9% when an MED unit is integrated with single- and double-stage NH_3-H_2O absorption systems, respectively, cooling capacity remains unchanged for the double-stage NH3-H_2O–MED system, and only decreases by 16% for the single-stage NH_3-H_2O–MED system. Moreover, the UPC of cooling decreases significantly by an average of 43% for both coupled systems, whereas the UPC of the produced water increases by only 19% and 3% for single- and double-stage NH3H2O–MED systems, respectively.

In the first part of Chapter 3, we proposed a novel combined cooling and power (CCHP) system based on a composition of a Rankine, gas refrigeration (reverse Brayton), liquid desiccant, ejector, and evaporative cooling cycles. The two proposed configurations, called the original cycle (OC) and the enhanced cycle (EC), utilize heat rejected by the Rankine cycle via its condenser in order to regenerate the liquid desiccant cycle. The desiccant cycle allows the cooling systems to decouple sensible and latent loads, and potentially reduce water consumption relative to pure evaporative cooling. Based on our thermodynamic calculations, the OC and EC are more feasible from an energy-saving viewpoint compared with separate systems that provide the same services for sensible heat ratios (SHR) less than 14% and 39%, respectively. At a fixed heat source input of about 2.4 MW$_{th}$ at 210°C, the OC is capable of generating 103 kW$_e$ of electrical power, 181 kW$_{th}$ of sensible cooling, 1631 kW$_{th}$ of latent cooling capacity, and fresh water at 2.7 m^3/hr capacity. At a SHR of 10%, the OC can achieve an exergy efficiency and primary energy saving ratio (*PESR*)

176

of 24% and 28%, respectively. Similarly, and at the same thermal energy input, the EC can supply 354 kW_e, 400 kW_{th}, and 1199 kW_{th}, and 1.8 m^3/hr of electrical power, sensible cooling capacity, latent cooling capacity, and fresh water capacity, respectively, at a SHR of 25%. Furthermore, the EC is more efficient than both the OC and stand-alone conventional systems as it shows a higher exergy efficiency of 53% and *PESR* of 29%.

In the second part of Chapter 3, we explored the opportunity of a combined cooling, desalination, and power (CCDP) unit that is thermally driven using low- to mid-grade heat input of 1940 kW_{th} (enthalpy of vaporization of steam at 200ºC). The proposed CCDP system is comprised of a Rankine cycle that partially drives a gas refrigeration (reverse Brayton) cycle by means of shaft work and thermally drives a multiple effect distillation (MED) unit by harnessing the condenser's rejected heat. Based on our thermodynamic model, the proposed CCDP system is more efficient from an energy-saving viewpoint compared to standalone systems that deliver the same services provided if there are ≥ 8 MED effects (units). Furthermore, the proposed polygeneration system is able to produce nearly 188 kW_e of electrical power output, 116 kW_{th} of cooling capacity, and 26 m^3/hr of fresh water capacity when water is employed as a working fluid and air as a refrigerant. In addition, the CCDP system attains an exergy efficiency of ≈42% and a primary energy saving ratio (PESR) of 28%. Because an organic Rankine cycle (ORC) is promising for the conversion of low- and mid-grade heat to electricity, various organic working fluids are investigated. The results show that when propane is used instead of water, the fresh water capacity rises by 3.4%. Likewise, the maximum exergy efficiency of about 42% is obtained when helium is utilized as a refrigerant instead of air.

In Chapter 4, a new adsorption-based cooling system was examined. This system couples an evacuated tube solar collector and adsorption heat pump system in one module, namely, an evacuated tube solar adsorption heat pump module. The module is basically a simple adsorption heat pump system placed inside an evacuated glass tube with a length of about 180 cm, and an internal diameter of 5.5 cm. One side (top section of the tube) represents the adsorbent bed (generator) and contains the adsorbent, while the other side (bottom section of the tube) represents the condenser/evaporator and contains the refrigerant. The module was studied experimentally and theoretically using various types of adsorbents such as Zeolite 13X and Silica Gel Type-RD. Our experimental results showed that the module is capable of producing 223 kJ of cooling in three hours when Zeolite is used and in six hours when Silica Gel is used. Our mathematical model showed a reasonable agreement with the experimental results with an average coefficient of performance of 0.13 and 0.185 when Zeolite 13X and Silica Gel are used, respectively.

6. FUTURE WORK

Regarding the second and third chapters associated with the poly-generation systems, these chapters have been completed and there is no planned future work. For the fourth chapter, on the other hand, the experimental and analytical work have shown some of the potential improvements by using the evacuated tube adsorption heat pump system. We believe there is a lot of room for further improvements to make this adsorption-based cooling concept more effective:

i. Due to its high rate of adsorption and adsorptive ability at elevated temperature, Zeolite has proven that it is a better adsorbent than Silica Gel. Nevertheless, Zeolite requires high temperature source (medium energy quality) to completely desorb the water vapor. Therefore, different desorption techniques (such as ultrasound energy) could be very attractive to work alongside thermal energy in a hybrid system. For instance, thermal energy input can possibly handle the early desorption stage (at high adsorbed ratio) and then ultrasound energy desorbs at a later desorption rate (at low adsorbed ratio).

ii. Alternatively, zeolite can possibly be completely regenerated by incorporating reflectors such as the one in a solar compound parabolic concentrator (CPC). Such a modification is to be evaluated mathematically and then experimentally. A reflector would also ensure to keep the temperature uniform in the radial direction especially at higher temperature.

iii. Analyze mathematically and then experimentally different types of working pairs such as zeolite-methanol, zeolite-ammonia, and activated carbon-methanol and compare the result with zeolite-water.

iv. Incorporate a simple valve between the adsorbent bed and the evaporator/condenser would allow the system to act as thermal cooling storage. It is worth noting that the valve (separator) does not need to completely isolate both sides but rather minimize vapor flow rate from the evaporator to the adsorbent bed (generator).

7. REFERENCE

[1] Mohanraj, M., Jayaraj, S., and Muraleedharan, C., 2009, "Environment Friendly Alternatives to Halogenated refrigerants—A Review," International Journal of Greenhouse Gas Control, **3**(1) pp. 108-119.

[2] EIA, U., 2011, "International Energy Outlook," US Energy Information Administration, Washington, DC, .

[3] Goetzler, W., Guernsey, M., Young, J., 2016, "The Future of Air Conditioning for Buildings," US Department of Energy, Energy Efficiency & Renewable Energy, Building Technologies Office, .

[4] Elson, A., Tidball, R., and Hampson, A., 2015, "Waste Heat to Power Market Assessment," Oak Ridge National Laboratory, .

[5] DOE, U., 2008, "Waste Heat Recovery: Techonology and Opportunities in US Industry," Washington DC: US Department of Energy Industrial Technologies Program, .

[6] Darwish, M. A., Abdulrahim, H. K., Hassan, A. S., 2016, "Retrofitting the Combined-Cycle Producing Electric Power and Desalted Seawater to Include District Cooling in GCC," Desalination and Water Treatment, **57**(12) pp. 5331-5344.

[7] Calise, F., and Dentice D'Accadia, M., 2016, Simulation of Polygeneration Systems, .

[8] Elimelech, M., and Phillip, W. A., 2011, "The Future of Seawater Desalination: Energy, Technology, and the Environment," Science (New York, N.Y.), **333**(6043) pp. 712-717.

[9] Li, H., Russell, N., Sharifi, V., 2011, "Techno-Economic Feasibility of Absorption Heat Pumps using Wastewater as the Heating Source for Desalination," Desalination, **281**pp. 118-127.

[10] Dai, A., 2013, "Increasing Drought Under Global Warming in Observations and Models," Nature Climate Change, **3**(1) pp. 52-58.

[11] McMullan, J. T., 2002, "Refrigeration and the Environment—issues and Strategies for the Future," International Journal of Refrigeration, **25**(1) pp. 89-99.

[12] Alarcón-Padilla, D., and García-Rodríguez, L., 2007, "Application of Absorption Heat Pumps to Multi-Effect Distillation: A Case Study of Solar Desalination," Desalination, **212**(1) pp. 294-302.

[13] Esfahani, I. J., Kang, Y. T., and Yoo, C., 2014, "A High Efficient Combined Multi-Effect Evaporation–absorption Heat Pump and Vapor-Compression Refrigeration Part 1: Energy and Economic Modeling and Analysis," Energy, **75**pp. 312-326.

[14] Aly, S., 1995, "A Study of a New Thermal Vapor Compression/Multi-Effect Stack (TVC/MES) Low Temperature Distillation System," Desalination, **103**(3) pp. 257-263.

[15] Wang, Y., and Lior, N., 2011, "Proposal and Analysis of a High-Efficiency Combined Desalination and Refrigeration System Based on the LiBr–H 2 O Absorption Cycle—part 1:

System Configuration and Mathematical Model," Energy Conversion and Management, **52**(1) pp. 220-227.

[16] Wang, Y., and Lior, N., 2011, "Proposal and Analysis of a High-Efficiency Combined Desalination and Refrigeration System Based on the LiBr–H 2 O Absorption cycle—Part 2: Thermal Performance Analysis and Discussions," Energy Conversion and Management, **52**(1) pp. 228-235.

[17] Gomri, R., 2010, "Thermal Seawater Desalination: Possibilities of using Single Effect and Double Effect Absorption Heat Transformer Systems," Desalination, **253**(1) pp. 112-118.

[18] Gude, V. G., and Nirmalakhandan, N., 2008, "Combined Desalination and Solar-Assisted Air-Conditioning System," Energy Conversion and Management, **49**(11) pp. 3326-3330.

[19] Abdulrahim, H. K., and Darwish, M. A., 2015, "Thermal Desalination and Air Conditioning using Absorption Cycle," Desalination and Water Treatment, **55**(12) pp. 3310-3329.

[20] Jana, A. K., 2014, "Advances in Heat Pump Assisted Distillation Column: A Review," Energy Conversion and Management, **77**pp. 287-297.

[21] Li, Y., Wang, L., Zhu, M., 2017, "Optimization Study of Distillation Column Based on Type I Absorption Heat Pump," Applied Thermal Engineering, .

[22] Ananthanarayanan, P., 2013, "Basic refrigeration and air conditioning," Tata McGraw-Hill Education, .

[23] Deng, J., Wang, R., and Han, G., 2011, "A Review of Thermally Activated Cooling Technologies for Combined Cooling, Heating and Power Systems," Progress in Energy and Combustion Science, **37**(2) pp. 172-203.

[24] Herold, K.E., Radermacher, R., and Klein, S.A., 2016, "Absorption chillers and heat pumps," CRC press, .

[25] Klein, S.A., and Alvarado, F., 1992, "EES: Engineering equation solver for the Microsoft Windows operating system," F-Chart Software, .

[26] Adewusi, S., and Zubair, S. M., 2004, "Second Law Based Thermodynamic Analysis of Ammonia–water Absorption Systems," Energy Conversion and Management, **45**(15) pp. 2355-2369.

[27] Al-Karaghouli, A., and Kazmerski, L. L., 2013, "Energy Consumption and Water Production Cost of Conventional and Renewable-Energy-Powered Desalination Processes," Renewable and Sustainable Energy Reviews, **24**pp. 343-356.

[28] Verdier, F., 2011, "MENA Regional Water Outlook Part II Desalination using Renewable Energy Task 1–Desalination Potential," .

[29] Schliephake, K., Brown, P., Mason-Jefferies, A., 2005, "Overview of Treatment Processes for the Production of Fit for Purpose Water: Desalination and Membrane Technologies, ASIRC Report No," R05-2207.Australian Sustainable Industry Research Centre Ltd., Churchill, .

[30] Negewo, B.D., 2012, "Renewable energy desalination: an emerging solution to close the water gap in the Middle East and North Africa," World Bank Publications, .

[31] Ettouney, H., 2009, "Seawater Desalination,"Springer, pp. 17-40.

[32] Mistry, K. H., McGovern, R. K., Thiel, G. P., 2011, "Entropy Generation Analysis of Desalination Technologies," Entropy, **13**(10) pp. 1829-1864.

[33] Kahraman, N., and Cengel, Y. A., 2005, "Exergy Analysis of a MSF Distillation Plant," Energy Conversion and Management, **46**(15) pp. 2625-2636.

[34] Esfahani, I. J., Ataei, A., Shetty, V., 2012, "Modeling and Genetic Algorithm-Based Multi-Objective Optimization of the MED-TVC Desalination System," Desalination, **292**pp. 87-104.

[35] Zarza, E., 1995, "Solar Thermal Desalination Project Phase II Results & Final Project Report," Ciemat Madrid,, Spain, .

[36] Hatzikioseyian, A., Vidali, R., and Kousi, P., 2003, "Modelling and Thermodynamic Analysis of a Multi Effect Distillation (MED) Plant for Seawater Desalination," National Technical University of Athens (NTUA) GREECE, .

[37] Sharqawy, M. H., Lienhard, J. H., and Zubair, S. M., 2010, "Thermophysical Properties of Seawater: A Review of Existing Correlations and Data," Desalination and Water Treatment, **16**(1-3) pp. 354-380.

[38] Alasfour, F., and Amer, A. B., 2006, "The Feasibility of Integrating ME-TVC MEE with Azzour South Power Plant: Economic Evaluation," Desalination, **197**(1-3) pp. 33-49.

[39] Farshi, L. G., Mahmoudi, S. S., and Rosen, M., 2013, "Exergoeconomic Comparison of Double Effect and Combined Ejector-Double Effect Absorption Refrigeration Systems," Applied Energy, **103**pp. 700-711.

[40] Cengel, Y., and Boles, M., 1989, "Molar Mass, Gas Constant and Critical-Point Properties. in "Thermodynamics and Engineering Approach," .

[41] Demirkaya, G., Padilla, R. V., and Goswami, D. Y., 2013, "A Review of Combined Power and Cooling Cycles," Wiley Interdisciplinary Reviews: Energy and Environment, **2**(5) pp. 534-547.

[42] Sherbeck, J., 2017, "Systems, Methods, and Apparatuses for Implementing a Closed Low Grade Heat Driven Cycle to Produce Shaft Power and Refrigeration," **WO/2017/112875A1**.

[43] Ferrari, M. L., Traverso, A., and Massardo, A. F., 2016, "Smart Polygeneration Grids: Experimental Performance Curves of Different Prime Movers," Applied Energy, **162**pp. 622-630.

[44] Fumo, N., Mago, P. J., and Chamra, L. M., 2009, "Emission Operational Strategy for Combined Cooling, Heating, and Power Systems," Applied Energy, **86**(11) pp. 2344-2350.

[45] Jana, K., Ray, A., Majoumerd, M. M., 2017, "Polygeneration as a Future Sustainable Energy solution–A Comprehensive Review," Applied Energy, **202**pp. 88-111.

[46] Alelyani, S. M., Fette, N. W., Stechel, E. B., 2017, "Techno-Economic Analysis of Combined Ammonia-Water Absorption Refrigeration and Desalination," Energy Conversion and Management, **143**pp. 493-504.

[47] Cho, H., Smith, A. D., and Mago, P., 2014, "Combined Cooling, Heating and Power: A Review of Performance Improvement and Optimization," Applied Energy, **136**pp. 168-185.

[48] Liu, M., Shi, Y., and Fang, F., 2014, "Combined Cooling, Heating and Power Systems: A Survey," Renewable and Sustainable Energy Reviews, **35**pp. 1-22.

[49] Al Moussawi, H., Fardoun, F., and Louahlia-Gualous, H., 2016, "Review of Tri-Generation Technologies: Design Evaluation, Optimization, Decision-Making, and Selection Approach," Energy Conversion and Management, **120**pp. 157-196.

[50] Han, W., Chen, Q., Lin, R., 2015, "Assessment of Off-Design Performance of a Small-Scale Combined Cooling and Power System using an Alternative Operating Strategy for Gas Turbine," Applied Energy, **138**pp. 160-168.

[51] Rostamzadeh, H., Ebadollahi, M., Ghaebi, H., 2017, "Energy and Exergy Analysis of Novel Combined Cooling and Power (CCP) Cycles," Applied Thermal Engineering, .

[52] Kang, S., Li, H., Lei, J., 2015, "A New Utilization Approach of the Waste Heat with Mid-Low Temperature in the Combined Heating and Power System Integrating Heat Pump," Applied Energy, **160**pp. 185-193.

[53] Li, H., Kang, S., Lu, L., 2017, "Optimal Design and Analysis of a New CHP-HP Integrated System," Energy Conversion and Management, **146**pp. 217-227.

[54] Cengel, Y. A., and Boles, M. A., 2002, "Thermodynamics: An Engineering Approach," Sea, **1000**pp. 8862.

[55] Michael, J. M., and Howard, N. S., 2011, "Fundamentals of Engineering Thermodynamics," Fundamentals of Engineering Thermodynamics, .

[56] Khalil, A., Fatouh, M., and Elgendy, E., 2011, "Ejector Design and Theoretical Study of R134a Ejector Refrigeration Cycle," International Journal of Refrigeration, **34**(7) pp. 1684-1698.

[57] Varga, S., Oliveira, A. C., and Diaconu, B., 2009, "Analysis of a Solar-Assisted Ejector Cooling System for Air Conditioning," International Journal of Low-Carbon Technologies, .

[58] Gandhidasan, P., 2004, "A Simplified Model for Air Dehumidification with Liquid Desiccant," Solar Energy, **76**(4) pp. 409-416.

[59] Gandhidasan, P., 2005, "Quick Performance Prediction of Liquid Desiccant Regeneration in a Packed Bed," Solar Energy, **79**(1) pp. 47-55.

[60] Conde, M. R., 2004, "Properties of Aqueous Solutions of Lithium and Calcium Chlorides: Formulations for use in Air Conditioning Equipment Design," International Journal of Thermal Sciences, **43**(4) pp. 367-382.

[61] Rosen, M., and Le, M., 1995, "'Efficiency Measures for Processes Integrating Combined Heat and Power and District Cooling," Thermodynamics and the Design, Analysis, and Improvement of Energy Systems, **35**pp. 423-434.

[62] Rafique, M. M., Rehman, S., Alhems, L. M., 2016, "Parametric Analysis of a Rotary Type Liquid Desiccant Air Conditioning System," Energies, **9**(4) pp. 305.

[63] Mohamed, A., Ahmed, M., Hassan, A., 2016, "Performance Evaluation of Gauze Packing for Liquid Desiccant Dehumidification System," Case Studies in Thermal Engineering, **8**pp. 260-276.

[64] Alelyani, S. M., Sherbeck, J. A., Fette, N. W., 2018, "Assessment of a Novel Heat-Driven Cycle to Produce Shaft Power and Refrigeration," Applied Energy, **215**pp. 751-764.

[65] Murugan, S., and Horák, B., 2016, "Tri and Polygeneration Systems-A Review," Renewable and Sustainable Energy Reviews, **60**pp. 1032-1051.

[66] Anvari, S., Taghavifar, H., and Parvishi, A., 2017, "Thermo-Economical Consideration of Regenerative Organic Rankine Cycle Coupling with the Absorption Chiller Systems Incorporated in the Trigeneration System," Energy Conversion and Management, **148**pp. 317-329.

[67] Ortega-Delgado, B., Palenzuela, P., and Alarcón-Padilla, D., 2016, "Parametric Study of a Multi-Effect Distillation Plant with Thermal Vapor Compression for its Integration into a Rankine Cycle Power Block," Desalination, **394**pp. 18-29.

[68] Mohan, G., Dahal, S., Kumar, U., 2014, "Development of Natural Gas Fired Combined Cycle Plant for Tri-Generation of Power, Cooling and Clean Water using Waste Heat Recovery: Techno-Economic Analysis," Energies, **7**(10) pp. 6358-6381.

[69] Akbari, M., Mahmoudi, S., Yari, M., 2014, "Energy and Exergy Analyses of a New Combined Cycle for Producing Electricity and Desalinated Water using Geothermal Energy," Sustainability, **6**(4) pp. 1796-1820.

[70] Sahoo, U., Kumar, R., Pant, P., 2015, "Scope and Sustainability of Hybrid Solar–biomass Power Plant with Cooling, Desalination in Polygeneration Process in India," Renewable and Sustainable Energy Reviews, **51**pp. 304-316.

[71] Ameri, M., and Jorjani, M., 2016, "Performance Assessment and Multi-Objective Optimization of an Integrated Organic Rankine Cycle and Multi-Effect Desalination System," Desalination, **392**pp. 34-45.

[72] Salimi, M., and Amidpour, M., 2017, "Investigating the Integration of Desalination Units into Cogeneration Systems Utilizing R-Curve Tool," Desalination, **419**pp. 49-59.

[73] Vetter, C., Wiemer, H., and Kuhn, D., 2013, "Comparison of Sub-and Supercritical Organic Rankine Cycles for Power Generation from Low-Temperature/Low-Enthalpy Geothermal Wells, Considering Specific Net Power Output and Efficiency," Applied Thermal Engineering, **51**(1) pp. 871-879.

[74] Quoilin, S., Van Den Broek, M., Declaye, S., 2013, "Techno-Economic Survey of Organic Rankine Cycle (ORC) Systems," Renewable and Sustainable Energy Reviews, **22**pp. 168-186.

[75] Turns, S.R., 1996, "An introduction to combustion," McGraw-hill New York, .

[76] Fernandes, M., Brites, G., Costa, J., 2014, "Review and Future Trends of Solar Adsorption Refrigeration Systems," Renewable and Sustainable Energy Reviews, **39**pp. 102-123.

[77] Younes, M. M., El-Sharkawy, I. I., Kabeel, A., 2017, "A Review on Adsorbent-Adsorbate Pairs for Cooling Applications," Applied Thermal Engineering, **114**pp. 394-414.

[78] Al-Alili, A., Hwang, Y., and Radermacher, R., 2014, "Review of Solar Thermal Air Conditioning Technologies," International Journal of Refrigeration, **39**pp. 4-22.

[79] Demir, H., Mobedi, M., and Ülkü, S., 2008, "A Review on Adsorption Heat Pump: Problems and Solutions," Renewable and Sustainable Energy Reviews, **12**(9) pp. 2381-2403.

[80] Sah, R. P., Choudhury, B., and Das, R. K., 2015, "A Review on Adsorption Cooling Systems with Silica Gel and Carbon as Adsorbents," Renewable and Sustainable Energy Reviews, **45**pp. 123-134.

[81] Sah, R. P., Choudhury, B., and Das, R. K., 2016, "A Review on Low Grade Heat Powered Adsorption Cooling Systems for Ice Production," Renewable and Sustainable Energy Reviews, **62**pp. 109-120.

[82] Sadineni, S. B., Atallah, F., and Boehm, R. F., 2012, "Impact of Roof Integrated PV Orientation on the Residential Electricity Peak Demand," Applied Energy, **92**pp. 204-210.

[83] Camacho, E. F., Samad, T., Garcia-Sanz, M., 2011, "Control for Renewable Energy and Smart Grids," The Impact of Control Technology, Control Systems Society, pp. 69-88.

[84] Critoph, R., 2002, "Multiple Bed Regenerative Adsorption Cycle using the Monolithic Carbon–ammonia Pair," Applied Thermal Engineering, **22**(6) pp. 667-677.

[85] Critoph, R., 2000, "Continuous multiple-bed regenerative adsorption cycle refrigerator/heat pump," Proc. IY Minsk Internat. Seminar. Heat pipes, heat pumps, refrigerators. Minsk, Anonymous pp. 77.

[86] Tamainot-Telto, Z., and Critoph, R., 2001, "Monolithic Carbon for Sorption Refrigeration and Heat Pump Applications," Applied Thermal Engineering, **21**(1) pp. 37-52.

[87] Critoph, R., 2001, "Simulation of a Continuous Multiple-Bed Regenerative Adsorption Cycle," International Journal of Refrigeration, **24**(5) pp. 428-437.

[88] Tamainot-Telto, Z., and Critoph, R., 2003, "Advanced Solid Sorption Air Conditioning Modules using Monolithic Carbon–ammonia Pair," Applied Thermal Engineering, **23**(6) pp. 659-674.

[89] Gupta, Y., Metchop, L., Frantzis, A., 2008, "Comparative Analysis of Thermally Activated, Environmentally Friendly Cooling Systems," Energy Conversion and Management, **49**(5) pp. 1091-1097.

[90] Haywood, A., Sherbeck, J., Phelan, P., 2012, "Thermodynamic Feasibility of Harvesting Data Center Waste Heat to Drive an Absorption Chiller," Energy Conversion and Management, **58**pp. 26-34.

[91] Ng, K. C., Thu, K., Kim, Y., 2013, "Adsorption Desalination: An Emerging Low-Cost Thermal Desalination Method," Desalination, **308**pp. 161-179.

[92] Schawe, D., 2001, "Theoretical and Experimental Investigations of an Adsorption Heat Pump with Heat Transfer between Two Adsorbers," .

[93] Bau, U., Hoseinpoori, P., Graf, S., 2017, "Dynamic Optimisation of Adsorber-Bed Designs Ensuring Optimal Control," Applied Thermal Engineering, **125**pp. 1565-1576.

[94] Jafarkazemi, F., and Abdi, H., 2012, "Evacuated Tube Solar Heat Pipe Collector Model and Associated Tests," Journal of Renewable and Sustainable Energy, **4**(2) pp. 023101.

[95] Paradis, P., Rousse, D. R., Hallé, S., 2015, "Thermal Modeling of Evacuated Tube Solar Air Collectors," Solar Energy, **115**pp. 708-721.

[96] Duffie, J.A., and Beckman, W.A., 2013, "Solar engineering of thermal processes," John Wiley & Sons, .

[97] Cengel, Y.A., Ghajar, A.J., and Kanoglu, M., 2011, "Heat and mass transfer: fundamentals & applications," McGraw-Hill New York, .

[98] Ratzel, A., Hickox, C., and Gartling, D., 1979, "Techniques for Reducing Thermal Conduction and Natural Convection Heat Losses in Annular Receiver Geometries," Journal of Heat Transfer, **101**(1) pp. 108-113.

[99] Shafii, M., Mamouri, S. J., Lotfi, M., 2016, "A Modified Solar Desalination System using Evacuated Tube Collector," Desalination, **396**pp. 30-38.

[100] Wang, Y., and LeVan, M. D., 2009, "Adsorption Equilibrium of Carbon Dioxide and Water Vapor on Zeolites 5A and 13X and Silica Gel: Pure Components," Journal of Chemical & Engineering Data, **54**(10) pp. 2839-2844.

[101] Cavenati, S., Grande, C. A., and Rodrigues, A. E., 2004, "Adsorption Equilibrium of Methane, Carbon Dioxide, and Nitrogen on Zeolite 13X at High Pressures," Journal of Chemical & Engineering Data, **49**(4) pp. 1095-1101.

[102] Afonso, M., and Silveira Jr, V., 2005, "Characterization of Equilibrium Conditions of Adsorbed Silica Gel/Water Bed According to Dubinin Astakhov and Freundlich," Revista De Engenharia Térmica, **4**(1) .

[103] Ho, Y., 2006, "Review of Second-Order Models for Adsorption Systems," Journal of Hazardous Materials, **136**(3) pp. 681-689.

[104] Chihara, K., and Suzuki, M., 1983, "Air Drying by Pressure Swing Adsorption," Journal of Chemical Engineering of Japan, **16**(4) pp. 293-299.

[105] Foo, K. Y., and Hameed, B. H., 2010, "Insights into the Modeling of Adsorption Isotherm Systems," Chemical Engineering Journal, **156**(1) pp. 2-10.

[106] Cho, S., and Kim, J., 1992, "Modeling of a Silica Gel/Water Adsorption-Cooling System," Energy, **17**(9) pp. 829-839.

[107] Otanicar, T., Taylor, R. A., and Phelan, P. E., 2012, "Prospects for Solar cooling–An Economic and Environmental Assessment," Solar Energy, **86**(5) pp. 1287-1299.

[108] Gebreslassie, B. H., Groll, E. A., and Garimella, S. V., 2012, "Multi-Objective Optimization of Sustainable Single-Effect Water/Lithium Bromide Absorption Cycle," Renewable Energy, **46**pp. 100-110.

[109] Turns, S.R., 1996, "An introduction to combustion," McGraw-hill New York, .

8. APPENDIX A

ECONOMIC MODEL OF ABSORPTION REFRIGERATION SYSTEM AND MULTI EFFECT DISTILLATION SYSTEM

Considering the ARS and MED components, namely the generator, condenser, evaporator, rectifier, absorber, solution heat exchanger, and MED's effects as simple heat exchangers, their capital cost can be calculated by the power law relation as [39]:

$$Z_k = Z_{R,k} \cdot \left(\frac{A_k}{A_R}\right)^{0.6} \tag{A1}$$

where Z represents the capital cost of a particular component, R the reference component, and k the subcomponents, e.g. rectifier, condenser, or MED effect. Note that effects in the MED system and the rectifier in the ARS system will be treated as an evaporator and condenser, respectively. Similarly, the pump capital cost can be estimated as [39]:

$$Z_p = Z_{R,p} \cdot \left(\frac{\dot{W}_p}{\dot{W}_{R,p}}\right)^{0.26} \cdot \left(\frac{1 - \eta_p}{\eta_p}\right)^{0.5} \tag{A2}$$

The reference costs of the reference year 2000, at a reference area of 100 m², are [39]:

$Z_{R,gen}$ = \$17,500	$Z_{R,con}$ = \$8,000	$Z_{R,eva}$ = \$16,000	$\dot{W}_{R,p}$ = 10 kW
$Z_{R,abs}$ = \$16,500	$Z_{R,HX1}$ = \$12,000	$Z_{R,p}$ = \$2,100	

The heat transfer areas of each component can be computed using the logarithmic mean temperature difference (LMTD) method:

$$\dot{Q}_k = U_k A_k \cdot \text{LMTD}_k \tag{A3}$$

$$\text{LMTD}_k = \frac{\left(T_{H,in} - T_{C,in}\right) - \left(T_{H,out} - T_{C,out}\right)}{\ln\left(\frac{T_{H,in} - T_{C,in}}{T_{H,out} - T_{C,out}}\right)} \tag{A4}$$

where $\dot{Q}_k$ is the heat transfer rate of the component, A_k the heat transfer area, U_k the overall heat transfer coefficient, and LMTD_k the log mean temperature difference for a parallel-flow heat exchanger. Subscripts H and C represent the hot and cold streams, respectively.

Overall heat transfer coefficients for the ARS generator, condenser, evaporator, absorber, rectifier, and solution heat exchanger are taken as 1.5, 2.5, 1.5, 0.7, 2.5, and 1 kW/m⁻² K⁻¹, respectively [108]. MED effects' overall heat transfer coefficients are calculated according to [34].

With the purpose of updating all costs obtained from Eqs. (A2)–(A4) to the year 2012, using the Marshall & Swift Equipment Index, the following relation is used in this work:

$$Z_{k,2012} = Z_k \cdot \left(\frac{\text{Cost index}_{2012}}{\text{Cost index}_k} \right) \tag{A5}$$

A. MED subsystem capital and operational costs

Both capital and operational costs can be estimated as recommended by Alasfour and Bin Amer [38].

A.1. Capital cost

$$C_{Area} = Z_{effect,2012} + Z_{MED,cond,2012} \tag{A6}$$

$$C_{Equipment} = 400\% \cdot C_{Area} \tag{A7}$$

$$C_{Site} = 400\% \cdot C_{Equipment} \tag{A8}$$

$$C_{Freight} = 5\% \cdot \left(C_{Area} + C_{Equipment} + C_{Site} \right) \tag{A9}$$

$$C_{Construction} = 15\% \cdot C_{Equipment} \tag{A10}$$

$$C_{Engineering} = 10\% \cdot C_{Equipment} \tag{A11}$$

$$C_{Contingency} = 10\% \cdot \left(C_{Area} + C_{Equipment} + C_{Site} \right) \tag{A12}$$

$$C_{CAPEX,total} = C_{Area} + C_{Equipment} + C_{Site} + C_{Freight} + C_{Construction} + C_{Engineering} + C_{Contingency} \tag{A13}$$

A.2. Annual operational cost

$$C_{Labor} = 10\% \cdot AOH \cdot \dot{V}_{Daily\ distilled} \tag{A14}$$

$$C_{Chemical} = 4\% \cdot AOH \cdot \dot{V}_{Daily\ distilled} \tag{A15}$$

$$C_{Insurance} = 0.5\% \cdot C_{Area} \tag{A16}$$

$$C_{pumping} = 1.75 \cdot AOH \cdot \dot{V}_{Daily\ distilled} \cdot C_{electricity} \tag{A17}$$

$$C_{maintenance} = 20\% \cdot TAC \tag{A18}$$

$$C_{OPEX,total} = C_{Labor} + C_{Chemical} + C_{Insurance} + C_{pumping} + C_{maintenance} \tag{A19}$$

where $C_{OPEX,total}$ [2012 USD] represents annual expenses (not adjusted to present value), AOH is annual operation hours (assuming 24 hours per day, and 345 days per year), $\dot{V}_{Daily\ distilled}$ the daily fresh water capacity in (m^3/day), and $C_{electricity}$ the electricity cost (assuming 0.07 \$/kWh). Note that, in eq. (A17), "1.75" refers to the MED's average pumping electrical energy consumption in (kWh/m^3) [27]. TAC is the total annual cost and can be calculated as:

$$TAC = ACC + AOC \tag{A20}$$

where AOC is the annual operational cost, and ACC the annual capital cost which can be obtained as:

$$\text{ACC} = \text{ZF} \cdot C_{CAPEX,total} \tag{A21}$$

$$\text{ZF} = \frac{i \cdot (1 + i)^{LC}}{(1 + i)^{LC} - 1} \tag{A22}$$

where ZF is the amortization factor, $C_{CAPEX,total}$ the total capital cost, i the interest rate (15%), and LC the plant life cycle (20 years).

Desalination processes, in general, are highly energy intensive processes, making energy operational costs critical. Annual energy costs can be calculated as below, if the thermal energy is supplied in the form of steam by burning fuel, e.g. natural gas:

$$C_{fuel} = \frac{C_f \cdot \dot{Q}_{Heat,in} \cdot \text{AOH} \cdot (3600 \text{ s/hr})}{\eta_{Boiler} \cdot \text{HHV} \cdot \rho_{fuel}} \tag{A23}$$

where C_f is the fuel specific cost in ($/m³), $\dot{Q}_{Heat,in}$ the heat input rate into the system in (kW), η_{Boiler} the boiler efficiency, HHV the higher heating value in (kJ/kg), and ρ_{fuel} the fuel density in (kg/m³) [109]. For exhaust-heat-driven systems, the cost of fuel is taken as zero.

B. ARS subsystem capital and operational costs

The ARS subsystem capital cost is simply the sum of all component costs:

$$Z_{ARS} = \sum Z_{k,2012} \tag{A24}$$

where k includes the absorber, solution heat exchanger, generator, rectifier, condenser, evaporator, and pump.

The pumping operational cost for the ARS is estimated as:

$$C_{ARS,pump} = \dot{W}_p \cdot \text{AOH} \cdot C_{electricity} \tag{A25}$$

Unit production cost of water ($/m³) and cooling ($/ton.hr) can be calculated as

$$\text{UPC}_{water} = \frac{\text{TAC}_{MED}}{\dot{V}_{hourly\ distilled} \cdot \text{AOH}} \tag{A26}$$

$$\text{UPC}_{cooling} = \frac{\text{TAC}_{NH3H2O}}{\dot{Q}_{eva} \cdot \text{AOH}} \tag{A27}$$

where $\dot{Q}_{eva}$ is the cooling capacity in tons.

9. APPENDIX B

STATE POINTS FOR 1S–NH3H2O–MED AND 2S–NH3H2O–MED SYSTEMS

Table A.1
State points for 1s–NH₃H₂O–MED system and the calculated results

	Point	m (kg/s)	P (kPa)	T (ºC)	x (kg/kg)*	h (kJ/kg)	s (kJ/kg.K⁻¹)
	1	6.57	244.9	40.0	0.3709	-43.3	0.472
	2	6.57	3328.4	40.5	0.3709	-38.5	0.476
	3	6.57	3328.4	148.9	0.3709	475.0	1.872
	4	5.67	3328.4	171.4	0.2709	596.3	2.108
	5	5.66	3328.4	40.5	0.2709	0.979	0.53
	6	5.66	244.9	41.1	0.2709	0.979	0.541
	7	1.07	3328.4	147.8	0.9008	1644.9	4.789
	8	0.17	3328.4	147.8	0.3709	457.6	1.831
	9	0.90	3328.4	71.7	0.9996	1283.6	3.872
	10	0.90	3328.4	70.0	0.9996	345.7	1.121
	11	0.90	3328.4	35.6	0.9996	169.3	0.579
	12	0.90	244.9	-14.1	0.9996	169.3	0.670
	13	0.90	244.9	-10.0	0.9996	1258.8	4.861
	14	0.90	244.9	65.9	0.9996	1435.3	5.447
	A1	1	1554	200.0	-	2793	6.431
	A2	1	1554	200.0	-	852.4	2.331
	S	39.62	101.3	27.0	0.0350	107.7	0.377
	R	28.56	101.3	33.5	0.0350	133.8	0.463
	F	11.07	101.3	33.5	0.0350	133.8	0.463
Cell 1	distilled 1	0.04			-	417.5	1.303
	vM 1	0.59	27.4	67.0	-	2621	7.799
	BC 1	10.48			0.0370	267.5	0.876
Cell 2	distilled 2	0.39			-	280.4	0.918
	vM 2	0.38	25.2	65.2	-	2618	7.827
	BC 2	10.10			0.0384	259.6	0.852
Cell 3	distilled 3	0.39			-	272.7	0.896
	vM 3	0.38	23.1	63.3	-	2614	7.857
	BC 3	9.72			0.0399	251.5	0.827
Cell 4	distilled 4	0.39			-	264.8	0.872
	vM 4	0.38	21.1	61.3	-	2611	7.888
	BC 4	9.34			0.0415	243.1	0.802
Cell 5	distilled 5	0.39			-	256.5	0.847
	vM 5	0.38	19.2	59.2	-	2607	7.920
	BC 5	8.96			0.0433	234.4	0.775
Cell 6	distilled 6	0.39			-	247.9	0.822
	vM 6	0.38	17.4	57.1	-	2604	7.955
	BC 6	8.58			0.0452	225.3	0.746
Cell 7	distilled 7	0.39			-	239	0.794
	vM 7	0.38	15.6	54.8	-	2600	7.992
	BC 7	8.20			0.0473	215.8	0.717
Cell 8	distilled 8	0.39			-	229.6	0.766
	vM 8	0.38	13.9	52.5	-	2596	8.032
	BC 8	7.82			0.0496	205.7	0.685
Cell 9	distilled 9	0.39			-	219.6	0.736
	vM 9	0.38	12.3	49.9	-	2591	8.075
	BC 9	7.44			0.0521	195.1	0.651
Cell 10	distilled 10	0.39			-	209.1	0.703
	vM 10	0.38	10.8	47.3	-	2586	8.123
	BC 10	7.06			0.0549	183.8	0.615
Cell 11	distilled 11	0.39			-	197.8	0.668
	vM 11	0.38	9.3	44.3	-	2581	8.175
	BC 11	6.69			0.0579	171.6	0.575
Cell 12	distilled 12	0.38			-	185.6	0.630
	vM 12	0.38	7.8	41.1	-	2575	8.234
	BC 12	6.31			0.0614	158.3	0.531
Cell 13	distilled 13	0.38			-	172.3	0.588
	vM 13	0.38	6.5	37.6	-	2569	8.301
	BC 13	5.93			0.0653	143.6	0.483
Cell 14	distilled 14	0.34			-	157.4	0.540
	vM 14	0.38	5.2	33.5	-	2562	8.38
	BC 14	5.55			0.0698	127.1	0.427

$\dot{Q}_{abs} = 1{,}583 \ kW_{th}$ $\quad$ $\dot{Q}_{rec} = 525 \ kW_{th}$ $\quad$ $\dot{Q}_{con} = 845 \ kW_{th}$ $\quad$ $\dot{Q}_{eva} = 982 \ kW_{th}$

$V_{distilled} = 19.96 \ m^3/hr$ $\quad$ COP = 0.498 $\quad$ GOR = 5.515 $\quad$ $\eta_{II,system} = 22.79 \ \%$

*Ammonia mass flow rate in the solution for ARS and water salinity for MED

Table A.2
State points for 2s–NH₃H₂O–MED system and the calculated results

	Point	m (kg/s)	P (kPa)	T (°C)	x (kg/kg)*	h (kJ/kg)	s (kJ/kg.K⁻¹)
	1	16.09	272.8	40	0.3883	-47.9	0.465
	2	16.09	1548.0	40.2	0.3883	-45.9	0.467
	3	16.09	1548.0	104.4	0.3883	255.3	1.337
	4	15.10	1548.0	112.1	0.3483	286.9	1.406
	5	15.10	1548.0	40.2	0.3483	-34.2	0.484
	6	15.10	272.8	40.5	0.3483	-34.2	0.489
	7	1.07	1548.0	103.4	0.9549	1524.5	4.835
	8	0.07	1548.0	103.4	0.3883	238.1	1.291
	9	1.00	1548.0	67.3	0.9950	1383.3	4.445
	10	1.24	1548.0	40	0.9950	187.3	0.662
	11	1.24	1548.0	-3.5	0.9950	-18.8	-0.046
	12	1.24	272.8	-11.4	0.9950	-18.8	-0.037
	13	1.24	272.8	-10	0.9950	1163.6	4.456
	14	1.24	272.8	35.2	0.9950	1369.8	5.195
	15	0.25	272.8	35.2	0.9950	1369.8	5.195
	16	4.09	272.8	112.2	0.0623	429.4	1.486
	17	4.09	1548.0	112.4	0.0623	431.2	1.487
	18	4.09	1548.0	184.6	0.0623	785.1	2.321
	19	3.84	1548.0	199.3	0.0023	847.7	2.333
	20	3.84	1548.0	112.4	0.0023	471.1	1.452
	21	3.84	272.8	112.6	0.0023	471.1	1.456
	22	1.01	1548.0	183.3	0.3159	2414.2	6.282
	23	0.71	1548.0	183.3	0.0623	742.6	2.228
	24	0.29	1548.0	112.4	0.9317	1572.8	4.954
	25	1.24	1548.0	67.3	0.9950	1383.3	4.445
	26	1.00	272.8	35.2	0.9950	1369.8	5.195
	27	0.25	1548.0	67.3	0.9950	1383.3	4.445
	28	0.05	1548.0	67.3	0.5938	79.6	0.832
	29	0.25	272.8	40.5	0.9950	1381.6	5.234
	A1	1	1554.0	200	-	2793.0	6.431
	A2	1	1554.0	200	-	852.4	2.331
	S	51.58	101.3	27	0.0350	107.7	0.377
	R	37.17	101.3	33.53	0.0350	133.8	0.463
	F	14.41	101.3	33.53	0.0350	133.8	0.463
Cell 1	distilled 1	0.06			-	417.5	1.303
	vM 1	0.76	27.4	67	-	2621.0	7.799
	BC 1	13.65			0.0370	267.5	0.876
Cell 2	distilled 2	0.51			-	280.4	0.918
	vM 2	0.50	25.2	65.16	-	2618.0	7.827
	BC 2	13.15			0.0385	259.6	0.852
Cell 3	distilled 3	0.51			-	272.7	0.896
	vM 3	0.50	23.1	63.25	-	2614.0	7.857
	BC 3	12.65			0.0400	251.5	0.827
Cell 4	distilled 4	0.51			-	264.8	0.872
	vM 4	0.50	21.1	61.28	-	2611.0	7.888
	BC 4	12.15			0.0417	243.1	0.801
Cell 5	distilled 5	0.51			-	256.5	0.847
	vM 5	0.50	19.2	59.23	-	2607.0	7.920
	BC 5	11.66			0.0436	234.4	0.774
Cell 6	distilled 6	0.51			-	247.9	0.822
	vM 6	0.49	17.4	57.09	-	2604.0	7.955
	BC 6	11.16			0.0456	225.2	0.746
Cell 7	distilled 7	0.51			-	239.0	0.794
	vM 7	0.49	15.6	54.84	-	2600.0	7.992
	BC 7	10.67			0.0478	215.6	0.716
Cell 8	distilled 8	0.51			-	229.6	0.766
	vM 8	0.49	13.9	52.46	-	2596.0	8.032
	BC 8	10.18			0.0502	205.5	0.684
Cell 9	distilled 9	0.50			-	219.6	0.736
	vM 9	0.49	12.3	49.95	-	2591.0	8.075
	BC 9	9.68			0.0529	194.9	0.650
Cell 10	distilled 10	0.50			-	209.1	0.703
	vM 10	0.49	10.8	47.25	-	2586.0	8.123
	BC 10	9.19			0.0558	183.5	0.613
Cell 11	distilled 11	0.50	9.3	44.33	-	197.8	0.668
	vM 11	0.49			-	2581.0	8.175

	BC 11	8.70			0.0591	171.3	0.574
Cell 12	distilled 12	0.50			-	185.6	0.630
	vM 12	0.49	7.8	41.14	-	2575.0	8.234
	BC 12	8.21			0.0628	158.0	0.530
Cell 13	distilled 13	0.50			-	172.3	0.588
	vM 13	0.49	6.5	37.58	-	2569.0	8.301
	BC 13	7.72			0.0671	143.3	0.481
Cell 14	distilled 14	0.44			-	157.4	0.540
	vM 14	0.49	5.2	33.53	-	2562.0	8.380
	BC 14	7.23			0.0719	126.6	0.425

$\dot{Q}_{abs.1} = 1{,}615 \text{ kW}_{th}$ $\dot{Q}_{abs.2} = 395 \text{ kW}_{th}$ $\dot{Q}_{rec,1} = 231 \text{ kW}_{th}$ $\dot{Q}_{rec,2} = 1{,}436 \text{ kW}_{th}$

$\dot{Q}_{rec,3} = 116 \text{ kW}_{th}$ $\dot{Q}_{con} = 1{,}486 \text{ kW}_{th}$ $\dot{Q}_{eva} = 1{,}469 \text{ kW}_{th}$ $V_{distilled} = 26 \text{ m}^3/\text{hr}$

$COP = 0.742$ $GOR = 7.178$ $\eta_{II,system} = 30.42$

*Ammonia mass flow rate in the solution for ARS and water salinity for MED

10. APPENDIX C

CALCULATION OF SPECIFIC THERMAL CAPACITY AND VAPOR PRESSURE OF LiCl AQUEOUS SOLUTION

i.   Specific thermal capacity ($c_{p,s}$) of LiCl aqueous solution

The specific thermal capacity ($c_{p,s}$) of the LiCl aqueous solution is calculated as introduced by Conde [60] in terms of its desiccant solution concentration (χ) and temperature (T) in Kelvin as follows:

$$C_{p,sol}(T,\chi) = C_{p,H2O}(T) \cdot [1 - f_1(\chi) \cdot f_2(T)] \tag{C1}$$

where $C_{p,H2O}$ is the specific heat at constant pressure of pure water in (kJ/kg). $f_1(\chi)$ and $f_2(T)$ can be evaluated as

$$f_1(\chi) = \begin{cases} A\chi + B\chi^2 + C\chi^3, & \chi \leq 0.31 \\ D + E\chi, & \chi > 0.31 \end{cases} \tag{C2}$$

$$f_2(T) = F\left(\frac{T}{228} - 1\right)^{0.02} + G\left(\frac{T}{228} - 1\right)^{0.04} + H\left(\frac{T}{228} - 1\right)^{0.06} \tag{C3}$$

The parameters of Eqs. (A2) and (A3) for the specific thermal capacity of the aqueous solutions of lithium chloride (LiCl) are shown below:

A	B	C	D	E	F	G	H
1.43980	-1.24317	-0.12070	0.12825	0.62934	58.5225	-105.634	47.7948

ii.   Vapor pressure (P_{sol}) of LiCl aqueous solution

The vapor pressure (P_{sol}) of LiCl aqueous solution is calculated as introduced by Conde [60] in terms of its desiccant solution concentration (χ) and temperature (T) in Kelvin;

$$P_{sol}(T,\chi) = P_{H2O}(T) \cdot (\pi\, f(T,\chi)) \tag{C4}$$

where $P_{H2O}(T)$ is the saturation pressure of water, and $f(T,\chi)$ and π can be calculated from

$$f(T,\chi) = 2 - \left[1 + \left(\frac{\chi}{a_0}\right)^{a_1}\right]^{a_2} + \left(\frac{T}{T_{c,H2O}}\right) \cdot \left(\left[1 + \left(\frac{\chi}{a_3}\right)^{a_4}\right]^{a_5} - 1\right) \tag{C5}$$

$$\pi = 1 - \left[1 + \left(\frac{\chi}{a_6}\right)^{a_7}\right]^{a_8} - a_9 \cdot exp(\frac{-(\chi - 0.1)^2}{0.005}) \tag{C6}$$

where $T_{c,H2O}$ is the temperature of water in (K) at the critical point. The parameters of Eqs. (C5) and (A6) for the vapor pressure of the aqueous solutions of lithium chloride (LiCl) are shown below:

a_0	a_1	a_2	a_3	a_4	a_5	a_6	a_7	a_8	a_9
0.28	4.30	0.60	0.21	5.10	0.49	0.362	-4.75	-0.40	0.03

11. APPENDIX D

STATE POINTS FOR THE ORIGINAL AND ENHANCED CYCLES

Table 24. State points for the original cycle (OC) and the calculated results

Point	m	P	T	x*	RH	h	s
	kg/s	kPa	C	kg/kg	%	kJ/kg	kJ/kg.K
1	1	101.3	100	-	-	419.1	1.31
2	1	1554	100.2	-	-	420.8	1.31
3	1	1554	210	-	-	2820	6.49
4	2.62	50	-	-	-	-	-
5 - H_2O	1	101.3	100	-	-	2423	6.68
5 - Air	1.62	101.3	81.3	0.018	5.8	130.2	6.04
6 - H_2O	0.97	101.3	35	-	-	146.7	0.50
6 - Air	1.65	101.3	35	0.037	100	129.1	5.90
7	1.65	101.3	35	0.037	100	129.1	5.90
8	1.60	101.3	35	0.001	3	37.9	5.74
9	1.60	50	-12.9	0.001	41.4	-10.4	5.77
10	1.62	50	13	0.018	95	59.1	6.03
11	13.57	101.3	34	0.380	-	95.4	-
12	13.63	101.3	35	0.378	-	98.5	-
13	13.77	101.3	35	0.375	-	98.8	-
14	13.77	101.3	35	0.375	-	98.8	-
15	13.57	101.3	95	0.380	-	285.8	-
16	0.19	101.3	95	-	-	2668	7.42
17	0.19	101.3	35	-	-	146.7	0.50
18	0.17	101.3	35	-	-	146.7	0.50
19	0.03	101.3	35	-	-	146.7	0.50
20	0.03	50	35	-	-	146.7	0.50
21	3.59	50	20	-	-	83.8	0.30
22	3.56	50	13	-	-	54.6	0.20
A1	6.81	101.3	35	0.029	80	109.5	5.99
A2	6.67	101.3	35	0.009	25.0	57.7	5.81
A3	6.67	101.3	25.19	0.009	44	47.7	5.78
A4	6.67	101.3	18	0.005	40	31.1	5.72
A5	6.70	101.3	21	0.009	60	44.8	5.77
A6	6.70	101.3	30.76	0.009	33.7	54.8	5.80

Heat input rate = 2399 kW$_{th}$	Q$_{HX1}$ = 111 kW$_{th}$
Net work output= 75 kW$_{th}$	Q$_{HX2}$ = 2583 kW$_{th}$
Condenser heat rate = 2278 kW$_{th}$	Q$_{HX3}$ = 489 kW$_{th}$
Fresh water production = 0.6 m³/hr	Q$_{HX5}$ = 67 kW$_{th}$

* Humidity ratio for Air-H_2O in (kg water/kg dry air) & desiccant solution concentration for LiCl-H_2O in (kg LiCl/ kg solution)

Table 25. State points for the enhanced cycle (EC) and the calculated results

Point	m	P	T	x*	RH	h	s
	kg/s	kPa	C	kg/kg	%	kJ/kg	kJ/kg.K
1	1	70.1	90	-	-	376.9	1.19
2	1	1554	90.2	-	-	378.7	1.19
3	1	1554	210	-	-	2820.0	6.49
4	1	70.1	90	-	-	2378.0	6.70
5	7.14	101.3	92.4	0.018	3.8	141.7	6.07
6	7.14	101.3	35	0.018	51.2	82.0	5.80
7	7.14	101.3	35	0.018	51.2	82.0	5.80
8	7.02	101.3	35	0.001	3	37.9	5.74
9	7.02	50	-12.9	0.001	41.4	-10.4	5.77
10	7.14	50	13	0.018	95	59.1	6.03
11	14.02	101.3	34	0.380	-	95.4	-
12	14.14	101.3	35	0.377	-	98.7	-
13	14.74	101.3	35	0.361	-	99.9	-
14	14.74	101.3	35	0.361	-	99.9	-
15	14.02	101.3	85	0.380	-	253.0	-
16	0.72	101.3	85	-	-	2651	7.54
17	0.72	101.3	35	-	-	146.7	0.50
18	0.60	101.3	35	-	-	146.7	0.50
19	0.12	101.3	35	-	-	146.7	0.50
20	0.12	50	35	-	-	146.7	0.50
21	22.11	50	18	-	-	75.5	0.27
22	21.99	50	13	-	-	54.6	0.20
A1	29.94	101.3	35	0.029	80	109.5	5.99
A2	29.34	101.3	35	0.009	25.0	57.7	5.81
A3	29.34	101.3	25.19	0.009	43.9	47.7	5.78
A4	29.34	101.3	18	0.005	40	31.1	5.72
A5	29.46	101.3	21	0.009	60	44.8	5.77
A6	29.46	101.3	30.76	0.009	33.7	54.8	5.80

Heat input rate = 2441 kW$_{th}$	Q$_{HX1}$ = 487 kW$_{th}$
Net work output= 191 kW$_{th}$	Q$_{HX2}$ = 2210 kW$_{th}$
Condenser heat rate = 2001 kW$_{th}$	Q$_{HX3}$ = 1814 kW$_{th}$
Fresh water production = 2.17 m³/hr	Q$_{HX4}$ = 426 kW$_{th}$
	Q$_{HX5}$ = 295 kW$_{th}$

* Humidity ratio for Air-H$_2$O in (kg water/kg dry air) & desiccant solution concentration for LiCl-H$_2$O in (kg LiCl/ kg solution)